UNIVERSITÉ DE MONTRÉAL

APPLICATION OF SPACE- AND TIME-MODULATED DISPERSION ENGINEERED METAMATERIALS TO SIGNAL PROCESSING AND MAGNETLESS NONRECIPROCITY

SAJJAD TARAVATI
DÉPARTEMENT DE GÉNIE ÉLECTRIQUE
ÉCOLE POLYTECHNIQUE DE MONTRÉAL

THÈSE PRÉSENTÉE EN VUE DE L'OBTENTION
DU DIPLÔME DE PHILOSOPHIÆ DOCTOR
(GÉNIE ÉLECTRIQUE)
SEPTEMBRE 2017

UNIVERSITÉ DE MONTRÉAL

ÉCOLE POLYTECHNIQUE DE MONTRÉAL

Cette thèse intitulée :

APPLICATION OF SPACE- AND TIME-MODULATED DISPERSION ENGINEERED METAMATERIALS TO SIGNAL PROCESSING AND MAGNETLESS NONRECIPROCITY

présentée par : TARAVATI Sajjad
en vue de l'obtention du diplôme de : Philosophiæ Doctor
avec M. CALOZ Christophe, Ph. D., directeur de recherche
a été dûment acceptée par le jury d'examen constitué de :

M. WU Ke, Ph. D., président
M. MÉNARD David, Ph. D., membre
M. LAURIN Jean-Jacques, Ph. D., membre
M. KOUKI Ammar, Ph. D., membre externe

DEDICATION

*This dissertation is lovingly dedicated to my mother,
Manzar Zaki, for her endless support and
constant love throughout my life.*

RÉSUMÉ

Les métamatériaux sont des structures conçues pour intéragir avec les composantes électriques et magnétiques de la lumière d'une manière particulière qui n'est pas possible avec des matériaux naturels. Elles sont composées de méta-atomes, qui sont faits d'un ensemble d'éléments de taille plus petite que la longueur d'onde, réalisés à partir de matériaux composites tels que des métaux ou des diélectriques. Les métamatériaux acquièrent leurs propriétés de leur structure macroscopique plutôt que des propriétés microscopiques des élements qui les composent. Le mot « méta » provient du Grec dont la signification est *au-delà*, indiquant le concept d'une abstraction au-delà d'un autre concept. Les métamatériaux statiques conventionnels tirent profit de l'ingénierie spatiale de la dispersion pour présenter des propriétés exotiques non observées dans les matériaux usuels, tel qu'un indice de réfraction négatif. Un type plus sophistiqué de métamatériaux statiques, basé sur une structure dispersive modulée spatialement, peut être employé pour former un manteau d'invisibilité.

Au cours de la dernière décennie, les métamatériaux dynamiques ont été présentés comme une nouvelle génération de systèmes électromagnétiques versatiles et ont rapidement acquis un grand intérêt de la part de la communauté scientifique. Les milieux modulés dans "l'espace-temps", dont les paramètres constitutifs varient périodiquement dans l'espace et le temps, représentent une classe avancée de métamatériaux dynamiques non-réciproques. De tels milieux sont dotés de propriétés particulières telles que la capacité à générer des fréquences de façon non-réciproque. Contrairement aux métamatériaux périodiques statiques tels que les cristaux photoniques, les milieux modulés dans l'espace-temps présentent une dispersion asymétrique. D'ailleurs, par analogie avec les milieux en mouvement, où la vitesse du milieu est limitée à la vitesse de la lumière, les milieux modulés dans l'espace-temps peuvent acquérir des vitesses subluminales et superluminales. En conséquence, un éventail varié de bandes d'énergie orientées horizontalement, obliquement et verticalement sont accessibles dans les milieux modulés dans l'espace-temps, alors que dans les métamatériaux conventionnels ou les réseaux de Bragg, les bandes d'énergie sont seulement orientées horizontalement. Ces bandes d'énergie obliques et verticales apportent des degrés de liberté additionnels qui peuvent être utilisés pour la conception de différents systèmes électromagnétiques. La non-réciprocité basée sur la modulation dans l'espace-temps offre un chemin viable vers la conception de systèmes électromagnétiques non-réciproques intégrés. Cette technique résoud les problèmes des méthodes conventionnelles pour réaliser de la non-réciprocité, telles que par exemple la grosseur et l'incompatibilité avec la technologie de circuits intégrés dont la non-réciprocité est basée sur l'application d'un champ magnétique, et la restriction en puissance des signaux actionnant

les systèmes non-linéaires non-réciproques.

Les techniques de modulation spatio-temporelles ainsi que les techniques d'ingénierie de la dispersion spatiale et temporelle offrent une grande gamme de propriétés électromagnétiques uniques à découvrir. Cette thèse révèle quelques propriétés sans précédent de structures dont la dispersion est contrôlée par modulation spatiale ou spatio-temporelle. En tirant profit de ces propriétés, une diversité de dispositifs électromagnétiques possédant une efficacité augmentée, dont la dispersion spatiale et temporelle est contrôlée par modulation spatiale ou spatio-temporelle du milieu, seront présentés.

Tout d'abord, deux phaseurs non-uniformes, ou spatiallement modulés, sont présentés : un phaseur non-uniforme de section en C et une ligne non-uniforme chargée de tronçons de ligne non-uniformes. La première structure, le phaseur de section en C, a une dispersion temporelle qui dépend du couplage non-uniforme. Ce phaseur, qui possède une taille plus petite que la longueur d'onde, est une évolution par rapport aux phaseurs qui sont faits d'une cascade de sections quart d'onde couplées. La non-uniformité de la structure augmente les degrés de liberté, et en exploitant ces degrés de liberté, ce phaseur présente un retard de groupe qu'il serait impossible de réaliser en utilisant des phaseurs à sections en C uniformes. De plus, il possède une plus grande largeur de bande due à l'apériodicité de son retard de groupe, et offre ainsi de grands avantages pour le traitement de signaux radio analogiques. La seconde structure, un phaseur à tronçons modulés spatiallement, est une alternative aux phaseurs conventionnels faits de sections à lignes couplées. Des lignes en circuit ouvert et en circuit fermé sont employées pour réaliser des formes flexibles spécifiques de retard de groupe avec des réponses plates de grandeur de transmission. Contrairement aux phaseurs conventionnels, qui sont basés sur le couplage et sont donc fabriqués en multi-couche, ce phaseur, qui se compose des lignes de transmission, peut être réalisé en technologie microruban. Il s'intègre donc avec différents composants mis en cascade sur une structures planaire. Puisque le dispositif est intégrable, il réduit la complexité, augmente la flexibilité de conception, et abaisse le coût de structures qui requièrent des phaseurs.

Deuxièmement, une métasurface dispersive non-gyrotropique et non-réciproque modulée spatio-temporellement est présentée. Cette métasurface, une version bidimensionnelle et compacte des métamatériaux conventionnels, qui sont volumiques, brise la symmétrie temporelle par un couplage unidirectionnel fort entre l'onde incidente, un circuit électronique unilatéral, et l'onde sortante. La métasurface n'exige pas d'aimant polarisant, et est donc légère et favorable à la fabrication de circuits intégrés. Elle fonctionne sur une large plage d'angles d'incidence et absorbe efficacement les ondes réfléchies pour tous les angles d'incidence. Il y a un gain de transmission sur une plage d'angle d'incidence d'environ 120^o, rendant cette structure intéressante pour des une quantité applications possibles telles que des isolateurs, des circulateurs et des manteaux d'invisibilité tels que les manteaux d'invisibilité.

La diffusion électromagnétique d'ondes incidentes obliques sur un bloc modulé périodiquement dans l'espace-temps sera étudiée. On montrera qu'un tel métamatériau dynamique génère des harmoniques et filtre les fréquences spatiales. Pour des ondes à incidence oblique, les harmoniques de basse fréquence sont transformées en ondes de surface, tandis que les harmoniques de haute fréquence sont transmises. Dans le régime de quasi-sonique, où la vitesse de la modulation spatio-temporelle est proche de la vitesse des ondes électromagnétiques dans le milieu non-modulé, l'onde incidente dans une une direction est fortement couplée aux harmoniques spatio-temporelles transmises, alors que dans l'autre direction il y a peu de couplage à d'autres harmoniques.

La non-réciprocité du milieu modulé spatio-temporellement dans la zone quasi-sonique sera alors exploitée pour la réalisation d'un isolateur électromagnétique et sera expérimentalement démontrée à des fréquences micro-ondes. Puis, la démonstration expérimentale d'un nouveau type d'isolateur optique sera présentée. Cet isolateur optique tire profit des bandes interdites qui sont asymétriques dans un milieu modulé spatio-temporellement. Ensuite, une nouvelle technique d'isolation électromagnétique basée sur la cohérence à sens unique entre l'onde d'entrée et la structure modulée est présentée. La modulation et l'onde incidente ont la même fréquence et l'opération de la structure est dictée par la différence de phase entre elles. Pour un déphasage et une profondeur de modulation donnée, correspondant à l'état de cohérence, la structure fonctionne en tant qu'isolateur. La structure proposée ne produit pas de fortes harmoniques indésirables et a une efficacité supérieure comparée aux isolateurs basés sur une modulation spatio-temporelles précédemment rapportés. D'ailleurs, le signal d'entrée module la structure elle-même, et par conséquent cette structure est auto-modulée.

Finalement, un système à onde de fuite qui effectue des opérations de mélangeur-duplexeur-antenne basé sur l'ingénierie spatiale de la dispersion et une modulation spatio-temporelle est présentée. Ce système fonctionne comme un émetteur-récepteur, avec les opérations de up-conversion et de down-conversion effectuées par des transitions spatio-temporelles. L'opération de duplexage est dûe à la nature non-réciproque de la structure, et l'opération de rayonnement est réalisée par la structure à onde de fuite. Une solution électromagnétique rigoureuse est dérivée pour la distribution du champ et la relation de dispersion. Le système est mis en application sous la forme d'une structure à onde de fuite en technologie microruban modulée spatio-temporellement. La modulation est réalisée par une rangée de varacteurs espacés à une distance inférieure à la longueur d'onde. En plus de l'opération globale de mélangeur-duplexeur-antenne, on observe que le faisceau généré balaie l'espace en fonction de la fréquence, pour une fréquence d'entrée fixe. Il s'agit d'une des caractéristiques intéressantes du système.

ABSTRACT

Metamaterials are engineered structures which interact with the electric and magnetic components of light in a peculiar way that natural materials do not. These so-called meta-atoms are made of assemblies of subwavelengthly spaced elements fashioned from composite materials such as metals or dielectrics. Metamaterials acquire their properties from their macroscopic structure rather than the microscopic material of which they are made of. The word “Meta” originates from Greek whose meaning is *beyond*, indicating a concept as an abstraction beyond another concept. Conventional static metamaterials take advantage of spatial dispersion engineering to exhibit exotic properties not observed in bulk materials, such as for instance negative refractive index. A more sophisticated type of conventional static metamaterials based on a space-modulated (gradient-index) spatially dispersive structure, was used to form an invisibility cloak.

Over the past decade, *dynamic metamaterials*, as a new generation of versatile electromagnetic systems, have been introduced and soon acquired a surge of scientific interest. “Space-time modulated” media, whose constitutive parameters are periodically varying in space and time, represent an advanced class of nonreciprocal dynamic metamaterials. Such media are endowed with peculiar properties such as nonreciprocal frequency generation. In contrast to static periodic metamaterials such as photonic crystals, periodic space-time modulated media exhibit asymmetric dispersion. Moreover, by analogy with the moving media, where the velocity of the medium is limited to the speed of light, space-time modulated medium may acquire both subluminal and superluminal velocities. As a result, a diverse range of horizontally-, obliquely- and vertically-oriented electromagnetic band-gaps are accessible in space-time modulated media, compared to horizontal bandgaps in conventional metamaterials and Bragg structures. These oblique and vertical electromagnetic band-gaps offer extra degrees of freedom which may be leveraged for the design of different electromagnetic systems. Nonreciprocity based on space-time modulation grants a viable path towards integrated nonreciprocal electromagnetic systems. This addresses issues of conventional nonreciprocity techniques, such as for instance bulkiness and incompatibility with integrated circuit technology in magnet-based nonreciprocity, and signal power restrictions in nonlinear-based nonreciprocity.

Space and time modulation combined with spatial and temporal dispersion engineering techniques offers a variety of unique electromagnetic properties to be discovered. This thesis discloses some unprecedented properties of space and space-time modulated dispersion en-

gineered structures. Leveraging these properties, a diversity of enhanced efficiency and integrated electromagnetic devices formed by spatial/temporal dispersion engineering of space and space-time modulated structures will be introduced.

First of all, two nonuniform, or space-modulated, phasers are presented: a nonuniform C-section phaser and a nonuniform stub-line phaser. The first structure, the nonuniform C-section phaser, is a static space-modulated temporal dispersion engineered C-section phaser, representing the subwavelength-section evolution of the end-connected cascaded quarter-wavelength section coupled-line phaser. This nonuniform C-section phaser, thanks to its extra topological degrees of freedom, presents group delay functions that are unattainable by uniform C-section phasers. Moreover, it exhibits larger bandwidth due to group delay aperiodicity, and thus offers great advantages for radio analog signal processing (R-ASP) systems. Moreover, a static and continuously space-modulated stub-line coupling-free phaser is presented as an alternative to conventional coupled-line sections based phasers to reduce the complexity, enhance the design flexibility, and lower the cost. Continuously space-modulated open- and short-terminated stubs are used to achieve specified flexible group delay shapes with flat transmission magnitude responses. This phaser does not require multilayer technologies since it consists of coupling-free transmission lines, and therefore it can be realized using microstrip technology and integrate with different lumped components and planar structures.

Next, a nonreciproal nongyrotropic magnet-less metasurface is introduced as a space-modulated (gradient), spatiotemporal dispersion engineered structure. This metasurface, a two-dimensional and compact version of conventional volume metamaterials, breaks the time-reversal symmetry by strong unidirectional coupling between the incident wave, a unilateral electronic circuit and the outgoing wave. The metasurface does not require a biasing magnet, and is therefore lightweight and amenable to integrated circuit fabrication, provides a very wide working angle and effectively absorbs backward propagating waves from all angles of incidence, while it exhibits transmission gain over about 120^o, making this structure interesting for a wealth of possible applications such as isolators, circulators and invisibility/illusion cloaks.

The electromagnetic scattering of an obliquely incident wave from a periodically space-time modulated slab will be investigated. It will be shown that such a dynamic metamaterial operates as a nonreciprocal harmonic generator and a spatial-frequency filter. Low frequency harmonics are filtered out in the form of surface-waves, while high-frequency harmonics are transmitted as space-waves. In the quasi-sonic regime, where the velocity of the space-time modulation is close to the velocity of the electromagnetic waves in the background medium, the incident wave strongly couples to space-time harmonics in the forward direction, while in the backward direction weak coupling occurs to other harmonics.

The quasi-sonic nonreciprocity of space-time modulated medium will be then leveraged for the realization of an electromagnetic isolator and will be experimentally demonstrated at microwave frequencies. Then, the experimental demonstration of a novel type of optical isolator will be presented. This optical isolator takes advantage of the asymmetric electromagnetic band-gaps in a space-time modulated medium. Next, a new technique for electromagnetic isolation based on one-way coherency between the input wave and space-time modulated structure will be presented. The modulation and the incident wave have the same frequency and the operation of the structure is dictated by the phase difference between them. At certain phase shifts and modulation depths, corresponding to the coherency condition, the structure operates as an isolator. The proposed structure does not produce strong undesirable harmonics and has superior efficiency compared to previously reported space-time isolators. Moreover, the input signal modulates the structure itself, and hence it operates as a self biased isolator.

Finally, a mixer-duplexer-antenna leaky-wave system based on spatial dispersion engineering of periodic space-time modulation is presented. This system operates as a full transceiver, where the upconversion and downconversion mixing operations are performed by space-time transitions, the duplexing operation is provided by the nonreciprocal nature of the structure, and the radiation operation is given by the leaky-wave nature of the wave. A rigorous electromagnetic solution is derived for the dispersion relation and field distributions. The system is implemented by modulating a microstrip leaky-wave structure by an array of sub-wavelengthly spaced varactors modulated by a RF bias. In addition to the overall mixer-duplexer-antenna operation, frequency beam scanning at fixed input frequency is demonstrated as one of the interesting features of the system.

TABLE OF CONTENTS

LIST OF TABLES

LIST OF FIGURES

LIST OF ACRONYMS AND SYMBOLS

Acronyms

ADS	Advanced Design System
AM	Amplitude Modulation
B	Backward problem
BPF	Band-Pass Filter
BW	Frequency Bandwidth
DCMA	Dispersion Code Multiple Access
F	Forward problem
FBW	Fractional Bandwidth
FDTD	Finite-Difference Time-Domain
LED	Light-Emitting Diode
LWA	Leaky Wave Antenna
MS	Metasurface
NLP	Nonlinear optimization problem
RF	Radio Frequency
RFID	Radio-Frequency Identification
R-ASP	Radio Analog Signal Processing
RX	Receiver
SCS	Surface-Circuit-Surface
S-T	Space-Time
TEM	Transverse Electromagnetic
TX	Transmitter
YIG	Yttrium Iron Garnet

Symbols

τ	Group delay
Γ	Reflection coefficient
ε	Fitness function
c	Speed of light
v	Phase velocity
L	Thickness
Z	Electrical Impedance
h	height of the substrate

W_{e}	Electric energy
W_{m}	Magnetic energy
θ	radiation angle
β	Spatial frequency, wavenumber
λ_{g}	Guided wavelength
T	Transmission
R	Reflection
d_n	Thickness of nth subsection
γ	Space-time velocity ratio
v_{b}	Phase velocity of the background medium
v_{m}	Phase velocity of the modulation
$f_{\mathrm{per}}(.)$	Arbitrary periodic function
k_0	Free-space spatial frequency
δ_{nn}	Kronecker delta
α	Attenuation
ϵ_{m}	Modulation depth
ϵ_{r}	Relative permittivity
ϵ_{av}	Average
ϵ_{e}	Effective permittivity
ϕ	Phase
η	Wave Impedance
ω_0	Temporal frequency of the fundamental temporal harmonic
ω_{m}	Temporal modulation frequency
β_0	Spatial frequency of the fundamental spatial harmonic
β_{m}	Spatial modulation frequency

LIST OF APPENDICES

CHAPTER 1 INTRODUCTION

1.1 History of Space and Time Modulated Dispersion Engineered Metamaterials

Over the past two decades, metamaterials and metasurfaces have spurred a surge of interest in the scientific community due to their unique optical properties [11–22]. The electromagnetic properties of these new class of ordered composites are deliberately engineered to offer a range of advantageous and exceptional responses not readily available in nature. Electromagnetic metamaterials are composed of an arrangement of macroscopic subwavelength scatterers emulating the microscopic particles, e.g. atoms or molecules, of real materials. Considering the sub-wavelength nature of inclusions, metamaterials may be classified in terms of their constitutive parameters, e.g. permittivity, permeability, conductivity and bi-anisotropic parameters. Tailoring these constitutive parameters, provides a variety of metamaterial systems. Metasurfaces are known as the two-dimensional counterparts of volume metamaterials [23–25], where Snell's law is generalized by the introduction of an abrupt phase shift along the optical path, leading to effects such as anomalous reflection and refraction of light [21] and a diversity of unprecedented wave transformation functionalities [26].

Conventional metamaterials are endowed by spatial and temporal dispersion engineering [11–14]. They are volume arrangements of resonant particles composed of wire media and splitring resonators, to realize effective negative permittivity and permeability depending on spatial and temporal frequencies, yielding negative refraction. However, these volume metamaterials suffer from narrow-band operation and losses which is due to the resonant nature of their particles. In contrast to conventional volume metamaterials, new generation of metamaterials are represented by space, time and space-time modulated constitutive parameters. Space and time modulated metamaterials offer various intriguing eletromagnetic properties, including broadband impedance matching [27] and reciprocal frequency generation [28]. However, over the past few years, periodic space-time modulated systems have represented the most celebrated metamaterials, owing to their peculiar properties such as for instance nonreciprocal frequency generation [7, 19, 29], and asymmetric electromagnetic bandgaps [7, 8]. It should be noted that space and time modulated metamaterials may also leverage the spatial and temporal dispersion engineering, representing the most sophisticated and flexible class of electromagnetic systems which provide various exotic and peculiar electromagnetic responses.

Nonuniform transmission lines, also known as width-modulated transmission lines, may represent the most common static space-modulated metamaterials [30]. Thanks to their extra topological degrees of freedom, nonuniform transmission lines are capable to provide variety of eletromagnetic responses that are unattainable by uniform transmission lines. They may be considered as subwavelength evolution of uniform transmission lines [30]. Analysis of continuously modulated nonuniform transmission lines has been investigated using different techniques, including using an iterative and adaptive perturbation technique [31–34], and Taylor series expansion [35]. Moreover, sensitivity analysis of nonuniform transmission lines has been reported in [36]. A variety of enhanced efficiency electromagnetic systems have been reported based on the use of continuously modulated nonuniform metamaterials, such as for instance VLSI interconnection structures to provide smooth connections between high-density IC chips and their chip carriers [37, 38], directional filters [39], impedance matching for complex loads lines [27,40], lowpass filter [41], generalized single-section broad-band asymmetrical Wilkinson power divider [42], miniaturized wide band rat race and branch-line couplers [43–45], dual- and wide-band power dividers with arbitrary power division [46], and matching circuits of multiplexers [47].

Time modulated medium may be represented by a moving medium. It may be shown that such a medium provides unique features, including periodic symmetric dispersion, electromagnetic bandgaps, and reciprocal frequency generation [28].

Spatial dispersion represents a phenomenon where constitutive parameters of the media have dependence on wavevector [48]. Eventhough such a dependence is neglected for simplicity, spatial dispersion exists to varying degrees in all media [48, 49]. All natural and artificial media are spatially discontinuous since they are formed by particles. However, majority of natural materials are represented as effectively continuous media since the optical size of particles, i.e. atoms and molecules, is very small at microwave and optical regimes. However, this homogenization is not valid for cases where the distance between the adjacent particles is non-negligible. In such cases, nonuniformity of the field over the particle and over the unit cell of the composite medium should be taken into account [24]. From the physical point of view, the origin of spatial dispersion is the non-locality of the polarization response, where the response to a force field appears at different locations even in locations where the force is zero [50]. From an engineering point of view, spatial dispersion occurs because of the coupling between particles. Wire media [2, 51], chiral anisotropic structures [52, 53] and uniform metasurfaces [54] are some examples of spatially dispersive metamaterial structures. Leaky-wave antennas are another type of spatially dispersive metamaterials [10]. Recently, there has been a regain interest in leaky-wave antennas due to discovery of new structures and systems [55,56]. Some of the most recent advances in this area include full-space scanners [57, 58], combined duplexer/diplexer-antennas [59] and nonreciprocal leaky-eave antennas utilized as low-profile traveling-wave monopole [60].

C-section phasers represent a temporally dispersive medium, a device providing specified group delay versus frequency responses (linear, quadratic, staircase, Chebyshev, etc.) depending on the application [3]. Various types of reflection-type (one-port) and transmission-type (two-port) microwave phasers have been developed along with corresponding synthesis techniques [61–64]. All-pass phasers based on contra-directional coupled transmission line couplers [65] are particularly attractive in Radio Analog Signal Processing (R-ASP) given their two-port configuration (avoiding the need for circulators or extra couplers), and their simplicity and flexibility responses [66, 67]. A number of applications have been reported based on C-section phasers, direction-of-arrival detectors [68], spectrum sniffers [69], and enhanced signal-to-noise receivers [70].

Space-time varying metamaterials whose constitutive parameters are spatiotemporally modulated, have been theoretically studied for a long time as travelling-wave parametric amplifiers [71–79]. In contrast to moving media, where the velocity of the medium is restricted to the speed of light, space-time modulated medium can present both subluminal and superluminal velocities. In contrast to static periodic media such as for instance photonic crystals, periodic space-time media exhibit asymmetric, tilted dispersion [74, 75]. Moreover, superluminal space-time media produce electromagnetic bandgaps that are oriented vertically, compared to horizontal bandgaps, in the $\omega - \beta$ dispersion diagram, in conventional photonic crystals and Bragg structures. These vertical bandgaps describe instabilities or unbounded growth [75]. Harmonic generation is another feature of space-time media. Recently, it has been pointed out that such unidirectionally modulated metamaterials are fundamentally nonreciprocal [19], and this has triggered a regain of interest in space-time modulated systems [19, 29, 80–83]. Such a medium provides exotic effects such as interband photonic transitions mediated by space-time varying metamaterials [84] and associated nonreciprocity [19,29], inverse Doppler effect in a shockwave induced photonic bandgap structure [85,86], electromagnetic isolation in oblique space-time bandgaps [8], nonreciprocal space-time metasurfaces [87–89], and nonreciprocal antenna systems [9,90–93]. Several applications of space-time modulated nonreciprocal metamaterials have been subsequently reported, including isolators [19], circulators [94, 95], nonreciprocal metasurfaces [6, 87–89] and nonreciprocal antennas [90–93, 96].

Space-modulated temporally dispersive media may be represented by reflective chirped delay lines [62, 97, 98]. Various electromagnetic components may be realized using this class of metamaterials, incluidng multichannel filter using chirped bandgap structure [99, 100], temporal magnification of signals in the ultra-wideband regime [101], and parallel-coupled-line bandpass filter with suppressed spurious passband [102]. Nonuniform leaky-wave antennas are another type of $\chi(\mathbf{r};\omega)$ media [103–105]. This class of leaky-wave antennas present various advantages such as for instance near-field focusing pattern synthesis [106].

1.2 Motivation and Objectives

The motivation for this thesis came from the fact that several key features of space-time modulated dispersion engineered metamatarials were still missing in the literature. This thesis focuses on some of the most unexplored space- and tme-modulated dispersion engineered metamaterials, and experimentally presents various enhanced efficiency and integrated electromagnetic components which may be used in different applications as desribed in the following.

- Coupled-line all-pass phasers, representing temporally dispersive metamaterials, are the most common type of phasers [3, 61, 67]. However, they suffer from restricted group delay responses, due to their periodic response, restricted bandwidth, due to the related presence of spurious group delay harmonic peaks, and substantial loss, due to their electrically large unfolded size. Chapter 3 shows how these limitations can be mitigated by using space-modulated temporally dispersive medium, i.e. *continuously nonuniform* C-section phasers [1, 107], as the sub-wavelength section limit of step-discontinuity multi-section coupled-line phasers [67]. Although this nonuniform C-section phasers may be considered as the most flexible transmission-type phasers [1], they still suffer from requiring high coupling coupled-line sections, demanding multilayer technologies which represents design complexity and high cost. To overcome this issue, nonuniform stub-line coupling-free phasers will be introduced as an alternative to conventional coupled-line sections based phasers to reduce the complexity and lower the cost in Radio Analog Signal Processing (R-ASP) systems. This nonuniform stub-line coupling-free phaser does not require multilayer technologies since it consists of coupling-free transmission lines, and therefore it can be realized using microstrip technology and integrate with different lumped components and planar structures.
- It will be shown that space-modulated nonreciprocal metasurfaces may be utilized to form a versatile nongyrotropic magnetless spatial isolator [6]. The vast majority of the metasurfaces reported to date are restricted to reciprocal responses. Introducing nonreciprocity requires breaking time reversal symmetry. This can be accomplished via the magneto-optical effect [108–113], nonlinearity [114–116], space-time modulation [19, 87–89, 93, 117, 118] or metamaterial transistor loading [119–122]. However, all these approaches suffer from a number of drawbacks. The magneto-optical approach requires bulky, heavy and costly magnets [110]. The nonlinear approach involves dependence to signal intensity and severe nonreciprocity-loss trade-off [123]. Finally, the transistor-based nonreciprocal metasurfaces reported in [120, 122] are intended to operate as Faraday rotators, whereas gyrotropy is undesired in applications requiring nonreciprocity without alteration of the wave polariza-

tion, such as for instance one-way screens, isolating radomes, radar absorbers or illusion cloaks.

- This thesis investigates different features of space-time modulated metamaterials. First, the nonreciprocal electromagnetic scattering of obliquely incident electromagnetic waves from a periodically space-time modulated slab will be thoroughly evaluated. It is shown that such structures operate as nonreciprocal harmonic generators and spatial-frequency filters. For oblique incidences, low frequency harmonics are filtered out in the form of surface waves, while high-frequency harmonics are transmitted as space waves. In the quasi-sonic regime, where the velocity of the space-time modulation is close to the velocity of the electromagnetic waves in the background medium, the incident wave is strongly coupled to space-time harmonics in the forward direction, while in the backward direction it exhibits low coupling to other harmonics. Previous research works on space-time modulated media have been mostly focused on propagation in infinite space-time media or normal incidence on a semi-infinite space-time modulated region. *Oblique* electromagnetic incidence on a space-time modulated *slab* has unique features that have been unexplored.
- Taking advantage of the unique features of the space-time modulated media, three magnetless isolators, with distinct properties and specifications and suitable for distinct applications, will be introduced. First, an efficient quasi-sonic isolator will be presented based on the properties of space-time modulated medium in the sonic region. This isolator presents a fairly high isolation, with a short length, which makes it a good candidate for isolation in microwave and milimeterwave regimes. Next, leveraging the electromagnetic bandgaps in a space-time modulated medium, an isolator will be shown which is more suitable for optical regime. Finally, a self-biased and broadband isolator with high efficiency based on the nonreciprocal electromagnetic coherency in a space-time modulated medium will be introdued.

Ferrite isolators are endowed with high power-handling capability, high isolation and no dc power consumption. However, they suffer from the bulkiness, heaviness, incompatibility with integrated circuits and high cost [124]. Active, transistor-based, isolators may overcome these shortcomings [6, 125], but they endure restricted power handling and noise by the transistors, sensitivity to reflected wave, and harmonic generation due to the nonlinearity. Moreover, these isolators may present the isolation in the cost of the passing-way gain, which may not be always desired [126]. Isolation based on nonlinearity suffers for requiring high signal levels [115, 116, 127–129], while in the presence of a high-level input signals in a nonlinear optical isolator, some low-level signals reciprocally pass through the isolator, and hence it does not really operate as an optical isolator [130]. Balanced loss-gain parity-time symmetric media [131–133], exhibit unidirectional properties [134–138].

However, the nonreciprocity of these devices [133, 135] is due to nonlinearity rather than being a consequence of PT symmetry. Linear PT media are constrained to be reciprocal according to Lorentz reciprocity theorem and can not produce optical isolation [139, 140].

- A mixer-duplexer-antenna leaky-wave system may be realized using a space-time modulated leaky-wave antenna. The first nonreciprocal leaky-wave system based on space-time modulation was independently proposed at the same time in [90] and [96]. Experimental demonstration of this single-port nonreciprocal leaky-wave antenna is then presented in [93], while the experimental demonstration of a two-port full transceiver, as the developed version of [90], is introduced in [9]. In addition to the overall mixer-duplexer-antenna operation, frequency beam scanning at fixed input frequency is demonstrated as one of the interesting features of the system. Most of previously reported nonreciprocal leaky-wave systems were based on magnetically biased ferrites [58,60,141–144,144–146], and hence suffer from the drawbacks inherent to ferrite technology, i.e. bulkiness and non-integrability.

1.3 Thesis Organization

Chapter 2 introduces the dispersion engineering techniques as well as the space, time, and space-time modulation techniques. Chapter 3 focuses on space modulated temporal dispersion engineered devices and proposes two different phasers which may be used in different applications. Next, a space modulated spatial dispersion and temporal dispersion engineered metasurface will be introduced in Chapter 4. Principle and characteristics of space-time modulated medium and nonreciprocal electromagnetic scattering from a space-time modulated slab will be investigated in Chapter 5. Based on the achieved results in Chapter 5, three different space-time modulated isolators will be presented in Chapter 6. These isolators operate based on different mechanisms and may be used in different applications. Chapter 7 shows how we can leverage the temporal dispersion engineering of space-time modulated media and realize an integrated electromagnetic components. This chapter presents the realization of an integrated mixer-duplexer-antenna leaky-wave system which operates as a full transceiver. Finally, Chapter 8 summarizes the achievements of the thesis and their significance for the future of metamaterials and metasurfaces.

CHAPTER 2 SPACE AND TIME MODULATION VERSUS SPATIAL AND TEMPORAL DISPERSION ENGINEERING

This chapter first presents operation principle of space, time and space-time-modulated structures, and then, introduces the concepts of spatial and temporal dispersion engineering. Starting from the space modulation, realization and general synthesis method of space-modulated (nonuniform) transmission lines will be presented. Next, a generic representation, functionality and the electromagnetic wave propagation in a time-modulated medium will be presented. Moreover, the realization of such a medium using array of distributed varactors will be shown. Then, an overview on the operation, functionality and the wave transmission through a space-time-modulated medium will be presented. Next, we will show the realization of such a spatiotemporally modulated medium using an array of distributed varactors. Finally, the principle of spatial and temporal dispersion engineering will be presented.

2.1 Space- and Time-Modulated Metamaterials

2.1.1 Space Modulation

Figure 2.1 illustrates a general continuously space-modulated (nonuniform) structure. In such a structure, the width of the transmission line is modulated along the propagation of the electromagnetic wave, introducing space-dependent permittivity of $\epsilon(z)$. As a result, the voltage and current through the lossless and non-dispersive space-modulated transmission line may be expressed as [30, 147]

$$\frac{dV(z)}{dz} = -j\omega L(z) I(z) \tag{2.1a}$$

$$\frac{dI(z)}{dz} = -j\omega C(z) V(z) \tag{2.1b}$$

where $L(z)$ and $C(z)$ are the space-dependent inductance and capacitance per unit length of the line. Solving these two equations together, we find the equation, with non-constant coefficients, for the voltage across the transmission line

$$\frac{d^2V(z)}{dz^2} - \left[\frac{1}{L(z)}\frac{dL(z)}{dz}\right]\frac{dV(z)}{dz} + \left[\omega^2 L(z)C(z)\right]V(z) = 0, \tag{2.2}$$

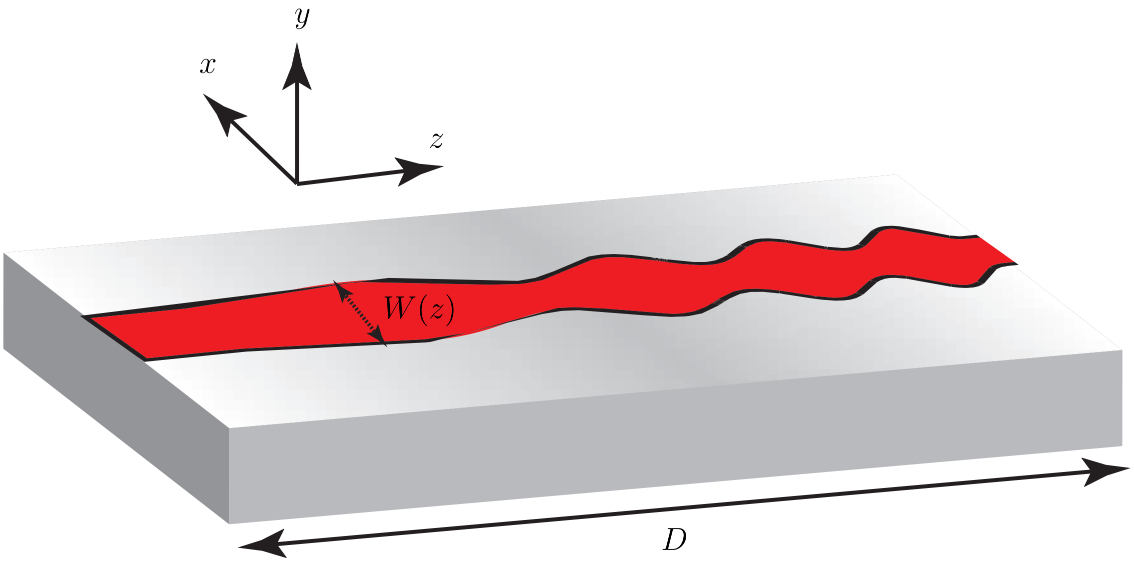

Figure 2.1 Continuously space-modulated transmission line.

In contrast to uniform transmission lines, general space-modulated transmission lines do not admit closed-form solutions [30, 148], since no analytical solution exists for 2.2 while $L(z)$ and $C(z)$ are general space-dependent functions. The classical and easiest approach to tackle this problem is to subdivide the space-modulated line into locally uniform sections and then analyze them using concatenation of their chain-parameter or ABCD matrices.

As mentioned in the previous chapter, a space-modulated structure may be utilized for different purposes, e.g. impedance matching or for the realization of a specified phase response in a broad frequency band. The goal of the synthesis is to determine the space-dependent permittivity function $\epsilon(z)$ (which corresponds to a space-dependent characteristic impedance function $Z_0(z)$) of the line which realizes the desired specifications. This function must typically satisfy the fabrication limitation condition as

$$\epsilon_{\text{min}} < \epsilon(z) < \epsilon_{\text{max}}, \tag{2.3}$$

A possible approach is to expand $\epsilon(z)$ in a Fourier series as

$$\epsilon(z) = a_0 + \sum_{q=1}^{Q} \left[a_q \cos(2\pi q z/D) + b_q \sin(2\pi q z/D) \right], \tag{2.4}$$

where D is the total length of the space-modulated transmission line. Equation (2.4) provides a continuous and smooth characteristic impedance variations with a moderate expansion terms, Q. We search for the appropriate unknown coefficients a_q and b_q in (2.4), and then, the space-dependent characteristics impedance of the transmission line, $Z_0(z)$, may be simply achieved [149]. Since no closed-form formulas exist for a general space-modulated transmission line, we discretize the nonuniform structure with the total length of D into M deep subwavelength uniform subsections, with the length of $d/\lambda_\mathrm{g} \to 0$, for which closed-form formulas are available. The length of each section reads

$$\Delta z = d = \frac{D}{M} \ll \lambda_\mathrm{min} = \lambda_\mathrm{g}(f_\mathrm{max}), \tag{2.5}$$

The inequality in (2.5) ensures subwavelength sampling over the entire operation bandwidth, where the highest frequency represents the most restrictive.

Figure 2.2 shows the discretization of the space-modulated, nonuniform, transmission line into M uniform subwavelength subsections. The corresponding space-dependent impedances are obtained by sampling (2.4) according to (2.5),

$$Z_{0\mathrm{p},m} = Z_{0\mathrm{p}}(md). \tag{2.6}$$

The input impedance of the m^th subsection, Z_m^in, are related to those of the $(m+1)^\mathrm{th}$ subsection, Z_{m+1}^in, by

$$Z_m^\mathrm{in} = Z_{0,m} \frac{Z_{m+1}^\mathrm{in} + jZ_{0,m}\tan(\Delta\theta)}{Z_{0,m} + jZ_{m+1}^\mathrm{in}\tan(\Delta\theta)}, \tag{2.7a}$$

with $m = 1, \ldots, M$, and

$$\Delta\theta = \beta d = \frac{\omega}{c\sqrt{\epsilon_\mathrm{eff}}} d \tag{2.7b}$$

being the electrical length of each subsection [149]. Iteratively computing Z_m^in from $m = M$ to 1, where $Z_{M+1}^\mathrm{in} = Z_\mathrm{load}$, provides the reflection coefficient at the input of the overall structures via

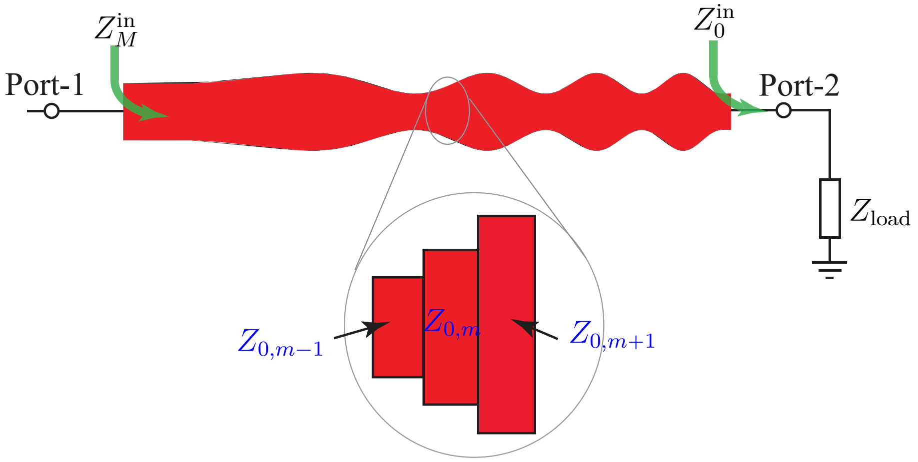

Figure 2.2 Discretization of space-modulated, nonuniform, transmission line into M uniform subwavelength subsections.

$$\Gamma^{\mathrm{in}} = \frac{Z_M^{\mathrm{in}} - Z_0}{Z_M^{\mathrm{in}} + Z_0}. \tag{2.8}$$

Then, using (3.11), we are able to calculate the total S-parameters and group delay of the structure [149], which may be used for the impedance matching or achieving specified group delay response by optimization of the profile of this nonuniform transmission line.

2.1.2 Time Modulation

A time-modulated permittivity may be considered as

$$\epsilon(t) = \epsilon_{\mathrm{av}} + \epsilon_{\mathrm{m}} \ \cos(\omega_{\mathrm{m}} t). \tag{2.9}$$

Figure 2.3 depicts electromagnetic wave transmission through a periodic time-modulated medium. The input single-tone plane wave, with frequency ω_0, as

$$\mathbf{E}_{\mathrm{I}}(z,t) = \hat{\mathbf{y}} E_0 e^{-j(k_0 z - \omega_0 t)}, \tag{2.10}$$

impinges on the time-modulated slab medium, and the slab introduces all Block-Floquet harmonics, i.e. $\omega_0 + n\omega_{\mathrm{m}}$. In (2.10), E_0 is the amplitude of the incident field, $k_0 = \omega_0/v_{\mathrm{b}}$, and v_{b} is the phase velocity of the background medium as

$$v_{\mathrm{b}} = \frac{c}{\sqrt{\epsilon_{\mathrm{r}}}}, \tag{2.11}$$

The electromagnetic fields inside such a medium may be formulated as [28, 150]

$$\mathbf{E}_{\mathrm{M}}(z,t)=\hat{\mathbf{y}}\sum_{n,p=-\infty}^{\infty}\left(A_{np}^{+}e^{-j\beta_{np}z}+A_{np}^{-}e^{j\beta_{np}z}\right)e^{j(\omega_0+n\omega_{\mathrm{m}})t}, \tag{2.12}$$

where n is the number of space-time harmonics. It will be shown in chapter 5 that each point (β_{0p},ω_0) represents a *mode* of the medium, itself constituted of an infinite number of oblique *space-time harmonics* corresponding to modes at other frequencies, since such a point is a solution to the complete wave equation.

The transmitted electric field through such a slab reads

$$\mathbf{E}_{\mathrm{T}}(z,t)=\hat{\mathbf{y}}\sum_{n=-\infty}^{\infty}E_{\mathrm{t}n}e^{-j[k_{0n}z-(\omega_0+n\omega_{\mathrm{m}})t]}, \tag{2.13}$$

A time-modulated structure may be realized in the form of a time varying artificial microstrip transmission line shown in Fig. 2.4 [151]. In order to provide temporal control on the capacitance of the transmission line, it is loaded with an array of sub-wavelengthly spaced shunt varactors. A power divider splits the power of the modulation signal and drive the distributed varactors. A DC bias V_{DC} ensures the operation of the varactors in the, reverse bias, capacitance region. Therefore, the varactors experience a time-dependent voltage as

$$V(t)=V_{\mathrm{DC}}+V_{\mathrm{m,n}}\cos(\omega_{\mathrm{m}}t) \tag{2.14}$$

where ω_{m} is the modulation frequency. The varactors are reverse biased in the linear region of the C-V curve and act as voltage controlled capacitors. Thus, they introduce the time varying distributed capacitance to the transmission line as

$$C(t)=C_{\mathrm{av}}+C_{\mathrm{m}}\ \cos(\omega_{\mathrm{m}}t) \tag{2.15}$$

Therefore, the structure in Fig. 2.4 emulates a medium with time varying permittivity in (2.9), background permittivity of ϵ_r and modulation depth $M=C_{\mathrm{m}}/C_{\mathrm{av}}$.

We will see in the following chapters that such a temporally modulated medium introduces spacial and temporal dispersions.

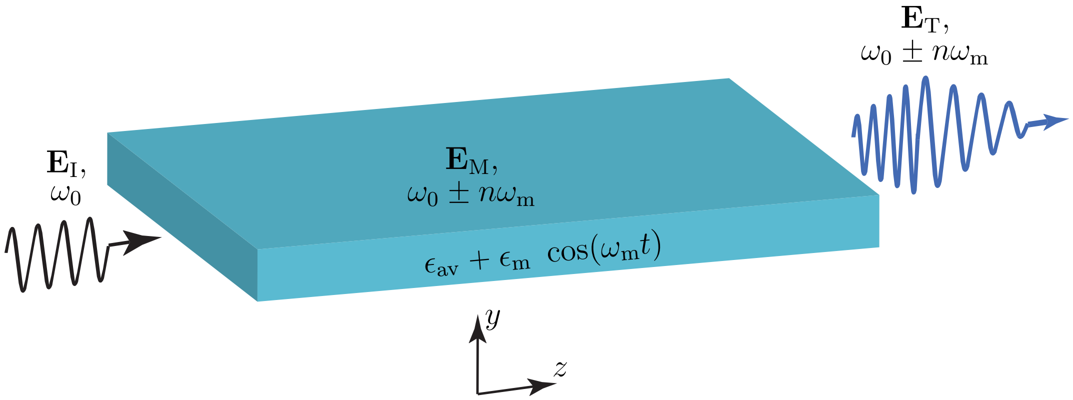

Figure 2.3 Illustration of wave transmission through a time-modulated medium.

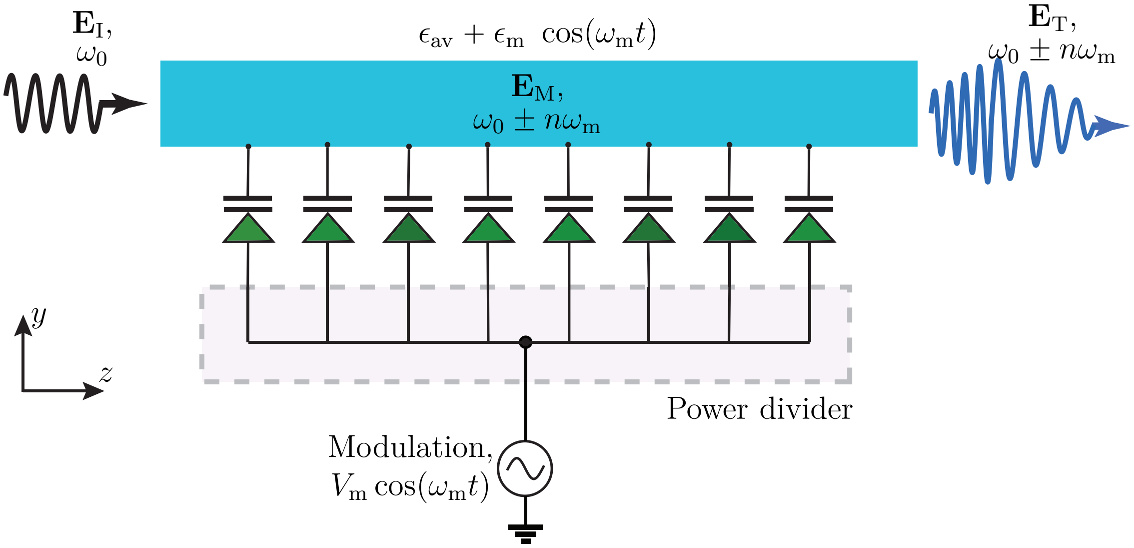

Figure 2.4 Realization of time-modulated medium using array of modulated varactors.

2.1.3 Space-Time Modulation

A space-time-modulated medium may assume the unidirectional forward relative permittivity as [7]

$$\epsilon(z,t) = f_{\text{per}}(\beta_{\text{m}} z - \omega_{\text{m}} t), \tag{2.16}$$

where $f_{\text{per}}(.)$ represents a general periodic function of the space-time phase variable, with β_{m} and ω_{m} being the spatial temporal modulation frequencies, respectively. Figure 2.5 presents schematic of a space-time-modulated slab medium, where a plane wave, $\mathbf{E}_{\text{I}}$, impinges in the forward $(+z)$ direction or backward $(-z)$ direction on a periodically space-time-modulated medium. The problem with the incident wave traveling towards the $+z$-direction is called the *forward problem*, denoted by the superscript "F", while the problem with the incident wave propagating towards the $-z$-direction is called the *backward problem*, denoted by the superscript "B".

Taking the time derivative of a constant phase point in (2.16) leads to the modulation phase velocity

$$v_{\text{m}} = \frac{\omega_{\text{m}}}{\beta_{\text{m}}}. \tag{2.17}$$

which may be smaller or greater than the phase velocity of the background medium, which we define here as the velocity

$$v_{\text{b}} = \frac{c}{\sqrt{\epsilon_{\text{r}}}}, \tag{2.18}$$

where $c = 1/\sqrt{\mu_0 \epsilon_0}$ is the speed of light, and ϵ_{r} is the average permittivity of the modulated medium. The ratio between the modulation and background phase velocities reads

$$\gamma = \frac{v_{\text{m}}}{v_{\text{b}}}, \tag{2.19}$$

is called the *space-time velocity ratio*. The limit $\gamma = v_{\text{m}} = 0$ corresponds to a purely space-modulated medium, while the limit $\gamma = v_{\text{m}} = \infty$ corresponds to a purely time-modulated medium [80]. Moreover, $\gamma = 1$ corresponds to the space-time-modulated medium where the modulation propagates exactly at the same velocity as a wave in the background medium.

As a particular case, a periodic sinusoidal space-time-modulated permittivity may be considered

$$\epsilon(z,t) = \epsilon_{\text{av}} + \epsilon_{\text{m}} \ \cos(\beta_{\text{m}} z - \omega_{\text{m}} t). \tag{2.20}$$

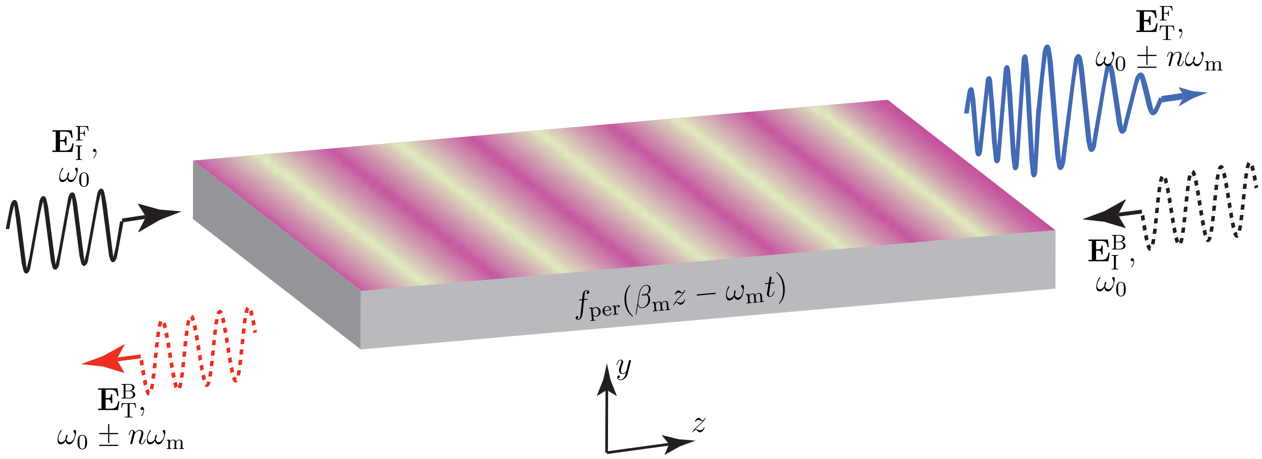

Figure 2.5 Space-time modulated structure. Unidirectionality of the space-time modulation leads to nonreciprocal frequency generation, $\mathbf{E}_\mathrm{T}^\mathrm{F} \neq \mathbf{E}_\mathrm{T}^\mathrm{B}$.

The incident fields may be written as

$$\mathbf{E}_\mathrm{I}(z,t) = \hat{\mathbf{y}} E_0 e^{\mp j(k_0 z - \omega_0 t)}, \tag{2.21}$$

where $-$ and $+$ signs respectively stand for the forward and backward problems, E_0 is the amplitude of the incident field and $k_0 = \omega_0/v_\mathrm{b}$. The electric and magnetic fields inside the slab may be formulated as

$$\mathbf{E}_\mathrm{M}(z,t) = \hat{\mathbf{y}} \sum_{n,p=-\infty}^{\infty} \left(A_{np}^{+} e^{-j(\beta_{0p}^{+} + n\beta_\mathrm{m})z} + A_{np}^{-} e^{j(\beta_{0p}^{-} - n\beta_\mathrm{m})z} \right) e^{j(\omega_0 + n\omega_\mathrm{m})t}, \tag{2.22}$$

The transmitted electric fields outside of the slab may be defined as

$$\mathbf{E}_\mathrm{T}(z,t) = \hat{\mathbf{y}} \sum_{n=-\infty}^{\infty} E_{\mathrm{t}n} e^{\mp j[k_{0n} z - (\omega_0 + n\omega_\mathrm{m})t]}, \tag{2.23}$$

where $-$ and $+$ signs respectively stand for the forward and backward problems. It will be shown that such a space-time-modulated medium introduces nonreciprocal transmission of the wave for forward and backward problems. Moreover, nonreciprocal temporal and spacial dispersions are introduced by the modulated medium provides extra functionalities. In the next chapters, we will present different applications of such a nonreciprocal spatiotemporally dispersive medium.

A space-time-modulated structure may be realized in the form of a space-time varying artificial microstrip transmission line shown in Fig. 2.6. The transmission line is loaded with an array of sub-wavelengthly spaced shunt varactors, providing spatiotemporal control on the distributed capacitance. The bias line at the bottom provides a DC bias V_{DC} plus a propagating modulation bias to the varactors as

$$V(z,t) = V_{\mathrm{DC}} + V_{\mathrm{m}} \cos(\beta_{\mathrm{m}} z - \omega_{\mathrm{m}} t) \tag{2.24}$$

where ω_{m} is the modulation frequency. The bias phase velocity $v_{\mathrm{m}} = \omega_{\mathrm{m}}/\beta_{\mathrm{m}}$. The varactors are reverse biased in the linear region of the C-V curve and act as voltage controlled capacitors, presenting a space-time varying distributed capacitance to the transmission line as

$$C(z,t) = C_{\mathrm{av}} + C_{\mathrm{m}} \ \cos(\beta_{\mathrm{m}} z - \omega_{\mathrm{m}} t) \tag{2.25}$$

The structure in Fig. 2.6 imitates a medium with space-time varying permittivity (5.22), with background permittivity ϵ_r and modulation depth $M = C_{\mathrm{m}}/C_{\mathrm{av}}$.

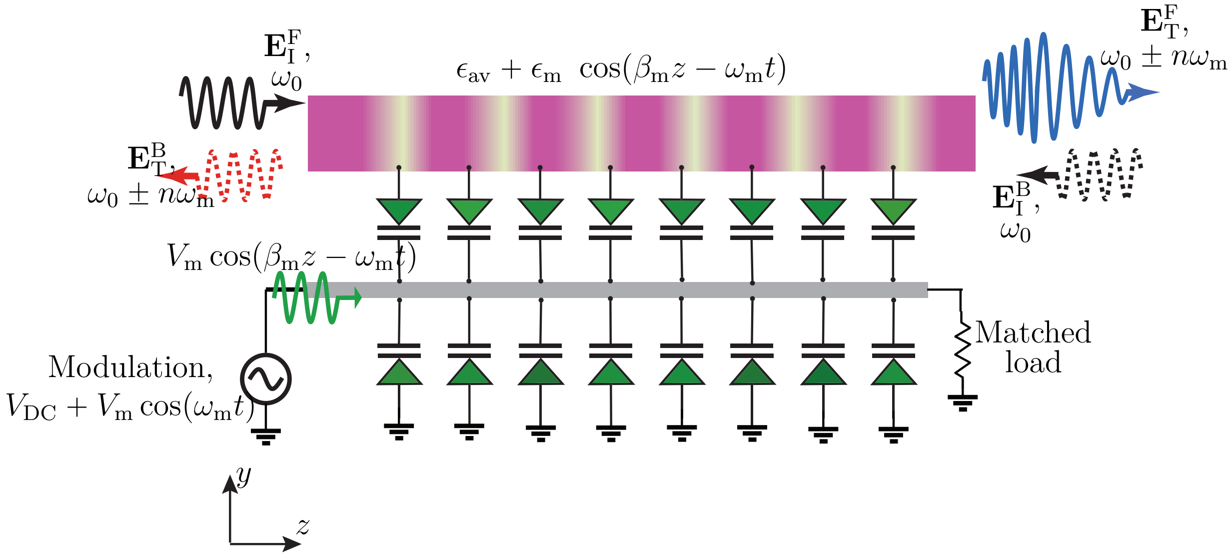

Figure 2.6 Realization of the periodic unidirectional space-time-modulated medium using a transmission line loaded with an array of unidirectionally modulated varactors.

2.2 Dispersion Engineering

2.2.1 Spatial Dispersion Engineering

Based on physics of continuous media, spatial dispersion represents a phenomenon where constitutive parameters of the media, such as permittivity, permeability or conductivity have dependence on wavevector, $\mathbf{k} = (k_x, k_y, k_z)$ [152]. Eventhough such a dependence is neglected for simplicity, spatial dispersion exists to varying degrees in all media [49, 152]. All natural and artificial media are spatially discontinuous since they are formed by particles. However, majority of natural materials are represented as effectively continuous media since the optical size of particles, i.e. atoms and molecules, is very small at microwave and optical regimes. However, this homogenization is not valid for cases where the distance between the adjacent particles, a, is non-negligible $a/\lambda > 0.01$. In such cases, nonuniformity of the field over the particle and over the unit cell of the composite medium should be taken into account [24].

From physical point of view, the origin of spatial dispersion is the non-locality of the polarization response, where the response to a force field appears at different locations even in locations where the force is zero [50]. The non-locality in an array of particles emerges due to two reasons, as follows [24].

- Particles have an optically non-negligible size. In this case, the field distributed over, optically finite volume of the particle excites the polarization currents, while the overall current distribution in the particle depends on the particle size and geometry. As a result, the polarization at any point of the particle feels the field at other points of the same particle. Therefore, the electric and magnetic responses of a large particle, except an isotropic and homogeneous particle, will strongly depend on the direction of the propagating wave and its polarization.
- Distances between the particles are optically non-negligible, even if the particles are optically vanishingly small. This results form averaging the microscopic fields over an optically large volume. The constitutive parameters of the medium represent the relations between the averaged electric and magnetic fields and electric and magnetic polarizations. Therefore, for optically small particles, their electric polarization is a response to the local electric field distributed in a small volume.

Figure 2.7 illustrates the most well-known spatially dispersive metamaterial, an artificial plasma called *simple wire medium* [2]. It represents a medium with negative permittivity as a square lattice of thin parallel wires which may be considered as a perfect conducting media in the microwave regime. The effective permittivity of such a medium may be achieved by a nonlocal model as [51]

$$\epsilon_{\text{eff}} = \epsilon_0 \left(1 - \frac{k_{\text{p}}^2}{k^2 - q_z^2}\right) \tag{2.26}$$

where $k = \omega/c$, and ω and c are respectively the frequency of the incident wave and the velocity of light. Also, q_z is the component of the wave vector $q = q_x, q_y, q_z$ along the wires, and k_p represents the plasma wave number, may be expressed as

$$k_p = \frac{1}{\sqrt{\frac{a^2}{2\pi}\left[\ln\left(\frac{a}{2\pi r}\right) + 0.5275\right]}} \tag{2.27}$$

for and for $a = b$, where a and b are the distances between the wires and r is the radius of the wires, as shown in Fig. 2.7. However, it may be shown that while the wave propagates normally with respect to the rods, the simple wire medium does not introduces the spatial dispersion [24, 51, 153].

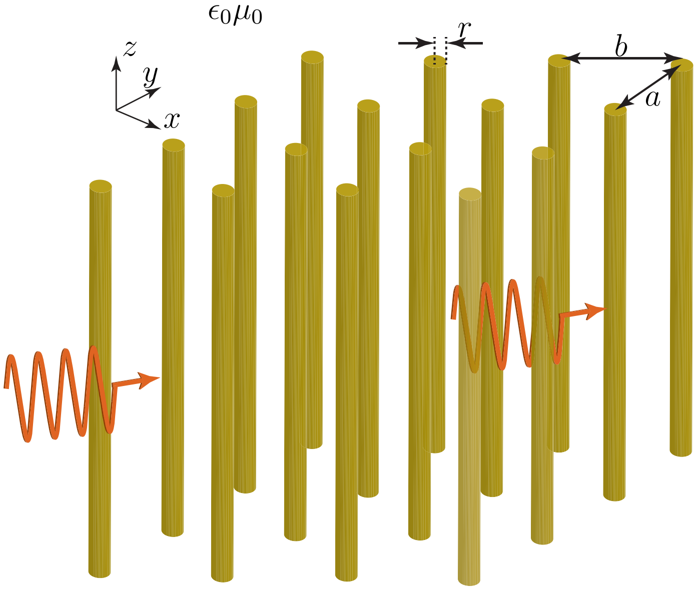

Figure 2.7 Conventional method for spatial dispersion engineering using simple wire medium [2].

Recently, the effects of spatial dispersion in the wire medium have been studied theoretically [51, 153–158], and experimental demonstrations of some of these effects were reported [54, 159, 160].

Figure 2.8 shows the architecture of a metasurface that consists of array of patch elements with a deep-subwavelength thickness, $t << \lambda$. Metasurface represents the state of the art technology for spatial dispersion engineering owing to its compactness and various exotic functionalities. In such a media, Snell's law is generalized by the introduction of an abrupt phase shift along the optical path, leading to effects such as anomalous reflection and refraction of light [21] and a diversity of unprecedented wave transformation functionalities [26]. It may be shown that a metasurface has a **k**-dependent susceptibility, which introduces spatial dispersion [161]. Metasurface technology represents a rapidly growing field of research with broad range of applications from microwave to visible. Different applications of metasurfaes have been recently proposed, including polarization conversion [162–164], broadband operation based on dielectric metasurface [165], wave guidance and radiation [166, 167], efficiency enhancement in LEDs [168], remote switches [169], metasurface antenna [170] and energy harvesting [171].

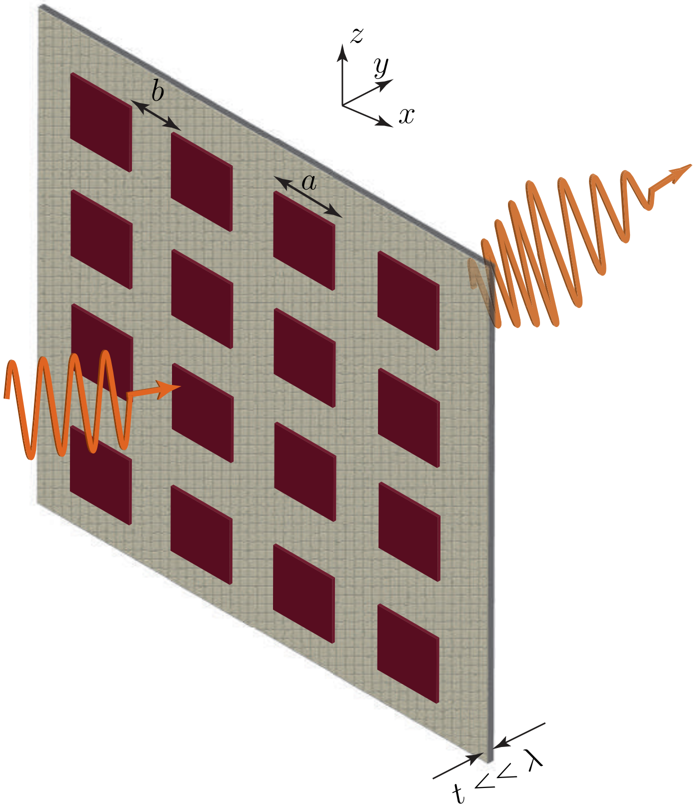

Figure 2.8 State of the art technology for spatial dispersion engineering using metasurface based on arrangement of optically large particles.

Spatial dispersion engineering represents a growing field of reasearch [172, 173], proving extra degrees of freedom for the design of novel metamaterials and metasurfaces. Chapter 4 of this thesis presents a space-modulated nonreciproal nongyrotropic magnetless metasurface based on spatial dispersion engineering. It will be shown that such a spatial dispersion engineered medium presents unprecedented functionalities.

2.2.2 Temporal Dispersion Engineering

Temporal dispersion engineering is the essence of Real-time Analog Signal Processing (R-ASP). R-ASP was initially inspired by ultrafast optics concepts [174], and has recently been considered as a potential alternative to dominantly digital radio technology given its unique real-time, low-consumption and frequency-scalability characteristics [3]. Over the past decade, various temporal dispersion engineered microwave systems have been introduced for enhanced efficiency and flexibility in Radio Analog Signal Processing (R-ASP), including direction-of-arrival detectors [68], spectrum sniffers [69], and enhanced signal-to-noise receivers [70].

The key element of a R-ASP system is the *phaser*, a temporal dispersion engineered device, $\chi(\omega)$, providing specified group delay versus frequency responses (linear, quadratic, quintic, staircase, Chebyshev, etc.) depending on the application. Various types of reflection-type (one-port) and transmission-type (two-port) microwave phasers have been recently developed along with corresponding synthesis techniques [62–64]. All-pass phasers based on contra-directional coupled transmission line couplers [65] are particularly attractive in R-ASP given their two-port configuration (avoiding the need for circulators or extra couplers), and their simplicity and flexibility responses [4, 66, 67].

Figure 2.9 shows two fundamental effects of the temporal dispersion, frequency discrimination in the time domain and frequency chirping with time spreading [3]. The phaser, as a temporally dispersive medium, is a linear element with transfer function $H(\omega) = \exp(j\phi(\omega))$, with unity magnitude and nonlinear phase as a function of frequency, yielding a frequency-dependent group delay response, where the bandwidth of $H(\omega)$ covers the entire spectrum of the input signal.

Figure 2.9(a) shows the application of a step-profile phaser for frequency discrimination. The input is a two-tone signal with frequencies ω_L and ω_H, passes through a phaser providing a negative stepped group delay response, with two steps, centered at ω_L and ω_H. As a result, the part of the input signal modulated at the lower frequency, ω_L, is delayed more than the part modulated at the higher frequency, ω_H, and therefore appears later in time. Therefore, the two signals are separated in the time domain.

Figure 2.9(b) presents another application of temporal dispersion engineering, frequency chirping. The frequency chirping represents a parasitic effect in optics, but it may be also used, in a sophisticated way, for instance in recently proposed Dispersion Code Multiple Access (DCMA) method [175, 176]. A modulated pulse passes through a phaser, which provides a negative linear group delay slope across a frequency band with the frequency of ω_c and group delay of τ_c. As a consequence of the temporal dispersion introduced by the phaser, different spectral components of the pulse experience different phase-shifts and therefore appear at different times, i.e. the high frequency components are less delayed and therefore appear earlier in time while the low frequency component are more delayed and appear later in time. This leads to frequency chirping, where the instantaneous frequency of the output pulse is progressively decreased. Another important phenomenon is the time spreading of the pulse, i.e. $T_{\text{out}} > T_0$, yielding reduced amplitude due to the energy conservation.

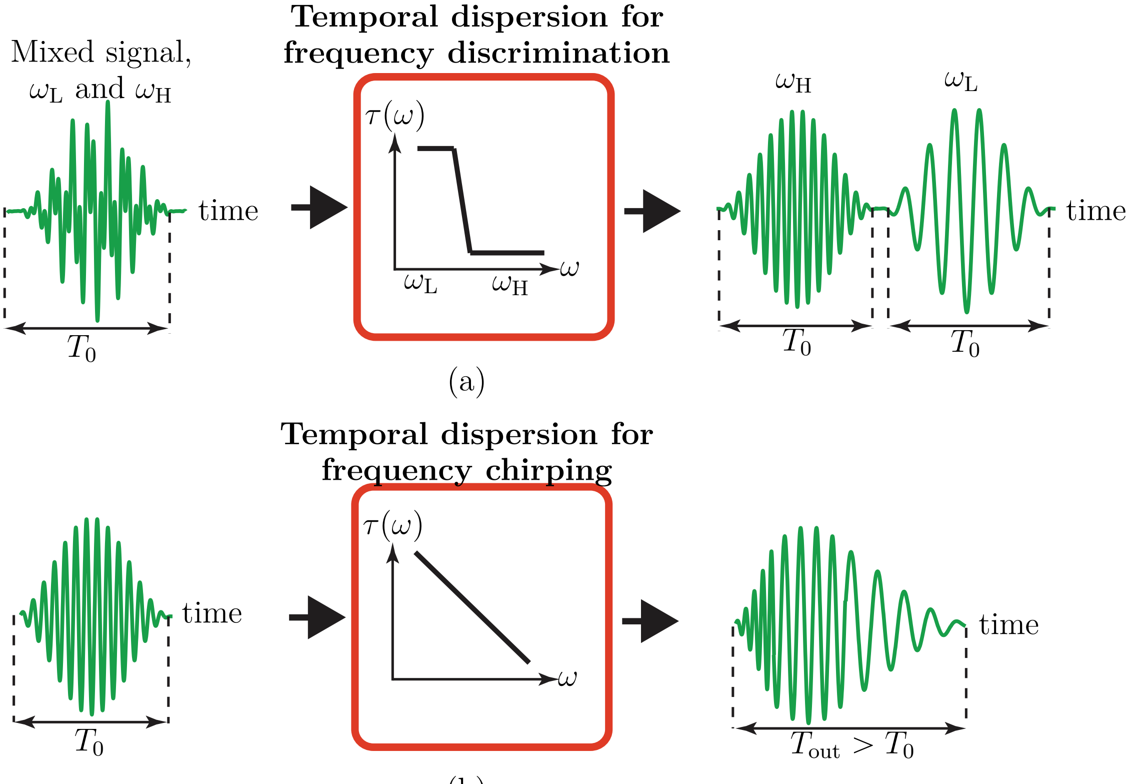

(a)

(b)

Figure 2.9 Temporal dispersion effect when a (a) mixed signal passes from a phaser with step group delay shape. (b) pulse signal passes from a phaser with linear group delay shape [3].

CHAPTER 3 ENHANCED EFFICIENCY AND VERSATILE PHASERS USING APERIODIC SPACE MODULATED TEMPORALLY DISPERSIVE MEDIA

This chapter has been partly taken from author's published articles [1, 5, 107].

Two static space-modulated (also known as nonuniform and width-modulated) phasers will be introduced as temporal dispersion engineered devices. Both phasers provide unique properties for enhanced efficiency and reduced complexity in Radio Analog Signal Processing [1,107], representing flexible phasers applicable for different applications and different frequency bands.

Section 3.1 introduces C-section space-modulated phasers for enhanced flexibility and increased bandwidth in radio analog signal processing. Unfortunately, coupled-line based all-pass phasers suffer from restricted group delay responses, due to their periodic response, restricted bandwidth, because of the related presence of spurious group delay harmonic peaks, and substantial loss, due to their electrically large unfolded size. In an attempt to remedy this issues, the concept of nonuniform C-section phasers is suggested in [6,107]. The first section provides a study of conventional C-section phasers [61, 67], the explanation of the trade-offs between group delay ripple levels and size and loss, a detailed comparison with Cristal's structure [67], demonstrations of the greater bandwidth, lower loss and smaller size of the space-modulated C-section structure, a detailed presentation of a simple synthesis procedure of the phaser, the presentation of Chebyshev higher-order group delay designs, experimental validations, and the explanation of the group delay response in terms of electromagnetic energy storage.

Section 3.2 proposes space-modulated stub-line phasers as a simple single-layer phasing mechanism, for reduced cost and complexity in radio analog signal processing. C-section space-modulated phasers may be considered as the most flexible and broadband transmission-type phasers [1]. However, they suffer from requiring high coupling coupled-line sections, which demands multilayer technologies, and leads to high complexity and high cost. In contrast, space-modulated stub-line phaser may be easily realized using microstrip lines since it requires no coupling element [5]. This phaser leverages the high group delay dispersion and swing of nonuniform stub-lines. We show that a shunt short/open stub provides greater group delay dispersion and group delay swing, in comparison with a series transmission line. The proposed phaser may realize different group delay shapes thanks to the nonuniformity and high group delay swing of stubs. Moreover, it may be designed as a reflection-type phaser to achieve higher group delay swing. It should be noted that C-section space-modulated phasers present, theoretically, infinite bandwidth while the bandwidth of space-modulated stub-line phasers is limited.

3.1 C-section Continuously Space-Modulated Phaser

3.1.1 Temporal Dispersion Engineering Using C-Section Phasers In Radio Analog Signal Processing

Radio Analog Signal Processing (R-ASP), inspired by ultrafast optics concepts [174], represents a potential alternative to dominantly digital radio technology given its unique real-time, frequency-scalability and low-consumption characteristics [3]. A number of R-ASP applications have been reported at microwave frequencies, including direction-of-arrival detectors [68], enhanced signal-to-noise receivers [70] and spectrum sniffers [69].

The key element of a R-ASP system is the phaser, a temporal dispersion engineered device, providing specified group delay versus frequency responses (linear, staircase, quadratic, quintic, Chebyshev, etc.) depending on the application, e.g. linear for real-time Fourier transformers [63] and Chebyshev for dispersion code multiple access (DCMA) [1, 107, 176].

Various types of reflection-type (one-port) and transmission-type (two-port) microwave phasers have been recently developed along with corresponding synthesis techniques [4, 62–64]. All-pass phasers based on contra-directional coupled transmission line couplers [65] are particularly attractive in R-ASP given their two-port configuration (avoiding the need for circulators or extra couplers), and their simplicity and flexibility responses [4, 66, 67].

Figure 3.1(a) represents a conventional C-section, which is two-port component consisting in a backward-wave coupled-line coupler with the two ports of one end interconnected and the other two ports representing the input and output of the structure. Such C-sections exhibit group delay maxima at the odd frequency harmonics of the quarter guided wavelength, $D = (2m + 1)\lambda_g/4$, where m is an integer.

The group delay, $\tau(\omega)$, is defined as the rate of change of the total phase shift with respect to angular frequency, i.e.

$$\tau(\omega) = -\frac{d\phi_{S_{21}}}{d\omega}. \tag{3.1}$$

Consider a lossy and matched transmission line with the length of L, where the transmission through this system reads $S_{21} = \exp(-j\beta L)$, with $\beta = \omega/v_0$ and v_0 being the phase velocity of the wave inside the transmission line. The group delay of this transmission line may be calculated, using (3.1), as

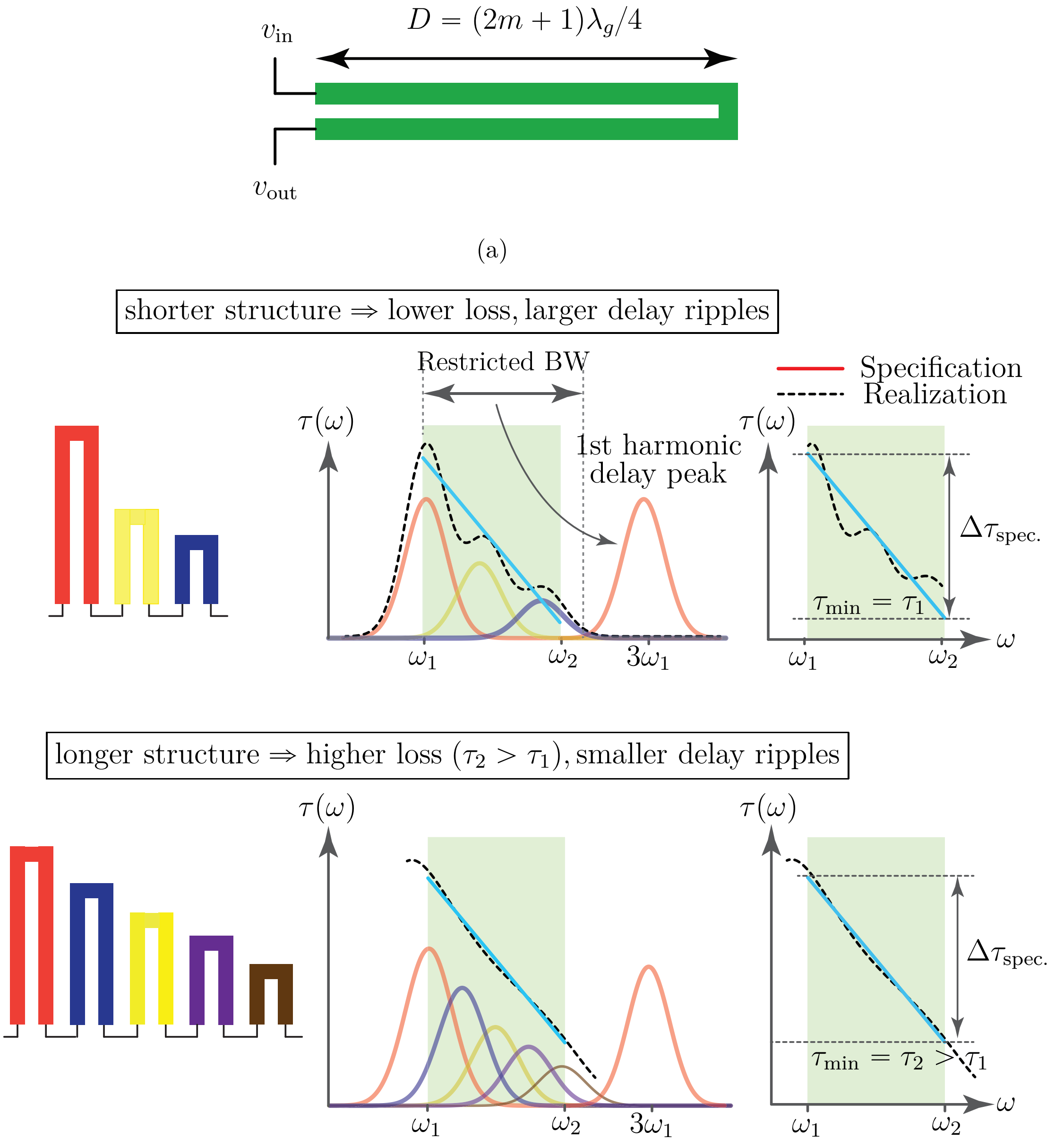

(a)

(b)

Figure 3.1 Limitations of conventional uniform C-section phaser structures in group delay engineering. Arbitrary case of a negatively-sloped group delay versus frequency specification. a) C-section structure, realized using a backward-wave coupled transmission line coupler. b) Cascaded C-section phasers [4] realizing a negatively sloped delay response in a restricted bandwidth, and associated trade-offs between size, dissipation loss and delay ripples.

$$\tau(\omega) = -\frac{d}{d\omega}\beta L = \frac{L}{v_0}. \tag{3.2}$$

Equation (3.2) reveals that the group delay is proportional to the length of the transmission line. However, for a lossy transmission line, larger length L corresponds to higher attenuation. As a result, the group delay of a non-ideal transmission line is proportional to the insertion loss, i.e. higher group delay represents higher insertion loss.

Figure 3.1(b) illustrates the limitations of conventional cascaded C-section phasers [4], which are composed of the cascade (or series) interconnection of conventional C-sections with generally different lengths designed so as to meet group delay versus frequency response specifications. The figure shows that, in the illustrated case of a negatively-sloped group delay versus frequency response, the bandwidth of conventional cascaded C-section phasers is restricted by the group delay harmonic frequency peak of the largest C-section in the structure. This situation differs for different specified group delays, but the bandwidth restriction due to harmonic peaks is a general issue in such phasers.

The first row in 3.1(b) represents a design with a minimal size, i.e. with a minimal number of C-sections. Such a design corresponds to a relatively small average group delay, as shown in the right, and therefore to relatively low dissipation loss. However, the number of C-sections is too small to closely sample the specified delay function, which results in strong spurious ripples in the delay response.

The second row in 3.1(b) represents a design with a larger number of C-sections, providing higher sampling, and hence an essentially ripple-less delay response. However, the size of the structure has increased, leading to a larger average group delay, as shown in the right, and the dissipation loss is therefore significantly increased.

Figure 3.2 shows a general step-discontinuity nonuniform coupled-line phaser with M sub-sections of lengths $d_1, d_2, ..., d_M$ and corresponding even- and odd-mode equivalent circuits, denoted by the subscript p (p =e,o, resp.), where $Z_\mathrm{e}^\mathrm{L} = \infty$, $Z_\mathrm{o}^\mathrm{L} = 0$. For small discontinuities, the total even/odd reflection coefficients at the input are [149]

$$\Gamma_p^\mathrm{in} = \Gamma_{p,0} + \Gamma_{p,1}e^{-j2\beta d_1} + ... + \Gamma_{p,M}e^{-j2M\beta d_M}, \tag{3.3}$$

where $\Gamma_{p,m}$ is the reflection coefficient between sections m and $m+1$ and β is the (m-independent, assuming TEM sections) guided wavenumber. The total transmission scattering

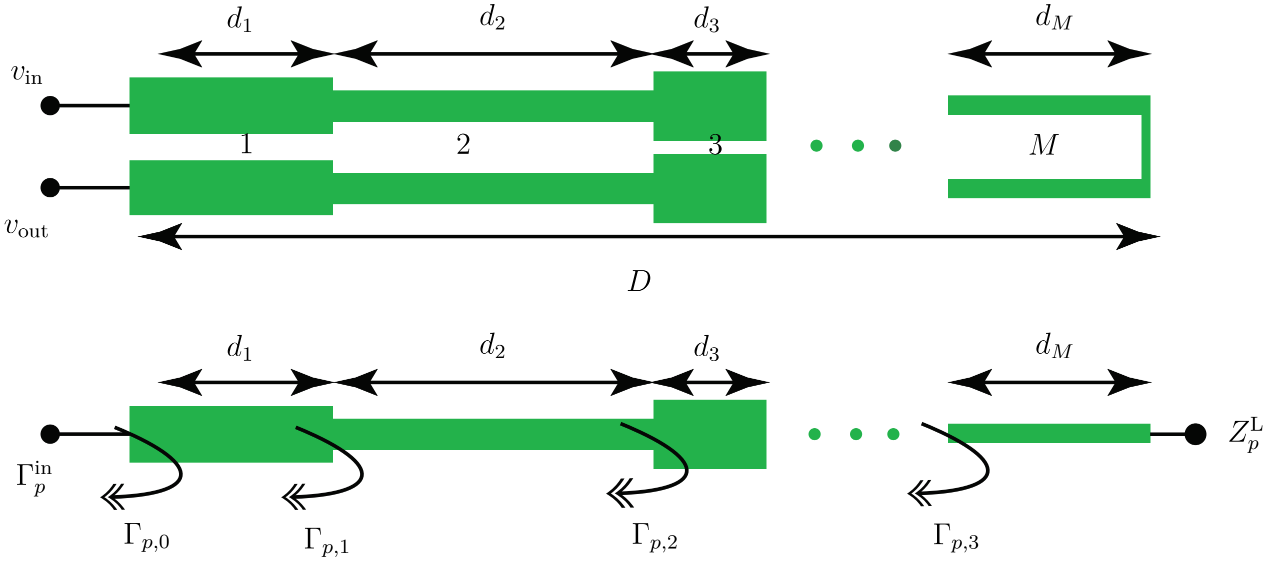

Figure 3.2 Non-commensurate C-section phaser (top), and corresponding even- and odd-mode equivalent circuits (bottom) [1].

parameter and group delay of the phaser follow as

$$S_{21} = \frac{1}{2}(\Gamma_{\text{e}}^{\text{in}} - \Gamma_{\text{o}}^{\text{in}}) = \frac{1}{2}\sum_{m=0}^{M-1}(\Gamma_{\text{e},m} - \Gamma_{\text{o},m})\, e^{-j2m\beta d_m}, \tag{3.4}$$

$$\tau(\omega) = -\frac{d\phi_{S_{21}}}{d\omega} = \sum_{m=0}^{M-1}\left(\frac{-d\phi_{(\Gamma_{\text{e},m}-\Gamma_{\text{o},m})}}{d\omega} + \frac{2md_m}{v}\right), \tag{3.5}$$

where $v = \omega/\beta$ is the phase velocity.

The group delay response of a single C-section is periodic, with peaks located at $\beta D = \pi(n + 1/2)$, for $n = 0, 1, ..., \infty$ and having a group delay swing depending on the coupling, C, and length, D, of the structure. In a commensurate cascaded M-section C-section, the periodicity is increased by a factor M (M propagation-coupled resonators) with up to M peaks depending on couplings, due to *coherent* multiple reflection [factor $e^{-j2m\beta d}$ in Eq. (3.4)]. Defining BW_{max} as the frequency bandwidth supporting a non-periodic specified group delay response (restricted by periodicity), one has from $2\beta d = 2\pi$ where $d = D/M$ that $BW_{\text{max}} = Mv/4D$. This reveals that the bandwidth of the phaser is increased by increasing M. Finally, the periodicity is lost in the case of non-commensurate sections, due to *incoherent* multiple reflection [factor $e^{-j2m\beta d_m}$ in Eq. (3.4)].

3.1.2 Synthesize of Continuously Space-Modulated Phasers

To synthesize the nonuniform coupled-line function $C(z)$

$$0 < C_{\min} < C(z) < C_{\max} < 1 \tag{3.6}$$

for the specified group delay response, one may use the Fourier series expansion

$$C(z) = a_0 + \sum_{q=1}^{Q} \left[a_q \cos(2\pi q z/d) + b_q \sin(2\pi q z/d) \right], \tag{3.7}$$

and search for the appropriate unknown expansion coefficients a_q and b_q. The corresponding nonuniform even and odd characteristic impedances are [149]

$$Z_{0e/o}(z) = Z_0(\sqrt{1 \pm C(z))/(1 \mp C(z))} \tag{3.8}$$

We shall satisfy the local matching condition as

$$\sqrt{Z_{0\mathrm{e}}(z) Z_{0\mathrm{o}}(z)} = Z_0, \quad \forall z, \tag{3.9}$$

where Z_0 is the ports characteristic impedance. The even and odd impedances at the input of the m^{th} subsection, $Z_{p,m}^{\text{in}}$, are related to those of the $(m+1)^{\text{th}}$ subsection, $Z_{p,m+1}^{\text{in}}$, by

$$Z_{p,m}^{\text{in}} = Z_{p,m} \frac{Z_{p,m+1}^{\text{in}} + jZ_{p,m} \tan(\beta d_m)}{Z_{p,m} + jZ_{p,m+1}^{\text{in}} \tan(\beta d_m)}. \tag{3.10}$$

Iteratively computing $Z_{p,m}^{\text{in}}$ from $m = M$ to $m = 1$ provides the even and odd reflection coefficients at the input of the overall even and odd structures via

$$\Gamma_p^{\text{in}} = (Z_{p,1}^{\text{in}} - Z_0)/(Z_{p,1}^{\text{in}} + Z_0). \tag{3.11}$$

Based on the above derivations, the synthesis procedure follows the flowchart given in Fig. 3.3. Once a $\tau(\omega)$ function has been synthesized for a trial expansion set $\{a_q, b_q\}$, it is injected in the fitness function

$$\varepsilon = \frac{1}{\omega_\mathrm{h} - \omega_l} \int_{\omega_\mathrm{l}}^{\omega_\mathrm{h}} \left| \tau(\omega) - \tau_{\mathrm{s}(\omega)} \right| d\omega, \tag{3.12}$$

which corresponds to the deviation of $\tau(\omega)$ from the specified function, $\tau_\mathrm{s}(\omega)$. If ε is smaller than a given threshold, ξ, considered acceptable for a given application, then the set $\{a_q, b_q\}$ forms an acceptable function $C(z)$ in (3.7), and the synthesis is complete. Otherwise, another set is tested, using a standard nonlinear problem optimization technique, such as for instance the sequential quadratic programming algorithm [177], until $\varepsilon < \xi$ is satisfied.

It may be argued that, if the specified bandwidth is small enough to avoid the issue of group delay harmonics [Fig. 3.1(b)], a cascaded C-section phaser [4] could meet the same group delay swing specification as the nonunifrom C-section. This is true. However, the corresponding unfolded length will be much larger, which would entail a much larger average group delay and hence much larger dissipation loss. This fact is illustrated in Fig. 3.4, where both designs provide the specified group delay swing of 0.4 ns but the nonuniform phaser exhibits about 1.5 dB s loss.

Figure 3.5 compares the performance of the continuously modulated nonuniform phaser with those of step-discontinuity nonuniform phasers. The goal is to achieve negative linearly chirped response of at least 30 ps swing over the largest possible bandwidth between 1 and 20 GHz. Note that the area under the $\tau(\omega)$ curve is constant for a given length D. Due to its zero subsection length ($d/\lambda \to 0$), the continuously modulated phaser exhibits, according to Sec. 3.1, an infinite periodicity, and reaches therefore the complete specified bandwidth. By contrast, the bandwidth of the step-discontinuous phasers is restricted by spurious peaks due to excessive subsection length. The oscillations in the group delay curves, more visible in the continuously nonuniform case due to smaller large-scale variations, correspond to the resonances of the overall C-section structures ($\beta D = \pi$, i.e. $\Delta f = 1.11$ GHz). These oscillations may be suppressed by using cascaded non-uniform C-sections, which also allows to increase the group delay swing, as will be shown later in Fig. 3.9.

In addition to bandwidth enhancement, the proposed phaser provides dispersion diversity enhancement and is capable to present quasi-arbitrary group delay shapes. This benefit comes from the virtually unlimited degrees of freedom of the continuously nonuniform structure. To illustrate this feature, we specify 1^st to 4^th orders Chebyshev group delay responses, used in Dispersion Code Multiple Access (DCMA) [176], in the frequency range from 1 to 3 GHz. Table 3.1 lists the corresponding dimensions and optimal values of the unknown coefficients a_q and b_q in (3.7) for each order, while the corresponding coupling and group delay responses are plotted in Fig. 3.6.

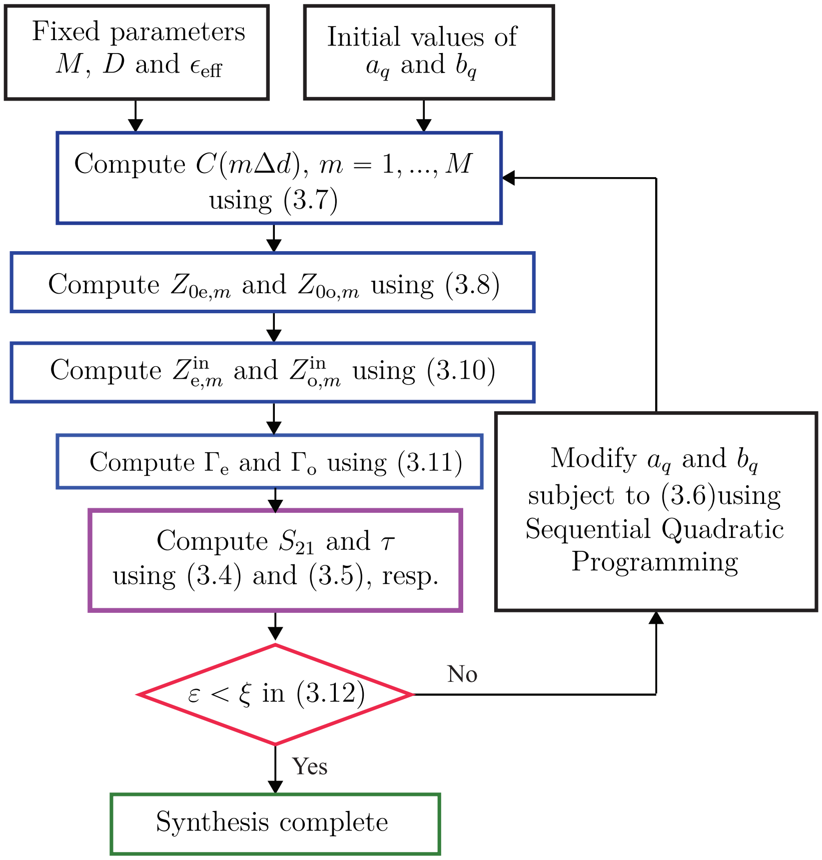

Figure 3.3 Synthesis flowchart for the design of the nonuniform C-section phaser.

Table 3.1 Optimal values of the coefficients a_q and b_q in Eq. (3.7) for the 1st to 4th order Chebyshev designs of Fig. 3.6 [1].

	Chebyshev 1st (D=3.4 cm)		Chebyshev 2nd (D=2.8 cm)		Chebyshev 3rd (D=3.4 cm)		Chebyshev 4th (D=4 cm)	
q	a_q	b_q	a_q	b_q	a_q	b_q	a_q	b_q
0	-0.180	0.000	-0.130	0.000	-0.051	0.000	-0.067	0.000
1	-0.045	0.703	-0.212	0.705	-0.291	0.683	-0.224	0.703
2	0.080	-0.111	0.103	0.102	0.044	0.113	0.062	0.093
3	0.221	0.178	-0.077	0.156	0.002	0.183	-0.014	0.184
4	0.107	-0.160	0.111	-0.054	0.121	-0.033	0.283	-0.001
5	-0.033	0.083	-0.056	0.060	-0.081	-0.049	-0.131	-0.089
6	0.152	-0.116	0.127	0.135	0.132	0.227	0.017	0.035
7	-0.095	-0.096	0.038	-0.082	0.058	-0.053	0.031	-0.134
8	0.069	0.025	0.026	0.207	-0.028	0.342	-0.037	0.127
9	-0.084	-0.159	0.297	-0.052	0.487	-0.045	0.229	-0.004
10	-0.115	0.098	-0.064	-0.239	-0.048	-0.321	-0.011	-0.083
11	0.049	0.030	-0.096	0.036	-0.103	0.022	-0.037	0.022

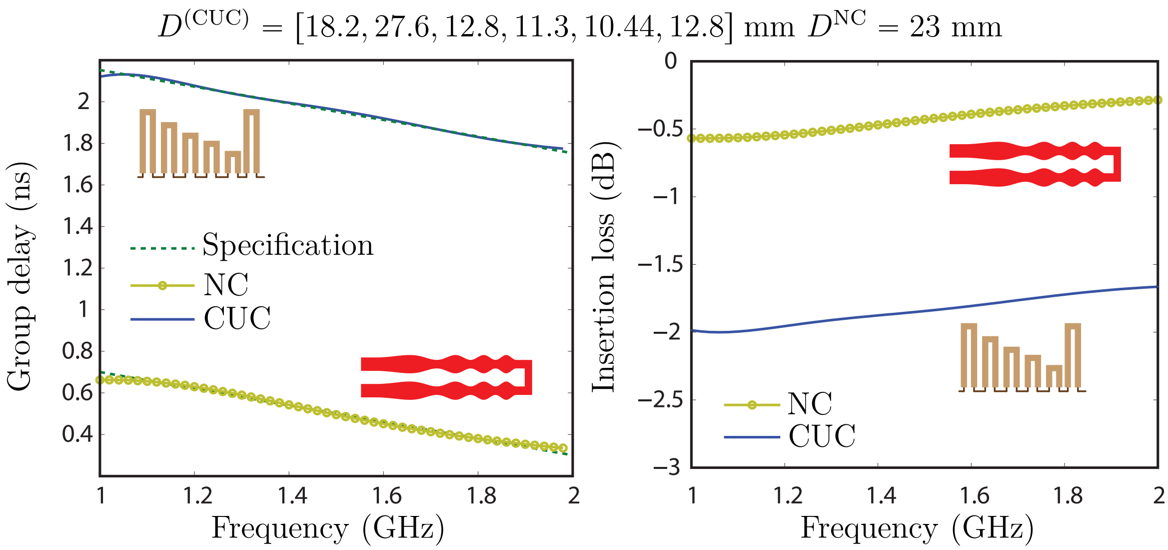

(a) (b)

Figure 3.4 Demonstration of the lower loss, following from the lower delay, of the nonuniform C-section (NC) phaser over the cascaded uniform C-section (CUC) structure [4] using analytical transfer functions for the case of a negatively-sloped group delay response. All designs have been optimized. a) Group delay response. b) Insertion loss. $\epsilon_{\mathrm{e}} = 7.7$ and $\tan\delta = 0.0027$ in both cases.

3.1.3 Experimental Demonstration

This section will experimentally demonstrate the 1st order and 2nd order Chebyshev designs of Fig. 3.6 in stripline technology using the RO3210 substrate with permittivity $\varepsilon_r = 10.2$, height $h = 50$ mil and $\tan\delta = 0.0027$. The fabrication limits in (3.6) were set to $C_{\min} = 0.05$ and $C_{\max} = 0.65$. From the even and odd impedances computed with (3.8) using the functions $C(z)$ plotted in Fig. 3.6, the dimensions of the structure, respecting the matching condition (3.9), are achieved for the given substrate using standard stripline synthesis formulas [149]. The fabricated prototypes are shown in Fig. 3.7.

The experimental results are presented in Fig. 3.8. Experimental results are found to be in good agreement with the specification and with full-wave simulation results, and reasonable matching is achieved.

3.1.4 Space-Modulated C-section Cascading

Although aperiodic space modulation breaks periodicity and hence allows for broader bandwidth designs [42, 43], there are naturally limits on the bandwidth that a single space-modulated C-section may accommodate. Another limitation occurs when the specified group

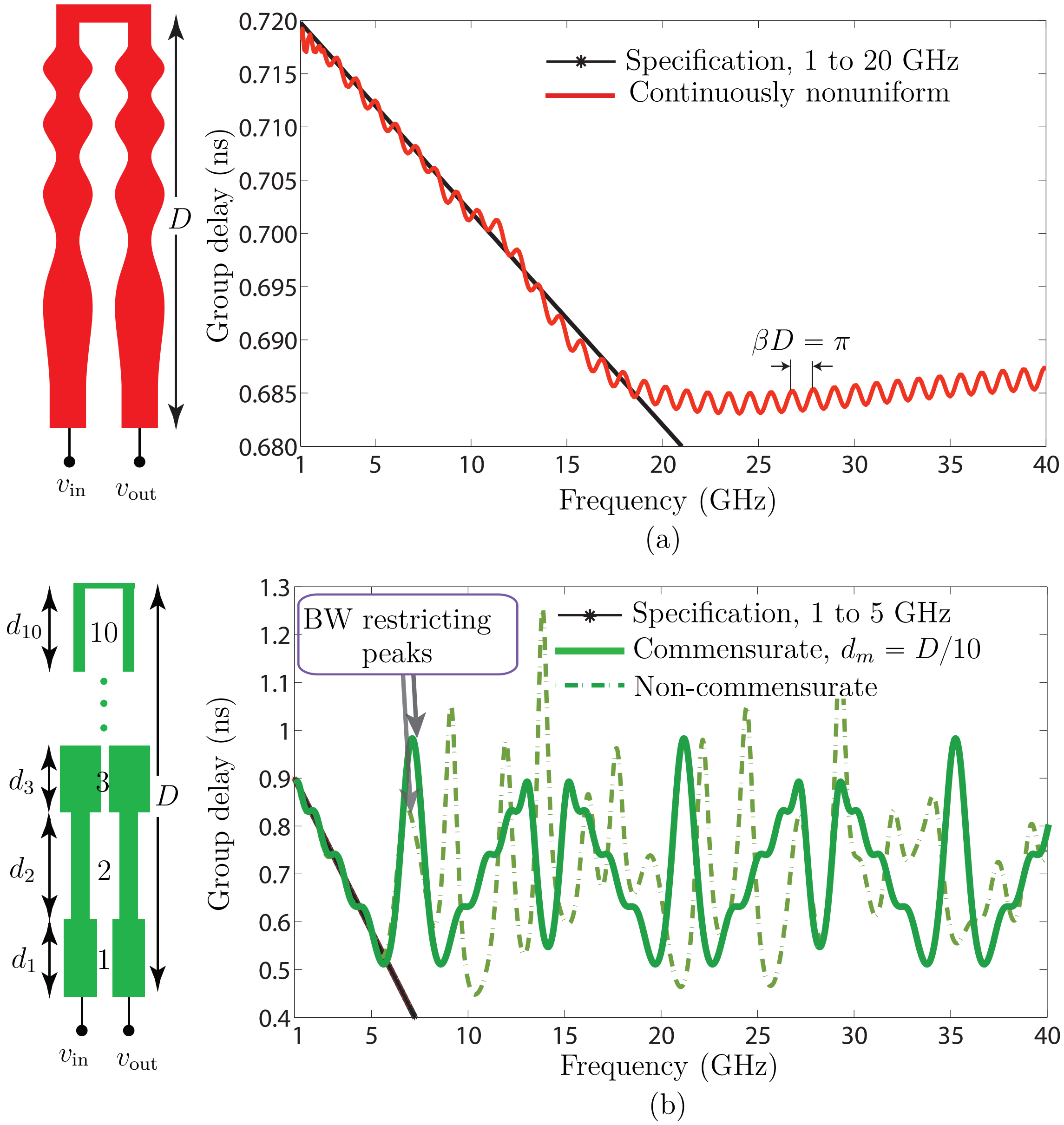

Figure 3.5 Realization of a broadband phasing (negative linear chirp) specification (D = 37 mm = $0.353\lambda_{g,1\text{GHz}}$). (a) Continuously nonuniform phaser, covering the 1 to 20 GHz bandwidth. (b) Step-discontinuity nonuniform commensurate and non-commensurate phasers with 10 sections, restricted to the 1 to 5 GHz bandwidth [1].

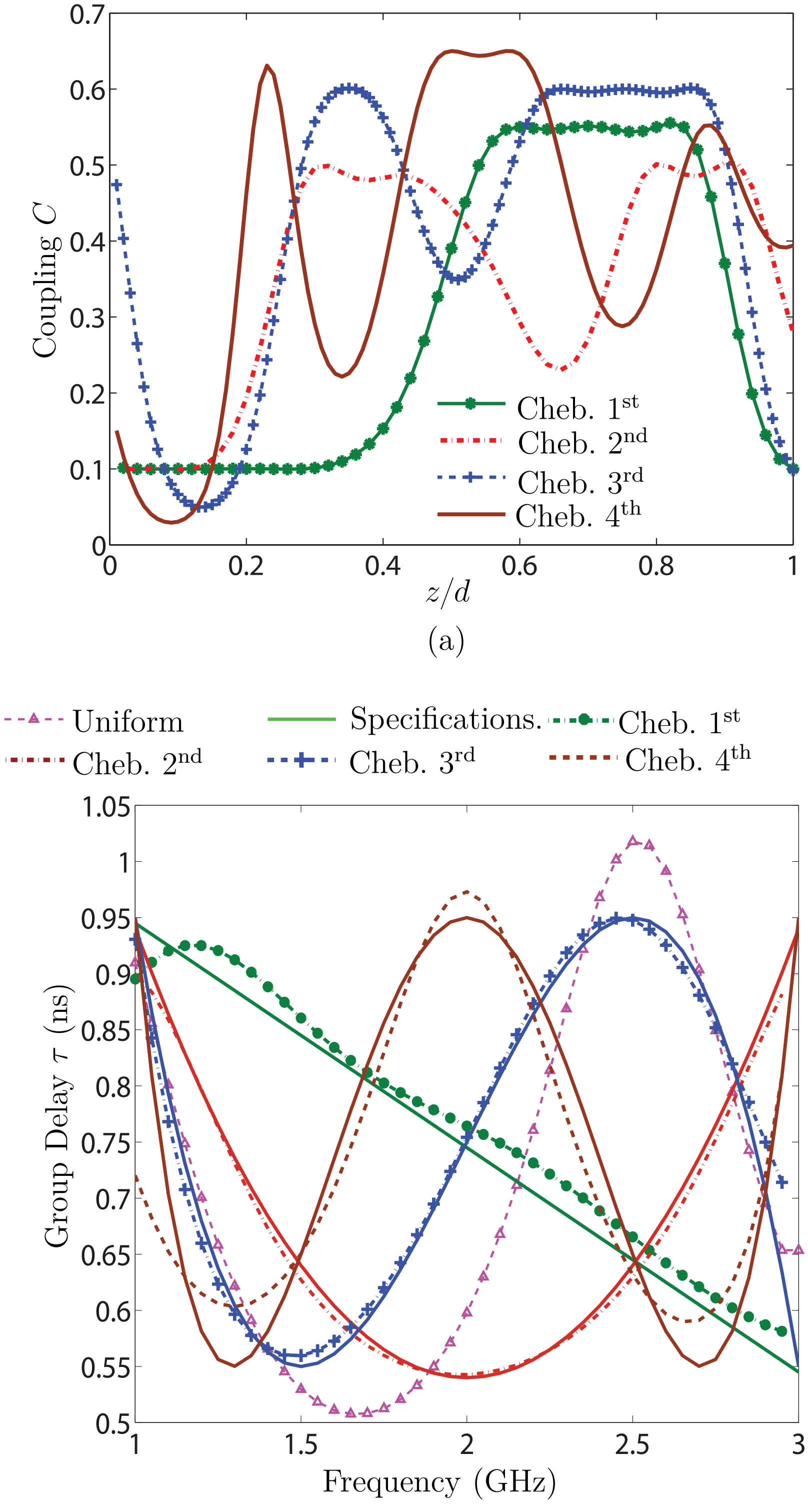

(a)

(b)

Figure 3.6 Realization of Chebyshev first four orders group delay responses. a) Nonuniform coupling function $C(z)$ [Eq. (3.7) with optimal values of a_q and b_q presented in Table 3.1]. b) Group delay response [Eq. (3.5)] [1].

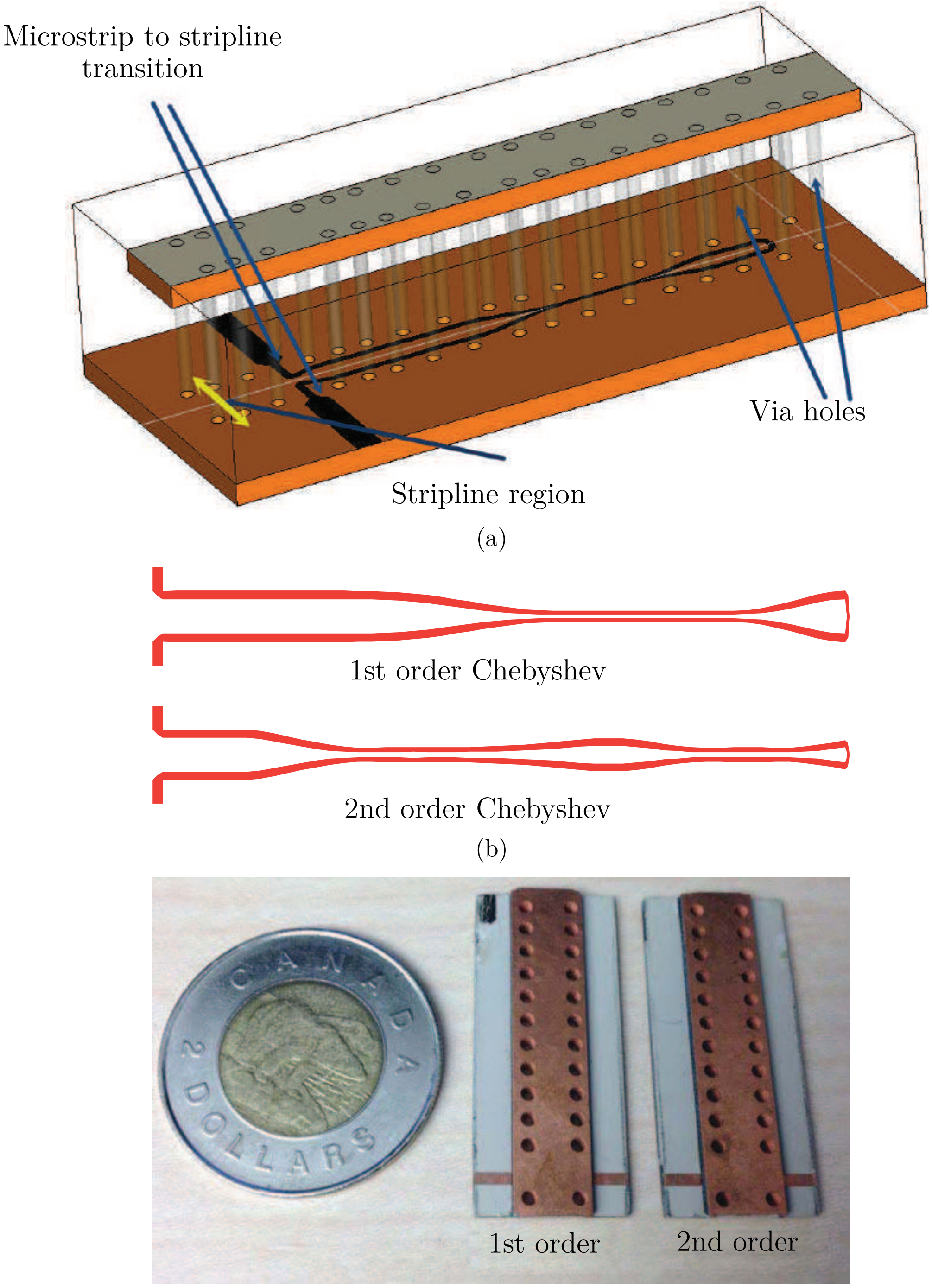

(c)

Figure 3.7 Fabricated nonuniform C-section phaser prototype. a) Exploded perspective view. b) Layouts. c) Photograph of the 1^{st} and 2^{nd} orders Chebyshev group delay responses. The structure includes metalized via holes for stable grounding and transitions from stripline to microstrip line for easier testing [1].

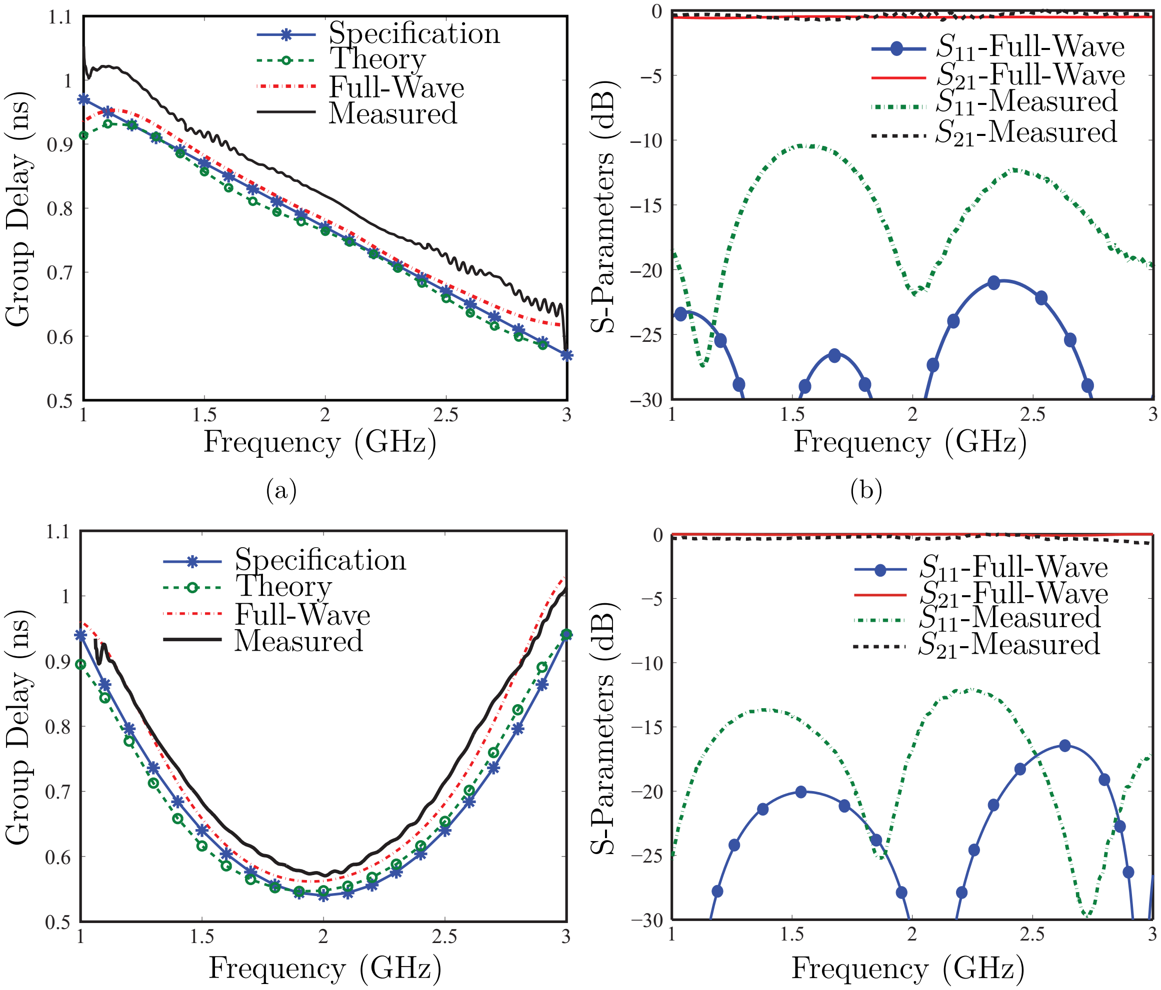

(a) (b)

(c) (d)

Figure 3.8 Experimental results compared with full-wave results (CST Microwave Studio) for the Chebyshev phaser prototypes in Fig. 3.7(c). a) 1st order group delay. b) 1st order S-parameters. c) 2nd order group delay. d) 2nd order S-parameters [1].

delay swing is beyond a certain limit. In both cases, the problem may be resolved by cascading space-modulated C-sections, just as uniform C-sections were cascaded in [4], but with much smaller size and lower loss due to the superiority of the nonuniform structure (Fig. 3.4). This is demonstrated in Fig. 3.9.

3.1.5 Correlation between the Group Delay and the Electromagnetic Fields

An interesting question is whether one could identify a correlation between the group delay and the electromagnetic field distribution in a nonuniform C-section phaser. The answer is positive, and the correlation may be explained with the help of Figs. 3.10 and 3.13.

Figure 3.10 plots the transverse electric field as a function of the position along the structure for three of the C-sections with group delay response plotted in Fig. 3.6. Specifically, the plotted quantity is the magnitude of the transverse component of the electric field in the direction of coupling in order to best capture coupling effects. A first obvious observation is that the field generally concentrates in different portions of the structure at different frequencies, which may have been expected from the different correspond wavelengths. A second clear observation is that whereas the field distributions in the uniform C-section are periodic or, more precisely, are exact sections of sinusoidal functions of the position (constant energy), starting at the end of the C-section with a zero field due to the C-section transverse connection, the field distributions of the nonuniform C-sections are aperiodic (energy depending on z). This is the reason why nonuniform C-sections are essentially immune to spurious group delay harmonics.

The third – less obvious but most important – fact in Fig. 3.10 is that different frequencies store different quantities of energy and that the distribution of energies are different for the different phasers. This is best visible in Figs. 3.11, 3.12 and 3.13, which plot the total time-average stored electric and magnetic energies in the structure versus frequency for the different phasers in Fig. 3.10. This figure strikingly shows that the frequency distributions of stored energy are perfectly correlated to the corresponding group delays, as may be seen by comparison with Fig. 3.6. This observation is consistent with previously reported interference explanations of the proportionality existing between stored energy and group delay and is intuitively sensible : the delay experienced by a wave, with a given frequency, is proportional to the amount of time the energy of the wave is stored in the system – higher stored energies correspond to larger delays.

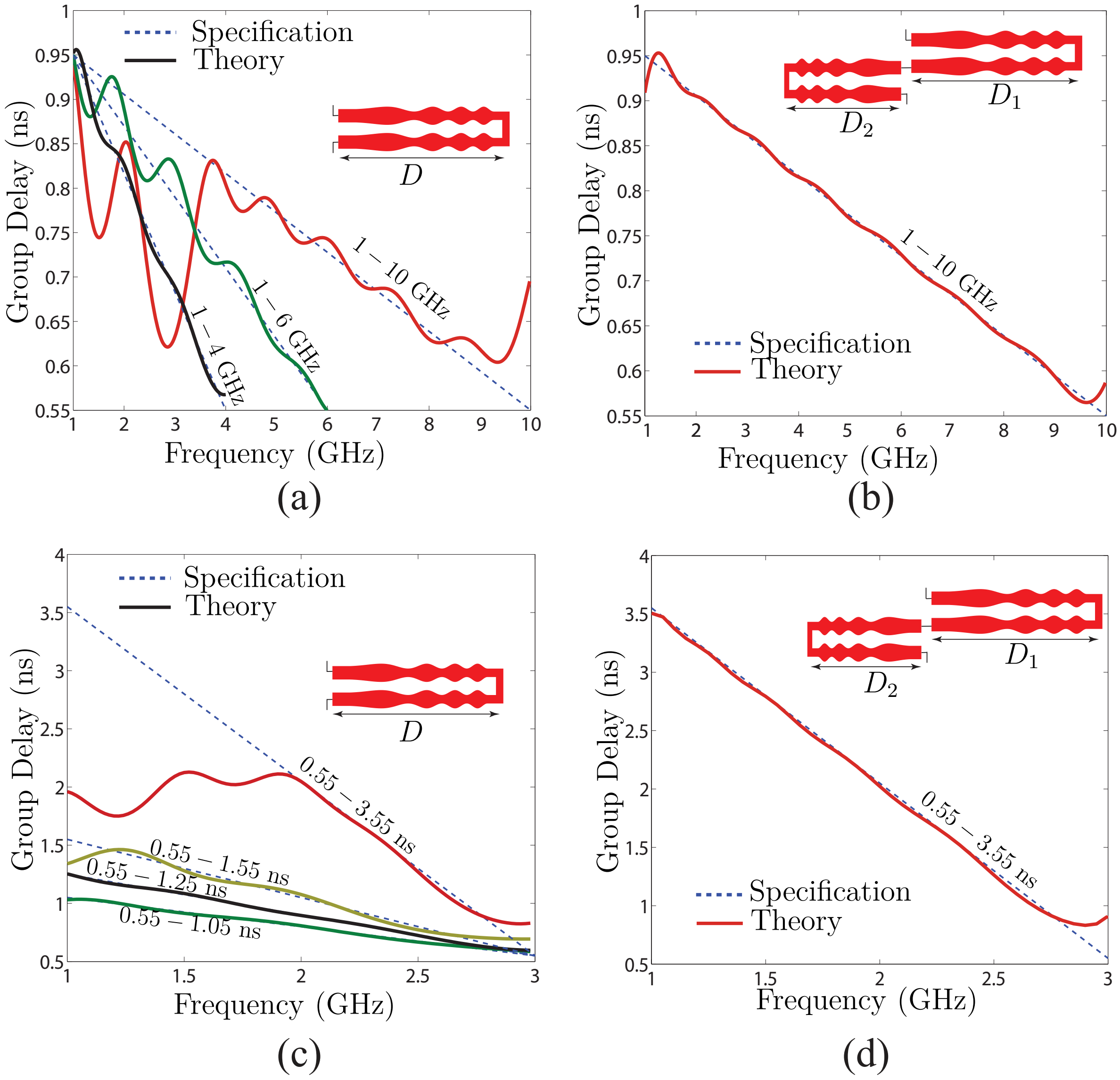

(a) (b)

(c) (d)

Figure 3.9 Continuously space-modulated C-section cascading solution when a single C-section is insufficient to meet specifications. a) Bandwidth increase from 100 % (Fig. 3.6) to 110 %, 143 % and 182 %, showing the failure of a single C-section to provide a bandwidth greater than 110 %. b) Resolution of single C-section issue in a) by cascading two different C-sections (D_1 = 28 mm and D_2 = 13 mm). c) Group delay swing increase from 0.4 ns (Fig. 3.6) to 0.5, 0.7, 1 and 3 ns, showing the failure of a single C-section to reach $\Delta\tau > 1$ ns. d) Resolution of single C-section issue in c) by cascading two different C-sections (D_1 = 82 mm and D_2 = 52 mm) [1].

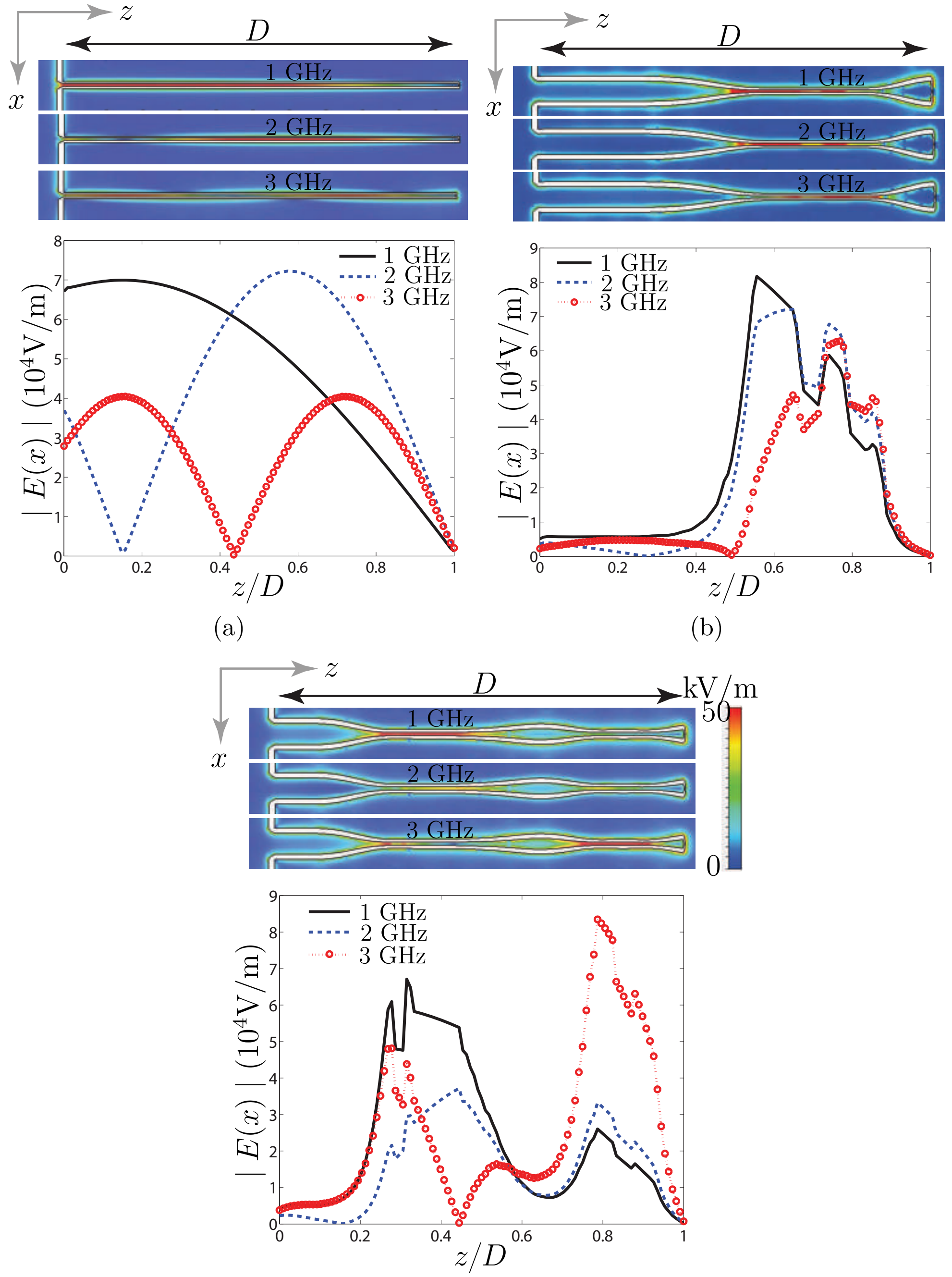

(a)

(b)

(c)

Figure 3.10 Transverse electric field distribution $|E_x(z)|$ along the phaser at $y = 0$, computed using CST Microwave Studio for three group delay designs in Fig. 3.6(b). a) Conventional uniform C-section. b) Nonuniform 1st order Chebyshev C-section. c) Nonuniform 2nd order Chebyshev C-section. The 1st and 2nd order Chebyshev delay response structures correspond to the fabricated prototypes shown in Fig. 3.7(b).

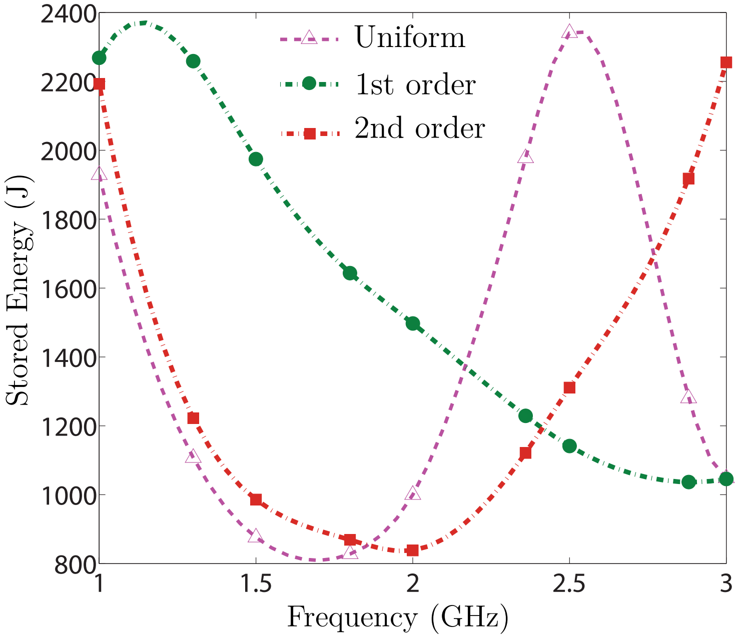

Figure 3.11 Computed stored electric energy in the 1st and 2nd order Chebyshev group delay phasers. The markers correspond to time-averaged energies computed via $W_\mathrm{e} = (\epsilon/4)\int_V E \cdot E^* dv$ while the curves are interpolations.

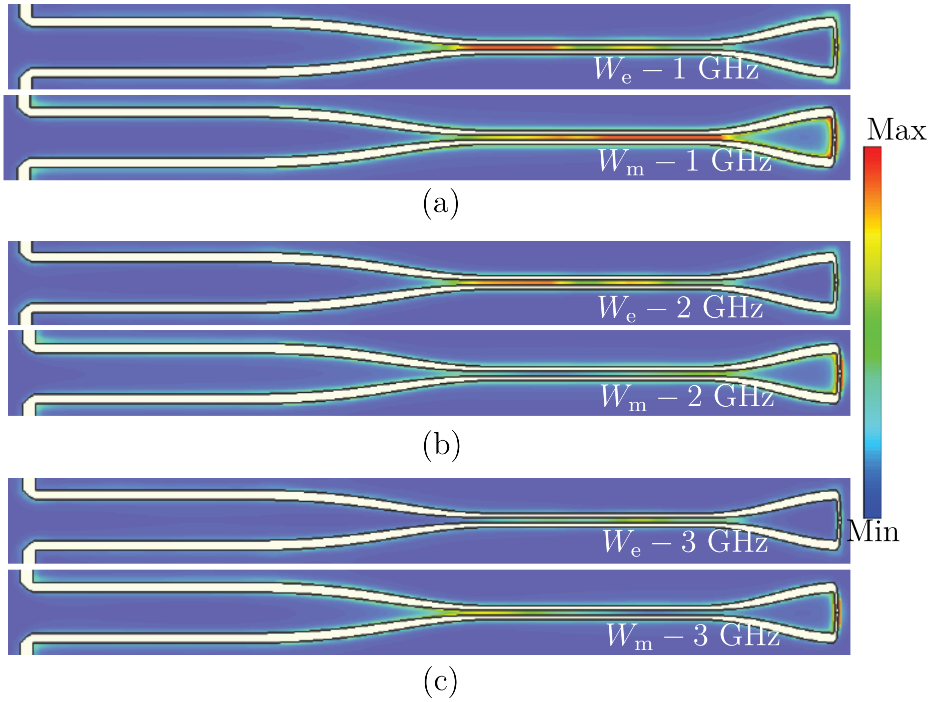

Figure 3.12 Electric and magnetic energy densities inside the 1st order Chebyshev phaser.

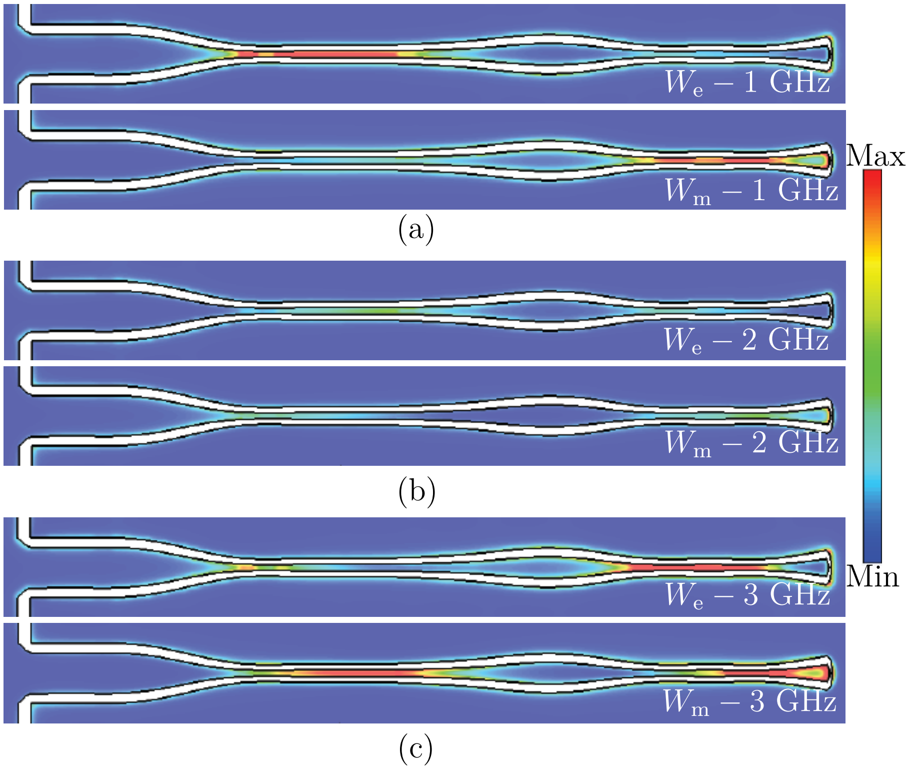

Figure 3.13 Electric and magnetic energy densities inside the 2nd order Chebyshev phaser.

3.2 Stub-line Coupling-free Space-Modulated Phaser

3.2.1 Group delay comparison of uniform parallel open/short stub with a direct transmission line

C-section phasers represent a conventional and useful structure for temporal dispersion engineering, owing to their all-pass property. However, to operate as a all-pass structure, C-section phasers require a structure that supports TEM propagation of the wave, e.g. strip-line, to ensure equal phase velocities for the even- and odd-modes [178]. TEM structures require multilayer technologies which represents design complexity, non-integrability with other devices and high cost. In contrast, series transmission line cannot be used as a broadband phaser due to its monochromatic operation. It is due to the fact that, it is not possible to control the transmission phase and magnitude of a direct transmission line across a bandwidth. To remedy this issue, this section proposes a new phasing structure using open or short terminated stubs, and then applies the static space-modulation to enhance the bandwidth of the phaser.

Let us first evaluate the group delay swing and dispersion of series, shunt short- and open-stub transmission lines. Figure 3.14(a) shows an end-terminated direct transmission line with length d_0,

The voltage across this transmission line may be represented in the form of

$$V(r) = V_0^+(e^{-j\beta r} + \Gamma_{\text{term}} e^{j\beta r}). \tag{3.13a}$$

where β is the wavenumber. The transfer function of this series transmission line may be easily achieved using ray transfer matrix analysis as

$$S_{21} = \left(\cos(\beta d_0) + j\frac{1}{2}\sin(\beta d_0)(z_0 + z_0^{-1})\right)^{-1}, \tag{3.13b}$$

with unity port impedances, and z_0 being the *normalized* characteristic impedance of the line. Then, using (3.13b), the corresponding group delay may be achieved as

$$\tau(\omega) = \frac{2d_0(z_0 + z_0^{-1})^{-1}\sec^2(\beta d_0)}{v\left(4(z_0 + z_0^{-1})^{-2} + \tan^2(\beta d_0)\right)}, \tag{3.13c}$$

where v is the velocity of light inside the medium. Figure 3.14(b) shows a shunt short-ended stub with length d_1, with

$$V(r) = -2jV_0^+\sin(\beta r) \tag{3.14a}$$

The transfer function may be achieved as

$$S_{21} = \left(1 - j\frac{1}{2}z_1^{-1}\cot(\beta d_1)\right)^{-1} \tag{3.14b}$$

where z_1 is the *normalized* impedance of the stub. The group delay of the system reads

$$\tau(\omega) = \frac{2d_1 z_1 \csc^2(\beta d_1)}{v\left(4z_1^2 + \cot^2(\beta d_1)\right).} \tag{3.14c}$$

Following the similar procedure, for a parallel open-ended stub shown in Fig. 3.14(c), the voltage across the line, the transfer function and the group delay may be expressed as

$$V(r) = 2V_0^+\cos(\beta r), \tag{3.15a}$$

$$S_{21} = \left(1 + j\frac{1}{2}z_1^{-1}\tan(\beta d_1)\right)^{-1}, \tag{3.15b}$$

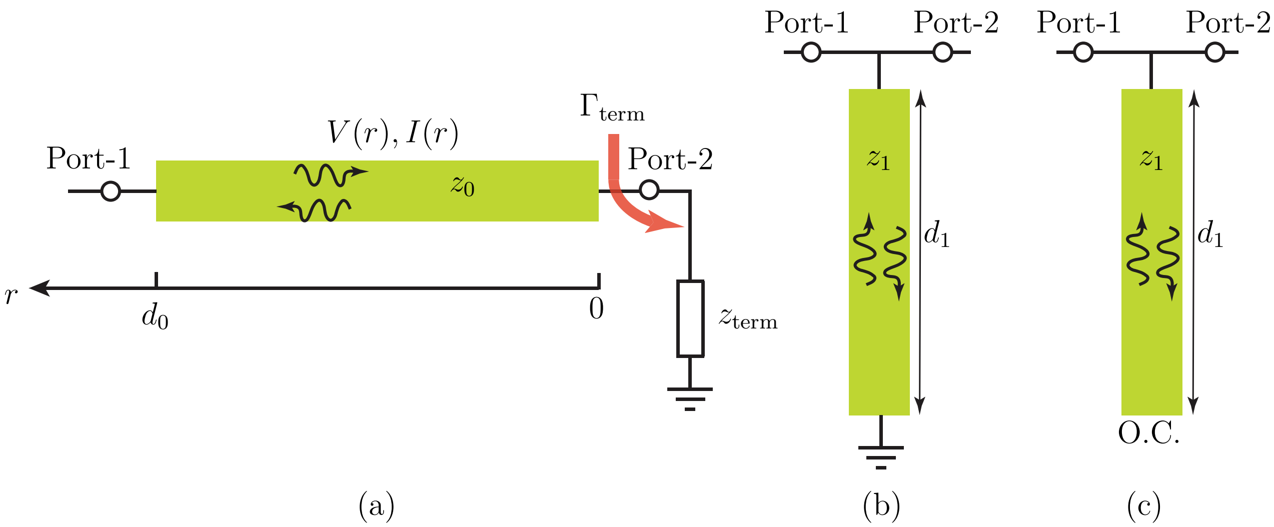

Figure 3.14 Uniform transmission line (a) direct line, series with the terminated load (b) parallel short-ended and (c) parallel open-ended.

$$\tau(\omega) = -\frac{\partial \angle S_{21}}{\partial \omega} = \frac{2d_1 z_1 \sec^2(\beta d_1)}{v\left(4z_1^2 + \tan^2(\beta d_1)\right)}. \tag{3.15c}$$

Figure 3.15 plots the group delay dispersion comparison of a transmission line with short- and open-terminated shunt stubs, for different normalized impedances, from 0.2 to 2.6. It may be seen from this figure that the short- and open-ended stubs provide higher dispersion than the series transmission line, for the transmission line impedances of higher than 0.6, while for the impedances of lower than 0.6 they present the same dispersion as the series transmission line. Moreover, it may be seen that varying the impedance of the line yields greater group delay swing for the stubs than the series transmission line. It may be shown that complete transmission occurs around $\beta d_1 = \pi/2$ for short-ended and $\beta d_1 = \pi$ for open-ended stub. Besides, varying z_1 from 0.2 to 2.6, provides $7.7d_1$ group delay swing group delay. In contrast, the series transmission line would be matched at $\beta d_0 = \pi$, providing $5.34d_0$ group delay swing. Complete reflection may be achieved at $\beta d_1 = \pi$ for the short-ended and $\beta d_1 = \pi/2$ for the open-ended stub, while at this points, varying z_1 from 0.2 to 2.6 offers $16d_1$ GD swing for both stubs. In contrast, in a series transmission line partial reflection occurs at $\beta d_0 = \pi/2$, providing $1.87d_0$ group delay swing. As a result, open- and short-terminated stubs provide much higher group delay swing than the series transmission line, while the series transmission line offers better and wider magnitude response.

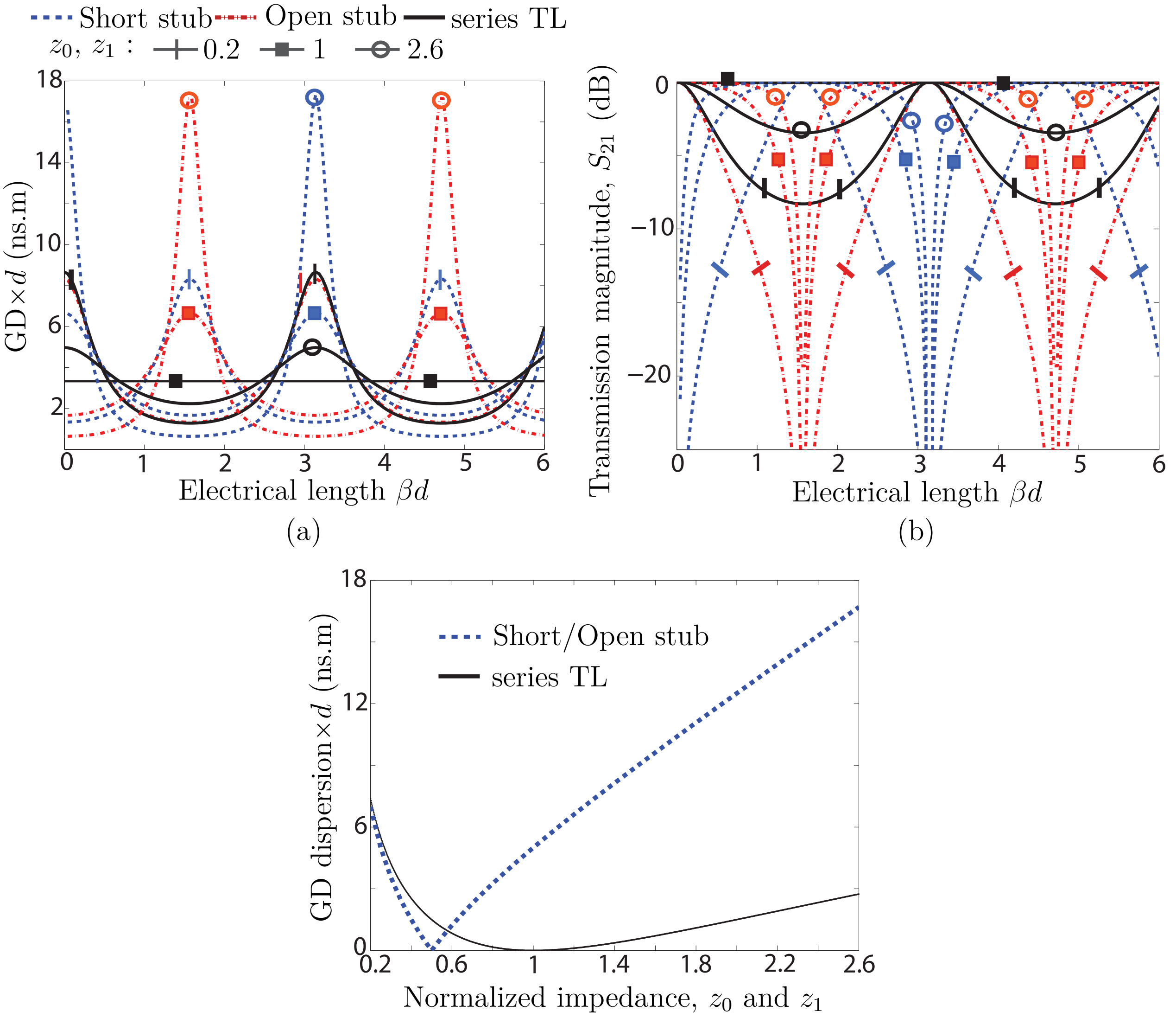

(a)

(b)

Figure 3.15 Group delay dispersion comparison of shunt stub with a terminated TL.

3.2.2 Operation Principle and Synthesis

Figure 3.16 shows structure of stub-line phaser, which takes advantage of the high group delay dispersion and swing of the shunt stubs, where two short/open shunt-stubs are employed to satisfy the transmission phase shift condition, while having minimum effect on the magnitude, and a series transmission line, interconnecting the two stubs, satisfies the magnitude condition.

It has been shown that static space-modulated transmission lines are capable to satisfy the magnitude [27,40] and phase [179] conditions across a broad frequency bandwidth. Therefore, we employ the continuous space modulated transmission lines to widen the bandwidth of the phaser in Fig. 3.16. Fig. 3.17 shows the structure of the continuously space-modulated phaser as a wider bandwidth version of the phaser in Fig. 3.16, where shunt stubs represent dispersive shunt indutances/capaticitances.

General continuously space-modulated, nonuniform, transmission lines do not admit closed-form solutions. However, a simple synthesis method may be used for their design as follows. The goal of the synthesis is to determine the space-dependent impedance functions, $z_n(r)$, with $n = 0, 1, 2$, which satisfies the specified group delay and magnitude conditions. This function must satisfy the fabrication condition of

$$z_{\min} < z_0(r), z_1(r), z_2(r) < z_{\max}. \tag{3.16}$$

A possible approach is to expand $z_n(r)$ in a Fourier series, which is expected to present continuous variations with a moderate number Q of expansion terms, as

$$z_n(r) = a_{n0} + \sum_{q=1}^{Q} \left[a_{nq} \cos\left(\frac{2\pi qr}{d_n}\right) + b_{nq} \sin\left(\frac{2\pi qr}{d_n}\right) \right]. \tag{3.17}$$

We discretize the three nonuniform lines into M deep subwavelength uniform line subsections, for which closed-form formulas are available. Then, The length of each subsection reads $\Delta d = d/M \ll \lambda_{\min}$. We first compute the input impedance of the stubs, where the input impedance at the input of the mth subsection, $z_{1,m}^{\text{in}}$ are related to those of the $(m-1)$th subsection, $z_{1,(m-1)}^{\text{in}}$

$$z_{1,m}^{\text{in}} = z_{1,m} \frac{z_{1,(m-1)}^{\text{in}} + jz_{1,m} \tan(\Delta\theta)}{z_{1,m} + jz_{1,(m-1)}^{\text{in}} \tan(\Delta\theta)}, \tag{3.18}$$

where $m = 0, 1, \ldots, M$, $\Delta\theta = \beta\Delta d = \omega d/c\sqrt{\epsilon_{\text{eff}}}$, as the electrical length of each subsection.

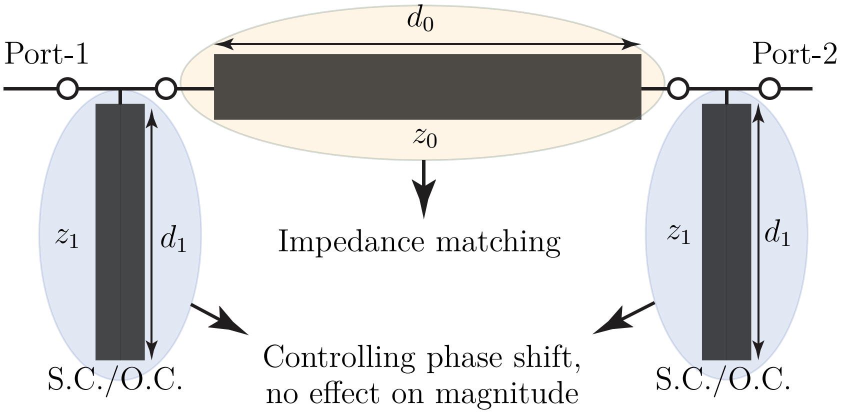

Figure 3.16 Uniform (narrowband) stub-line phaser.

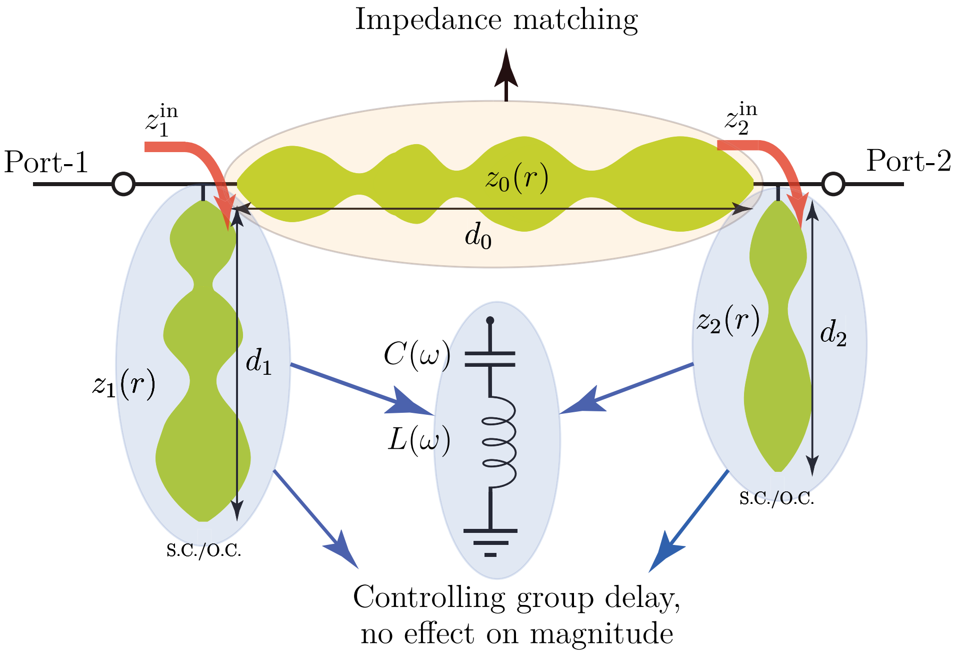

Figure 3.17 Nonuniform stub-line phaser as a widened-bandwidth version of the phaser in Fig. 3.16 [5].

Iteratively computing from $m = 1$ to $m = M$ provides the input impedance of the stub. Next, to achieve the transfer matrix of the series line, we calculate the transfer matrix of its subsection as

$$\begin{bmatrix} A_{0,m} & B_{0,m} \\ C_{0,m} & D_{0,m} \end{bmatrix} = \begin{bmatrix} \cos(\Delta\theta) & jz_{0,m}\sin(\Delta\theta) \\ jy_{0,m}\sin(\Delta\theta) & \cos(\Delta\theta) \end{bmatrix}, \tag{3.19}$$

and then the transfer matrix of the entire series transmission line would be achieved by multiplying its subsections as

$$\begin{bmatrix} A_0 & B_0 \\ C_0 & D_0 \end{bmatrix} = \begin{bmatrix} A_1 & B_1 \\ C_1 & D_1 \end{bmatrix} \cdot \begin{bmatrix} A_2 & B_2 \\ C_2 & D_2 \end{bmatrix} \cdots \begin{bmatrix} A_M & B_M \\ C_M & D_M \end{bmatrix} \tag{3.20}$$

Finally, the total transfer matrix of the phaser will be calculated by multiplying the one of the three sections, i.e. the first shunt stub, the series line, and the second shunt stub, as

$$\begin{bmatrix} A^{\mathrm{T}} & B^{\mathrm{T}} \\ C^{\mathrm{T}} & D^{\mathrm{T}} \end{bmatrix} = \begin{bmatrix} 1 & 0 \\ y_{\mathrm{s1}}^{\mathrm{in}} & 1 \end{bmatrix} \cdot \begin{bmatrix} A_0 & B_0 \\ C_0 & D_0 \end{bmatrix} \cdot \begin{bmatrix} 1 & 0 \\ y_{\mathrm{s2}}^{\mathrm{in}} & 1 \end{bmatrix}, \tag{3.21}$$

Next, the scattering vectors S_{11}, S_{21} are obtained from the overall ABCD matrix of the phaser as [149],

$$S_{11} = \frac{A^{\mathrm{T}} + B^{\mathrm{T}}Z_0^{-1} - C^{\mathrm{T}}Z_0 - D^{\mathrm{T}}}{A^{\mathrm{T}} + B^{\mathrm{T}}Z_0^{-1} + C^{\mathrm{T}}Z_0 + D^{\mathrm{T}}} \tag{3.22a}$$

$$S_{21} = \frac{2}{A^{\mathrm{T}} + B^{\mathrm{T}}Z_0^{-1} + C^{\mathrm{T}}Z_0 + D^{\mathrm{T}}} \tag{3.22b}$$

Finally, the group delay of the phaser is computed by differentiating the phase of S_{21} over the frequency

$$\tau = -\frac{\partial \phi_{S_{21}}}{\partial \omega} \tag{3.23}$$

Once a $\tau(\omega)$ function is established for a trial expansion set a_{nq} and b_{nq}, it is injected in the fitness function $\varepsilon = (1/\omega_{\mathrm{b}}^2)\int_{\omega_{\mathrm{l}}}^{\omega_{\mathrm{h}}} \left(\left|\tau - \tau_{\mathrm{s}}\right| + \left|S_{p1}\right|\right) d\omega$, which corresponds to the deviation of $\tau(\omega)$ from the specified function, $\tau_{\mathrm{s}}(\omega)$, while minimizing the reflection, S_{11}, or transmission S_{21} scattering parameter, respectively for transmission- and reflection-type phasers. Figure 3.18 shows the design procesdure.

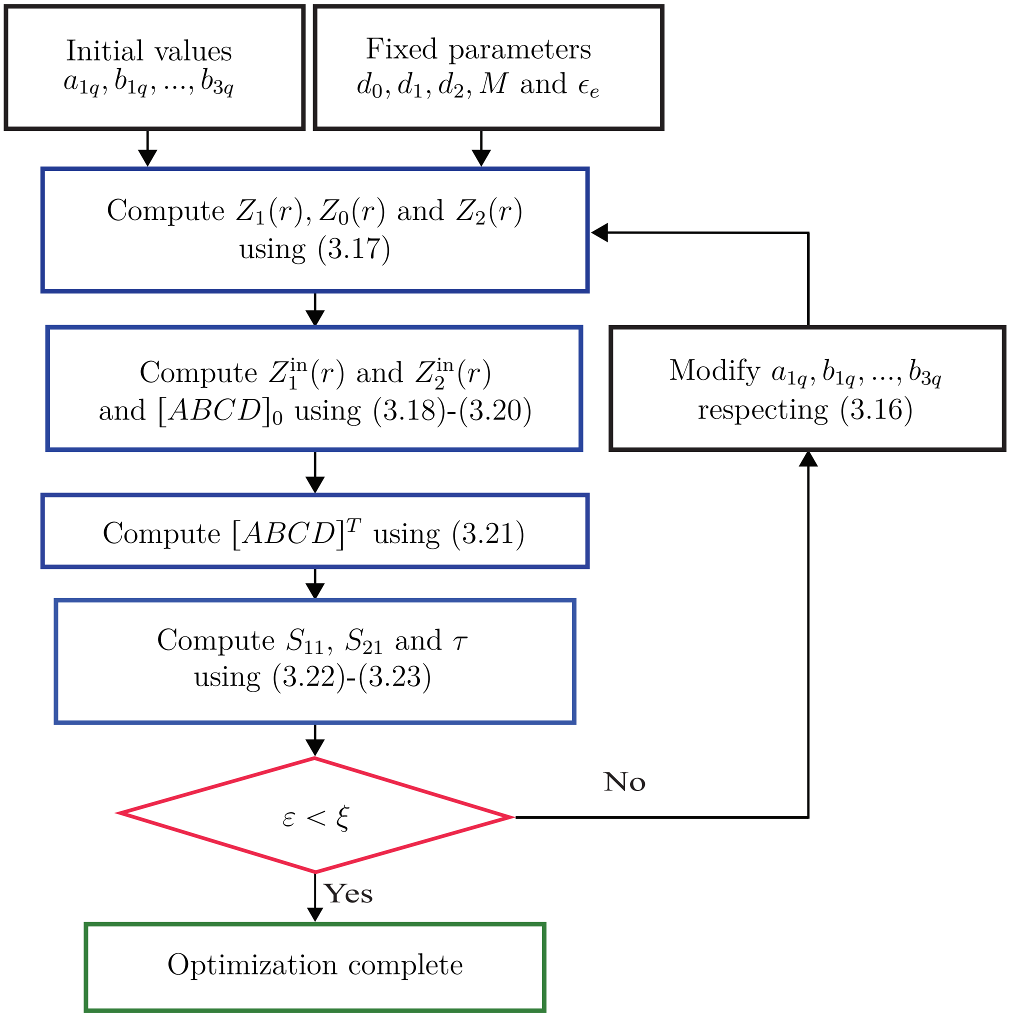

Figure 3.18 Design procedure.

Sequential Quadratic Programming (SQP) represents one of the most successful methods for the numerical solution of constrained nonlinear optimization problems (NLP). SQP is an iterative procedure which models the NLP for a given $x^n, n \in \mathbb{N}$ by a Quadratic Programming (QP) subproblem, solves that QP subproblem and then uses the solution to construct a new iterative x^{n+1}. The construction is done in a way that the sequence x^n converges to a local minimum x of the problem as $n \rightarrow \infty$

$$\text{minimize} \quad f(a_q, b_q) \tag{3.24a}$$

$$\text{over} \quad a_q, b_q \in \mathbb{R} \tag{3.24b}$$

$$\begin{aligned} \text{subject to} \quad & Z_{\text{d}}(r = 0, (a_q, b_q)) - Z_0 = 0, \\ & Z_{\text{d}}(r = d, (a_q, b_q)) - Z_0 = 0 \end{aligned} \tag{3.24c}$$

$$\begin{aligned} & Z_{0,1,2}(r, (a_q, b_q)) - Z_{\max} \leqslant 0, \\ & Z_{\min} - Z_{0,1,2}(r, (a_q, b_q)) \leqslant 0 \end{aligned} \tag{3.24d}$$

The functional L defined by means of

$$\begin{aligned} L(a_q, b_q; \lambda, \mu) =& f(a_q, b_q) + \lambda_1(Z_0(r = 0) - Z_0) \\ & + \lambda_2(Z_0(r = d) - Z_0) + \mu_1(Z_1(r) - Z_{\max}) \\ & + \mu_2(Z_{\text{d}}(r) - Z_{\max}) + \mu_3(Z_2(r) - Z_{\max}) \\ & + \mu_4(Z_{\min} - Z_1(r)) + \mu_5(Z_{\min} - Z_{\text{d}}(r) \\ & + \mu_6(Z_{\min} - Z_2(r)) \end{aligned} \tag{3.25}$$

is called the Lagrangian functional of the NLP. The vectors $\lambda \in \mathbb{R}$ and $\mu \in \mathbb{R}_+$ are Lagrangian multipliers.

3.2.3 Experimental Demonstration and Discussion

This section presents experimental demonstration of the phaser in Fig. 3.17, where transmission-type and reflection-type versions with different properties will be introduced.

Transmission-Type Phaser

Fig. 3.19 shows the wave path through the transmission-type continuously space-modulated phaser with open-terminated stubs. To design a transmission-type phaser operating inside a given frequency bandwidth, all interband transmission zeroes resulted from the open-stubs should be canceled. To best investigate this issue, let us first consider the uniform transmission-type phaser with uniform open-ended stubs in Fig. 3.16, operating at center frequency of f_c. The input impedance of the stub may be found as $Z_{\mathrm{s}}^{\mathrm{in}} = -jZ_{\mathrm{s}}^{0}\cot(\theta_{\mathrm{c}})$. The transmission zeros of such a phaser occur at $\theta_{\mathrm{c}} = \beta_{\mathrm{c}} d_1 = \pi(n+1/2)$, for $n = 0, 1, 2, ...$ At each transmission, zero complete reflection occurs, where depending on the operation frequency bandwidth, a couple of this transmission zeros may happen in the frequency band. Then, for an efficient and broadband design, these transmission zeroes should be pushed outside the frequency band. To ensure minimum number of transmission zeros occur inside the band, the length of the stubs could be set as

$$d_1, d_2 \approx k\frac{\lambda_c}{2} \qquad k = 0, 1, \ldots, \infty \tag{3.26}$$

with λ_{c} being the guidance wavelength of the center frequency.

Next, the nonuniformity of the stubs could help to cancel the remained transmission zeroes inside the frequency band. It is shown in the previous section how nonuniformity of the stub may be leveraged to cancel the transmission zeroes. Also, comparing the input impedance of the nonuniform stubs with lumped inductance or capacitance, reveals how these stubs behave as dispersive, controllable lumped inductance and capacitances, yielding band-broadening of the structure. Afterwards, we experimentally demonstrate the 2nd order Chebyshev transmission-type phaser of Fig. 3.17, using open stubs, in microstrip technology. We use alumina substrate with permittivity $\epsilon_{\mathrm{r}} = 9.9$ and height $h = 10$ mil. The phaser presents 53.3% frequency bandwidth, i.e. from 1.1 to 1.9 GHz, with 0.38 ns group delay swing. Figure 3.20 (a) plots achieved optimal normalized space-dependent characteristic impedances of the phaser. Table 1.2 shows the optimal coefficients of (3.17) for the 2^{nd} order Chebyshev.

Figure 3.20 (b) plots dispersion comparison of input impedance of the shunt space-modulated open-stub with the one of shunt uniform open-stub, shunt inductance and shunt capacitance. It may be seen from this figure that, nonuniform stub behaves as dispersive inductance and capacitance. Moreover, space modulation provides a great control on the dispersion of the stubs, providing high input impedance stubs, so that they do not affect the magnitude. It also helps to cancel the transmission zeros across the operation bandwidth. Figure 3.21

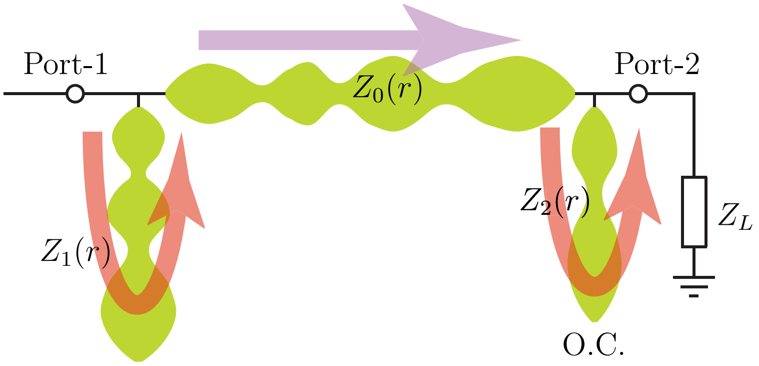

Figure 3.19 Wave path through the transmission-type phaser.

Table 3.2 Optimal values of the coefficients a_{1q}, b_{1q}, a_{2q}, b_{2q}, a_{3q} and b_{3q} for the 2$^{\text{nd}}$ order Chebyshev transmission-type phaser.

q	0	1	2	3	4	5	6	7	8	9	10
a_{1q}	-0.2600	0.2645	0.0234	0.0454	-0.0366	-0.0077	-0.0228	-0.0195	-0.0057		
b_{1q}		1.3121	-0.1112	0.2454	-0.0127	0.0659	0.0434	-0.0007	0.0473		
a_{2q}	0.4713	-0.3441	0.0862	0.0489	-0.0450	-0.0080	0.0113				
b_{2q}		0.1715	0.0640	-0.0096	-0.0083	-0.0338	-0.0293				
a_{3q}	-0.2924	0.5564	-0.0900	0.1518	0.0186	0.0094	0.0195	0.0114	-0.0273	-0.0043	-0.0203
b_{3q}		0.9986	0.0918	-0.0130	0.0095	-0.0376	-0.0653	-0.0358	-0.0600	-0.0275	-0.0026

shows the corresponding group delay and S-parameters of the phaser. Then, the nonuniform characteristic impedance of the stubs and series transmission line would be achieved through minimization of the fitness function $\varepsilon_{\text{trans}}$, as

$$\varepsilon_{\text{trans}} = \frac{1}{\omega_b^2} \int_{\omega_l}^{\omega_h} \left|\tau - \tau_{\text{s}}\right| d\omega \cdot \int_{\omega_1}^{\omega_N} \left|S_{11}\right| d\omega \tag{3.27}$$

Reflection-Type Phaser

Here, we show that a space-modulated stub-loaded phaser can be designed as reflection-type to provide enhanced resolution, i.e. higher group delay swing across the operation bandwidth. Figure 3.22 shows the structure and wave path through the reflection-type phaser with short-terminated stubs.

In such a reflection-type phaser, all interband reflection zeroes should be canceled. To best investigate this issue, let's consider uniform version of the reflection-type phaser in Fig. 3.22, as shown in Fig. 3.14 with short-ended stubs $Z_{term} = 0$, operating at center frequency f_c. The input impedance of the first stub reads $Z_{\text{s}}^{\text{in}} = jZ_{\text{s}}^{0}\tan(\theta_{\text{c}})$ and reflection zeros occur at $\theta_{\text{c}} = n\lambda_{\text{c}}/2$. Reflection zeros yield undesirable zero reflection of input signal. Depending on the operation frequency bandwidth and length of stubs, there might be couple of refletion zeros in the frequency band, while for the efficient and broadband operation, these zeroes should be canceled. For an efficient design, the length of the stubs may be set as

$$d_1, d_2 \approx (2k+1)\frac{\lambda_c}{4} \qquad k = 0, 1, \ldots, \infty \tag{3.28}$$

It should be noted that the reflection poles are undesirable as well as reflection zeroes since they cause huge discontinuity in group delay response. For the reflection type of Fig. 3.22, the first stub mainly provides the specified group delay swing, while the series-line along with the second stub are used to present an appropriate impedance mis-matching.

Depending on the required group delay swing, $\Delta\tau$, the termination of the stubs would be determined to be short or open, so that exhibit minimum stub lengths and maximum voltage at the input of the stub at center frequency, according to equations (3.14a) and (3.15a). Then, the nonuniform characteristic impedance of the stubs and series transmission line would be achieved through minimization of the fitness function as

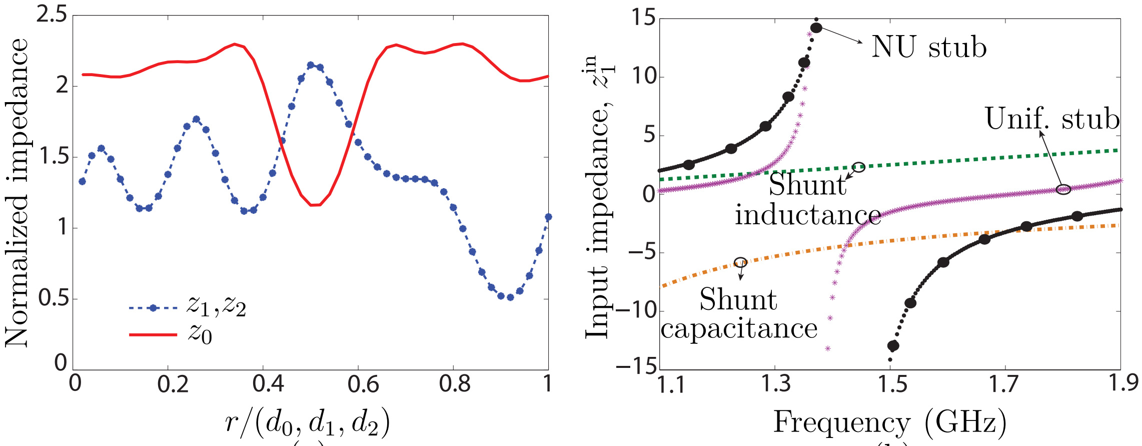

(a) (b)

Figure 3.20 Transmission-type stub-line phaser. (a) Continuous space-varying characteristic impedances in Fig. 3.17 with open stubs, with $d_0 = d_1 = d_2 = 3.6$ cm. (b) Dispersion comparison of the input impedance of the shunt shunt open-ended stub with shunt uniform open-stub, shunt inductance and shunt capacitance.

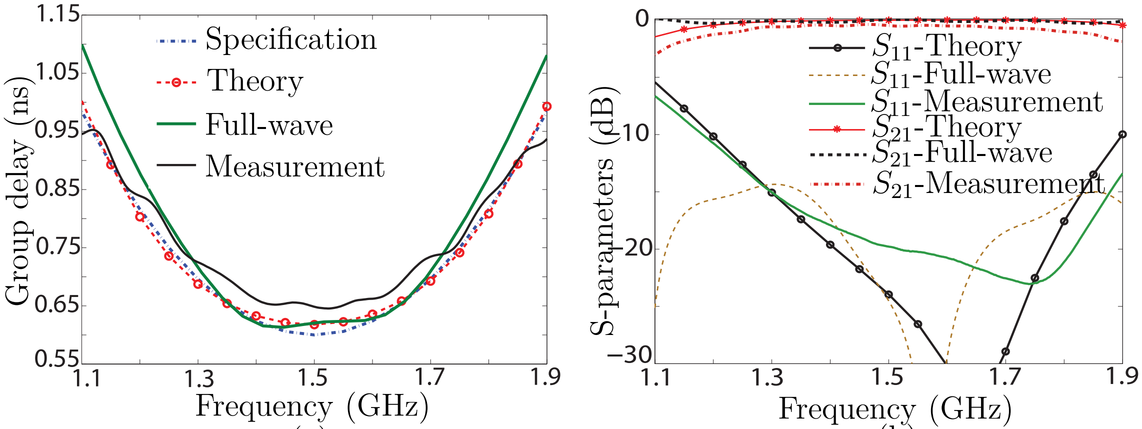

(a) (b)

Figure 3.21 Experimental, full-wave and analytical results for the 2nd order Chebyshev transmission-type phaser prototype. a) Group delay. b) S-parameters.

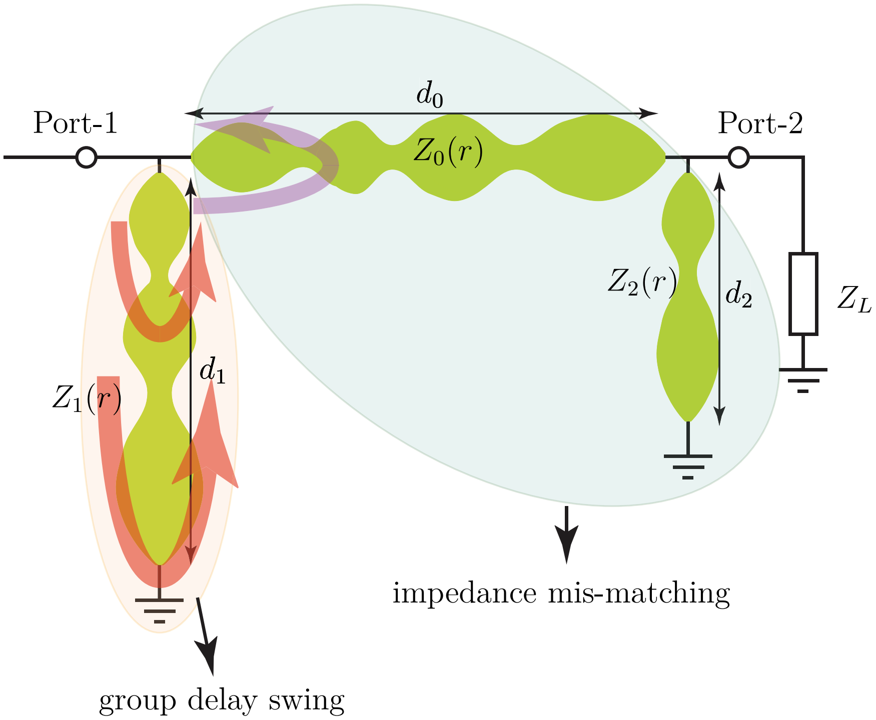

Figure 3.22 Schematic of the proposed short-terminated stub-loaded reflection-type phaser.

$$\varepsilon_{\text{refl}} = \frac{1}{\omega_b^2} \int_{\omega_l}^{\omega_h} \left|\tau - \tau_{\text{S}}\right| d\omega \cdot \int_{\omega_1}^{\omega_N} \left|S_{21}\right| d\omega. \tag{3.29}$$

A prototype reflection-type phaser is designed and fabricated with the following characteristics. The phaser presents 2nd order Chebyshev group delay response with 100% frequency bandwidth, i.e. from 1 to 3 GHz, with 1 ns group delay swing. Figure 3.23 (a) and (b) plot the space-varying impedances of the phaser, and dispersion comparison of the space-varying (nonuniform) and space-invariant (uniform) short-ended stubs.

Table 3.3 lists the optimized coefficients in 3.17 for the reflection-type 2nd order Chebyshev. Figure 3.24(a) and (b) respectively show the group delay and S-parameters of the phaser.

Figures 3.25 and 3.26 show the photograph of the fabricated reflection-type and transmission-type phasers and the corresponding electric and magnetic energy densities inside them, for three different frequencies. We may identify a correlation between the group delay and the electromagnetic field distribution in a nonuniform stub-line phaser. These figures show that distributions of stored energy are perfectly correlated to the corresponding group delays, as may be seen by comparison with Figs. 3.21(a) and 3.24(a), respectively for transmission-

Table 3.3 Optimum values of the coefficients a_{1q}, b_{1q}, a_{2q}, b_{2q}, a_{3q} and b_{3q} for the 2$^{\text{nd}}$ order Chebyshev reflection-type phaser.

q	0	1	2	3	4	5
a_{1q}	-0.2208	0.4778	-0.6798	-0.2303	-0.1438	0.0530
b_{1q}		-0.4079	0.8776	0.2040	0.1383	0.2083
a_{2q}	-0.1191	-1.0627	0.0456	0.0728	-0.1776	-0.1363
b_{2q}		0.1496	0.5514	0.42066	-0.0768	-0.0941
a_{3q}	-0.2458	-0.7644	-0.0212	-0.3048	0.0707	0.0184
b_{3q}		-0.9888	0.0969	0.1399	0.0121	0.1419

q	6	7	8	9
a_{1q}	-0.0512	-0.0028	0.0097	0.0065
b_{1q}	0.1244	0.0613	0.0408	0.0133
a_{2q}	-0.1066	-0.0770	0.0067	0.0201
b_{2q}	0.0810	-0.0055	-0.0853	-0.0334
a_{3q}	0.0161	0.0485	-0.0204	0.0117
b_{3q}	-0.0549	0.0213	-0.0174	-0.0047

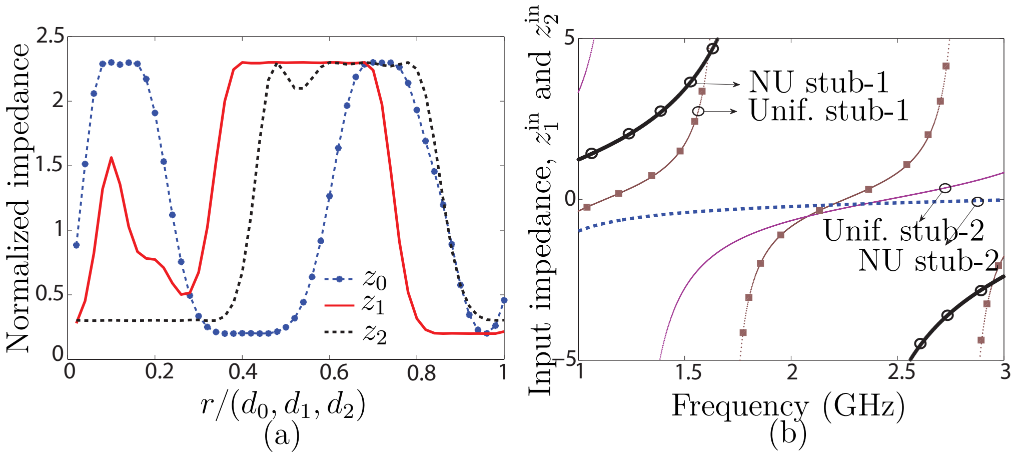

(a) (b)

Figure 3.23 Reflection-type phaser. (a) Nonuniform impedances in Fig. 3.17, with $d_0 = 3.4, d_1 = 4.8, d_2 = 2.2$ cm. (b) Dispersion comparison of the input impedance of the nonuniform and uniform short-stubs.

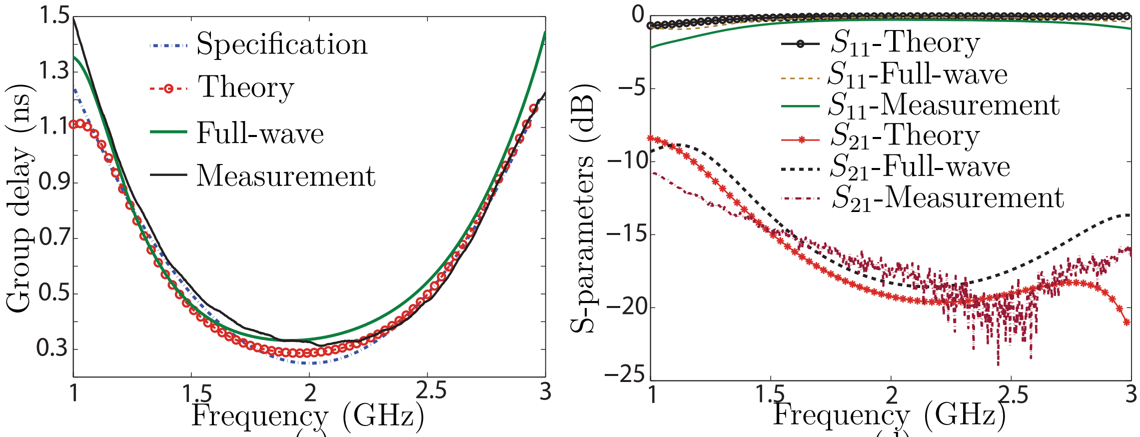

(c) (d)

Figure 3.24 Experimental, full-wave and analytical results for the 2nd order Chebyshev reflection-type phaser prototype. a) Group delay. b) S-parameters.

and reflection-type phasers. The delay seen by a wave, for a given frequency, is proportional to the amount of time the energy of the wave is stored in the system, where higher stored energies correspond to larger delays.

Table 3.4 shows ideal input impedances for different sections of transmission-type and reflection-type phasers.

Table 3.4 Ideal input impedance for different sections of the transmission-type and reflection-type phasers of Figs. 3.23(a) and 3.22.

–	Transmission	Reflection
$Z_{\mathrm{s1}}^{\mathrm{in}}(\omega)$	$0 \pm j\mathrm{high}$	$0 \pm j\mathrm{high}$
$Z_{\mathrm{s2}}^{\mathrm{in}}(\omega)$	$0 \pm j\mathrm{high}$	$0 - j\mathrm{low}$
$Z_{\mathrm{b}}^{\mathrm{in}}(\omega) = Z_{\mathrm{s2}}^{\mathrm{in}}(\omega) \Vert Z_L$	$Z_{\mathrm{L}} \pm j\mathrm{low}$	$+\mathrm{low} - j\mathrm{low}$
$Z_{\mathrm{d}}^{\mathrm{in}}(\omega)$	$Z_{\mathrm{L}} \pm j\mathrm{low}$	$0 \pm jZ_{\text{in-d}}$
$Z_{\mathrm{t}}^{\mathrm{in}}(\omega) = Z_{\mathrm{s1}}^{\mathrm{in}}(\omega) \Vert Z_{\mathrm{d}}^{\mathrm{in}}(\omega)$	$Z_{\mathrm{L}} \pm j\mathrm{low}$	$0, \infty \pm jZ_{\mathrm{in}}$

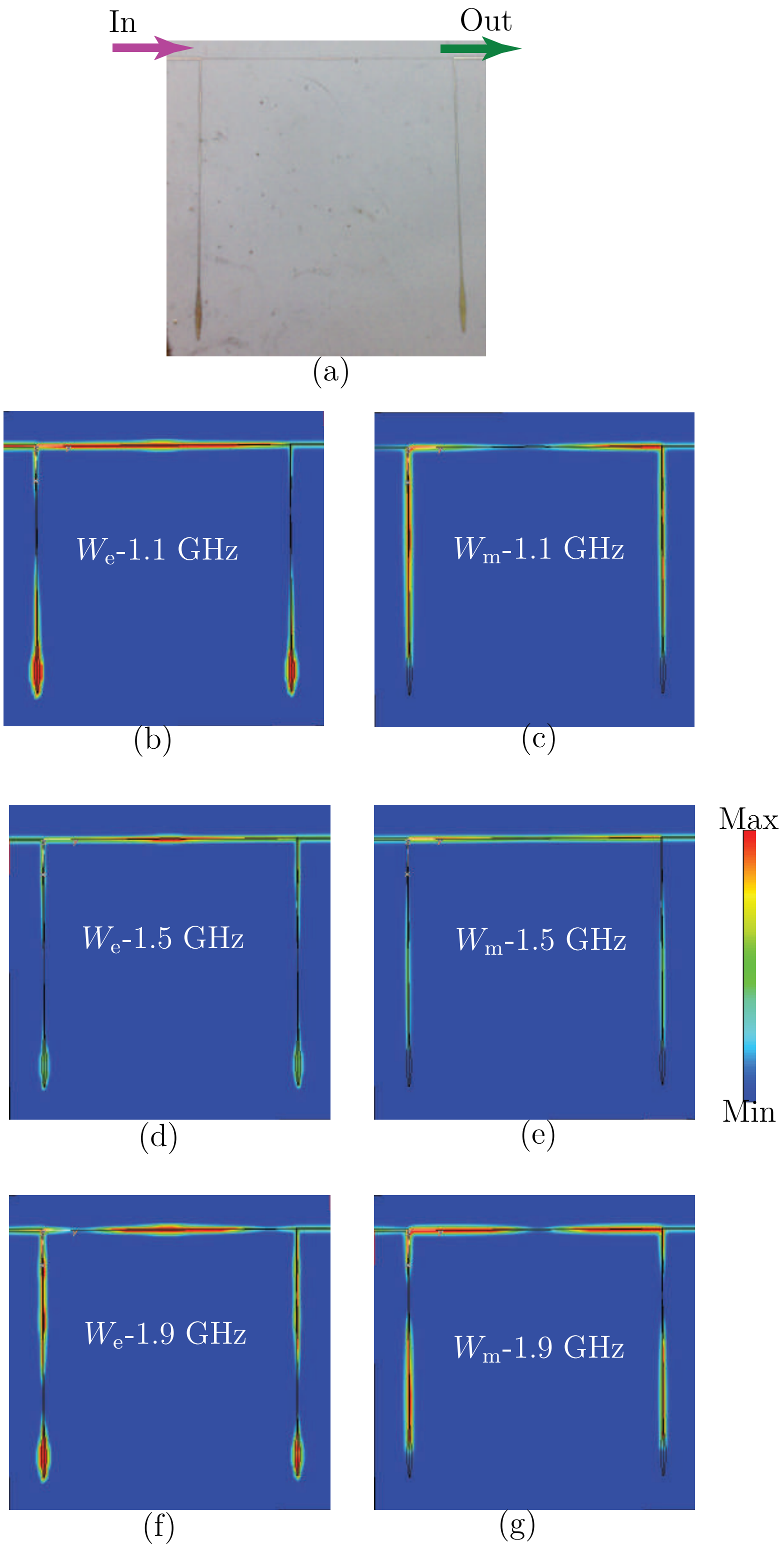

Figure 3.25 Transmission-type nonuniform phaser. (a) Photo of the fabricated phaser. (b) Electric energy density, W_e at 1.1 GHz. (c) Magnetic energy density, W_m, at 1.1 GHz. (d) Electric energy density at 1.5 GHz. (e) Magnetic energy density at 1.5 GHz. (f) Electric energy density at 1.9 GHz. (g) Magnetic energy density at 1.9 GHz.

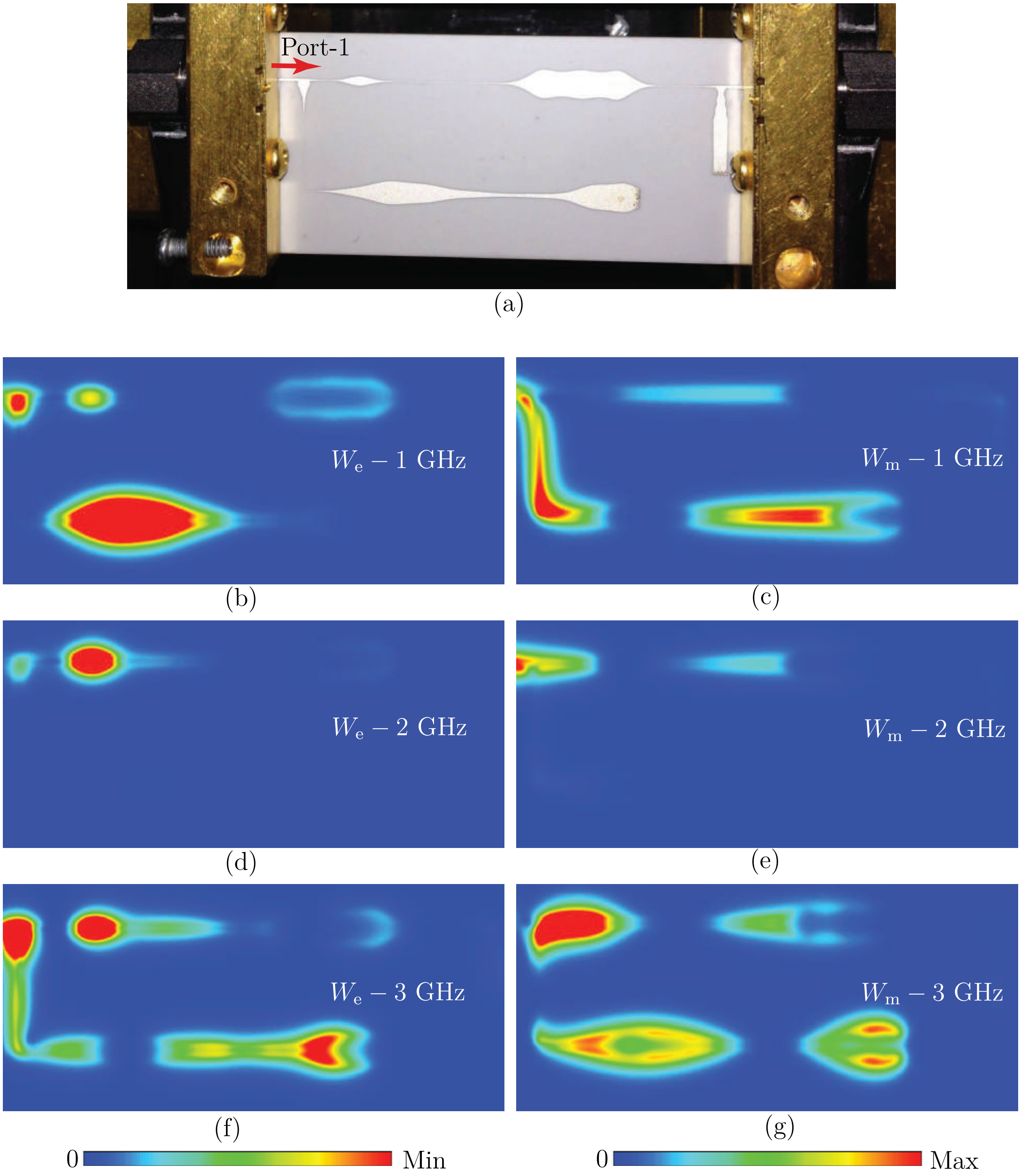

(a)

(b) (c)

(d) (e)

(f) (g)

Figure 3.26 Reflection-type nonuniform phaser. (a) Photo of the fabricated phaser. (b) Electric energy density at 1 GHz, $W_e - 1$ GHz. (c) Magnetic energy density at 1 GHz, $W_m - 1$ GHz. (d) Electric energy density at 2 GHz, $W_e - 2$ GHz. (e) Magnetic energy density at 2 GHz, $W_m - 2$ GHz. (f) Electric energy density at 3 GHz, $W_e - 3$ GHz. (g) Magnetic energy density at 3 GHz, $W_m - 3$ GHz.

CHAPTER 4 NONRECIPROCAL NONGYROTROPIC MAGNETLESS METASURFACE USING SPACE-MODULATED SPATIOTEMPORALLY DISPERSIVE MEDIUM

This chapter has been largely taken from author's published article [6].

Over the past decade, metasurfaces have spurred huge interest in the scientific community due to their unique optical properties [20, 22]. Metasurfaces may be represented as the two-dimensional counterparts of volume metamaterials [23–25, 180–183]. The vast majority of the metasurfaces reported to date are restricted to reciprocal responses. Introducing nonreciprocity requires breaking time reversal symmetry. Time reversal symmetry is the theoretical symmetry of physical laws under the transformation of time reversal. Breaking time reversal symmetry can be accomplished via the magneto-optical effect [108–113], nonlinearity [114–116], space-time modulation [19, 87, 88, 90, 117, 118] or metamaterial transistor loading [119–122]. However, all these approaches suffer from a number of drawbacks. The magneto-optical approach requires bulky, heavy and costly magnets [110]. The nonlinear approach involves dependence to signal intensity and severe nonreciprocity-loss trade-off [123]. The space-time modulation approach implies high design complexity, especially for a spatial device such as a metasurface. Finally, the transistor-based nonreciprocal metasurfaces reported in [120, 122] are intended to operate as Faraday rotators, whereas gyrotropy is undesired in applications requiring nonreciprocity without alteration of the wave polarization, such as for instance one-way screens, isolating radomes, radar absorbers or illusion cloaks.

This chapter introduces the concept of a nonreciprocal nongyrotropic magnetless metasurface as a space modulated spatiotemporally dispersion engineered medium. A simple three-layer Surface-Circuit-Surface (SCS) implementation of this structure will be demonstrated. In the proposed metasurface, time reversal symmetry is broken by the presence of unilateral transistors in the circuit part of the SCS structure, which is appropriate in the microwave and millimeter-wave regime. A space-time modulated version of the structure, although nontrivial, may also be envisioned for the optical regime. The metasurface is shown to work for all incidence angles and to provide gain.

4.0.4 Operation Principle

Figure 4.1 depicts the functionality of the nonreciprocal nongyrotropic metasurface. A wave traveling along the $+z$ direction impinges the metasurface under the angel θ_1, $\boldsymbol{\psi}_{\text{in},1}$, passes through the metasurface from side 1 to side 2, possibly with gain, without polarization alteration and radiates under the angel θ_2. By contrast, a wave traveling along the opposite direction from side 2, $\boldsymbol{\psi}_{\text{in},2}$, is being absorbed and reflected (still without polarization alteration) by the metasurface and can not pass through the metasurface from side 2 to side 1. Such a metasurface is nonreciprocal, and may hence be characterized by asymmetric scattering parameters, $S_{21} \neq S_{12}$, where $S_{21} = \boldsymbol{\psi}_{\text{out},2}/\boldsymbol{\psi}_{\text{in},1} > 1$ and $S_{12} = \boldsymbol{\psi}_{\text{out},1}/\boldsymbol{\psi}_{\text{in},2} < 1$. Moreover, the metasurface is nongyrotropic since it does not induce any rotation of the incident electromagnetic field.

To realize such a nonreciprocal and nongyrotropic metasurface, we employ the three-layer Surface-Circuit-Surface (SCS) architecture represented in Fig. 4.2. The first surface receives the incoming wave from one side of the metasurface and feeds it into the circuit while the second surface collects the wave exiting the circuit and radiates it to the other side of the metasurface.

The metasurface is constituted of an array of unit cells, themselves composed of two subwavelengthly spaced microstrip patch antennas interconnected by the circuit that will introduce transmission gain with gradient phase in one direction and transmission loss in the other direction. The phase gradient may be calculated as [21]

$$\sin(\theta_2)k_0 = \sin(\theta_1)k_0 + \frac{\partial \phi_{\text{MS}}}{\partial x}, \tag{4.1}$$

where ϕ_{MS} is the phase gradient along the metasurface, and θ_1 and θ_2 are the radiation angles of the input and output waves, respectively.

To best understand the impact of the circuit on the metasurface functionality, first consider the reciprocal unit cell of Fig. 4.3(a), where the interconnecting circuit is a direct connection (simple conducting wire). A conducting sheet is placed between the two patches to prevent any interaction between them. Figures 4.3(b) and 4.3(c) show the Finite Difference Time Domain (FDTD) response of structure in Fig. 4.3(a). Figure 4.3(b) plots the electric field distribution for wave incidence from the left and right, with the metasurface being placed at $z = 0$. The response is obviously reciprocal. The corresponding pass-bands are apparent in the scattering parameter magnitudes plotted in Fig. 4.3(c).

Consider now the nonreciprocal unit cell of Fig. 4.3(d), where the interconnecting circuit is a unilateral device, typically a transistor-based amplifier. Figures 4.3(e) and 4.3(f) show the corresponding FDTD response, where an ideal amplifier with a gain of $G = 20$ dB is used as the unilateral device. Figure 4.3(e) plots the electric field distribution for wave incidence from the left and right. When the excitation is from the left, the incoming wave passes through the structure, where it also gets amplified, and radiates to the right of the metasurface.

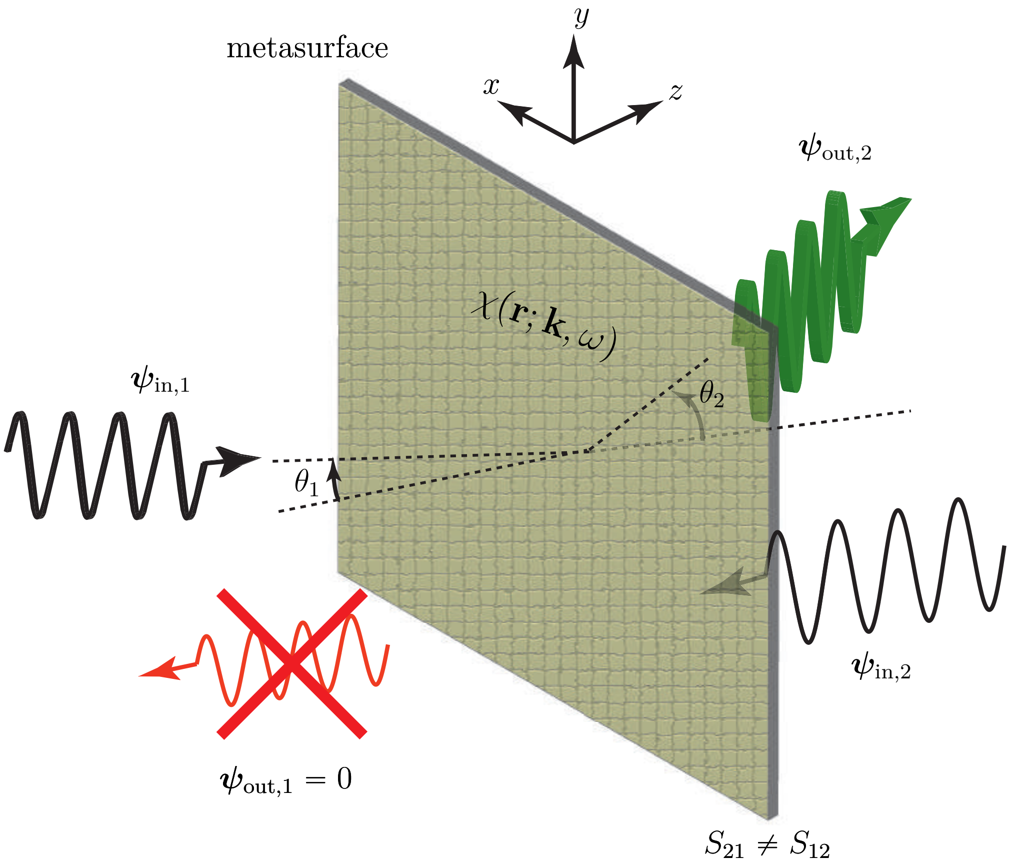

Figure 4.1 Nonreciprocal nongyrotropic metasurface functionality [6].

When the excitation is from the right, the incoming wave is blocked, namely absorbed and reflected, by the metasurface. The pass-band ($S_{11} \simeq 0$) and stop-band ($S_{11} \simeq 1$) are shown in in Fig. 4.3(f). The explanation of the multiple pass-bands suppression is provided in the next section.

4.0.5 Coupled-Structure Resonances Suppression

In this section, we provide the exact analytical solution for the scattering parameters of the normal incidence to the reciprocal and nonreciprocal unit cells in Figs. 4.3(a) and 4.3(d). While the solution for the former case gives more insight into the patch and coupled-structure resonances, plotted in Fig. 4.3(c), the solution for the latter case explains how the unilateral device suppresses the coupled-structure resonances, leading to the result of Fig. 4.3(f).

Figure 4.4 shows the general representation of the unfolded version of the SCS structures in Figs. 4.3(a) and 4.3(d), where wave propagation through the SCS structure from one side to

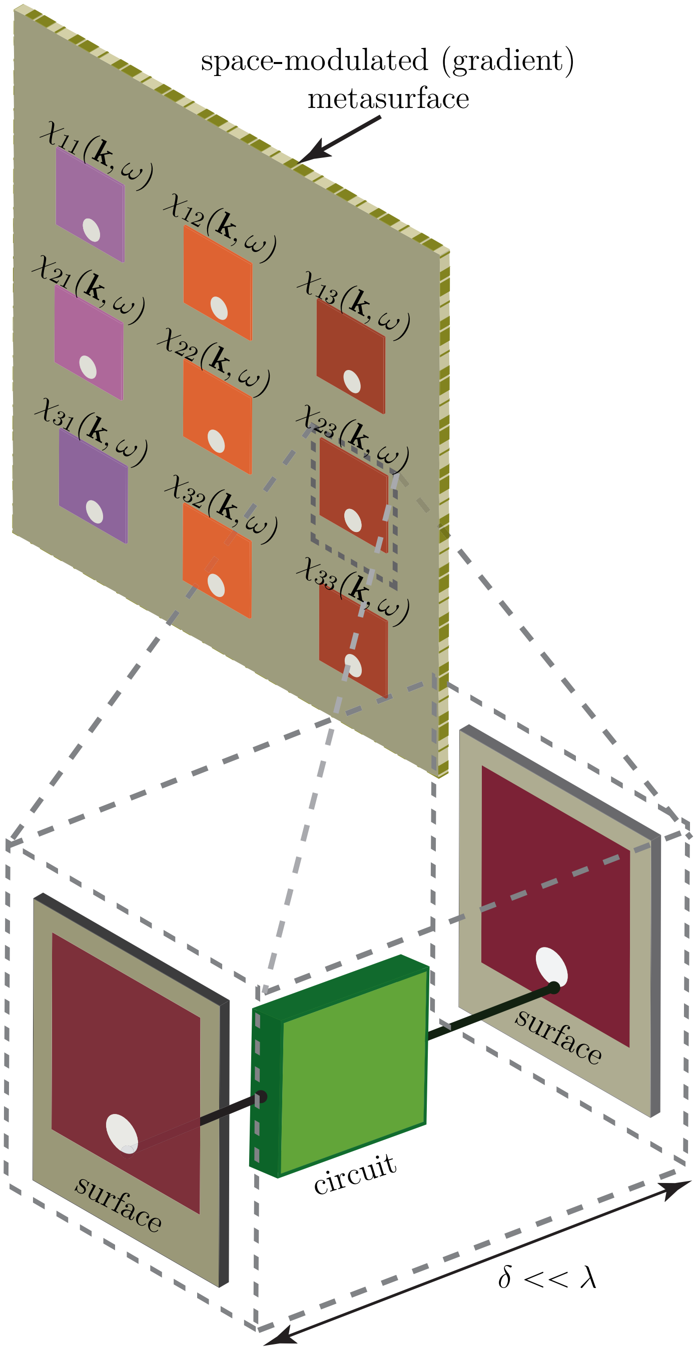

Figure 4.2 Nonuniform surface-Circuit-Surface (SCS) metasurface architecture for the magnetless implementation of the nonreciprocal nongyrotropic metasurface in Fig. 4.1 [6].

the other side of the metasurface is decomposed in five propagation regions. In this generic model, each of the five regions may represent either a reciprocal or nonreciprocal structure or device. Since microstrip transmission lines are inhomogeneous, their wavenumbers depend

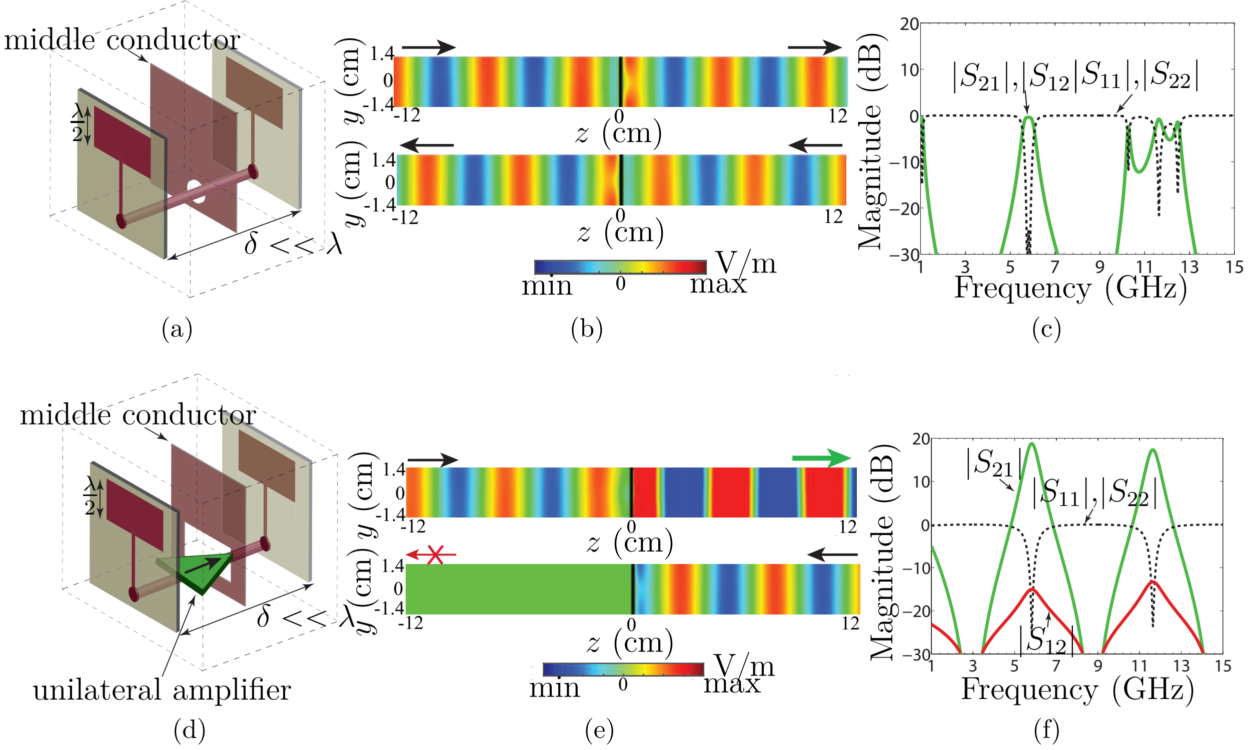

Figure 4.3 Unit cell of the metasurface in Fig. 4.2 with (a,b,c) a direct connection for the circuit, corresponding to a reciprocal metasurface, and (d,e,f) a unilateral device (typically a transistor) for the circuit, corresponding to a nonreciprocal metasurface. (a,d) Structure. (b,e) Full-wave (FDTD) electric field distribution for excitations from the left and right (bottom). (c,f) Full-wave (FDTD) scattering parameter magnitudes [6].

on the width of the structure [184], and therefore the wavenumbers in different regions are different, i.e. $\beta_1(=\beta_5) \neq \beta_2(=\beta_4) \neq \beta_3$.

The total electric field in the nth region, where $n = 1, \ldots, 5$, consists of forward and backward waves as

$$E_n = V_n^+ e^{-j\beta_n z} + V_n^- e^{j\beta_n z}, \tag{4.2}$$

where V_n^+ and V_n^- are the amplitudes of the forward traveling and backward traveling waves, respectively, and β_n is the wavenumber. It should be noted that the backward waves, propagating along $-z$ direction, are due to reflection at the different interfaces between adjacent regions. Upon application of boundary conditions at the interface between regions n and $n+1$, the total transmission and total reflection coefficients between regions n and $n+1$ are

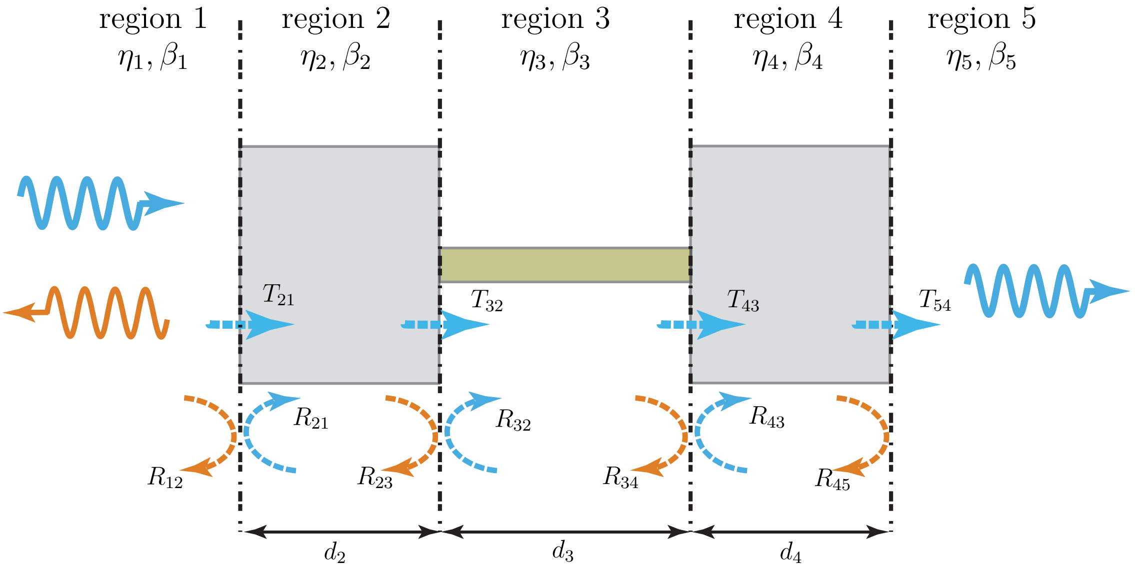

Figure 4.4 Generic representation of multiple scattering in the unfolded version of the SCS structures in Figs. 4.3(a) and 4.3(d) [6].

found as as [185]

$$\widetilde{T}_{n+1,n} = \frac{V_{n+1}^{+}}{V_{n}^{+}} = \frac{T_{n+1,n}e^{-j(\beta_n-\beta_{n+1})z}}{1 - R_{n+1,n}\widetilde{R}_{n+1,n+2}e^{-j2\beta_{n+1}d_{n+1}}}, \tag{4.3a}$$

$$\widetilde{R}_{n,n+1} = \frac{R_{n,n+1} + \widetilde{R}_{n+1,n+2}e^{-j2\beta_{n+1}d_{n+1}}}{1 + R_{n,n+1}\widetilde{R}_{n+1,n+2}e^{-j2\beta_{n+1}d_{n+1}}}. \tag{4.3b}$$

where $R_{n,n+1} = (\eta_{n+1} - \eta_n)/(\eta_{n+1} + \eta_n)$, with η_n being the intrinsic impedance of region n, is the local reflection coefficient within region n between regions n and $n+1$, and $R_{n+1,n} = -R_{n,n+1}$. The local transmission coefficient from region n to region $n+1$ is then found as $T_{n+1,n} = 1 + R_{n,n+1}$.

The factor $e^{-j(\beta_n-\beta_{n+1})z}$ in (4.3a) shows that, due to the nonuniformity of structure in Fig. 4.4, a phase shift corresponding to the difference between the wavenumbers in adjacent regions occurs at each interface. The total transmission from region 1 to region N is the product of the transmissions from all interfaces and phase shift inside each region

$$s_{\mathrm{N},1} = \prod_{n=1}^{N-1} \widetilde{T}_{n+1,n}e^{-j\beta_n d_n}. \tag{4.4}$$

Figure 4.5(a) shows the unfolded version of the SCS architecture in Fig. 4.3(a) where, comparing with the general representation of the problem in Fig. 4.4, we denote $\beta_1 = \beta_5 = \beta_0$, $\beta_2 = \beta_4 = \beta_\mathrm{p}$ and $\beta_3 = \beta_\mathrm{t}$ the wavenumbers in the air, in the two patches, and in the interconnecting transmission line, respectively. We subsequently denote $R_{1,2} = -R_{2,1} = -R_{4,5} = R_\mathrm{p} = (\eta_\mathrm{p} - \eta_0)/(\eta_\mathrm{p} + \eta_0)$ the reflection coefficient at the interface between a patch and the air, and $R_{2,3} = -R_{3,2} = -R_{3,4} = R_{4,3} = R_\mathrm{t} = (\eta_\mathrm{t} - \eta_\mathrm{p})/(\eta_\mathrm{t} + \eta_\mathrm{p})$ the local reflection coefficient at the interface between a patch and the interconnecting transmission line.

The total transmission coefficient for the reciprocal SCS metasurface of Fig. 4.5(a), from region 1 to region 5, reads then

$$S_{21,\mathrm{Rec}} = s_{5,1} = \prod_{n=1}^{4} \widetilde{T}_{n+1,n} e^{-j\beta_n d_n}, \tag{4.5}$$

where $\widetilde{T}_{n+1,n}$, for $n = 1, \ldots, 4$ is provided by (4.3a) with (4.3b). In particular,

$$\begin{aligned} \widetilde{R}_{2,3,\mathrm{Rec}} &= \frac{R_\mathrm{t} + \widetilde{R}_{3,4} e^{-j2\beta_\mathrm{t} d_\mathrm{t}}}{1 + R_\mathrm{t} \widetilde{R}_{3,4} e^{-j2\beta_\mathrm{t} d_\mathrm{t}}} \\ &= \frac{R_\mathrm{t} + R_\mathrm{t}^2 R_\mathrm{p} e^{-j2\beta_p d_p} - (R_\mathrm{t} + R_\mathrm{p} e^{-j2\beta_p d_p}) e^{-j2\beta_t d_t}}{1 + R_\mathrm{t} R_\mathrm{p} e^{-j2\beta_p d_p} - R_\mathrm{t}(R_\mathrm{t} + R_\mathrm{p} e^{-j2\beta_p d_p}) e^{-j2\beta_t d_t}} \end{aligned} \tag{4.6}$$

will be used later.

After some algebraic manipulations in (4.5), the total transmission coefficient from the reciprocal SCS structure in Fig. 4.5(a) is found in terms of local reflection coefficients as

$$S_{21,\mathrm{Rec}} = \frac{(1 - R_\mathrm{p}^2)(1 - R_\mathrm{t}^2) e^{j(\beta_\mathrm{p} + \beta_0 - 2\beta_\mathrm{t}) d_\mathrm{t}}}{(R_\mathrm{p} R_\mathrm{t} + e^{j2\beta_\mathrm{p} d_\mathrm{p}})^2 - (R_\mathrm{t} e^{j2\beta_\mathrm{p} d_\mathrm{p}} + R_\mathrm{p})^2 e^{-j2\beta_\mathrm{t} d_\mathrm{t}}}. \tag{4.7}$$

The term $e^{-j2\beta_\mathrm{t} d_\mathrm{t}}$ in the denominator of this expression corresponds to the round-trip propagation through the middle transmission line, whose multiplication by $e^{j4\beta_\mathrm{p} d_\mathrm{p}}$ in the adjacent bracket corresponds to the patch-line-patch coupled-structure resonance, with length $2d_\mathrm{p} + d_\mathrm{t}$.

Figure 4.5(b) shows the unfolded version of the nonreciprocal SCS structure in Fig. 4.3(d), where a unilateral device is placed at the middle of the interconnecting transmission line. Note that in this case the structure is decomposed in 7 (as opposed to 5) regions, with extra parameters straightforwardly following from the reciprocal case.

Assuming that the input and output ports of the unilateral device are matched, i.e. $R_{34} = R_{54} = 0$, then one has $\widetilde{R}_{34} = 0$ and the backward wave is completely absorbed by the device,

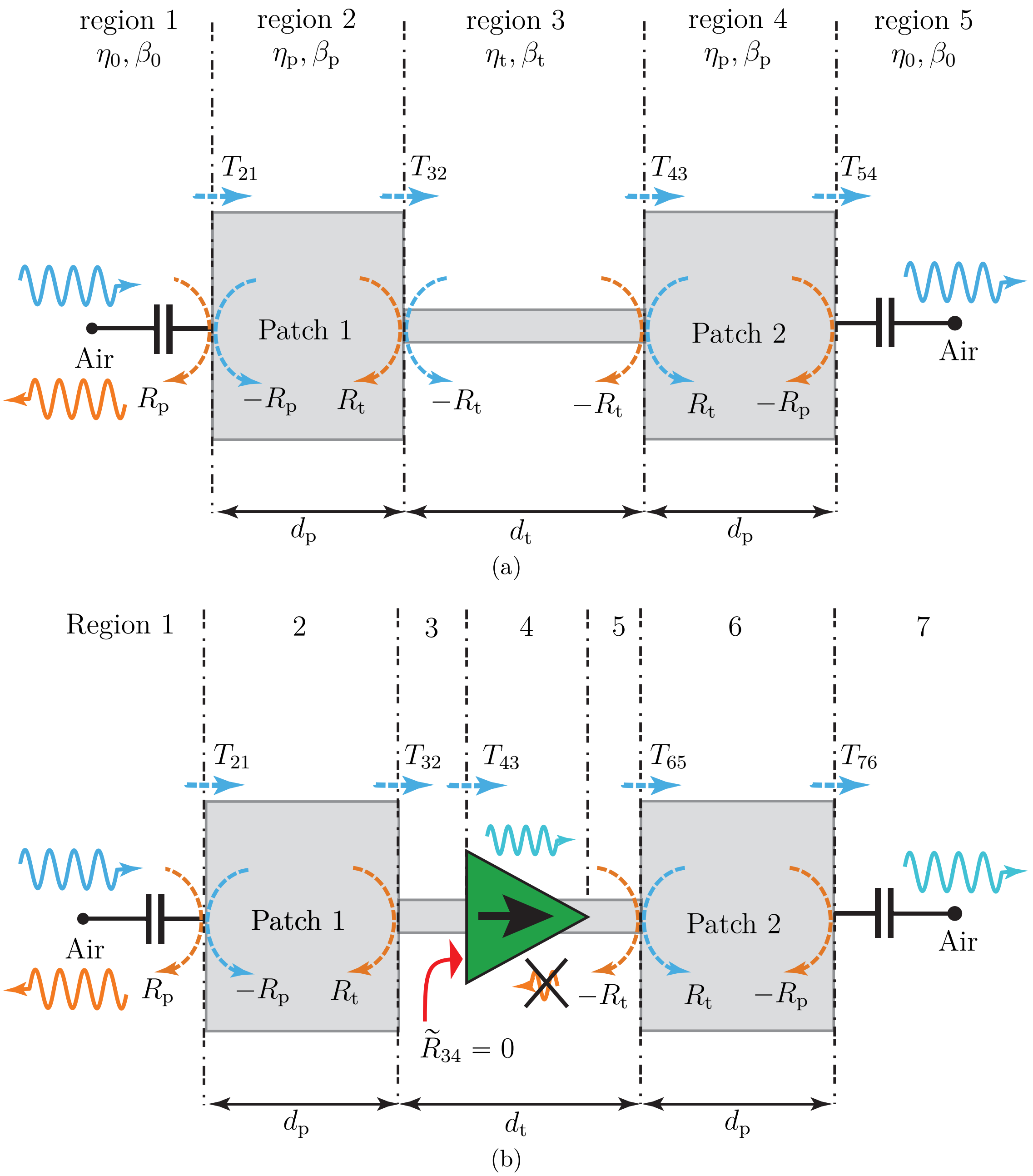

Figure 4.5 Wave interference explanation of the responses in Fig. 4.3. (a) Reciprocal case, Figs. 4.3(a), 4.3(b), 4.3(c). (b) Nonreciprocal case, Figs. 4.3(d), 4.3(e), 4.3(f) [6].

i.e. $T_{34} = \widetilde{T}_{34} = 0$ while the forward wave is amplified by the device as $T_{43} = \widetilde{T}_{43} = G$. Then, the total reflection coefficients at the interface between regions 2 and 3, given by (4.6) in the reciprocal case, reduces to

$$\widetilde{R}_{2,3,\mathrm{NR}} = R_{\mathrm{t}}. \tag{4.8}$$

This relation, compared with the one for the reciprocal case, reveals the suppression of the multiple reflections in the interconnecting transmission line. The total transmission coefficient from the nonreciprocal SCS structure may be found as

$$S_{21,\mathrm{NRec}} = \frac{G(1-R_\mathrm{p}^2)(1-R_\mathrm{t}^2)e^{-j(\beta_\mathrm{t}d_\mathrm{t}-2\beta_0 d_\mathrm{p})}}{(R_\mathrm{p}R_\mathrm{t}+e^{j2\beta_\mathrm{p}d_\mathrm{p}})^2}. \tag{4.9}$$

Comparing the denominator of (4.9) with that of the reciprocal case in (4.7), shows that the coupled-structure resonances, corresponding to the second term of the denominator, have disappeared due to the suppression of the multiple reflections in the middle transmission line, restricting the spectrum to the harmonic resonances of the two patches, amplified by G.

Figure 4.6(a) shows the magnitude of the scattering parameters for a single isolated patch, where transmission ($|S_{21}| = 1$) occurs at the harmonic resonance frequencies of the patch, nf_0 (n integer), where $d_\mathrm{p} = n\lambda_\mathrm{p}/2 = n\lambda_0/(2\sqrt{\epsilon_\mathrm{eff}})$ with ϵ_eff being the effective permittivity [184]. Figure 4.6(b) plots the magnitude of the scattering parameters of the coupled structure formed by the two patches interconnected by a short transmission line of $d_\mathrm{t} = 0.3\lambda_0$, given by (4.7). We see that, in addition to the single patch resonances at $f = nv_\mathrm{p}/(2d_\mathrm{p})$, extra resonances appear in the spectrum, corresponding to the aforementioned coupled-structure resonances. Increasing the length of the interconnecting transmission line to $d_\mathrm{t} = 3\lambda_0$ yields the results presented in Fig. 4.6(c). As expected, more coupled-structure resonances appear in the response due to the longer electrical length of the overall structure, while the patch resonances remain fixed. Finally, we place the unilateral device in the middle of the interconnecting transmission line, still with $d_\mathrm{t} = 3\lambda_0$. Figure 4.6(d) shows the corresponding scattering parameters, where all the coupled resonances in Fig. 4.6(c) have been completely suppressed due to the absorbtion of multiple reflections from the patches by the unilateral device. It should be noted that the forward amplification, $|S_{21}| > 1$, and backward isolation, $|S_{12}| \ll 1$, are due to the nonreciprocal amplification of the unilateral device.

4.0.6 Experimental Demonstration

Figure 4.7 shows the realized 3×3 metasurface, based on the SCS architecture of Fig. 4.3(d). The metasurface is designed to operate in the frequency range from 5.8 to 6 GHz with $\theta_1 = \theta_2 = 0$. Its *thickness* is deeply subwavelength, specifically $\delta \approx \lambda_0/30$, where λ_0 is the wavelength at the center frequency, 5.9 GHz, of the operating frequency range. The metasurface was realized using multilayer circuit technology, where two 6.2 in × 6.2 in RO4350 substrates with thickness $h = 30$ mil were assembled to realize a three metallization layer structure. The permittivity of the substrates are $\epsilon = \epsilon_\mathrm{r}(1 - j\tan\delta)$, with $\epsilon_\mathrm{r} = 3.66$ and

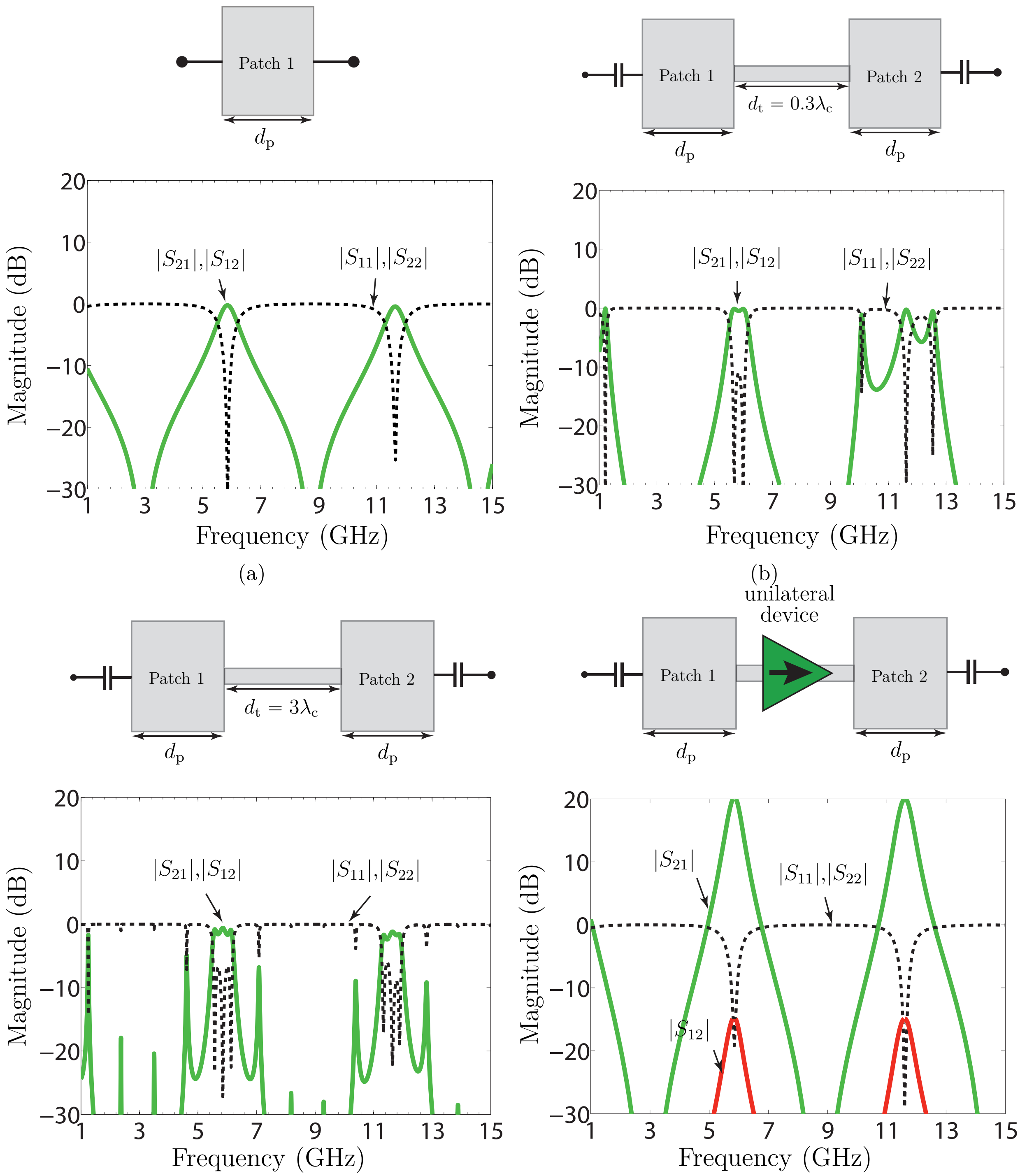

(a)

(b)

(c)

(d)

Figure 4.6 Scattering parameter frequency responses of the structures in Fig. 4.5. (a) Isolated patch. (b) Structure (reciprocal) in Fig. 4.5(a) with $d_t = 0.3\lambda_c$. (c) Same structure (reciprocal) as in (b) except for $d_t = 3\lambda_c$ (d) Structure in Fig. 4.5(b) (nonreciprocal) still with $d_t = 3\lambda_c$ [6].

$\tan\delta = 0.0037$ at 10 GHz. The middle conductor of the structure (Fig. 4.7) both supports the DC feeding network of the amplifiers and acts as the RF ground plane for the patch antennas. The dimensions of the 2×9 microstrip patches are 1.08 in × 0.49 in.

The connections between the layers are provided by an array of circular metalized via holes, with 18 vias of 30 mil diameter connecting the DC bias network to the amplifiers, while the ground reference for the amplifiers is ensured by 18 sets of 6 vias of 20 mils diameter with 60 mils spacing. The connection between the two sides of the metasurface is provided by 9 via holes (Fig. 4.7), with optimized dimensions of 60 mils for the via diameters, 105 mils for the pad diameters and 183 mils for the hole diameter in the via middle conductor.

For the unilateral components, we used 18 Mini-Circuits Gali-2+ Darlington pair amplifiers. To achieve a total gain of 20 dB, each unit-cell contains two cascaded Gali-2 amplifiers, each of which provides about 10 dB gain across the operation bandwidth.

The amplifier circuit is shown in Fig. 4.8, where C_{in} =1 pF and C_{out} =1 pF are DC-block capacitors, and $C_{\text{b1}} = 4.7$ pF, $C_{\text{b2}} = 1$ nF and $C_{\text{b3}} = 1$ are a set of AC by-pass capacitors. A 4.5-V DC-supply provides the DC signal for all the amplifiers (for uniform case with $\theta_1 = \theta_2 = 0$) through the DC network with a bias resistor of $R_{\text{bias}} = 39$ Ohm corresponding to a DC current of 40 mA for each amplifier. It should be noted that, to make a space-modulated (gradient) metasurface with $\theta_1, \theta_2 \neq 0$, different DC bias voltages, or different bias resistors, may be considered for the amplifiers.

The measurements were performed by a 37369D Anritsu network analyzer where two microstrip array antennas were placed at two sides of the metasurface to transmit and receive the electromagnetic wave.

Figure 4.9 compares the measurement results with the simulation results of Fig. 4.6(d) for transmission scattering parameters versus frequency for normally aligned transmit and receive antennas. In the $1 \rightarrow 2$ direction, more than 17 dB transmission gain is achieved in the frequency range of interest, while in the $2 \rightarrow 1$ direction, more than 10 dB transmission loss is ensured across the same range, corresponding to an isolation of more than 27 dB.

Two other experiments are next carried out to investigate the operational angular sector of the metasurface. In the first experiment, we fix the position of one antenna normal to the metasurface and rotate the other antenna from 0 to 180° with respect to the metasurface, as illustrated at the top of Fig. 4.10(a). The bottom of Fig. 4.10(a) shows the measured transmission levels for both directions, $|S_{21}|$ and $|S_{12}|$. We observe that the metasurface passes the wave with gain over a beamwidth of about 110° from $\theta = 35^\circ$ to 145° in the $1 \rightarrow 2$ direction and attenuates it by more than 12 dB in the $2 \rightarrow 1$ direction, which corresponds to

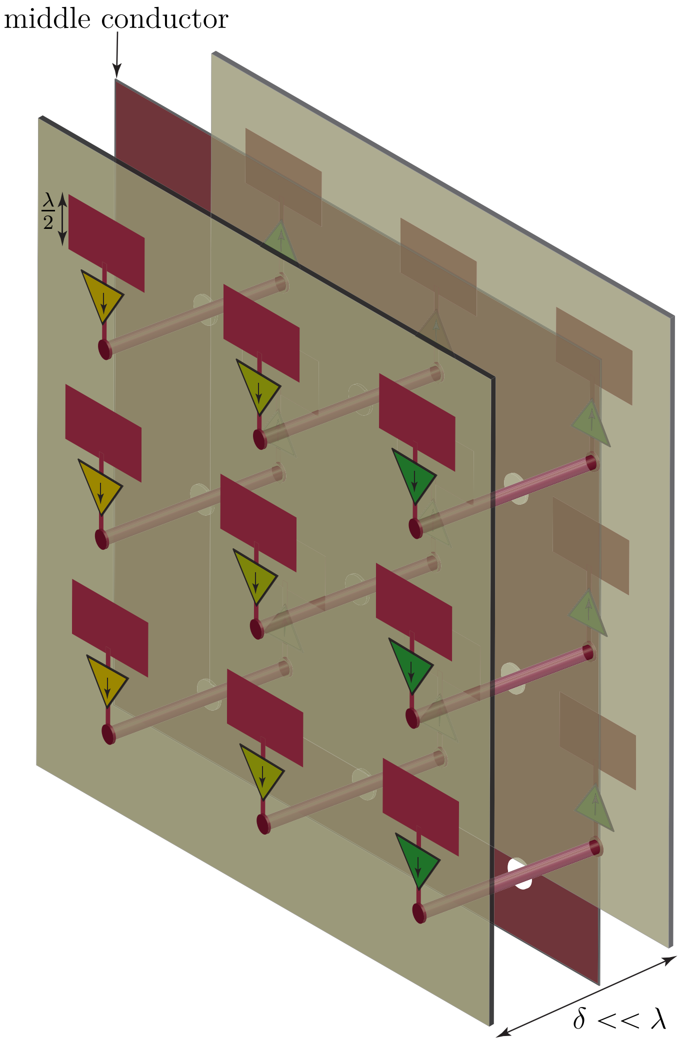

Figure 4.7 Exploded perspective view of the realized 3 × 3-cell implementation of the metasurface, where, compared to Fig. 4.3(d), the transistors have been shifted to the surfaces for fabrication convenience [6].

a minimum isolation of about 15 dB across the aforementioned beamwidth.

In the next angular dependence experiment, we rotate two antennas rigidly aligned from 0 to 180° with respect to the metasurface, as illustrated at the top of Fig. 4.10(b). The bottom of Fig. 4.10(b) shows the measured transmission levels for both directions. We observe that the metasurface passes the wave with gain over a beamwidth of about 130° from $\theta = 25^\circ$ to 155° in the $1 \rightarrow 2$ direction and attenuates it by more than 12 dB in the $2 \rightarrow 1$ direction, which corresponds to a minimum isolation of about 21 dB across the aforementioned beamwidth.

Comparing Figs. 4.10(a) and 4.10(b) reveals that the transmission gain is less sensitive to

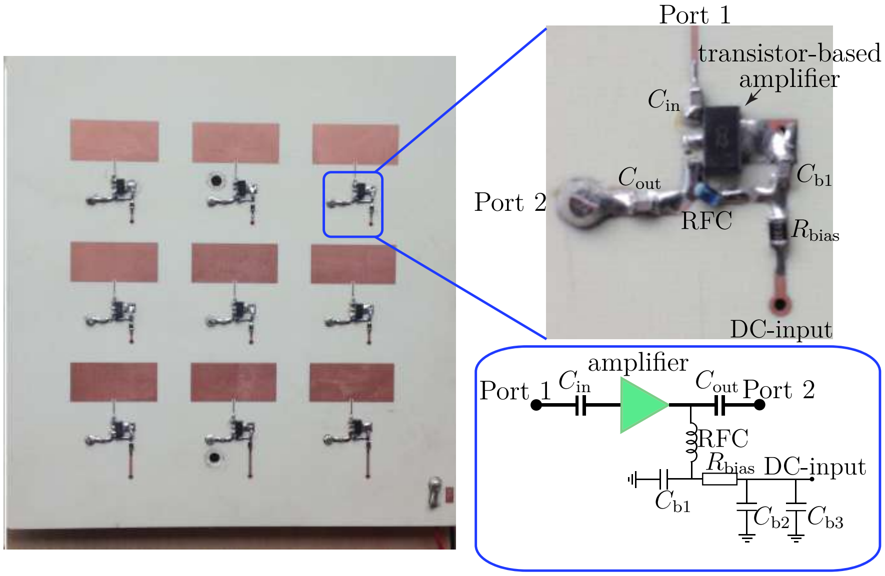

Figure 4.8 Photograph of the realized 3 × 3-cell implementation of the metasurface with zoom on transistor part and corresponding biasing network [6].

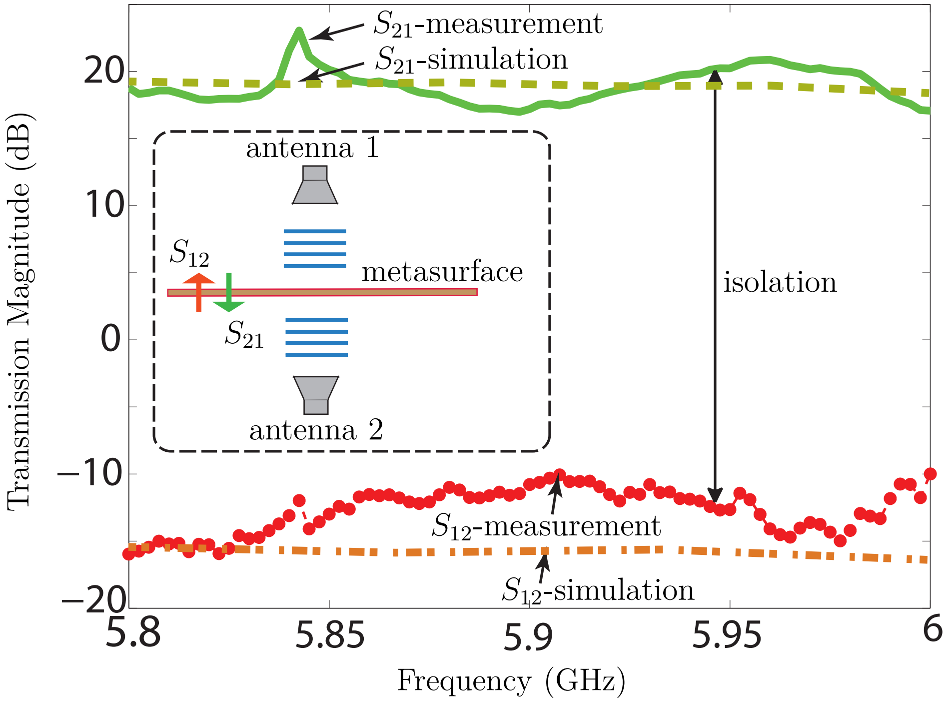

Figure 4.9 Experimental results compared with simulation results in Fig. 4.6(d) for scattering parameters versus frequency for normal incidence and transmission [6].

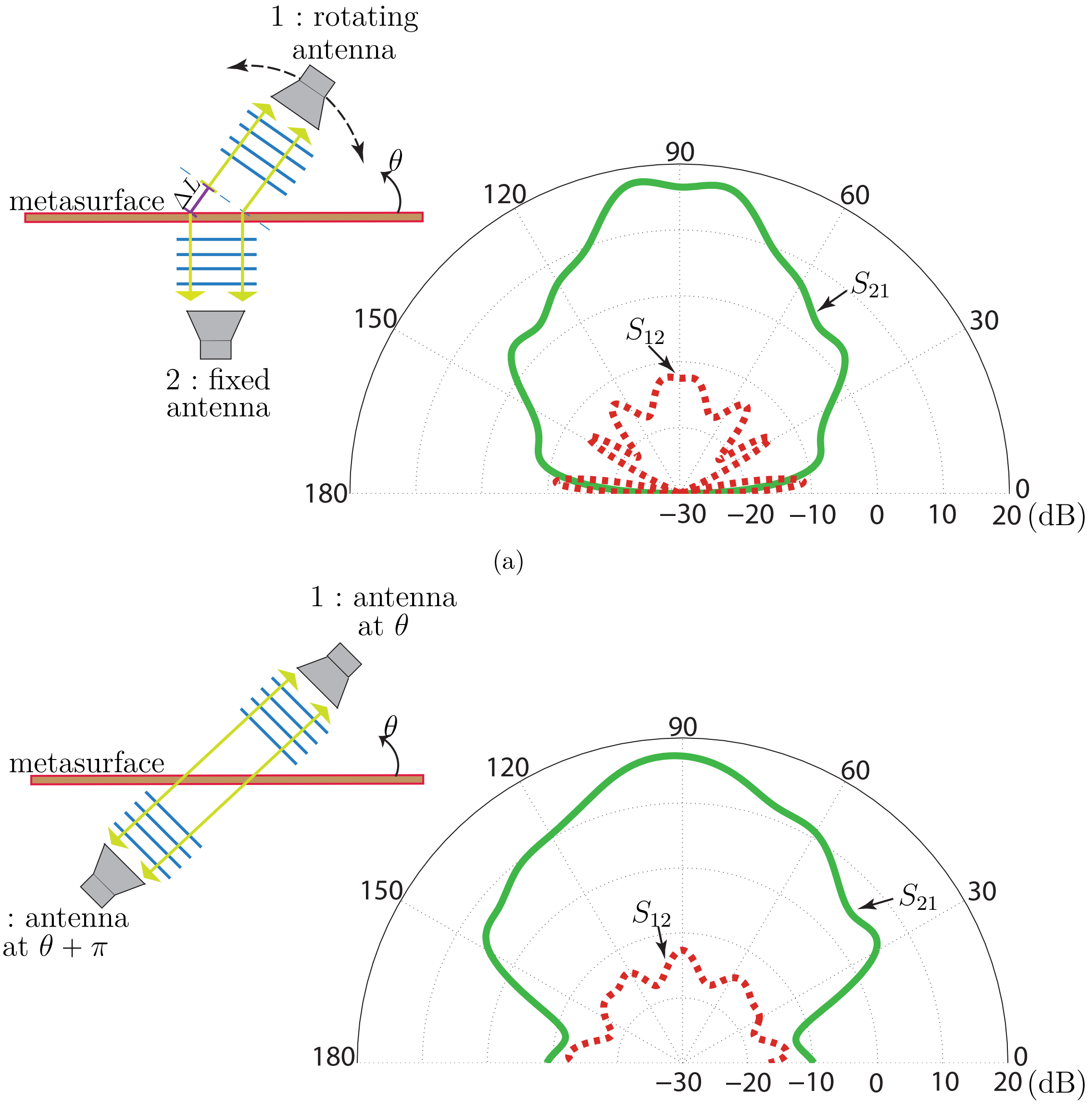

(a)

(b)

Figure 4.10 Experimental scattering parameters versus angle at $f = 5.9$ GHz for transmission (a) under normal (one side) and oblique (other side) angles, (b) in a straight line under an oblique angle [6].

angle in the latter case. This is due to the fact that the optical path difference between any pair of rays across the SCS structure is null when the antennas are aligned, as in Fig. 4.10(b), whereas it is angle-dependent otherwise, as in Fig. 4.10(a) (path difference ΔL).

The experimental results presented above show that the proposed nonreciprocal nongyrotropic metasurface works as expected, with remarkable efficiency. Moreover, it exhibits the following additional favorable features. Firstly, it provides gain, which makes it particularly efficient as a repeater device. Secondly, in contrast to other nonreciprocal metasurfaces, the structure is not limited to the monochromatic regime since patch antennas are fairly broadband and their bandwidth can be enhanced by various standard techniques [184]. Note that the structure presented here has not been optimized in this sense but already features a bandwidth of over 3%. Thirdly, the metasurface exhibits a very wide operating angular sector, due to both aforementioned small or null optical path difference between different rays, due to the SCS architecture, and the inherent low directivity of patch antenna elements. The reported operating sectors, of over 100°, are much larger than those of typical metasurfaces.

CHAPTER 5 NONRECIPROCAL ELECTROMAGNETIC SCATTERING FROM A PERIODIC SPACE-TIME MODULATED SLAB

This chapter has been largely taken from author's published article [7].

In 1950s-1960s, the space-time modulated medium whose constructive parameters are spatiotemporally modulated, has been studied as traveling-wave parametric amplifier. In that era, it has been shown that an infinite space-time modulated medium transforms the spectrum [71, 72, 74–79, 186], where the problem of interest was the forward propagation in an infinite medium where the permittivity or permeability is sinusoidally varying in space and time. However, several interesting features of such a medium have not been studied, including the backward propagation and nonreciprocity of such an infinite medium, the wave propagation in a general space-time modulated medium, and the electromagnetic scattering form a space-time modulated slab. Such media are endowed with peculiar properties. In contrast to moving media, where the velocity of the medium is restricted to the speed of light, space-time modulation can take both subluminal and superluminal velocities. In contrast to static periodic media such as photonic crystals, periodic space-time media exhibit asymmetric, tilted dispersion [74, 75]. Moreover, superluminal space-time media produce electromagnetic bandgaps that are oriented vertically, compared to horizontal bandgaps in conventional photonic crystals and Bragg structures. These vertical bandgaps describe instabilities or unbounded growth [75]. Harmonic generation is another feature of space-time media. In contrast to nonlinear harmonics, space-time harmonics are not governed by the classical Manley-Rowe relations [75]. This result stems from violation of energy conservation in space-time modulated media, as energy is pumped into the system through the modulation.

This technique has regained attention in the past years due to recently discovered exotic effects such as interband photonic transitions mediated by space-time varying media [84] and associated nonreciprocity [19, 29], inverse Doppler effect in a shockwave induced photonic bandgap structure [85, 86], electromagnetic isolation in oblique space-time bandgaps [8], nonreciprocal space-time metasurfaces [87–89], and nonreciprocal antenna systems [9, 90–93]. Nonreciprocity based on space-time modulation seems to offer a viable path towards integrated nonreciprocal photonic and electromagnetic devices. This technique addresses issues of conventional nonreciprocity techniques, such as incompatibility with integrated circuit technology in magnet-based nonreciprocity, signal power restrictions in nonlinear-based nonreciprocity [123], and low power handling and frequency limitation in transistor-based nonreciprocity [187].

Various electromagnetic modelings of spatitemporally modulated medium have been reported in the past including Bloch-Floquet [74, 186], coupled-mode approximate [19, 72, 80] and perturbation approximate [188] solutions. The Bloch-Floquet form provides the complete spectrum and more insight into the medium, where the two later cases, coupled-mode and perturbation solutions, provide a closed form approximate spectrum. However, the Bloch-Floquet form does not converge for a specific range of parameters, where the phase velocities of the background and modulation are close, which is called *sonic region* [186]. Up to now, all reported space-time modulated systems are limited to one-dimensional, infinite and sinusoidally modulated media. In this chapter, we consider a general two-dimensional space-time modulated slab and present the electromagnetic scattering from and into the finite medium. The rigorous analytical wave solution for for the field inside and outside of the slab are achieved based on the electromagnetic fields mode matching at the interfaces of the slab. We will then discuss about the dispersion and the isofrequency diagrams of the medium, for different set of parameters corresponding to different operation regimes, to best understand the wave propagation inside such a medium. Next, we will discuss about the quasi-sonic region for a general modulation and present the analytical and numerical results for a finite slab. Interesting features of the oblique shinned space-time modulated slab may pave the road for further research works in this area. In contrast to the infinite space-time modulated medium, where operating toward the sonic region leads to instability due to the infinite gain, the corresponding spatiotemporally modulated slab presents a progressive finite gain, given by the finiteness of the medium, which provides an extra degrees of freedom to have strong transitions.

Previous research on space-time media has been mostly focused on propagation in infinite space-time media or normal incidence on a semi-infinite space-time modulated region. *Oblique* electromagnetic incidence on a space-time modulated *slab* has unique features that have been unexplored. This chapter shows that such a structure operates as a nonreciprocal harmonic generator and filter. It is demonstrated that a space-time slab operates as a high-pass spatial frequency filter. For oblique incidence, low frequency harmonics are filtered out in the form of surface waves, while high frequency harmonics are transmitted as space waves. In the quasi-sonic regime, where the velocity of the space-time modulation is close to the velocity of the electromagnetic waves in the background medium, the incident wave is strongly coupled to space-time harmonics in the forward direction while in the backward direction it exhibits low coupling to other harmonics. This nonreciprocity is leveraged for the realization of an electromagnetic isolator in the quasi-sonic regime and is experimentally demonstrated at microwave frequencies.

The chapter is organized as follows. Section 5.1 presents an analytical solution for electromagnetic scattering from a space-time slab. Section 5.2 derives analytical expressions describing electromagnetic scattering from a sinusoidally modulated space-time slab. Dispersion diagrams and isofrequency curves are described in Sec. 5.3. Space-time transitions and their nonreciprocal nature are highlighted in details in Sec. 5.3.

5.1 General Analytical Solution

The problem of interest is represented in Fig. 5.1. A plane wave, $\mathbf{E}_\mathrm{I}$, impinges in the forward ($+z$) direction or backward ($-z$) direction under the angle θ_i on a periodically space-time modulated slab of thickness L sandwiched between two semi-infinite unmodulated media. Hereafter, the problem with the incident wave propagating towards the $+z$-direction, depicted at the top of Fig. 5.1, will be called the *forward problem*, denoted by the superscript "F", while the problem with the incident wave propagating towards the $-z$-direction, depicted at the bottom of Fig. 5.1, will be called the *backward problem*, denoted by the superscript "B". Note that, as illustrated in Fig. 5.1, the forward and backward problems both include forward and backward waves. The slab assumes the unidirectional forward relative permittivity

$$\epsilon(z,t) = f_\mathrm{per}(\beta_\mathrm{m} z - \omega_\mathrm{m} t), \tag{5.1}$$

where $f_\mathrm{per}(.)$ is an arbitrary periodic function of the space-time phase variable $\xi = \beta_\mathrm{m} z - \omega_\mathrm{m} t$, with β_m being the spatial modulation frequency and ω_m the temporal modulation frequency. Taking the time derivative of a constant phase point in (5.1) yields $d\xi/dt = 0 = \beta_\mathrm{m} dz/dt - \omega_\mathrm{m}$,

$$v_\mathrm{m} = \frac{\omega_\mathrm{m}}{\beta_\mathrm{m}}. \tag{5.2}$$

This velocity may be smaller or greater than the phase velocity of the background medium, which we define here as the velocity

$$v_\mathrm{b} = \frac{c}{\sqrt{\epsilon_\mathrm{r}}}, \tag{5.3}$$

where $c = 1/\sqrt{\mu_0 \epsilon_0}$ is the speed of light in vacuum, and where ϵ_r is the relative permittivity common to media 1 and 3 and to the average permittivity of medium 2. The ratio between the modulation and background phase velocities,

$$\gamma = \frac{v_\mathrm{m}}{v_\mathrm{b}}, \tag{5.4}$$

is called the *space-time velocity ratio*. The limit $\gamma = 0$ corresponds to a purely space-modulated medium, while the limit $\gamma = \infty$ corresponds to a purely time-modulated medium [80]. Moreover, $\gamma = 1$ corresponds to the space-time-modulated medium where the modulation propagates exactly at the same velocity as a wave in the background medium. We wish to calculate the fields scattered by the slab, namely the reflected fields, $\mathbf{E}_{\mathrm{R}}^{\mathrm{F,B}}$, the fields in the modulated medium, $\mathbf{E}_{\mathrm{M}}^{\mathrm{F,B};\pm}$, and the transmitted fields, $\mathbf{E}_{\mathrm{T}}^{\mathrm{F,B}}$, in Fig. 5.1.

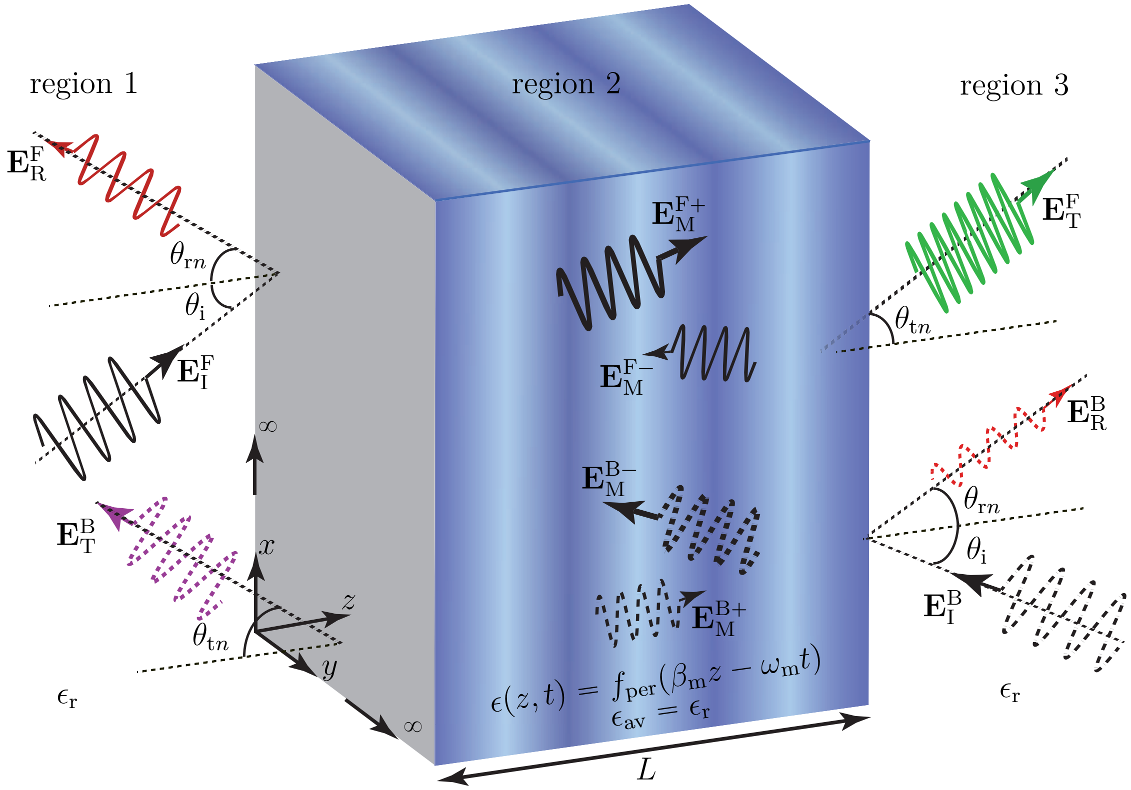

Figure 5.1 Electromagnetic scattering from a periodically space-time modulated slab (region 2) sandwiched between two semi-infinite unmodulated media (regions 1 and 3). Due to the unidirectionality of the modulation, $\epsilon(z,t) = f_{\mathrm{per}}(\beta_{\mathrm{m}}z - \omega_{\mathrm{m}}t)$, the system is nonreciprocal, with different temporal and spatial frequencies scattered in the two directions [7].

Since the slab medium permittivity is periodic in space, with spatial frequency β_{m}, and in time, with temporal frequency ω_{m}, it may be expanded in the space-time Fourier series

$$\epsilon(z,t) = \sum_{k=-\infty}^{\infty} \tilde{\epsilon}_k e^{-jk(\beta_{\mathrm{m}}z - \omega_{\mathrm{m}}t)}, \tag{5.5}$$

where $\tilde{\epsilon}_k$ is the coefficient of the k^{th} term and $\tilde{\epsilon}_0 = \epsilon_{\mathrm{r}}$. Moreover, assuming TM$_y$ or E_y polarization, the electromagnetic fields inside the slab may be represented in the double space-time Bloch-Floquet form

$$\mathbf{E}_{\mathrm{M}}(x,z,t)=\mathbf{E}_{\mathrm{M}}^{+}(x,z,t)+\mathbf{E}_{\mathrm{M}}^{-}(x,z,t)=\sum_{n=-\infty}^{\infty}\left(\mathbf{E}_{n}^{+}+\mathbf{E}_{n}^{-}\right), \tag{5.6a}$$

where the superscripts F and B have been omitted for notational simplicity and where the ± superscripts represent $\pm z$-propagating wave components. In (5.6),

$$\mathbf{E}_{n}^{+}=\hat{\mathbf{y}}A_{n}^{+}e^{-j(k_x x+\beta_0^{+}z-\omega_0 t)}e^{-jn(\beta_{\mathrm{m}}z-\omega_{\mathrm{m}}t)}, \tag{5.6b}$$

$$\mathbf{E}_{n}^{-}=\hat{\mathbf{y}}A_{n}^{-}e^{-j(k_x x-\beta_0^{-}z-\omega_0 t)}e^{-jn(\beta_{\mathrm{m}}z-\omega_{\mathrm{m}}t)}. \tag{5.6c}$$

where β_0 and ω_0 are the spatial and temporal frequencies of the fundamental temporal and spatial harmonics, respectively, in the slab, and $k_x = k_0\sin(\theta_{\mathrm{i}}) = (\omega_0/v_{\mathrm{b}})\sin(\theta_{\mathrm{i}})$ is the x-component of the spatial frequency, $\mathbf{k}$.

It is shown in Sec. 1 of [189] that the Bloch-Floquet solution in (5.6) is valid everywhere except in the interval

$$\gamma_{\mathrm{s,min}}=\sqrt{\frac{\epsilon_{\mathrm{r}}}{\tilde{\epsilon}_0+\epsilon_{\mathrm{m}}}}\leqslant\gamma\leqslant\sqrt{\frac{\epsilon_{\mathrm{r}}}{\tilde{\epsilon}_0-\epsilon_{\mathrm{m}}}}=\gamma_{\mathrm{s,max}}, \tag{5.7}$$

where $\tilde{\epsilon}_0$ is the average of $\epsilon(z,t)$, as seen in (5.5), and ϵ_{m} is the maximal (symmetric) variation of $\epsilon(z,t)$ from $\tilde{\epsilon}_0$, and is called the modulation depth. Upon multiplication by v_{b} and usage of (5.4) and (5.3), this interval may also be expressed in terms of the modulation velocity as

$$v_{\mathrm{m,s,min}}=\frac{c}{\sqrt{\tilde{\epsilon}_0+\epsilon_{\mathrm{m}}}}\leqslant v_{\mathrm{m}}\leqslant\frac{c}{\sqrt{\tilde{\epsilon}_0-\epsilon_{\mathrm{m}}}}=v_{\mathrm{m,s,max}}, \tag{5.8}$$

and is called the “sonic regime” [186] in analogy with a similar interval first identified in acoustic space-time modulated problems. It has been established that, in the case of the (nonperiodic) space-time slab $\epsilon(z,t) = \mathrm{rect}(\beta_{\mathrm{m}}z-\omega_{\mathrm{m}}t)$, the sonic regime (5.8) supports both a space-like reflected wave and a time-like reflected wave, whereas only a space-like reflected wave exists when $v_{\mathrm{m}} < v_{\mathrm{m,s,min}}$ and only a time-like reflected wave exists when $v_{\mathrm{m}} > v_{\mathrm{m,s,max}}$ [190]. The sonic interval thus represents a regime requiring a special mathematical treatment, that has not yet been reported in the literature to the best of the authors' knowledge. When the space-time modulation is made periodic, as in (5.5), the same phenomenon occurs for each interface, and therefore the interval (5.8) still corresponds to the same sonic regime. In the middle of the sonic interval, i.e. at $\gamma = 1$ or $v_{\mathrm{m}} = v_{\mathrm{b}}$, all the forward space-time harmonics merge into a single dispersion curve, as will be explained later, leading to a shock wave as in the phenomenon of sound barrier breaking in acoustics.

To find the unknown coefficients, β_0^+, β_0^-, A_n^+ and A_n^- in (5.6), we shall first fix ω_0, as the source frequency, and then find the corresponding discrete β_0 solutions, β_{0p}, forming the dispersion diagram of the slab. Next, we shall apply the spatial boundary conditions at the edges of the slab, i.e. at $z = 0$ and $z = L$, for all the (ω_0, β_{0p}) states in the dispersion diagram, which will provide the unknown slab coefficients $A^+_{n(p)}$ and $A^-_{n(p)}$ in (5.6b) and (5.6c), respectively, and the corresponding coefficients in the unmodulated regions, i.e. the fields everywhere.

Consider the Maxwell equations for a general space-time modulated permittivity as

$$\nabla \times \mathbf{E}_\mathrm{M}(x,z,t) = -\frac{\partial \mathbf{B}_\mathrm{M}(x,z,t)}{\partial t}, \tag{5.9a}$$

$$\nabla \times \mathbf{H}_\mathrm{M}(x,z,t) = \frac{\partial \mathbf{D}_\mathrm{M}(x,z,t)}{\partial t}, \tag{5.9b}$$

$$\nabla \cdot \mathbf{E}_\mathrm{M}(x,z,t) = 0, \tag{5.9c}$$

$$\nabla \cdot \mathbf{H}_\mathrm{M}(x,z,t) = 0. \tag{5.9d}$$

which may be written as

$$\nabla \times (\nabla \times \mathbf{E}_\mathrm{M}(x,z,t)) = -\frac{\partial \mathbf{B}_\mathrm{M}}{\partial t} = -\mu_0 \frac{\partial}{\partial t}\left(\frac{\partial \mathbf{D}_\mathrm{M}(x,z,t)}{\partial t}\right), \tag{5.10}$$

and then, using (5.9c), the source-less wave equation reads

$$\begin{aligned} \nabla^2 \mathbf{E}_\mathrm{M}(x,z,t) &= \mu_0 \frac{\partial}{\partial t}\left(\frac{\partial \mathbf{D}_\mathrm{M}(x,z,t)}{\partial t}\right) \\ &= \frac{1}{c^2}\frac{\partial}{\partial t}\left(\frac{\partial\left[\epsilon(z,t)\mathbf{E}_\mathrm{M}(x,z,t)\right]}{\partial t}\right), \end{aligned} \tag{5.11}$$

Inserting (5.6) into the first term of (5.11), and (S10) in Sec. 2 of [189] [product of (5.5) and (5.6)] into the second term of (5.11), and next using (S12), yields the relation

$$A_n^\pm \left[\frac{k_x^2 + (\beta_0 \pm n\beta_\mathrm{m})^2}{\left[(\omega_0 + n\omega_\mathrm{m})/c\right]^2}\right] - \sum_{k=-\infty}^{\infty} \tilde{\epsilon}_k A^\pm_{n-k} = 0. \tag{5.12}$$

Equation (5.12) may be cast, after truncation to $2N+1$ terms, to the matrix form

$$[K^\pm] \cdot [A^\pm] = 0, \tag{5.13}$$

where $[K^{\pm}]$ is the $(2N+1)\times(2N+1)$ matrix with elements

$$\begin{aligned} K_{nn}^{\pm} &= \left[\frac{k_x^2 + (\beta_0 \pm n\beta_\mathrm{m})^2}{\left[(\omega_0 + n\omega_\mathrm{m})/c\right]^2}\right] - \epsilon_0, \\ K_{nk}^{\pm} &= -\tilde{\epsilon}_{n-k}, \quad \text{for } n \neq k, \end{aligned} \tag{5.14}$$

and $[A^{\pm}]$ is the $(2N+1)\times 1$ vector containing the $A_n^{\pm}$ coefficients. The dispersion relation is then given by

$$\det\left\{[K^{\pm}]\right\} = 0, \tag{5.15}$$

and the $(2N+1)$ forward and backward dispersion curves $\beta_{0p}(\omega_0)$, whose number is here finite due to truncation but theoretically infinite, are formed by solving this equation separately for the $\pm z$-propagating waves for a given set of modulation parameters ω_m, β_m and $\tilde{\epsilon}_k$, and for values of ω_0 swept across the temporal frequency range of interest. Note that each point (β_{0p}, ω_0) represents a *mode* of the medium, itself constituted of an infinite number of oblique *space-time harmonics* corresponding to modes at other frequencies, since such a point is a solution to the complete wave equation by virtue of (5.15).

Once the dispersion diagram has been constructed, i.e. once the $\beta_{0p}^{\pm}$ states, solutions to (5.11), have been determined versus ω_0, the unknown field amplitudes $A_{np}^{\pm}$ in the slab are found by solving (5.13) after determining the $A_{0p}^{\pm}$ terms satisfying boundary conditions. These terms are derived in Sec. 3 of [189] as

$$A_{0p}^{\mathrm{F}+} = \frac{E_0 k_0[\cos(\theta_\mathrm{i}^{+}) + \cos(\theta_\mathrm{r0}^{+})]}{\beta_{0p}^{+} + k_0\cos(\theta_\mathrm{r0}^{+}) - \frac{\beta_{0p}^{-} - k_0\cos(\theta_\mathrm{r0}^{+})}{e^{j(\beta_{0p}^{+}+\beta_{0p}^{-})L}}\frac{\beta_{0p}^{+} - k_0\cos(\theta_\mathrm{t0}^{+})}{\beta_{0p}^{-} + k_0\cos(\theta_\mathrm{t0}^{+})}}, \tag{5.16a}$$

$$A_{0p}^{\mathrm{F}-} = A_{0p}^{\mathrm{F}+} e^{-j(\beta_{0p}^{+}+\beta_{0p}^{-})L}\frac{\beta_{0p}^{+} - k_0\cos(\theta_\mathrm{t0}^{+})}{\beta_{0p}^{-} + k_0\cos(\theta_\mathrm{t0}^{+})}, \tag{5.16b}$$

for the forward problem, and

$$A_{0p}^{\mathrm{B}-} = \frac{E_0 k_0[\cos(\theta_\mathrm{i}^{-}) + \cos(\theta_\mathrm{r0}^{-})]e^{jk_0\cos(\theta_\mathrm{i}^{-})L}}{\frac{\beta_{0p}^{-} + k_0\cos(\theta_\mathrm{r0}^{-})}{e^{-j\beta_{0p}^{-}L}} - \frac{\beta_{0p}^{+} - k_0\cos(\theta_\mathrm{r0}^{-})}{e^{j\beta_{0p}^{+}L}}\frac{\beta_{0p}^{-} - k_0\cos(\theta_\mathrm{t0}^{-})}{\beta_{0p}^{+} + k_0\cos(\theta_\mathrm{t0}^{-})}}, \tag{5.17a}$$

$$A_{0p}^{\mathrm{B}+} = A_{0p}^{\mathrm{B}-}\frac{\beta_{0p}^{-} - k_0\cos(\theta_\mathrm{t0}^{-})}{\beta_{0p}^{+} + k_0\cos(\theta_\mathrm{t0}^{-})}, \tag{5.17b}$$

for the backward problem, where $k_0 = \omega_0\sqrt{\epsilon_\mathrm{r}}/c$ is the spatial frequency in the unmodulated media. As expected from the unidirectionality of the perturbation [Eq. (5.1)], we have $A_{0p}^{\mathrm{F}+} \neq A_{0p}^{\mathrm{B}-}$ and $A_{0p}^{\mathrm{F}-} \neq A_{0p}^{\mathrm{B}+}$. It may be easily verified that in the particular case where the temporal perturbation is switched off ($\omega_\mathrm{m} = 0$), so that $\beta_{0,p}^{+} = \beta_{0,p}^{-} = \beta_{0,p}$, these inequalities transform to equalities after compensating for the round-trip phase shift $-2\beta_{0,p}L$, as expected for the resulting reciprocal system.

From this point, the scattered fields in the unmodulated media, also derived in Sec. 3 of [189], are found as

$$\begin{aligned}\mathbf{E}_\mathrm{R}^\mathrm{F} = \hat{\mathbf{y}} \sum_{n=-\infty}^{\infty} & e^{-j[k_0 \sin(\theta_\mathrm{i})x - k_{0n}\cos(\theta_{\mathrm{r}n})z - (\omega_0 + n\omega_\mathrm{m})t]} \\ & \cdot \left[\sum_{p=-\infty}^{\infty} \left(A_{np}^{\mathrm{F}+} + A_{np}^{\mathrm{F}-} \right) - E_0^{+}\delta_{n0} \right],\end{aligned} \tag{5.18a}$$

$$\begin{aligned}\mathbf{E}_\mathrm{T}^\mathrm{F} =& \hat{\mathbf{y}} \sum_{n=-\infty}^{\infty} e^{-j[k_0 \sin(\theta_\mathrm{i})x + k_{0n}\cos(\theta_{\mathrm{t}n})z - (\omega_0 + n\omega_\mathrm{m})t]}, \\ & \cdot \sum_{p=-\infty}^{\infty} \left(A_{np}^{\mathrm{F}+} e^{-j(\beta_{0p} + n\beta_\mathrm{m})L} + A_{np}^{\mathrm{F}-} e^{j(\beta_{0p} - n\beta_\mathrm{m})L} \right).\end{aligned} \tag{5.18b}$$

and

$$\begin{aligned}\mathbf{E}_\mathrm{R}^\mathrm{B} = \hat{\mathbf{y}} \sum_{n=-\infty}^{\infty} & e^{-j[k_0 \sin(\theta_\mathrm{i})x + k_{0n}\cos(\theta_{\mathrm{r}n})z - (\omega_0 + n\omega_\mathrm{m})t]} \\ \cdot \Bigg[\sum_{p=-\infty}^{\infty} & \left(A_{np}^{\mathrm{B}+} e^{-j(\beta_{0p} + n\beta_\mathrm{m})L} + A_{np}^{\mathrm{B}-} e^{j(\beta_{0p} - n\beta_\mathrm{m})L} \right) \\ & - E_0^{-}\delta_{n0} e^{jk_0 L} \Bigg],\end{aligned} \tag{5.19a}$$

$$\begin{aligned}\mathbf{E}_\mathrm{T}^\mathrm{B} =& \hat{\mathbf{y}} \sum_{n=-\infty}^{\infty} \left(A_{np}^{\mathrm{B}+} + A_{np}^{\mathrm{B}-} \right) \\ & \cdot e^{-j[k_0 \sin(\theta_\mathrm{i})x - k_{0n}\cos(\theta_{\mathrm{t}n})z - (\omega_0 + n\omega_\mathrm{m})t]},\end{aligned} \tag{5.19b}$$

where $k_{0n} = (\omega_0 + n\omega_\mathrm{m}/v_\mathrm{b})$.

The scattering angles of the different space-time harmonics in (5.18) for the forward problem, are represented in Fig. 5.2. They are obtained from the corresponding Helmholtz relations

$$[k_0 \sin(\theta_\mathrm{i})]^2 + [k_{0n}\cos(\theta_{\mathrm{r}n})]^2 = k_{0n}^2, \tag{5.20a}$$

and

$$[k_0 \sin(\theta_\mathrm{i})]^2 + [k_{0n}\cos(\theta_{\mathrm{t}n})]^2 = k_{0n}^2, \tag{5.20b}$$

yielding

$$\sin(\theta_{\mathrm{r}n}) = \sin(\theta_{\mathrm{t}n}) = \frac{\sin(\theta_{\mathrm{i}})}{1 + n\omega_{\mathrm{m}}/\omega_0}, \tag{5.20c}$$

where $\theta_{\mathrm{r}n}$ and $\theta_{\mathrm{t}n}$ are the reflection and transmission angles of the n^{th} space-time harmonic. Equation (5.20c) describes the space-time spectral decomposition of the scattered wave. The reflection and transmission angles for a given harmonic n are equal, due to phase matching, i.e due to the unique tangential wavenumber, $k_x = k_0 \sin(\theta_{\mathrm{i}})$ in all the regions [Eqs. (5.20a) and (5.20b)]. The harmonics in the n-interval $[\omega_0(\sin\theta_{\mathrm{i}} - 1)/\omega_{\mathrm{m}}, +\infty[$ are scattered (reflected and transmitted) at angles ranging from $\pi/2$ to 0 through θ_{i} for $n = 0$. The harmonics outside of this interval correspond to imaginary $k_{znp}^{\pm}$ and are hence not scattered. Rather, they travel as surface waves along the boundary. In the modulated medium, the scattering angles are found from the dispersion relation as

$$\tan(\theta_{np}^{\pm}) = \frac{k_x}{k_{znp}^{\pm}} = \frac{k_0 \sin(\theta_{\mathrm{i}})}{\beta_{0p}^{\pm} \pm n\beta_{\mathrm{m}}}. \tag{5.21}$$

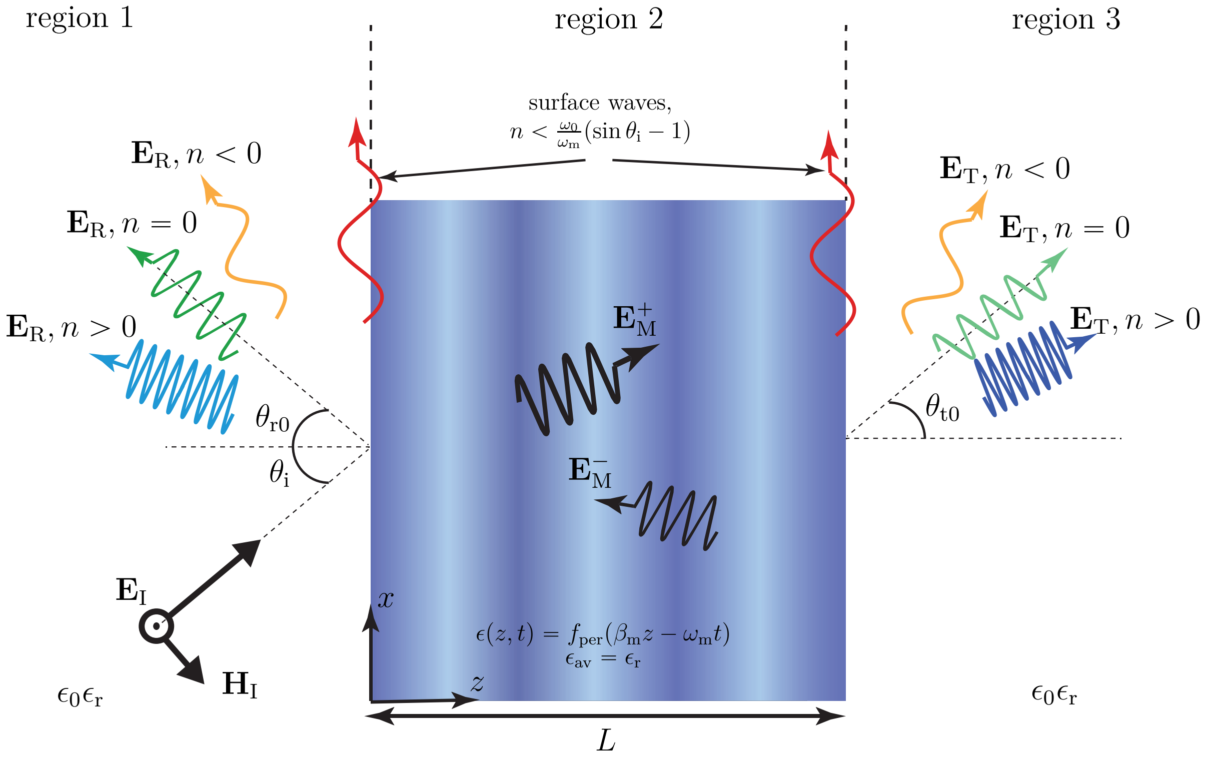

Figure 5.2 Scattered space-time harmonics (shown here for the forward problem) [7].

5.2 Sinusoidally Modulated Slab

We next consider a sinusoidal forward space-time permittivity as a particular case of the general periodic permittivity in (5.1), namely

$$\epsilon(z,t) = \epsilon_\mathrm{r} + \epsilon_\mathrm{m}\ \cos(\beta_\mathrm{m} z - \omega_\mathrm{m} t). \tag{5.22}$$

Such a permittivity has been used in [71] for the realization of a traveling-wave parametric amplifier. For the computation of the solution derived in Sec. 5.1, we write the expression (5.22) in terms of its space-time Fourier components, i.e.

$$\epsilon(z,t) = \tilde{\epsilon}_{-1} e^{-j(\beta_\mathrm{m} z - \omega_\mathrm{m} t)} + \tilde{\epsilon}_0 + \tilde{\epsilon}_{+1} e^{+j(\beta_\mathrm{m} z - \omega_\mathrm{m} t)}, \tag{5.23a}$$

with

$$\tilde{\epsilon}_{-1} = \tilde{\epsilon}_{+1} = \epsilon_\mathrm{m}/2 \quad \text{and} \quad \tilde{\epsilon}_0 = \epsilon_\mathrm{r}. \tag{5.23b}$$

Inserting (5.23) into (5.12) and subsequently following [9], we find the analytic expressions

$$A_{np}^{\pm} = A_{n+1,p}^{\pm} \frac{1}{-K_{np}^{\pm} + \frac{1}{K_{n-1,p}^{\pm} + \frac{1}{-K_{n-2,p}^{\pm} + \frac{1}{K_{n-3,p}^{\pm} + \dots}}}} \tag{5.24}$$

for $n < 0$, and

$$A_{np}^{\pm} = A_{n-1,p}^{\pm} \frac{1}{-K_{np}^{\pm} + \frac{1}{K_{n+1,p}^{\pm} + \frac{1}{-K_{n+2,p}^{\pm} + \frac{1}{K_{n+3,p}^{\pm} + \dots}}}}, \tag{5.25}$$

for $n > 0$, where

$$K_{np}^{\pm} = \frac{2\epsilon_\mathrm{r}}{\epsilon_\mathrm{m}} \left[1 - \left(\frac{k_x^2 + (\beta_0^{\pm} \pm n\beta_\mathrm{m})^2}{\left[(\omega_0 + n\omega_\mathrm{m})/v_\mathrm{b}\right]^2} \right) \delta_{nn} \right]. \tag{5.26}$$

The sonic interval associated with the sinusoidal permittivity in (5.22) is obtained by inserting $\tilde{\epsilon}_0$ into (5.7) as

$$\gamma_\mathrm{s,min} = \frac{1}{\sqrt{1 + \epsilon_\mathrm{m}/\epsilon_\mathrm{r}}} \leqslant \gamma \leqslant \frac{1}{\sqrt{1 - \epsilon_\mathrm{m}/\epsilon_\mathrm{r}}} = \gamma_\mathrm{s,max}, \tag{5.27}$$

where it is understood that $|\epsilon_\mathrm{m}\cos(\beta_\mathrm{m}z-\omega_\mathrm{m}t)| \leqslant \epsilon_\mathrm{m}$. Following again [9], we also find the following analytic form for the dispersion relation of the slab :

$$\begin{aligned} &\frac{1}{-K_{p,-1}^{\pm}+\frac{1}{K_{p,-2}^{\pm}+\frac{1}{-K_{p,-3}^{\pm}+\frac{1}{K_{p,-4}^{\pm}+\ldots}}}}+K_{0p}^{\pm} \\ &\qquad +\frac{1}{-K_{p,1}^{\pm}+\frac{1}{K_{p,2}^{\pm}+\frac{1}{-K_{p,3}^{\pm}+\frac{1}{K_{p,4}^{\pm}+\ldots}}}}=0. \end{aligned} \tag{5.28}$$

This equation, which uses the $K_{np}^{\pm}$'s in (5.26), provides, for a given set of modulation parameters (ϵ_m, ϵ_r, ω_m, β_m, γ) and variable ω_0, the periodic dispersion diagram (β_{0p}'s) of the system.

Finally, the local space-time phase velocity and characteristic impedance read

$$v(z,t)=\frac{c}{\sqrt{\epsilon(z,t)}}=\frac{c}{\sqrt{\epsilon_\mathrm{r}+\epsilon_\mathrm{m}\cos(\beta_\mathrm{m}z-\omega_\mathrm{m}t)}} \tag{5.29a}$$

and

$$Z_0(z,t)=\sqrt{\frac{\mu}{\epsilon(z,t)}}=\sqrt{\frac{\mu_0}{\epsilon_0\left(\epsilon_\mathrm{r}+\epsilon_\mathrm{m}\ \cos(\beta_\mathrm{m}z-\omega_\mathrm{m}t)\right)}}, \tag{5.29b}$$

respectively. Equation (5.29) indicate that the scattering angles and matching level both vary in space and time when $\epsilon_\mathrm{m}\neq 0$.

5.3 Quasi-Sonic Nonreciprocity

5.3.1 Dispersion and Isofrequency Diagrams of the Unbounded Modulated Slab Medium

In order to gain deeper insight into the wave propagation phenomenology within the space-time modulated slab medium, we next study the dispersion and isofrequency diagrams of the corresponding unbounded medium. Both are generally computed using (5.15) with (5.14) and (5.23).

In the limiting case of a vanishingly small (but non zero) modulation depth, $\epsilon_\mathrm{m}\to 0$, the aforementioned equations lead to the closed-form dispersion relation

$$k_x^2+(\beta_0^{\pm}\pm n\beta_\mathrm{m})^2=\left(\frac{\omega_0+n\omega_\mathrm{m}}{v_\mathrm{b}}\right)^2. \tag{5.30}$$

Using (5.2) and (5.4), this relation may be more conveniently rewritten as

$$\left(\frac{k_x}{\beta_\mathrm{m}}\right)^2 + \left(\frac{\beta_0^\pm}{\beta_\mathrm{m}} \pm n\right)^2 = \gamma^2 \left(\frac{\omega_0}{\omega_\mathrm{m}} + n\right)^2, \tag{5.31}$$

which represents an infinite periodic set of double cones with apexes at $k_x = 0$ and $\beta_0 = \pm n\beta_\mathrm{m}$ and slope v_m, as illustrated in Fig. 5.3. A vertical cross section of this 3D diagram at $k_x = 0$ produces an infinite periodic set of straight lines in the $\beta_0/\beta_\mathrm{m} - \omega_0/\omega_\mathrm{m}$ plane, and a horizontal cut produces an infinite periodic set of circles centered at $(\beta_0^\pm/\beta_\mathrm{m}, k_x/\beta_\mathrm{m}) = (\mp n, 0)$ with radius $\gamma\left(\omega_0/\omega_\mathrm{m} + n\right)$ in the $\beta_0/\beta_\mathrm{m} - k_x/\beta_\mathrm{m}$ plane, as depicted in Fig. 5.3.

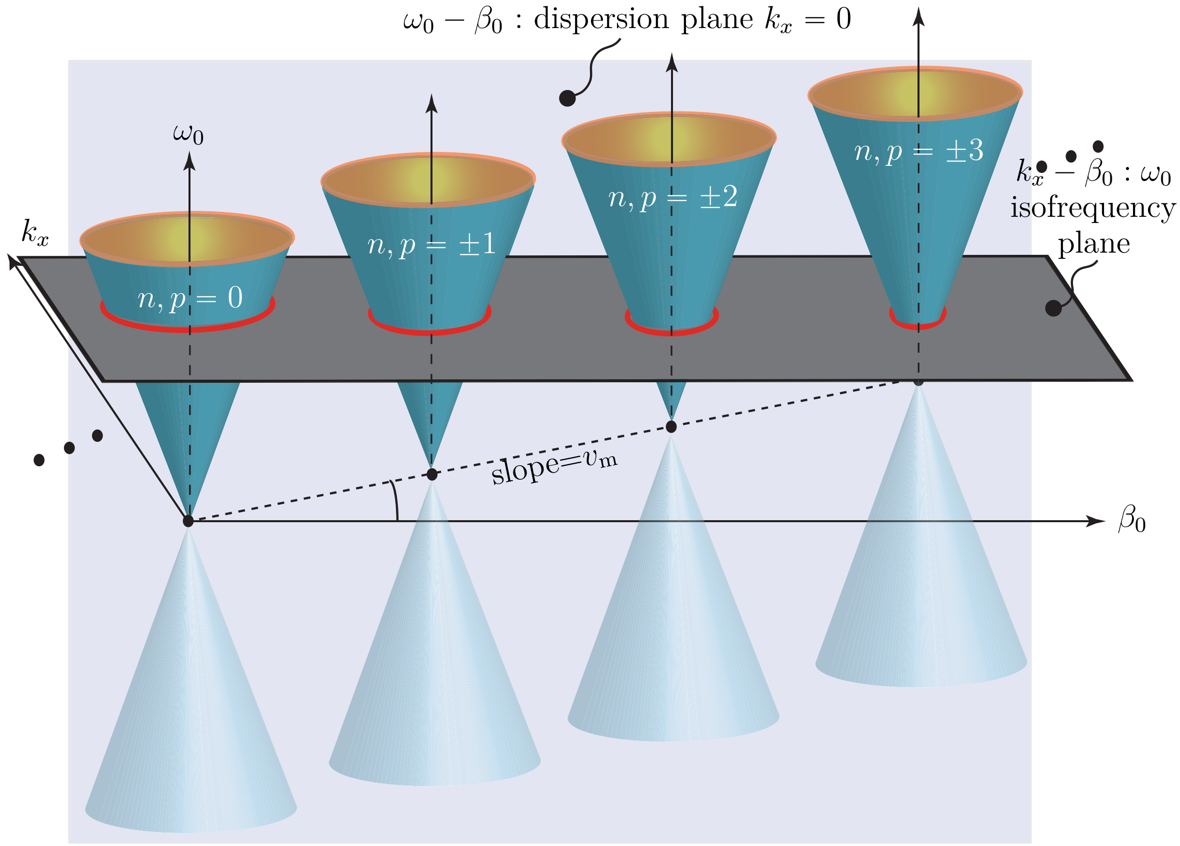

Figure 5.3 Illustration of the three dimensional dispersion for the unbounded sinusoidally space-time modulated permittivity (5.22). A vertical cut at $k_x = 0$ produces the dispersion diagrams, (ω_0, β_0). A horizontal cut at the excitation frequency, ω_0, produces isofrequency diagrams, (β_0, k_x). Note that the ω_0, β_0 and k_x axes are mutually orthogonal [7].

We shall now consider the dispersion diagrams plotted in Fig. 5.4 for the case of normal incidence, and therefore normal propagation everywhere, i.e. $k_x = 0$, for different sets of parameters. Figure 5.4(a) plots the dispersion diagram for a vanishingly small modulation depth, i.e. $\epsilon_{\mathrm{m}} \to 0$, and for $\gamma = 0.3$. In such a case, Eq. (5.31) reduces to the very simple dispersion relation

$$\frac{\beta_0^{\pm}}{\beta_{\mathrm{m}}} = \gamma\frac{\omega_0}{\omega_{\mathrm{m}}} + n\left(\gamma \mp 1\right). \tag{5.32}$$

This diagram consists of the infinite periodic set of $\beta_0/\beta_{\mathrm{m}} - \omega_0/\omega_{\mathrm{m}}$ straight curves, labeled by n. To any frequency, ω_0, corresponds an infinite number of modes, labeled by p, each of which consisting in the infinite number of forward and backward space-time harmonics $(\beta_{0p}^{\pm} + n\beta_{\mathrm{m}}, \omega_0 + n\omega_{\mathrm{m}})$ located on the corresponding oblique curve with slope v_{m}. Note that, as pointed out in Sec. 5.1, any (oblique) space-time harmonic point may be seen as corresponding to a different mode, excited at a different frequency, or, equivalently, that any mode, excited at ω_0, may be seen as corresponding to an oblique space-time harmonic of another mode, with different excitation frequency. Given the vanishingly small periodic perturbation ($\epsilon_{\mathrm{m}} \to 0$), the medium is here quasi homogeneous, with most of the energy residing in the $n = 0$ forward and backward space-time harmonics, which would in fact represent the only remaining curves for exactly $\epsilon_{\mathrm{m}} = 0$ (homogeneous non-periodic medium).

We note in Fig. 5.4(a) that when the velocity ratio is non-zero (here $\gamma = 0.3$), the distances between the forward and backward space-time harmonics, $\Delta\beta^{\pm} = \beta_{n+1}^{\pm} - \beta_n^{\pm}$, are different. Specifically, as γ increases, $\Delta\beta^{+}$ decreases and $\Delta\beta^{-}$ increases. This may be explained as follows, considering the horizontal cut $\omega_0 = 0$, where $\Delta\beta$ represents the spatial-frequency period or Brillouin zone edge. In the static case, $v_{\mathrm{m}} = 0$ (not shown in Fig. 5.4), we have $\Delta\beta^{\pm} = \Delta\beta = 2\pi/p_{\mathrm{stat}}$, where p_{stat} is the static period seen by both the forward and backward waves. As $v_{\mathrm{m}} > 0$ (all of Figs. 5.4), the forward and backward waves see the velocities, $v^{\pm} = v_{\mathrm{b}} \mp v_{\mathrm{m}}$, respectively, *relative to the modulating wave*, with limits $v^{+}(v_{\mathrm{m}} = v_{\mathrm{b}}) = 0$ and $v^{-}(v_{\mathrm{m}} = v_{\mathrm{b}}) = 2v_{\mathrm{b}}$. The corresponding relative periods, satisfying the conditions $p_{\mathrm{mov}}^{\pm}(v_{\mathrm{m}} = 0) = p_{\mathrm{stat}}$, $p_{\mathrm{mov}}^{+}(v_{\mathrm{m}} = v_{\mathrm{b}}) = \infty$ (synchronization with modulation and hence no period seen, i.e. infinite period) and $p_{\mathrm{mov}}^{-}(v_{\mathrm{m}} = v_{\mathrm{b}}) = p_{\mathrm{stat}}/2$ (due to opposite propagation at same velocity as modulation), are found as $p_{\mathrm{mov}}^{\pm} = p_{\mathrm{stat}}v_{\mathrm{b}}/(v_{\mathrm{b}} \mp v_{\mathrm{m}})$. Thus, $\Delta\beta_{\mathrm{mov}}^{\pm} = 2\pi/p_{\mathrm{mov}}^{\pm} = (2\pi/p_{\mathrm{stat}})(v_{\mathrm{b}} \mp v_{\mathrm{m}})/v_{\mathrm{b}}$ or $\Delta\beta_{\mathrm{mov}}^{\pm}/\beta_m = 1 \mp \gamma$, indicating that distances between the forward and between the backward space-time harmonics decrease and increase, respectively, tending to the limits $\Delta\beta_{\mathrm{mov}}^{+}(\gamma = 1)/\beta_m = 0$ and $\Delta\beta_{\mathrm{mov}}^{-}(\gamma = 1)/\beta_m = 2$. This result, deduced from a physical argument, is in agreement with the mathematical result of (5.32), evaluating $\beta_{0,n+1}^{\pm}/\beta_{\mathrm{m}} - \beta_{0,n}^{\pm}/\beta_{\mathrm{m}}$ at $\omega_0 = 0$.

Figure 5.4(b) plots the dispersion diagram for the greater modulation depth $\epsilon_{\mathrm{m}} = 0.22\epsilon_{\mathrm{r}}$. In this case, the periodic perturbation is much more pronounced. Therefore, a substantial number of space-time harmonics contribute to the fields and the interferences between these harmonics are sufficiently strong to open up stop-bands. These stop-bands are naturally

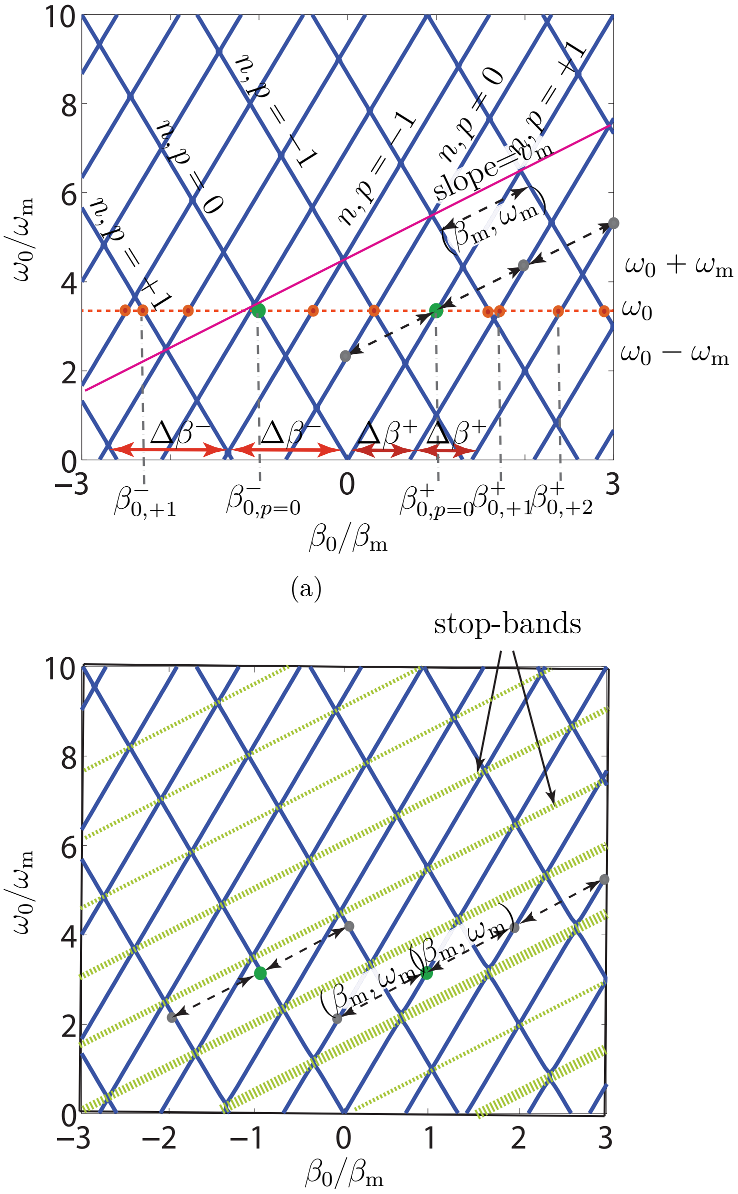

(a)

(b)

Figure 5.4 Normal-incidence ($k_x = 0$) dispersion diagrams for the sinusoidally space-time modulated (unbounded) slab medium with the permittivity (5.22), computed using (5.15) with (5.14) and (5.23). (a) Space-time modulated medium with vanishingly small modulation depth, i.e. $\epsilon_\mathrm{m} \to 0$ and for $\gamma = 0.3$ [Eq. (5.31)]. (b) Same as (a) except for the greater modulation depth $\epsilon_\mathrm{m} = 0.22\epsilon_\mathrm{r}$ [7].

oblique, again with slope v_m, as they have to occur at the space-time synchronization points, i.e. at the intersections of the space-time harmonics which lie on oblique lines according to Fig. 5.4(a). The stopband asymmetry with respect to the $\beta_0 = 0$ axis may be used for optical isolation [8].

Figure 5.5 plots the dispersion diagram for the greater space-time modulation ratio $\gamma = 0.85$, which is subsonic ($\gamma < 1$) and quasi-sonic ($\gamma \approx \gamma_{\text{s,min}}$) given $\gamma_{\text{s,min}} = 0.905$. What is observed corresponds to the expectation from the above explanation and related formula $\Delta\beta^{\pm}_{\text{mov}}/\beta_m = 1 \mp \gamma$. The forward space-time harmonics get closer to each other (they would in fact completely fill up the diagram in the limit $\gamma \to 1$) and eventually collapse into a single curve at $\gamma = 1$ since $\Delta\beta^{+}_{\text{mov}}(\gamma = 1)/\beta_m = 0$, producing the shock wave. On the other hand, the backward space-time harmonics tend to be separated by the distance $\Delta\beta^{-}_{\text{mov}}(\gamma = 1)/\beta_m = 2$. In this quasi-sonic regime, the closest space-time harmonics strongly couple to each other at a given frequency ω_0 because they possess very close phase velocities and are hence essentially phase-matched to each other. Therefore, this regime is of particular interest, as will be seen in the application of Sec. 6.1. As mentioned in Sec. 5.1, the analytical results presented in this chapter are restricted to the subsonic regime, but the quasi-sonic condition $\gamma \approx \gamma_{\text{s,min}}$ allows one to reap the essential benefits of the physics occurring in the sonic regime, as will be seen in Sec. 6.1.

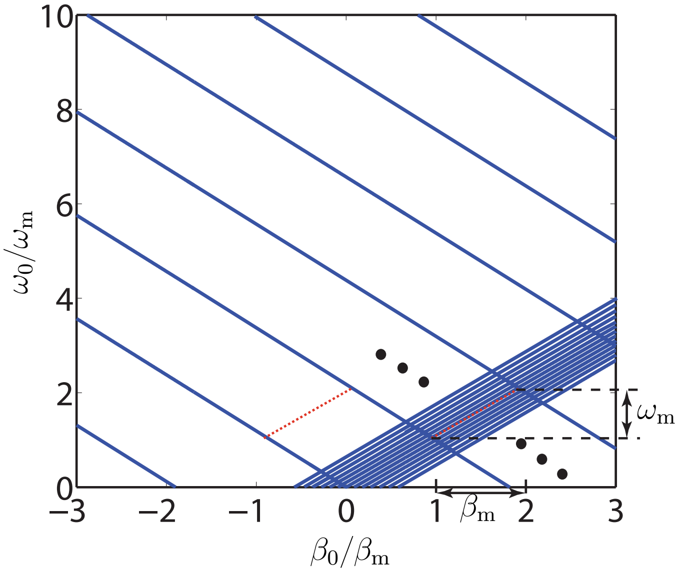

Figure 5.5 Normal-incidence ($k_x = 0$) dispersion diagrams for the sinusoidally space-time modulated (unbounded) slab medium with the permittivity (5.22), computed using (5.15) with (5.14) and (5.23). (a) Space-time modulated medium with vanishingly small modulation depth, i.e. $\epsilon_\text{m} \to 0$ and for $\gamma = 0.3$ [Eq. (5.31)]. Same as Fig. 5.4(b) except for the subsonic ($\gamma < \gamma_{\text{s,min}}$) quasi-sonic ($\gamma \approx \gamma_{\text{s,min}}$) space-time modulation ratio $\gamma = 0.85$ ($\gamma_{\text{s,min}} = 0.905$) [7].

We shall now consider the isofrequency diagrams plotted in Fig. 5.7 for different sets of parameters. These diagrams may be easiest understood using the 3D perspective in Fig. 5.3.

Figure 5.6(a) plots the isofrequency curves for a purely space modulated medium, where $\omega_\mathrm{m} = \gamma \to 0$, with vanishingly small modulation depth, i.e. $\epsilon_\mathrm{m} \to 0$, and $\epsilon_\mathrm{m} = 0.2$. In the former case ($\epsilon_\mathrm{m} \to 0$), the curves are the circles given by (5.31), corresponding to the infinite number of space harmonics n and reducing to the center circle, $k_x^2 + \beta_0^2 = k^2 - k_0^2/\epsilon_\mathrm{r}$, in the trivial limiting case of a perfectly homogenous medium ($\epsilon_\mathrm{m} = 0$). In the latter case ($\epsilon_\mathrm{m} = 0.2$), Eq. (5.31) is not valid any more and one must resort to the general relation (5.15). Here, spatial ($k_x - \beta$) stop-bands open up at the intersection points for $\epsilon_\mathrm{m} = 0$, due to space harmonic coupling. Note that in such a purely spatially modulated medium, the space harmonics are simply related by $\beta_{0,n}^{\pm} = \beta_{0,0}^{\pm} + n\beta_\mathrm{m}$, where, for a given k_x, all the spatial harmonics propagate, attenuate (near stop-bands edges, when $\epsilon_\mathrm{m} > 0$) or get cut off.

Figure 5.6(b) plots the isofrequency diagram for a space-time modulated medium, where $\beta_\mathrm{m}, \omega_\mathrm{m} > 0$, still with vanishingly small modulation depth, i.e. $\epsilon_\mathrm{m} \to 0$, and $\omega_0 = 1.5\omega_\mathrm{m}$, $\gamma = 0.15$. The isofrequency circles have now different radii, corresponding to $\gamma\left(\omega_0/\omega_\mathrm{m} + n\right)$ [Eq. (5.31)], with envelope slope of $-\gamma$. This is because, in contrast to the purely spatial medium in Fig. 5.6(a), the space-time medium supports, for fixed incidence angle (i.e. fixed k_x), an infinite number of modes (labeled by p), each of them composed of an infinite number of forward and backward space-time harmonics ($\beta_{0p}^{\pm} + n\beta_\mathrm{m}, \omega_0 + n\omega_\mathrm{m}$), as previously explained. The medium operates as a spatial (β) high-pass filter, some modes above the cutoff propagating and those below the cut off, as shown in Fig. 5.2 and related explanation.

Figure 5.6(c) shows the same diagram as Fig. 5.6(b), for the larger space-time modulation ratio, $\gamma = 0.3$. As γ increases, the isofrequency circles in the forward region, $\beta_0 > 0$, get smaller and appear farther apart. In contrast, those in the backward region, $\beta_0 < 0$, get bigger, and eventually intersect. This behavior can be intuitively understood from the 3D dispersion curves in Fig. 5.3.

Figure 5.7(a) shows isofrequency curves for the stronger modulation depth $\epsilon_\mathrm{m} = 0.22\epsilon_\mathrm{r}$. As the modulation depth is increased, forward and backward waves at the intersections of the isofrequency circles couple more strongly and a visible bandstop appears in the isofrequency diagram. In the limit of vanishingly small modulation depth, these bandstops become vanishingly narrow. Depending on the incidence frequency and angle, some modes propagate and some are cut off. For instance, for $\theta_\mathrm{i} = 44^\circ$, mode $p = -1$ is evanescent, while modes $p = 0$ and $p = +2$ represent forward propagating waves.

Finally, Fig. 5.7(b) plots the isofrequency diagram in the quasi-sonic regime. The forward waves are synchronized and exhibit similar group and phase velocities, leading to strong interaction and coupling, while backward waves are more distant and therefore interact relatively weakly.

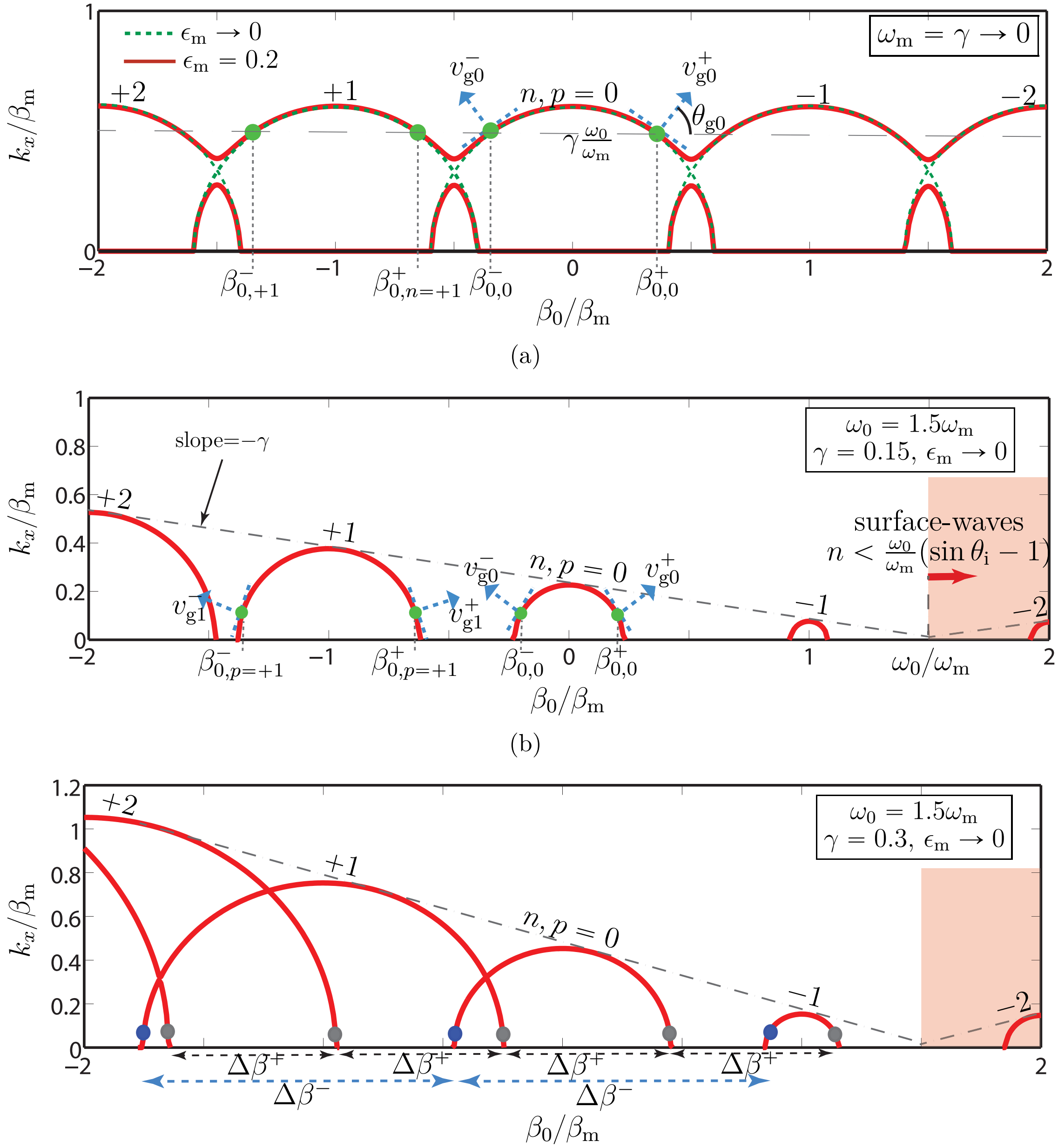

Figure 5.6 Isofrequency diagrams for the unbounded sinusoidally space-time modulated medium (5.22), computed using (5.15) with (5.14) and (5.23). (a) Purely space-modulated medium, i.e. $\omega_{\mathrm{m}} = \gamma \to 0$ (but finite $\gamma\omega_0/\omega_{\mathrm{m}} = 0.6$). (b) Space-time modulated medium with vanishingly small modulation depth, i.e. $\epsilon_{\mathrm{m}} \to 0$, and for $\omega_0 = 1.5\omega_{\mathrm{m}}$ and $\gamma = 0.15$. (c) Same as (b) except for the greater space-time modulation ratio $\gamma = 0.3$ [7].

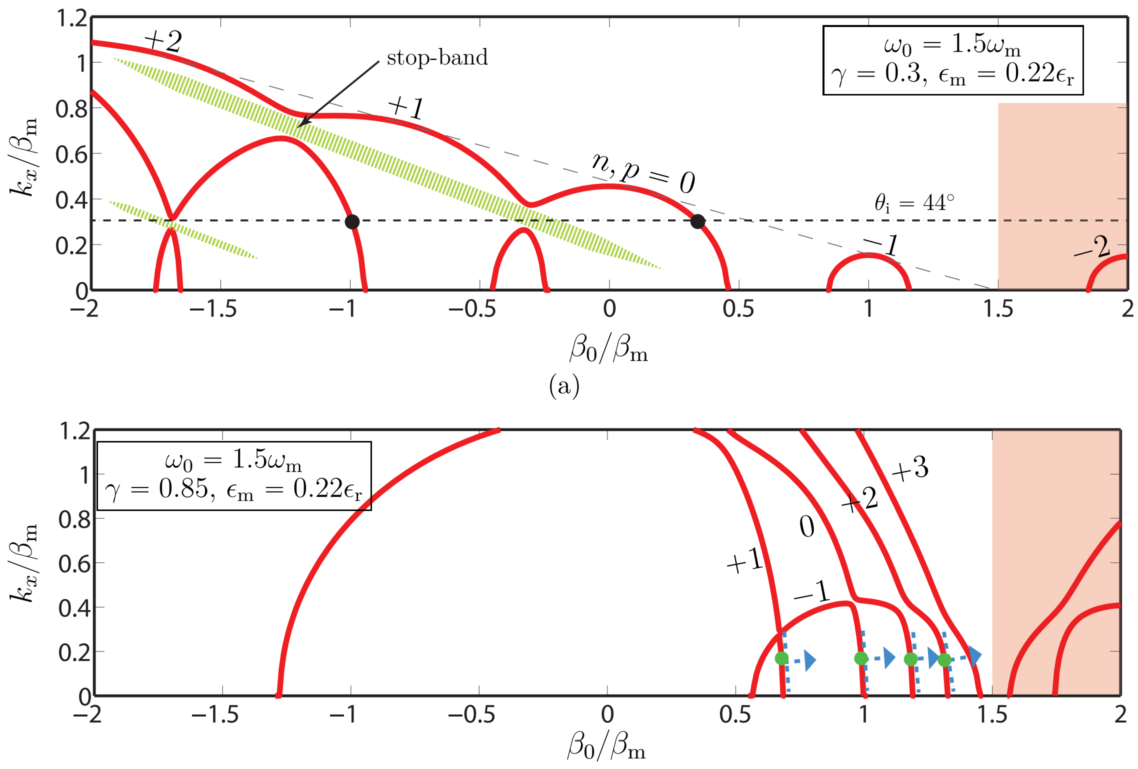

(a)

(b)

Figure 5.7 Isofrequency diagrams for the unbounded sinusoidally space-time modulated medium (5.22), computed using (5.15) with (5.14) and (5.23). (a) Space-time modulated medium with space-time modulation depth $\epsilon_\mathrm{m} = 0.22\epsilon_\mathrm{r}$ and for $\omega_0 = 1.5\omega_\mathrm{m}$ and $\gamma = 0.15$. (b) Same as (a) but in the quasi-sonic regime with $\gamma = 0.85$ ($\gamma_\mathrm{s,min} = 0.905$) [7].

5.3.2 Nonreciprocal Scattering from the Slab

This section studies the nonreciprocity of the space-time modulated system in Fig. 5.1. The structure is analyzed with the analytical technique presented in Sec. 5.2 and verified using full-wave finite difference frequency domain (FDTD) simulations.

First consider the forward problem in Fig. 5.1. A wave is normally incident on the slab with sinusoidal permittivity (5.22) and operated in the quasi-sonic regime with velocity ratio $\gamma = 0.85$ ($\gamma_\mathrm{s,min} = 0.867$). Figure 5.8(a) shows the FDTD response for the amplitude of the electric field. The wave strongly interacts with the medium as it passes through the slab and generates all the space-time harmonics. The corresponding temporal frequency spectrum for the transmitted wave is plotted in Fig. 5.9(a). The incident power at ω_0 is effectively converted in the space-time harmonics $\omega_0 \pm n\omega_\mathrm{m}$, $n \geqslant 1$, yielding a transmitted wave carrying weak power at the incident frequency ω_0.

Next, consider the backward problem. Figure 5.8(b) shows the FDTD response for the amplitude of the electric field. The wave weakly interacts with the medium as it passes through the slab and remains almost unaltered. The corresponding temporal-frequency spectrum, plotted in Fig. 5.9(a), confirms this fact. The two weak harmonics at $\omega_0 + \omega_\mathrm{m}$ and $\omega_0 - \omega_\mathrm{m}$ are due to local impedance mismatch [Eq. (5.29b)] in the medium.

The space-time medium affects forward and backward waves differently, producing strong harmonics in the forward problem and almost no harmonics in the backward problem. This nonreciprocity is exploited in Sec. 6.1 for realizing of a quasi-sonic isolator. It should be noted that both in the forward and backward problems the incident wave couples to an infinite number space-time harmonics. However, in the backward problem this coupling is extremely weak.

Figures 5.10(a) and 5.10(b) plot temporal frequency spectrum of the reflected wave, for the same parameters as in Fig. 5.9, for forward and backward excitations, respectively. In both cases the structure is well matched and reflects weakly. The reflection level is directly proportional to the modulation depth.

5.3.3 Effect of the Velocity Ratio

This section investigates the effect of the velocity ratio on the power conversion efficiency of the space-time modulated slab, i.e. the amount of power that is transmitted to desired space-time harmonics $\omega_0 \pm n\omega_\mathrm{m}$, $n \geqslant 1$. Figure 5.11 shows the distribution of the transmitted power in different harmonics versus the velocity ratio γ. The highlighted region represents the sonic regime. In the subsonic regime, where $\gamma \rightarrow 0$, little energy is transferred to harmonics. As γ approaches the sonic regime, power conversion efficiency is increased. In the quasi-sonic and sonic regimes most of the power is transferred to other harmonics with only a small amount of power remaining in the fundamental ($n = 0$).

In the quasi-sonic and sonic regimes, the total wave power grows quasi-exponentially as the wave propagates along the space-time modulated section. Figure. 5.12 compares the wave amplitudes in subsonic and quasi-sonic regimes for $\gamma = 0.3$ and $\gamma = 0.85$, respectively, versus the position. In the subsonic regime the wave and the modulation are not synchronized and there is only weak coupling between the two. As a result the wave magnitude is almost flat. In contrast, in the quasi-sonic and sonic regimes the wave and modulation velocities are synchronized. Consequently, the two are strongly coupled and the wave amplitude grows quasi-exponentially along the space-time modulated slab. This observation is not at odds with power conservation, as energy is pumped into the system through space-time modulation. However, this exponential growth can not be efficiently used for wave amplification, since

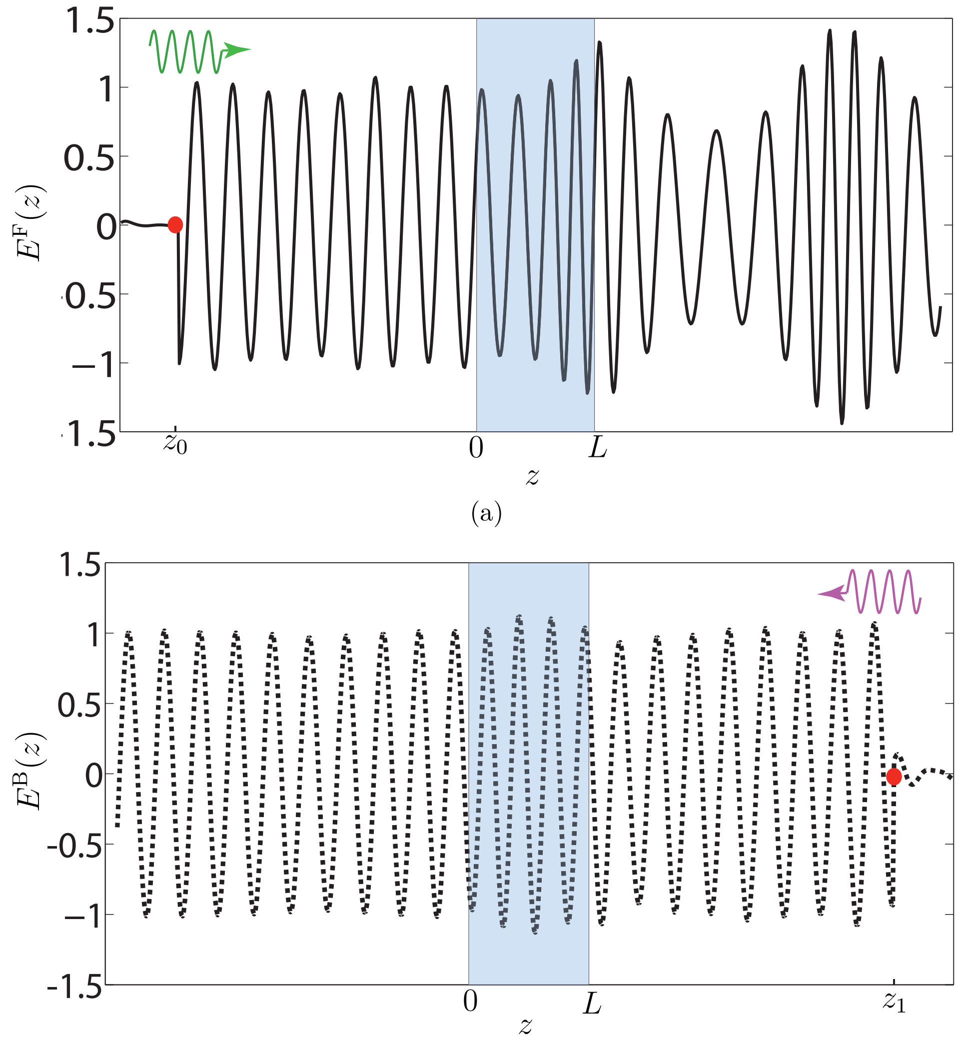

(a)

(b)

Figure 5.8 Analytical [Eqs. (5.18b) and (5.19b)] and numerical (FDTD) results for the forward and backward problems in the quasi-sonic regime with parameters $\epsilon_{\mathrm{m}} = 0.3\epsilon_{\mathrm{r}}$, $\omega_0 = 2\pi \times 1.5$ GHz, $\omega_{\mathrm{m}} = 2\pi \times 0.2$ GHz, $L = 3\lambda_0$ and $\gamma = 0.85$. FDTD waveforms showing the electric field amplitude for the forward and backward problems, respectively [7].

power is distributed among infinite space-time harmonics, as seen in the temporal frequency spectrum in Fig. 5.12(b).

5.3.4 Effect of the Length

Figure 5.13 plots the magnitude of first harmonics with respect to the length of the space-time modulated slab. The structure operates in the middle of the sonic regime, i.e. $\gamma = 1$. As the length of the slab is increased, the input power is more efficiently coupled to the space-

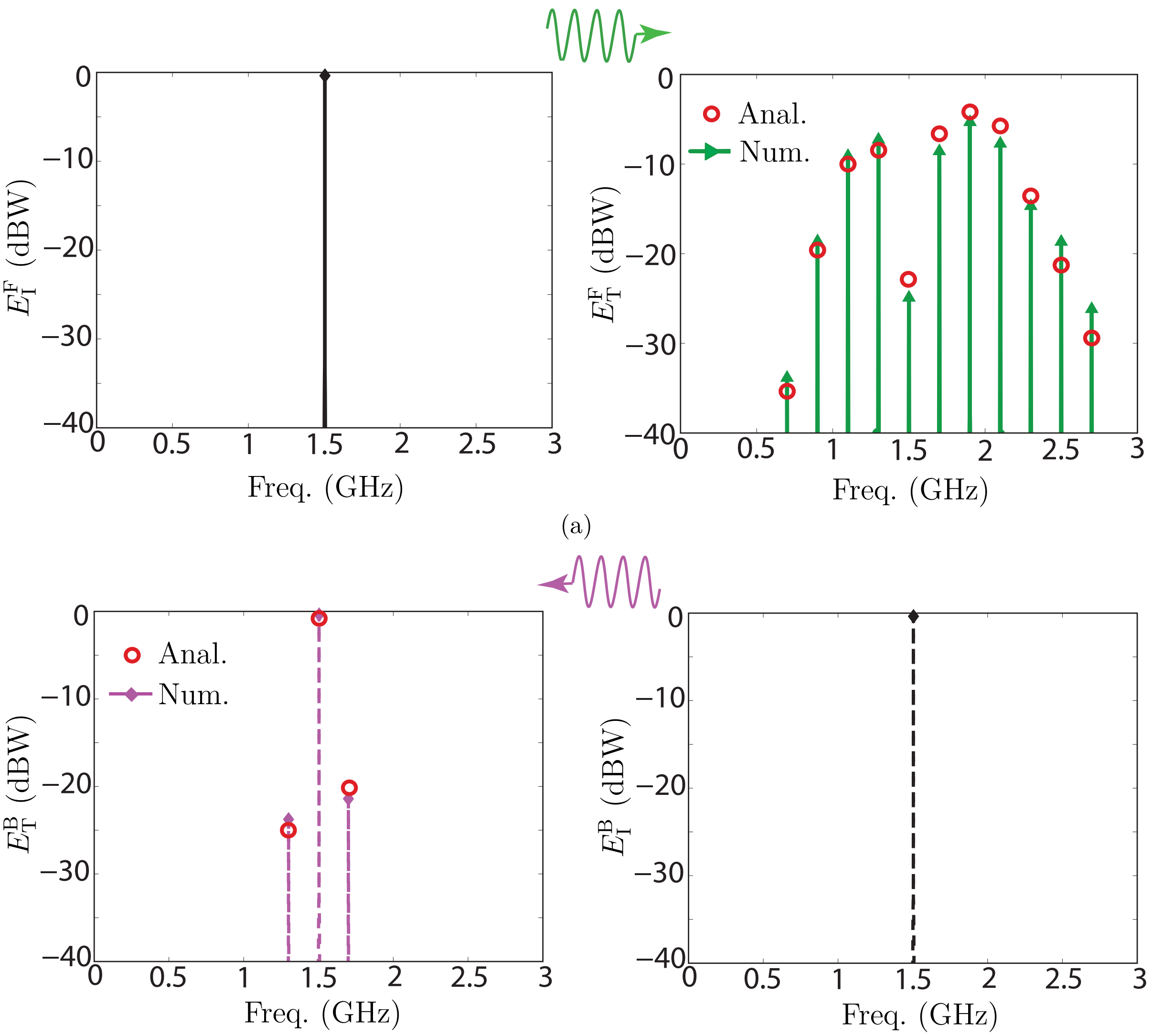

(a)

(b)

Figure 5.9 Analytical [Eqs. (5.18b) and (5.19b)] and numerical (FDTD) results for the forward and backward problems in the quasi-sonic regime with parameters $\epsilon_{\mathrm{m}} = 0.3\epsilon_{\mathrm{r}}$, $\omega_0 = 2\pi \times 1.5$ GHz, $\omega_{\mathrm{m}} = 2\pi \times 0.2$ GHz, $L = 3\lambda_0$ and $\gamma = 0.85$. Temporal frequency spectrum of the transmitted field for the forward and backward problems, respectively [7].

time harmonics $\omega_0 \pm n\omega_{\mathrm{m}}$, $n \geqslant 1$. The incident wave gradually couples its energy to these harmonics as it propagates along the slab. Therefore, a longer slab exhibits more efficient power conversion. However, this effect saturates at some point as the power in these higher order modes couples back and transfers its energy back to the fundamental mode. Therefore, power conversion efficiency shows a quasi-periodic behavior with respect to the length of the slab.

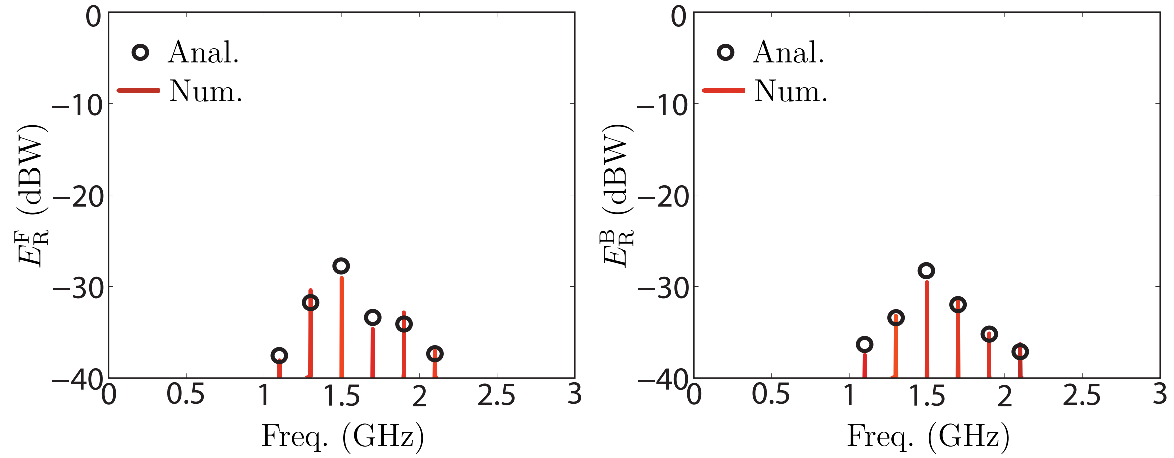

(a) (b)

Figure 5.10 Temporal frequency spectrum of the reflected field from a space-time modulated slab with the same parameters as in Fig. 5.9. (a) Forward problem, $E_{\mathrm{R}}^{\mathrm{F}}$. (b) Backward problem, $E_{\mathrm{R}}^{\mathrm{B}}$ [7].

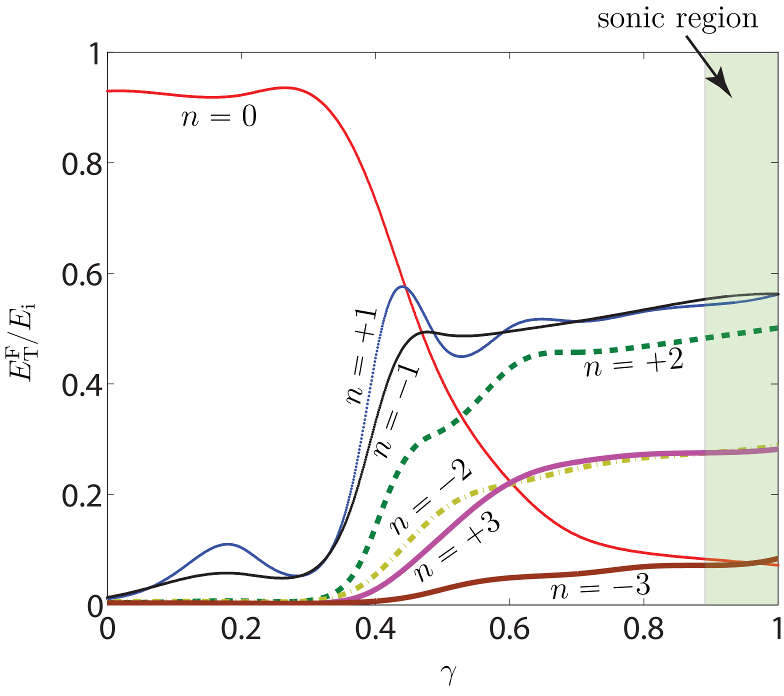

Figure 5.11 FDTD (FFT) transmitted field versus velocity ratio (γ) showing the harmonics distribution for a space-time slab with parameters $\epsilon_{\mathrm{m}} = 0.22\epsilon_{\mathrm{r}}$ ($\gamma_{\mathrm{s,min}} = 0.905$), $\omega_{\mathrm{m}} = 2\pi \times 0.2$ GHz, $\omega_0 = 2\pi \times 1.5$ GHz and $L = 3.5\lambda_0$ [7].

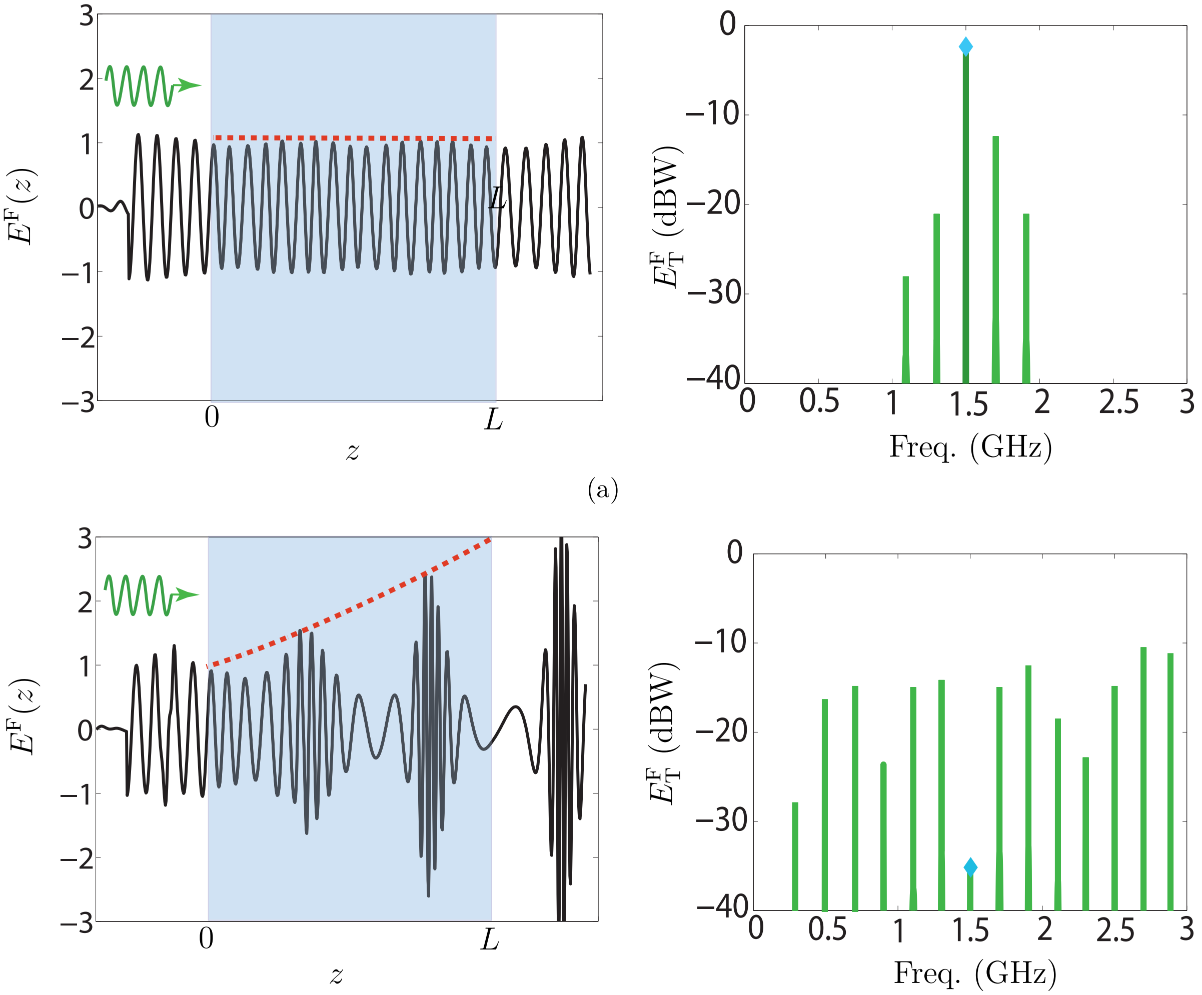

(a)

(b)

Figure 5.12 FDTD comparison of the rate of power growth (forward problem) in subsonic and quasi-sonic regimes for (a) The subsonic space-time velocity ratio $\gamma = 0.3$ and (b) The quasi-sonic space-time velocity ratio $\gamma = 0.85$ ($\gamma_{\mathrm{s,min}} = 0.905$), where $\epsilon_{\mathrm{m}} = 0.22\epsilon_{\mathrm{r}}$, $\omega_{\mathrm{m}} = 2\pi \times 0.2$ GHz, $\omega_0 = 2\pi \times 1.5$ GHz and $L = 15\lambda_0$ [7].

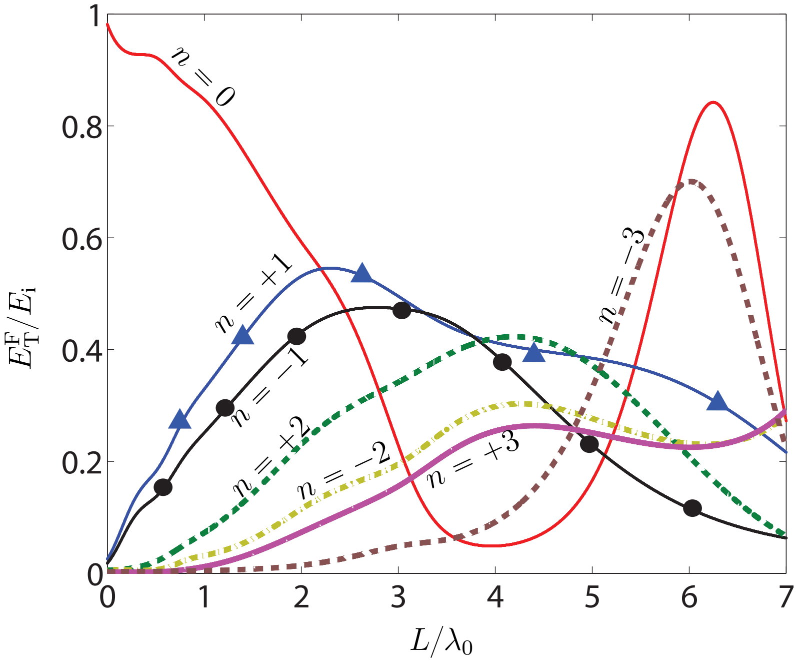

Figure 5.13 Magnitude of different harmonics versus the length of the space-time slab (FDTD). The slab operates in the middle of sonic regime with parameters $\epsilon_{\mathrm{m}} = 0.22\epsilon_{\mathrm{r}}$, $\omega_{\mathrm{m}} = 2\pi \times 0.2$ GHz, $\omega_0 = 2\pi \times 1.5$ GHz [7].

CHAPTER 6 PERIODIC SPACE-TIME MODULATED ISOLATORS

Isolators are key elements in radar, optical and communication systems and are used to reduce the reflection from antennas and minimize the standing waves seen by the sources. Isolators based on ferrimagnetic materials are widely employed for nonreciprocal purposes, such as for instance isolators based on yttrium–iron–garnet (YIG), ferrite-based gyromagnetic [112, 191, 192] or semiconductor-based gyroelectric [193, 194]. On the other hand, active, transistors-based, isolators may have been also used for the isolation in the microwave regime [120, 121, 125, 195, 196], and the isolators based on nonlinear materials have found various applications in optical systems [115, 116, 127–129].

Ferrite isolators are endowed with high power-handling capability, high isolation and no dc power consumption. However, they suffer from the bulkiness, heaviness, incompatibility with integrated circuits and high cost [124]. Active, transistor-based, isolators may overcome these shortcomings [125, 196], but they endure restricted power handling and noise by the transistors, sensitivity to reflected wave, and harmonic generation due to the nonlinearity. Moreover, these isolators may present the isolation in the cost of the passing-way gain, which may not be always desired [126]. Isolation based on nonlinearity suffers for requiring high signal levels, while in the presence of a high-level input signals in a nonlinear optical isolator, some low-level signals reciprocally pass through the isolator, and hence it does not really operate as an optical isolator [130].

Over the past few years, space-time modulated nonreciprocal devices have been reported for microwave and optical isolations [7, 8, 19, 29, 82]. Such a nonreciprocal device operates based on the nonreciprocal frequency generations which may be used for realization of integrated devices [118]. However, all reported space-time modulated isolators suffer from strong waste of energy due to the generation of unwanted space-time harmonics [7, 19].

This chapter presents three magnet-less space-time modulated isolators based on different techniques. We take advantage of the unique and intriguing features of the space-time modulation and realize three isolators for different applications. Section 6.1 introduces an efficient quasi-sonic isolator based on the properties of space-time modulated slab in the sonic region. This isolator presents a fairly high isolation, with a short length, which makes it a good candidate for isolation in microwave and milimeter wave regimes. Next, Sec. 6.2 leverages the electromagnetic band-gaps in a space-time modulated medium and presents an isolator, which is more suitable for optical regime. Finally, Sec. 6.3 introduces a self-biased and broadband isolator with high efficiency based on the nonreciprocal electromagnetic coherency in a space-time modulated medium.

6.1 Quasi-Sonic Isolator

This section has been largely taken from author's published article [7].

This section exploits the strong nonreciprocity of the quasi-sonic and sonic regimes for the realization of an electromagnetic isolator. The principle of operation of the proposed isolator is illustrated in Figs. 7.2 and 6.2. A space-time slab is operated in the quasi-sonic or sonic regime. The length and modulation ratio are adjusted such that in the forward direction the incident power is efficiently converted to higher order space-time harmonics $\omega_0 \pm \omega_\mathrm{m}$, $n \geqslant 1$, little energy is transmitted at the fundamental frequency ω_0. In contrast, in the backward direction the space-time slab interacts weakly with the incident wave and therefore the incident wave passes through almost unaltered. If the transmitted wave is passed through a bandpass filter with bandpass frequency ω_0, as in Fig. 6.2, in the forward direction most of the power is in the stopband and is therefore dissipated or reflected by the filter. However, in the backward direction most of the power is at fundamental frequency ω_0 and passes through. Thus, the structure operates as an isolator.

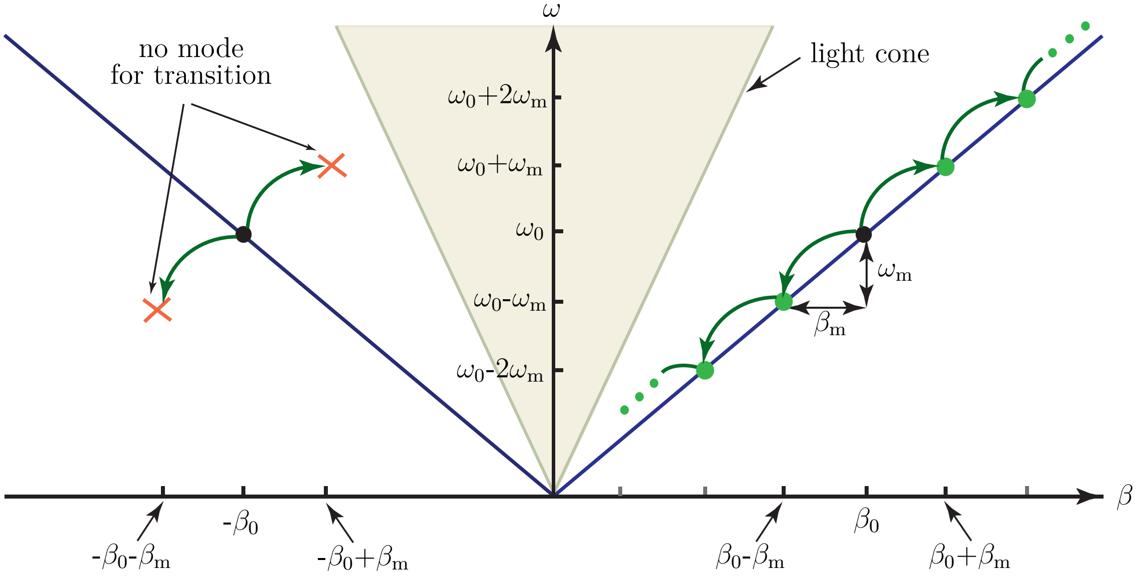

Figure 6.1 A space-time modulated slab operated in the quasi-sonic or sonic regime. In the forward direction the incident energy is transferred in cascade to space-time harmonics. In the backward direction the wave passes through with little interaction [7].

We realized the space-time modulated slab with permittivity (5.22) using a microstrip transmission line loaded with an an array of sub-wavelengthly spaced varactors. The fabricated

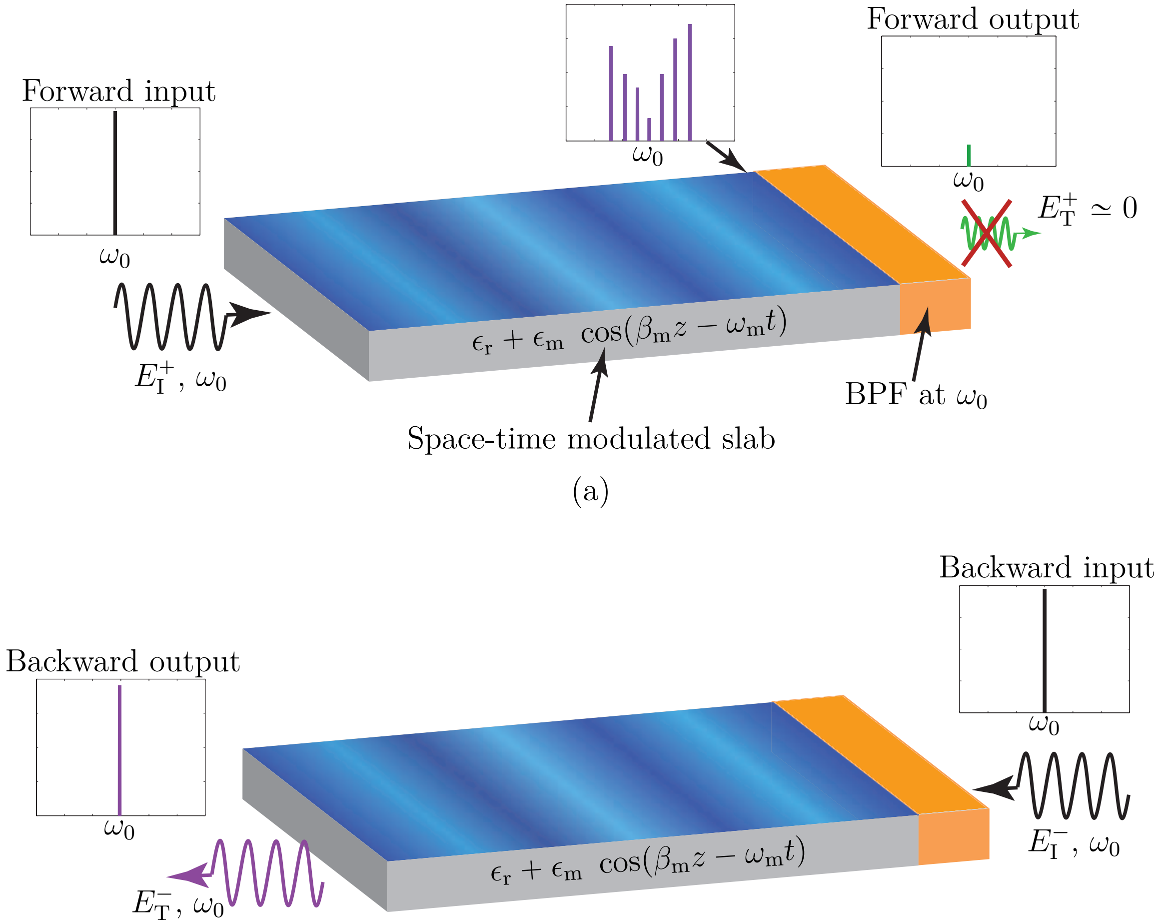

(a)

(b)

Figure 6.2 Quasi-sonic isolator. The quasi-sonic or sonic space-time modulated slab in Fig. 7.2 is connected to a bandpass filter. (a) In the forward direction, the incident power is converted to higher order harmonics and eliminated by the band-pass filter (BPF). (b) In the backward direction, the wave passes through the system [7].

prototype is shown in Fig. 6.3. We employed SMV1247 varactors manufactured by Skyworks Solutions with capacitance ratio $C_{\mathrm{max}}/C_{\mathrm{min}} = 10$. The specifications of the structure are $L = 11.7$ cm, RT6010 substrate with permittivity 10.2, thickness $h = 100$ mil and $\tan\delta = 0.0023$. We consider $\epsilon_{\mathrm{m}} = 0.22\epsilon_{\mathrm{r}}$, $\omega_0 = 2\pi \times 1.5$ GHz, $\omega_{\mathrm{m}} = 2\pi \times 0.2$ GHz, $\beta_{\mathrm{m}} = 3.55\pi$ m^{-1}, $L = 3.5\lambda_0$ and $\gamma \rightarrow 1$. The modulation circuit is composed of 39 unit cells of antiparallel varactors with uniform spacing of $p = 5$ mm, which corresponds to $p/\lambda_{\mathrm{s}} = p\beta_{\mathrm{m}}/(2\pi) \approx 1/11.3$, and therefore safely satisfies medium homogeneity in accordance with (6.3). The varactors are reversed biased by a DC voltage and are spatio-temporally modulated by an RF bias, realizing the space-time varying capacitance $C(z,t) = C_{\mathrm{av}} + C_{\mathrm{m}}\ \cos(\beta_{\mathrm{m}} z - \omega_{\mathrm{m}} t)$. This circuit emulates a medium with effective permittivity $\epsilon(z,t) = \epsilon_{\mathrm{av}} + \epsilon_{\mathrm{m}}\ \cos(\beta_{\mathrm{m}} z - \omega_{\mathrm{m}} t)$, with $\epsilon_{\mathrm{av}} = \epsilon_{\mathrm{ef}} + \epsilon_{\mathrm{av,var}}$, where ϵ_{ef} is the effective permittivity of the microstrip line and $\epsilon_{\mathrm{av,var}}$ is the average permittivity introduced by the varactors. The modulation depth is controlled through the amplitude of the RF bias.

Figures 6.4(a), 6.4(b) and 6.5 show the measurement results for the transmitted and reflected electroc fields for the forward and backward problems. The space-time varying microstip circuit was connected to a bandpass filter, and forward and backward transmission and reflection coefficients were measured. In the forward direction, corresponding to Fig. 6.4(a), the transmission level is less than −20 dB at the fundamental harmonic, and less than −30 dB in other spacetime harmonics. Figure 6.5(a) shows that the power injected into the higher order harmonics $\omega_0 \pm n\omega_{\mathrm{m}}$ is reflected by the bandpass filter. In the backward direction, shown in Fig. 6.4(b), the incident wave is almost fully transmitted at the fundamental frequency, with less than −30 dB reflection. Thus, the structure realizes an isolator with more than 20 dB isolation.

6.2 Isolator Based on Space-Time Engineered Asymmetric Electromagnetic Band-Gaps

6.2.1 Operation Principle

This section presents the idea which was proposed by my colleague, Dr. Nima Chamanara, and I carried out the experimental demonstration of it. This section has been largely taken from author's published article [8].

This section introduces a new concept for the realization of electromagnetic isolation based on the space-time engineered asymmetric electromagnetic band-gaps [8]. This approach leverages the space-time variation in the permittivity of a medium to generate electromagnetic band structures that are asymmetrically aligned with respect to the direction of propagation, as

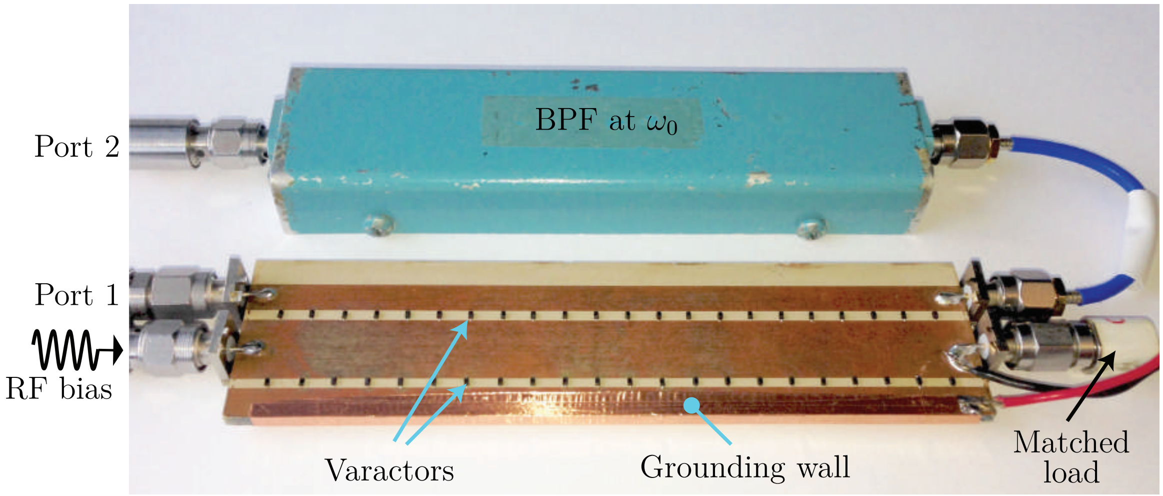

Figure 6.3 Photograph of the fabricated isolator, employing SMV1247 varactors manufactured by Skyworks Solutions with capacitance ratio $C_{\max}/C_{\min} = 10$. The specifications of the structure are $L = 11.7$ cm, RT6010 substrate with permittivity 10.2, thickness $h = 100$ mil and $\tan\delta = 0.0023$ [7].

it is previously shown in in Figs. 5.4 and 5.5. Figure 6.6 shows that the band-gap edges in a space-time modulated medium are different for the positive and negative propagating waves. When the structure is excited from the left, i.e. the forward problem, at the frequency corresponding to the horizontal line, the evanescent mode, marked by the red dot, is excited. If the structure is long enough, almost no power reaches the opposite end of it and the wave is fully reflected. In contrast, when the structure is excited from the right, the mode marked by the blue dot in Fig. 6.6, i.e. a propagating mode, is excited. Therefore, the incident electromagnetic power is transferred to the other side of the structure, and, assuming proper matching, is fully transmitted across it.

With proper excitation, such a system may operate as a nonreciprocal electromagnetic device, i.e. an isolator. In contrast to the optical isolation in [19], we employ a uniform modulation in the cross section of the waveguide, which leads to a much simpler structure. In addition, the required modulation frequency is relatively low, and may thus be conveniently provided by acoustic waves. The proposed approach may find applications in various integrated magnetless nonreciprocal optical systems. An experimental proof-of-concept at microwave frequencies is presented. In a conventional reciprocal medium supporting the electromagnetic band-gaps, e.g. a Bragg grating or a waveguide filter, the band-gaps are perfectly horizontal in the dispersion diagram, i.e. symmetric with respect to positive and negative Bloch-Floquet wavenumbers. In the band-gaps, the Bloch-Floquet harmonics acquire an imaginary part in

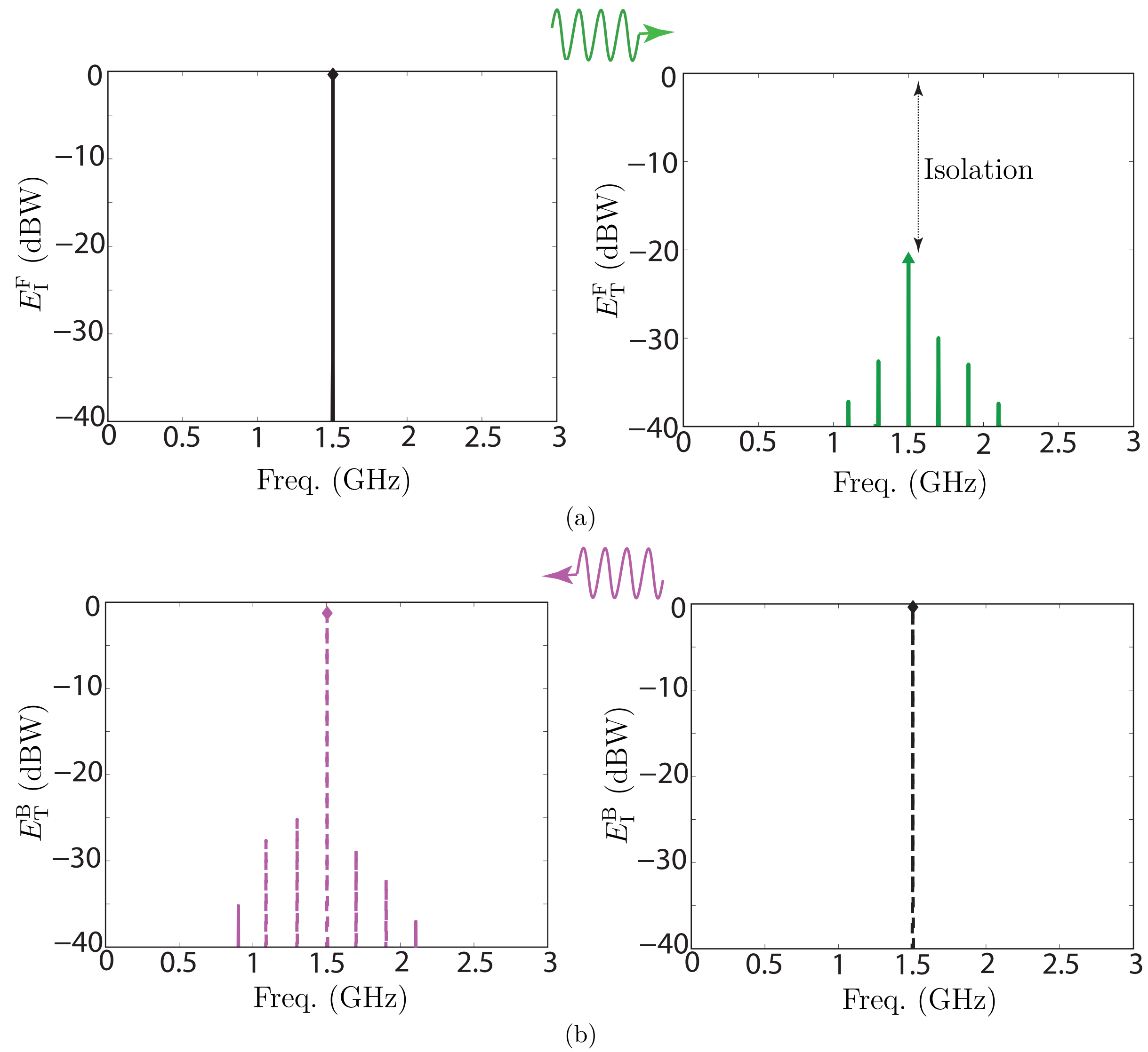

(a)

(b)

Figure 6.4 Experimental results for the isolator in Figs. 6.2 and 6.3 with $\epsilon_{\mathrm{m}} = 0.22\epsilon_{\mathrm{r}}$, $\omega_0 = 2\pi \times 1.5$ GHz, $\omega_{\mathrm{m}} = 2\pi \times 0.2$ GHz, $L = 3.5\lambda_0$ and $\gamma \to 1$. (a) Forward problem. (b) Backward problem [7].

their wavenumber and hence become evanescent. Thus, when a wave incident on the structure is modulated at a frequency falling within a gap, it excites a complex, and hence evanescent, gap mode. Now, consider the structure in Fig. 6.7 with an oblique, and hence asymmetric band-gap.

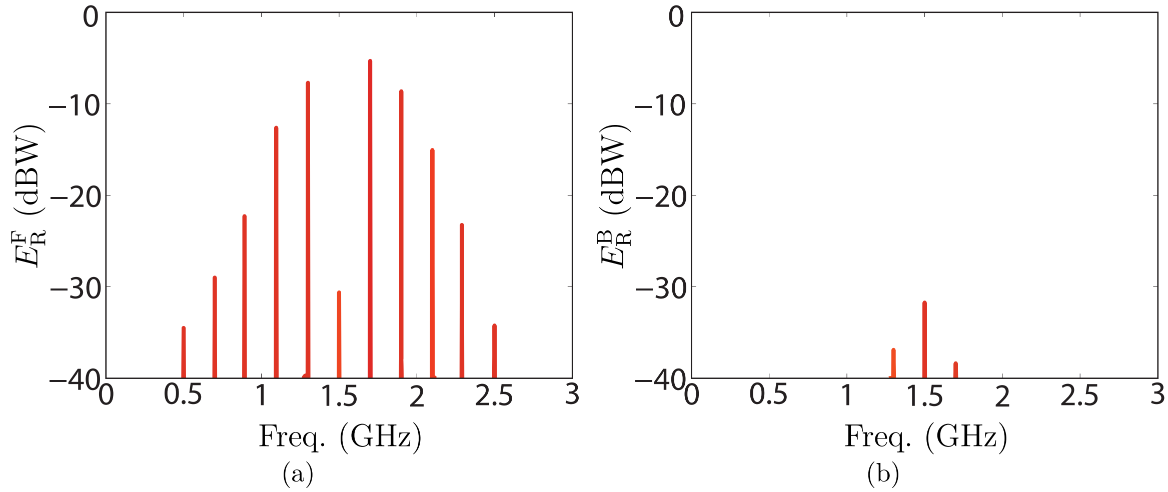

Figure 6.5 Measured reflections from the isolator slab in Figs. 6.2 and 6.3 with the same parameters as in Fig. 6.4. (a) Forward problem. (b) Backward problem [7].

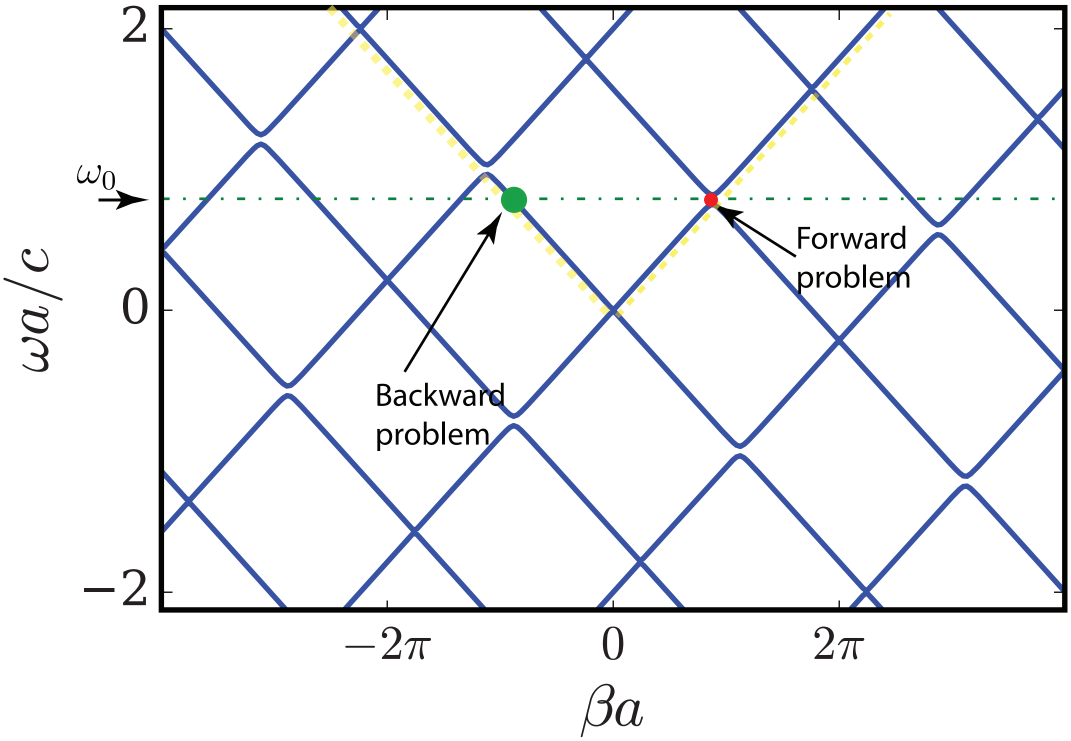

Figure 6.6 Dispersion diagram of a periodic space-time modulated medium with the asymmetric band-gap structure in Fig. 6.7. The red and blue dots represent the dominantly excited mode for forward and backward excitations, respectively [8].

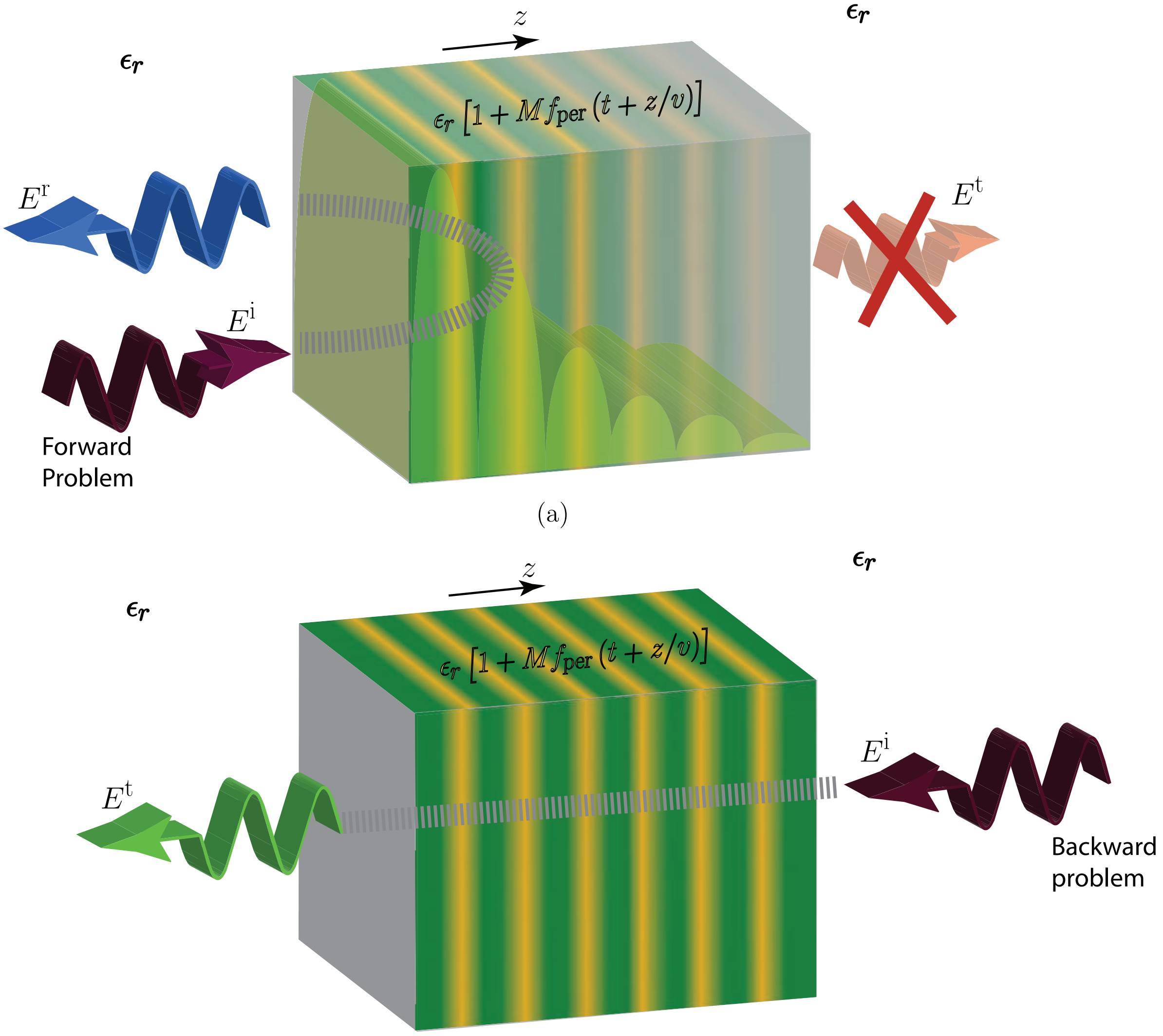

(a)

(b)

Figure 6.7 Isolator based on nonreciprocal Bragg reflections in a space-time modulated medium with asymmetric electromagnetic band-gaps. (a) Forward problem : propagation of wave in the electromagnetic band-gap of the structure yields complete-reflection. (b) Backward problem : propagation of wave in the pass-band of the structure leads to full-transmission.

6.2.2 Forward and Backward Problems

Consider a space-time modulated slab with space-time permittivity (5.22), background permittivity $\epsilon_r = 12.25$, modulation depth $M = \epsilon_{\text{m}}/\epsilon_{\text{r}} = 0.02$, temporal and spatial modulation frequencies $\omega_{\text{m}} = 0.13\omega_0$ and $\beta_{\text{m}} = -2.27\beta_0$, respectively, and length $L = 200\lambda_{\text{g}}$, excited at the normalized frequency $\omega_0 = 0.259c/a$, where a is the spatial period of the space-time modulated slab. The corresponding permittivity profile represents a sinusoidal Bragg grating, whose permittivity perturbation propagates towards the left inside the space-time modulated region, with velocity $v_\mathrm{m} = -|\omega_\mathrm{m}/\beta_\mathrm{m}|$.

Fig. 6.6 shows that mode $p = 0$ falls in a band-gap of the modulated structure. It is thus evanescent and exponentially decaying in the modulated structure, carrying almost no power to its right end. Since the system is assumed to be lossless, the incident power can only be reflected towards to input medium. This is confirmed in Fig. 6.8(a), which plots the transmitted and reflected amplitudes for different temporal frequency harmonics. The transmission level is below -40 dB for all frequency harmonics, and the power is almost fully reflected at the blue-shifted frequency $\omega_0 + \omega_\mathrm{m}$. This is a space-time blue Doppler shift due to the fact that the space-time varying medium profile has an opposite (negative) phase velocity, $v_\mathrm{m} = \omega_\mathrm{m}/\beta_\mathrm{m}$, with respect to the source on the left.

The levels of the transmitted and reflected power may be controlled by tuning the modulation depth and the length of the slab. For a given modulation depth, it is always possible to reduce the transmitted power to a desired level by increasing the length of the slab. Notice that the reflected power is slightly greater than unity. This is not at odds with energy conservation since energy is pumped into the space-time varying medium.

For the backward problem, the amplitudes of the harmonics are plotted in Fig. 6.8(b). Almost all the power is transmitted at the incident frequency, and the reflected power from the slab is below -40 dB for all the harmonics. The amount of reflected power is proportional to the mismatch between the space-time modulated and incident media, which is in turn proportional to the modulation depth.

The frequency shift may also be explained in terms of intraband electromagnetic transitions between the forward and backward propagating modes of a single-mode waveguide. For small modulation depth ($M \ll 1$), instead of considering the exact periodic problem involving the infinite set of space-time harmonics, the problem may be approximated as follows. As an electromagnetic wave with momentum and frequency (β_0, ω_0) in the background medium penetrates into the space-time modulated section, the space-time medium provides the extra momentum and energy corresponding to $\pm(\beta_\mathrm{m}, \omega_\mathrm{m})$ to the wave. If the resulting momentum and energy $(\beta_0 \pm \beta_\mathrm{m}, \omega_0 \pm \omega_\mathrm{m})$ correspond to a mode of the waveguide, coupling to this mode occurs and the incoming waveguide mode is then gradually transformed into the waveguide mode at $(\beta_0 \pm \beta_\mathrm{m}, \omega_0 \pm \omega_\mathrm{m})$. In contrast, if $(\beta_0 \pm \beta_\mathrm{m}, \omega_0 \pm \omega_\mathrm{m})$ does not correspond to a mode of the waveguide, the corresponding wave passes through the space-time modulated region almost unaffected. This interband transition picture and the associated coupled mode analysis are accurate only for very small modulation depths, and should therefore be considered with great care in the case of strong modulations, as it ignores the rich spectral features of

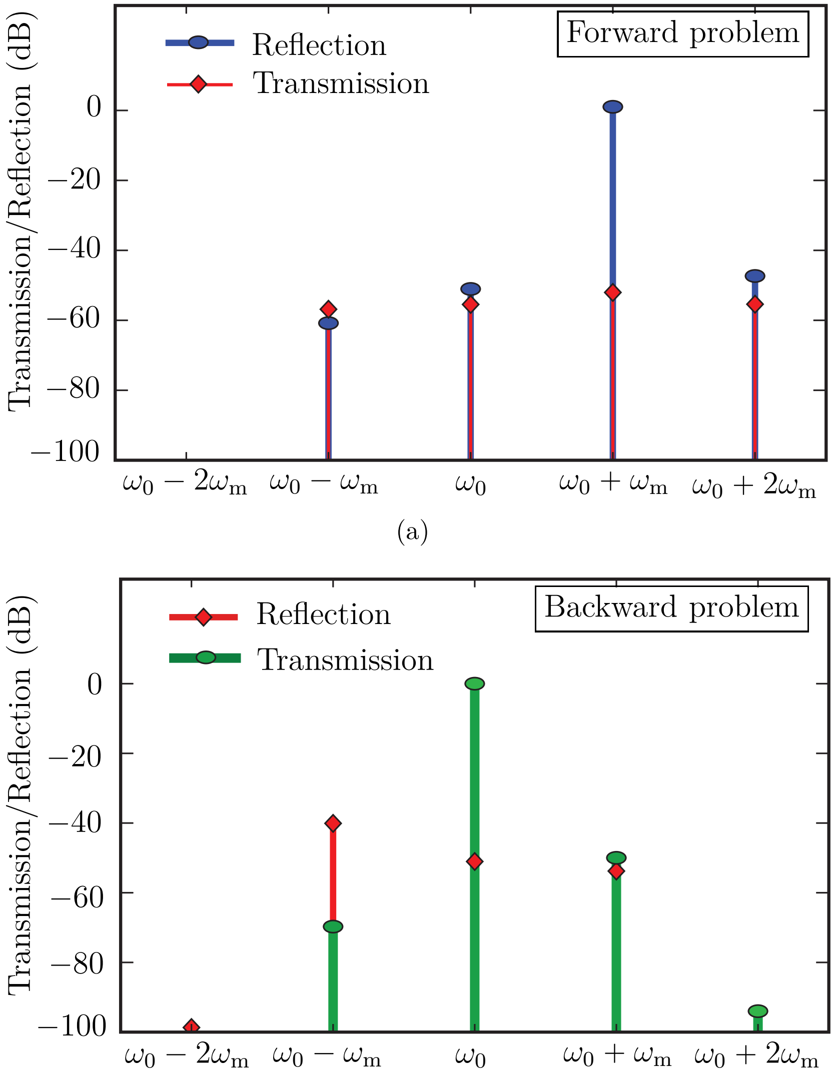

(a)

(b)

Figure 6.8 Experimental results for the reflection and transmission (outside the modulated slab) for the space-time modulated slab with the same parameters as in Fig. 6.6. (a) Slab excited from the left. The dominantly excited evanescent gap mode decays exponentially and conveys no power to the transmitted region. All of the power is reflected. The reflected wave is blue-shifted. (b) Slab excited from the right. The dominantly excited propagating mode transfers all its energy to the other end. Almost all the power is transmitted at the fundamental frequency (ω_0) [8].

the electromagnetic band structure of the space-time modulated system. Nonetheless, this explanation provides an alternative intuitive understanding of the Doppler frequency shift described above.

For the space-time modulated problem, the dispersion curves of the single mode background medium and the corresponding momentum and energy, $\pm(\beta_\mathrm{m}, \omega_\mathrm{m})$, provided by the space-time medium, are plotted in Fig. 6.9(a), for excitation from the left. As $(\beta_0 + \beta_\mathrm{m}, \omega_0 + \omega_\mathrm{m})$ corresponds to a backward propagating mode of the background medium, the incident forward propagating mode gradually transforms to a blue-shifted backward propagating mode, i.e. reflects with a frequency up-shift exactly equal to $\Delta\omega = \omega_\mathrm{m}$. In contrast, for a wave exciting the space-time modulated region from the right, the corresponding momentum and energy, $\pm(\beta_\mathrm{m}, \omega_\mathrm{m})$ provided by the space-time medium, is plotted in Fig. 6.9(b). As $(\beta_0 + \beta_\mathrm{m}, \omega_0 + \omega_\mathrm{m})$ does not correspond to a mode of the background medium, it passes through the space-time region almost unaffected.

6.2.3 Experimental Demonstration

The space-time modulated system was realized at microwave frequencies in the form of a space-time varying artificial microstrip transmission line shown in Fig. 6.10. In order to provide spatio-temporal control on the distributed capacitance of the transmission line, it is loaded with an array of sub-wavelengthly spaced shunt varactors. The bias line at the bottom provides a DC bias V_DC plus a propagating RF bias,

$$V(z,t) = V_\mathrm{DC} + V_\mathrm{m} \cos(\omega_\mathrm{m} t + \beta_\mathrm{m} z) \tag{6.1}$$

to the varactors, where ω_m is the modulation frequency. The bias phase velocity $v_\mathrm{m} = \omega_\mathrm{m}/\beta_\mathrm{m}$ is related to the bias line per-unit-length capacitance (C_av) and inductance (L_av) by $v_\mathrm{m} = 1/\sqrt{L_\mathrm{av} C_\mathrm{av}}$. The varactors are reverse biased and act as voltage controlled capacitors. They thus add the space-time varying distributed capacitance

$$C(z,t) = C_\mathrm{av} + C_\mathrm{m} \ \cos(\omega_\mathrm{m} t + \beta_\mathrm{m} z) \tag{6.2}$$

to the signal transmission line. The structure in Fig. 6.10 therefore emulates a material with space-time varying permittivity (5.22), with background permittivity $\epsilon_r \propto C_\mathrm{av}$ and modulation depth $M = C_\mathrm{m}/C_\mathrm{av}$.

Figure 6.10 shows a photograph of the space-time varying microstrip line. The modulation circuit is comprised of 39 unit cells of antiparallel varactors, uniformly distributed along the microstrip line, with the subwavelength period $p = 5$ mm, corresponding to $p/\lambda_\mathrm{m} \approx 1/19$. Therefore, effectively, the structure represents a medium with the continuous permittivity (5.22). The corresponding dispersion curves are plotted in Fig. 6.6, where the horizontal line represents the excitation frequency. The incident frequency is chosen to excite the evanescent

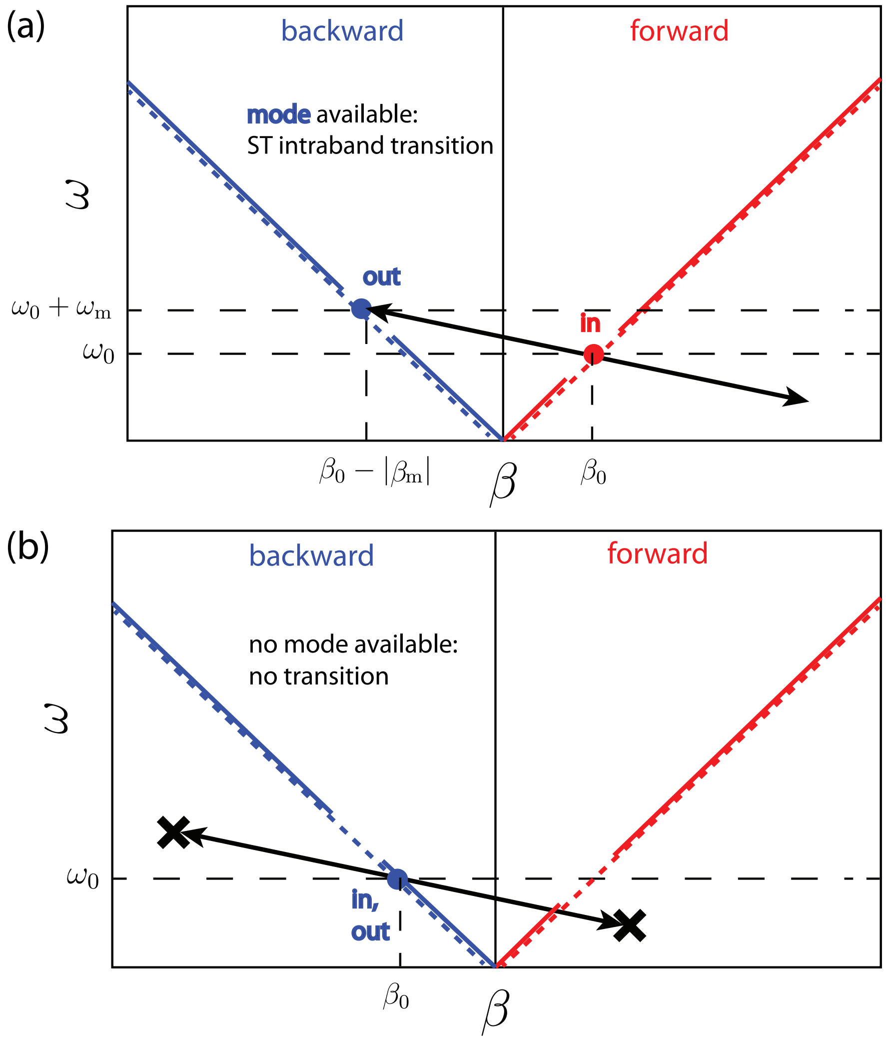

Figure 6.9 Explanation of the frequency up-shift in the reflected field in terms of intraband electromagnetic transitions. The dashed lines correspond to the dispersion curves of the background medium. The arrows represent the momentum end energy provided by the space-time modulated region, $\pm(\beta_\mathrm{m}, \omega_\mathrm{m})$. (a) Left excitation : the forward propagating mode gradually transforms into a backward propagating mode with frequency $\omega_0 + \omega_\mathrm{m}$ and is reflected. (b) Right excitation : the propagating mode passes through the space-time section as $(\beta_0 \pm \beta_\mathrm{m}, \omega_0 \pm \omega_\mathrm{m})$ does not correspond to any waveguide mode [8].

mode marked by the red dot in the forward direction and the propagating mode marked by the blue point in the backward direction. The corresponding length at this frequency is $L = 6\lambda_0$.

The scattering parameters are plotted in Figs. 6.11(a) and 6.11(b) for forward and backward excitations, respectively. The evanescent mode decays by 10.5 dB before reaching the end of

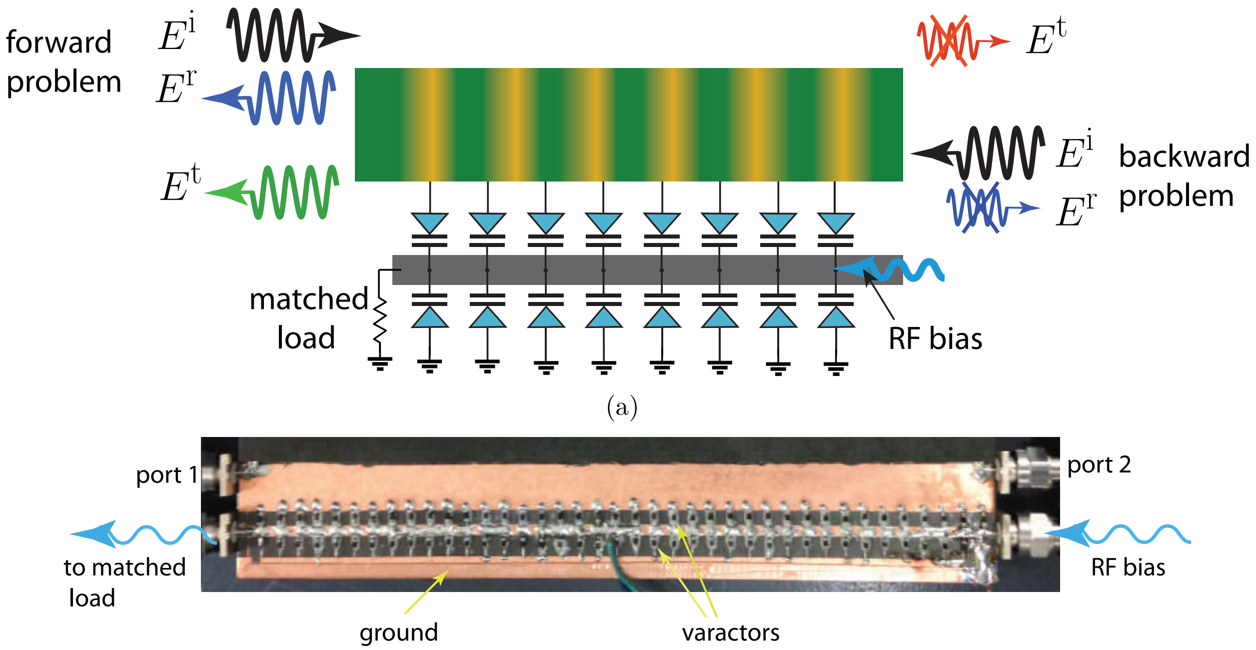

(a)

(b)

Figure 6.10 Experimental realization of the space-time varying system in the form of a space-time varying artificial microstrip transmission line. (a) Schematic of the system, with distributed-capacitance varactors modulated by a radio wave emulating (5.22). (b) Photograph of the fabricated structure. The varactors were are the BB833 from Infineon Technologies, with capacitance ratio $C_{\mathrm{max}}/C_{\mathrm{min}} = 12$. The structure is $L = 8$ inches long and is excited at $\omega_0 = 2\pi \times 2.5$ GHz. The substrate is RT6010 from Rogers with permittivity 10.2, thickness $h = 100$ mil and $\tan\delta = 0.0023$ [8].

the structure, corresponding to -10.5 dB attenuation in Fig. 6.11(a). The rest of the power is reflected at the up-shifted frequency $\omega_0 + \omega_{\mathrm{m}} = 2\pi \times 3.175$ GHz. In the backward direction the incident wave is almost fully transmitted. Therefore, the isolation level is 10.5 dB. Higher isolation levels may be achieved by increasing the length of the structure. The small discrepancy between theory and experiment are attributed to the metallic and dielectric losses in the experiment that have not been accounted for in the theory.

6.3 Self-Biased Broadband Magnet-Free Space-Time Modulated Isolator

This section introduces a new technique for isolation based on the nonreciprocal electromagnetic coherency between the input wave and space-time modulated structure. The isolator takes advantage of the input signal and operates as a self-biased nonreciprocal device. We

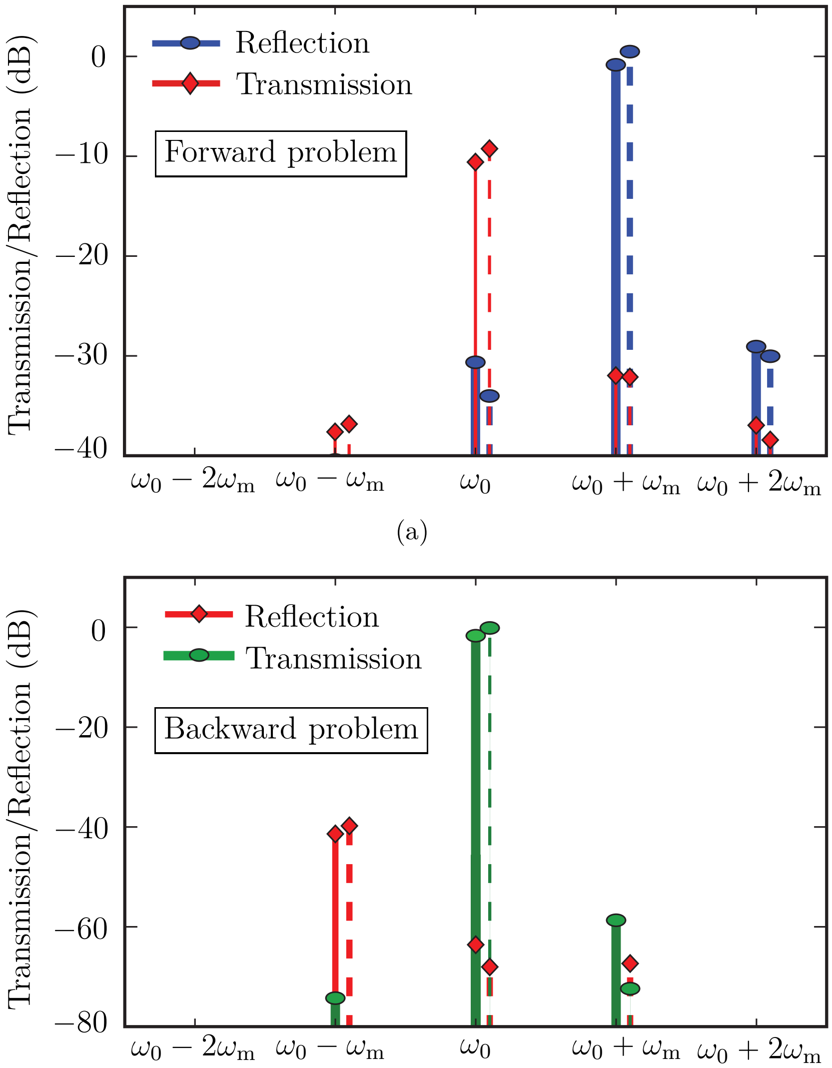

(a)

(b)

Figure 6.11 Experimental (solid lines) vs. theoretical (dashed lines) results for the isolator in Fig. 6.10 for the same parameters as in Fig. 6.6. (a) Forward problem : the wave is almost fully reflected at the blue-shifted frequency $\omega_0 + \omega_{\rm m} = 2\pi \times 3.175$ GHz with a transmission level less than -10 dB. (b) Backward problem : the backward incident wave is fully transmitted at $\omega_0 = 2\pi \times 2.5$ GHz. For clarity, the theoretical results are shifted by $0.1\omega_{\rm m}$ [8].

will experimentally demonstrate the operation of the isolator, without requiring any external bias-field, in broad frequency bandwidth. The isolator generates no space-time frequency harmonic, and hence does not suffer from the waste of energy. As a result, it presents a superior efficiency and the possibility of having gain in the passing direction which may be useful for some applications.

6.4 Operation Principle

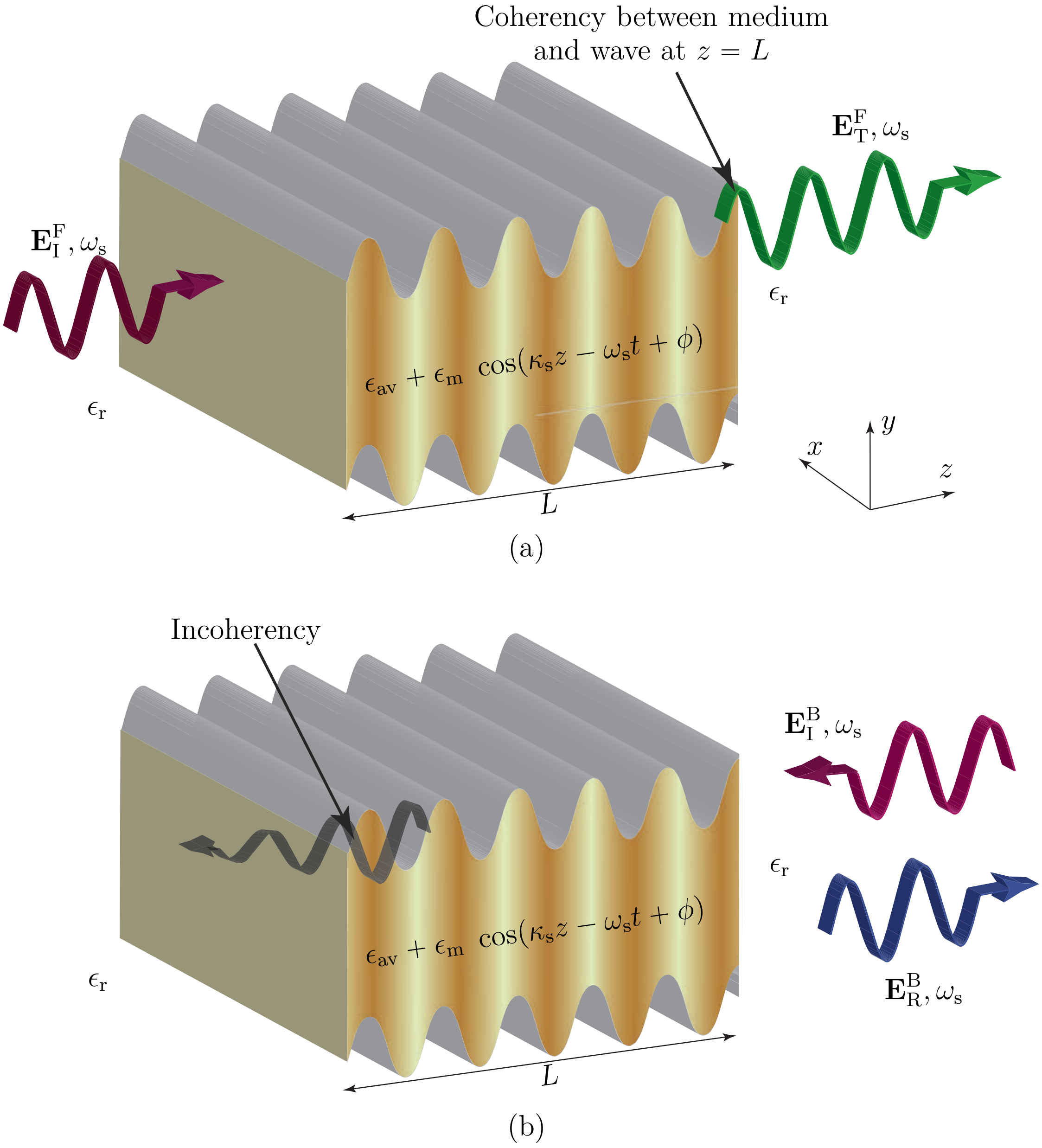

Figure 6.12 Electromagnetic isolation based on nonreciprocal coherency of the wave with a periodically space-time modulated slab. (a) Coherency between the space-time variation of the $+z$ propagating wave and the slab leads to full transmission of the wave. (b) Incoherency between the space-time variation of the $-z$ propagating wave and the slab yields complete reflection of the wave.

Figure 6.12 illustrates transmission of an electromagnetic wave, with frequency ω_s, through a space-time modulated slab with thickness L. The permittivity of the medium is space-time modulated as

$$\epsilon(z,t) = \epsilon_{\text{av}} + \epsilon_{\text{m}} \ \cos(\kappa_{\text{s}} z - \omega_{\text{s}} t + \phi), \tag{6.3}$$

where ϵ_{av} denotes the average effective permittivity of the unmodulated medium, ϵ_{m} is the modulation depth, ω_{s} and κ_{s} represent respectively the modulation temporal and spatial frequencies, and ϕ is the modulation phase. The phase velocity of the modulation is defined as $v_{\text{m}} = \omega_{\text{s}}/\kappa_{\text{s}}$, which may be smaller or greater than the phase velocity of the background medium, $v_{\text{b}} = c/\sqrt{\epsilon_{\text{r}}}$, with $c = 1/\sqrt{\mu_0 \epsilon_0}$ as the speed of light in vacuum, and ϵ_{r} being the relative permittivity. The ratio between the modulation and background phase velocities reads

$$\gamma = \frac{v_{\text{m}}}{v_{\text{b}}} = \frac{\beta_{\text{s}}}{\kappa_{\text{s}}}, \tag{6.4}$$

which is called the *space-time velocity ratio* [7].

A y polarized plane wave, $\mathbf{E}_{\text{I}}$, given by

$$\mathbf{E}_{\text{I}}(z,t) = \hat{\mathbf{y}} E_0 e^{-j(\pm\beta_{\text{s}} z - \omega_{\text{s}} t)}, \tag{6.5}$$

impinges the space-time modulated medium in the forward $(+z)$ direction or backward $(-z)$ direction on the periodically space-time modulated medium of Fig. 6.12. In (6.5), E_0 is the amplitude of the incident wave and β_{s} is the spatial frequency of the wave outside the modulated medium, where $\beta_{\text{s}} = \omega_{\text{s}}/v_r = \omega_{\text{s}} c/\sqrt{\epsilon_{\text{r}}}$. We call the problem with the incident wave propagating towards the $+z$-direction, shown in Fig. 6.12(a), as the *forward problem*, represented by the superscript "F", while the problem with the incident wave propagating towards the $-z$-direction, shown in Fig. 6.12(b), will be called the *backward problem*, represented by the superscript "B". However, the forward and backward problems both create forward and backward waves, inside and outside of the modulated slab. The temporal frequency of the incident wave, ω_{s}, and the one of the space-time modulated medium are assumed to be equal. This leads to nonreciprocal electromagnetic coherency between the wave and the medium.

To best understand the operation principle of the structure in Fig. 6.12, here we investigate effect of the modulation phase ϕ, on nonreciprocal transmission through the structure. Here, we denote the modulation phase at $z = L$ as ϕ_L, i.e.

$$\phi_L = \phi - \kappa_{\text{s}} L. \tag{6.6}$$

Considering $L = n\lambda_{\text{g}}$, the Figure 6.13 plots the closed form solution for the forward transmission versus ϕ_L for different modulation depths, where $\kappa_{\text{s}} L = \omega_{\text{s}} L/(\gamma v_{\text{b}}) = \pi$. It may be seen that the maximum forward transmission is achieved while the medium and the input wave are coherent at $z = L$, i.e. for $\phi_L = 2n\pi$ with $n = 0, 1, \ldots.$

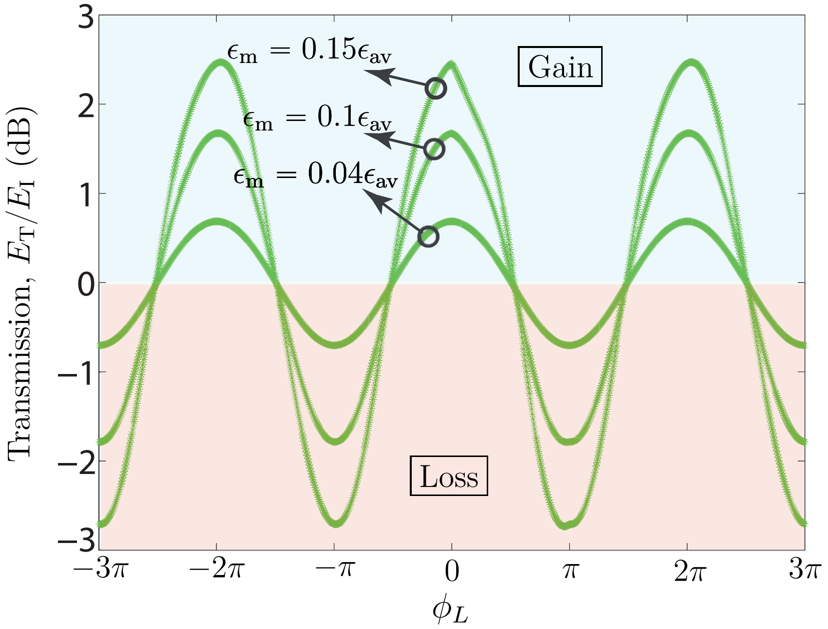

Figure 6.13 Effect of the coherency of the space-time modulated medium and the wave at $z = L$, given in (6.6), on forward transmission with $\kappa_{\mathrm{s}}L = \pi$, and for different modulation depths $\epsilon_{\mathrm{m}}/\epsilon_{\mathrm{av}}$.

For the sake of simplicity, and to best observe the nonreciprocal coherency in the closed form solutions for forward and backward problems, we assume a $+z$ propagating incident field, given in (6.5), for both forward and backward problems and consider a $+z$ traveling modulation for the forward problem $[\epsilon(z,t) = \epsilon_{\mathrm{av}} + \epsilon_{\mathrm{m}} \cos(\kappa_{\mathrm{s}}z - \omega_{\mathrm{s}}t + \phi)]$ and a $-z$ traveling modulation for the backward problems $[\epsilon(z,t) = \epsilon_{\mathrm{av}} + \epsilon_{\mathrm{m}} \cos(\kappa_{\mathrm{s}}z + \omega_{\mathrm{s}}t + \phi)]$. Figure 6.14 shows forward and backward transmission through the structure in Figs. 6.12(a) and (b), for $\epsilon_{\mathrm{m}}/\epsilon_{\mathrm{av}} = 0.15$ and $\kappa_{\mathrm{s}}L = \pi$. It may be seen from this figure that maximum isolation is achieved while the forward wave is completely coherent with the medium at $z = L$, i.e. $\phi_L^{\mathrm{F}} = 2n\pi$, and the backward wave in completely incoherent with the medium, $\phi_L^{\mathrm{B}} = (2n{+}1)\pi$.

Therefore, we may achieve an appropriate isolation between forward and backward transmissions, possibly with forward gain, using proper modulation parameters, i.e. ϕ, ϵ_{m} and $\kappa_{\mathrm{s}}L$. A complete parametric study will be presented in Sec. 6.6.

6.5 Closed-Form Field Solutions

As shown in Appendix 8.2, considering an appropriate change of variables as

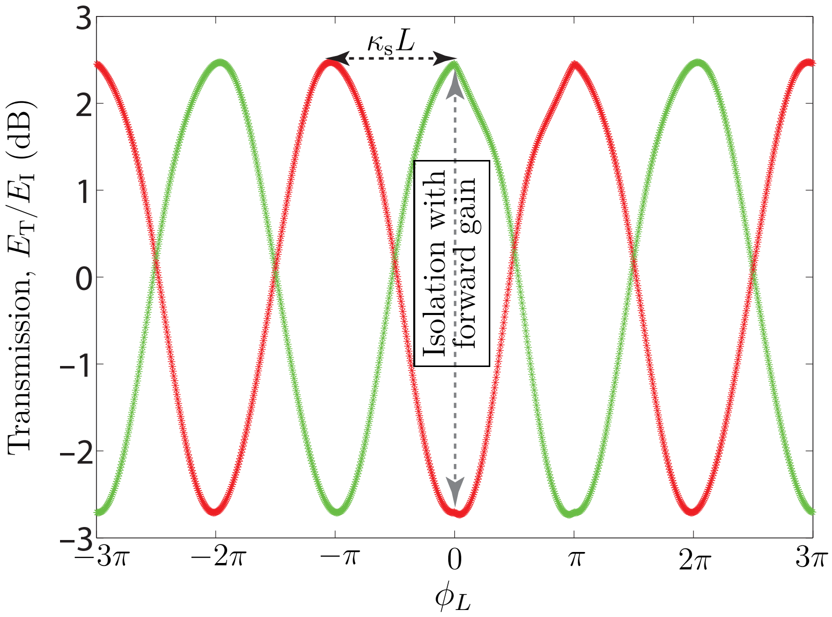

Figure 6.14 Effect of the coherency of the space-time modulated medium and the wave at $z = L$, given in (6.6), on forward and backward transmissions for $\epsilon_\mathrm{m}/\epsilon_\mathrm{av} = 0.15$, $\gamma = 1$ and $\phi_0 = \kappa_\mathrm{s}L = \pi$.

$$W = \frac{2\sqrt{2\epsilon_\mathrm{m}}\omega_\mathrm{s}}{c\kappa_\mathrm{s}}e^{j(\kappa_\mathrm{s}z-\omega_\mathrm{s}t+\phi)/2}, \qquad t' = t, \tag{6.7}$$

the electric field inside the space-time modulated medium may be achieved as

$$\mathbf{E}_\mathrm{M}(W,t') = \hat{\mathbf{y}}A^\mathrm{F,B}I_\alpha(W) + \hat{\mathbf{y}}B^\mathrm{F,B}K_\alpha(W), \tag{6.8a}$$

where $I_\alpha(W)$ and $K_\alpha(W)$ are the solution to the modified Bessel differential equation in (B-7), and α is defined as

$$\alpha = 2\frac{\beta_\mathrm{s}}{\kappa_\mathrm{s}} = 2\gamma. \tag{6.8b}$$

The unknown field amplitudes in (6.8a), $A^\mathrm{F,B}$ and $B^\mathrm{F,B}$, will be found by applying the spatial boundary conditions at $W = W_0 = W(z = 0, t)$ and $W = W_L = W(z = L, t)$, separately for forward and backward problems. We wish to calculate the fields scattered by the slab. As it is shown in 8.2, we may find the fields scattered by the slab for forward and backward problems, namely the reflected fields, $\mathbf{E}_\mathrm{R}^\mathrm{F,B}$, and the transmitted fields, $\mathbf{E}_\mathrm{T}^\mathrm{F,B}$, as

$$\mathbf{E}_\mathrm{R}^\mathrm{F,B}(z,t') = \hat{\mathbf{y}}\left(A^\mathrm{F,B}I_\alpha(W_0^\mathrm{F,B}) - B^\mathrm{F,B}K_\alpha(W_0^\mathrm{F,B}) - E_0e^{j\omega_\mathrm{s}t'}\right)e^{j\beta_\mathrm{s}z} \tag{6.9a}$$

$$\mathbf{E}_{\mathrm{T}}^{\mathrm{F,B}}(z,t') = \hat{\mathbf{y}}\left(A^{\mathrm{F,B}}.I_\alpha(W_L^{\mathrm{F,B}}) + B^{\mathrm{F,B}}.K_\alpha(W_L^{\mathrm{F,B}})\right)e^{-j\beta_{\mathrm{s}}(z-L)} \tag{6.9b}$$

with

$$W_0^{\mathrm{F}} = W_0^{\mathrm{B}} = W(z=0) = \frac{2\sqrt{2\epsilon_{\mathrm{m}}}\omega_{\mathrm{s}}}{c\kappa_{\mathrm{s}}}e^{j(-\omega_{\mathrm{s}}t+\phi)/2} \tag{6.9c}$$

and

$$W_L^{\mathrm{F,B}} = W(z=L) = \frac{2\sqrt{2\epsilon_{\mathrm{m}}}\omega_{\mathrm{s}}}{c\kappa_{\mathrm{s}}}e^{j(\pm\kappa_{\mathrm{s}}L-\omega_{\mathrm{s}}t+\phi)/2} \tag{6.9d}$$

where $+$ and $-$ signs respectively stand for the forward and backward problems. The unknown field amplitudes $A^{\mathrm{F,B}}$ and $B^{\mathrm{F,B}}$ are derived in 8.2 and represented as

$$A^{\mathrm{F}} = B^{\mathrm{F}}\frac{K_{\alpha+1}(W_L^{\mathrm{F}})}{I_{\alpha+1}(W_L^{\mathrm{F}})} \tag{6.10a}$$

$$B^{\mathrm{F}} = \frac{-2\alpha E_0 e^{j\omega_{\mathrm{s}}t'}}{W_0\left(K_{\alpha-1}(W_0) - K_{\alpha+1}(W_L^{\mathrm{F}})I_{\alpha-1}(W_0)/I_{\alpha+1}(W_L^{\mathrm{F}})\right)} \tag{6.10b}$$

for the forward problem, and

$$A^{\mathrm{B}} = B^{\mathrm{B}}\frac{K_{\alpha-1}(W_L^{\mathrm{B}})}{I_{\alpha-1}(W_L^{\mathrm{B}})} \tag{6.11a}$$

$$B^{\mathrm{B}} = \frac{2\alpha E_0 e^{j\omega_{\mathrm{s}}t'}}{W_0\left(K_{\alpha+1}(W_0) - K_{\alpha-1}(W_L^{\mathrm{B}})I_{\alpha+1}(W_0)/I_{\alpha-1}(W_L^{\mathrm{B}})\right)} \tag{6.11b}$$

for the backward problem.

6.6 Parametric Study

This section investigates effect of the specifications of the periodic space-time modulated isolator in Fig. 6.12 on the nonreciprocal transmission. We use the analytical formulas in Sec. 6.4 to show the effect of different parameters, i.e. the thickness L, the modulation phase ϕ, the space-time velocity ratio γ, and the modulation depth ϵ_{m}.

It may be seen form (6.9) that, all the parameters ω_{s}, L, γ, ϕ, ϵ_{m} and v_{b} affect the profile, i.e. amplitude and phase, of the transmitted and reflected waves. The scattered waves acquire a periodic profile versus varying ϕ (shown in Fig. 6.14), providing the same profile for forward and backward problems but with a phase difference, appeared in (6.9d), corresponding to

$$\phi_{\mathrm{L}}^{\mathrm{F}} - \phi_{\mathrm{L}}^{\mathrm{B}} = \kappa_{\mathrm{s}}L = \frac{\omega_{\mathrm{s}}}{\gamma v_{\mathrm{b}}}L. \tag{6.12}$$

Therefore, the parameters ω_{s}, L, γ, and v_{b} affect the phase difference between the forward and backward transmitted fields, while ϕ and ϵ_{m} determine the profile, amplitude and phase, of the transmitted fields.

Figure 6.15 presents amplitude of the forward and backward transmitted waves versus the modulation depth for different space-time velocity ratios of $\gamma = 1, 2, 6.66$ and 9, computed using (6.9b) with $\phi = 1.318\pi$, $\epsilon_\mathrm{e} = 7.06$, $\omega_\mathrm{s} = 2\pi \times 2$ GHz, and $L = 2\lambda_\mathrm{g}$. A Forward transmission of $E_\mathrm{T}^\mathrm{F}/E_\mathrm{I}^\mathrm{F} = 0$ dB, with the corresponding isolation of 24.5 dB, is achieved for $\gamma = 6.66$ and $\epsilon_\mathrm{m}/\epsilon_\mathrm{r} = 0.3$.

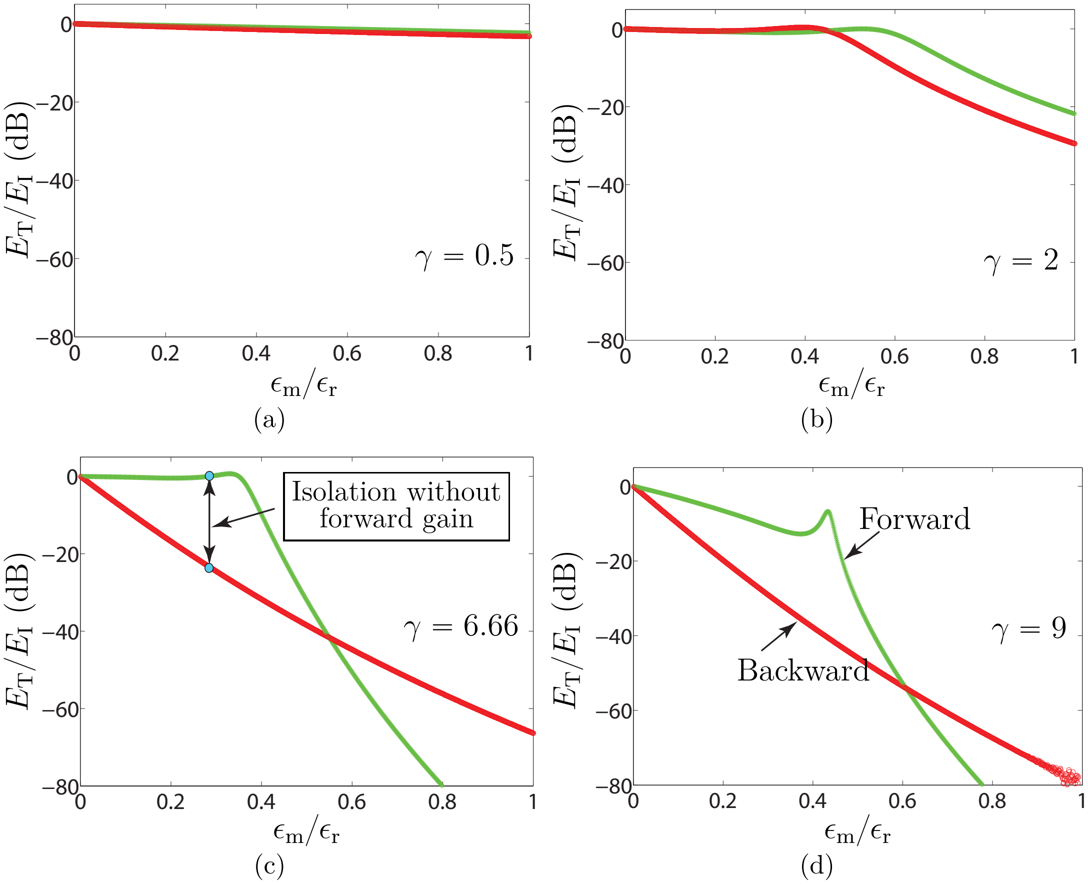

Figure 6.15 Nonreciprocal transmission from the space-time modulated isolator in Fig. 6.12 versus the modulation depth, computed using (6.9b) for $\phi = 1.318\pi$ and $L = 2\lambda_\mathrm{g}$, $\epsilon_\mathrm{e} = 7.06$, $\omega_\mathrm{s} = 2\pi \times 2$ GHz, and for various space-time velocity ratios. (a) $\gamma = 0.5$. (b) $\gamma = 2$. (c) $\gamma = 6.66$. (d) $\gamma = 9$.

Next, we investigate the effect of the space-time velocity ratio of the structure on the isolation between the forward and backward transmissions. Figure 6.16 shows the transmissions, computed using (6.9b), for $\phi = 1.318\pi$, $\epsilon_\mathrm{m} = 0.3\epsilon_\mathrm{r}$ and $L = 2\lambda_\mathrm{g}$.

Figure 6.17 plots effect of the length L of the space-time modulated isolator in Fig. 6.12 on forward and backward transmissions, computed using (6.9b), with $\phi = 1.318\pi$, $\epsilon_\mathrm{m} = 0.3\epsilon_\mathrm{e}$

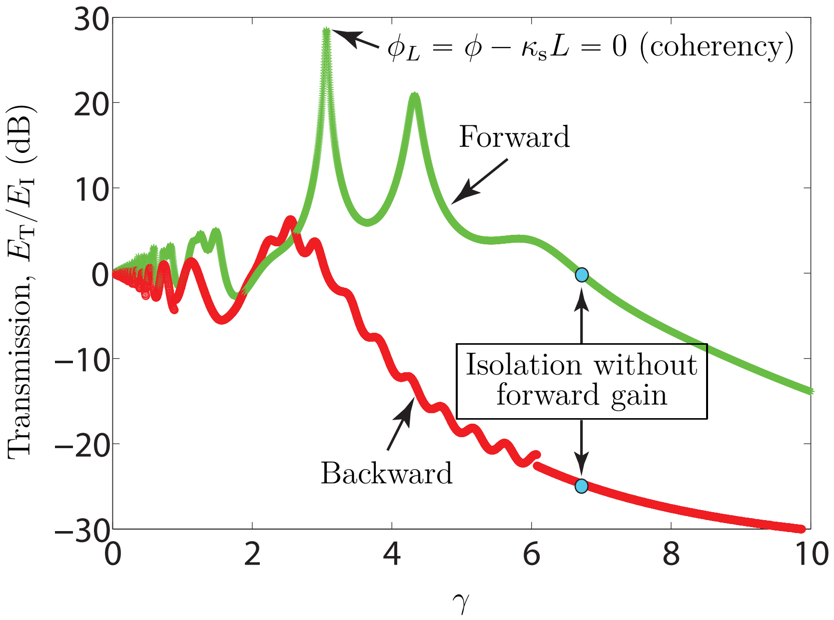

Figure 6.16 Effect of the velocity ratio of the space-time modulated isolator in Fig. 6.12 on forward and backward transmissions and isolation, computed using (6.9b), for the same parameters as in Fig. 6.15(c), except for varying γ and $\epsilon_\mathrm{m} = 0.3\epsilon_\mathrm{e}$.

and $\gamma = 6.66$. It may be seen that the transmission from the isolator versus L is periodic, with a period of $L = 13.45\lambda_\mathrm{g}$. The structure introduces reciprocal transmission, $\mathbf{E}_\mathrm{T}^\mathrm{F} = \mathbf{E}_\mathrm{T}^\mathrm{B}$, for some specific lengths, e.g. $L = 6.8\lambda_\mathrm{g}$, while it presents nonreciprocal transmission with forward gain, $\mathbf{E}_\mathrm{T}^\mathrm{F} > 1 > \mathbf{E}_\mathrm{T}^\mathrm{B}$. This represents an extra functionality of the proposed isolator, as forward transmission gain may be desired in some applications. For specific lengths, e.g. $L = 2\lambda_\mathrm{g}$, isolation, without forward gain, is provided by the structure.

Figure 6.18 shows effect of the modulation phase, ϕ, on forward and backward transmissions through the structure in Fig. 6.12, computed using (6.9b), with $\epsilon_\mathrm{m} = 0.3\epsilon_\mathrm{e}$, $\gamma = 6.66$ and $L = 2\lambda_\mathrm{g}$.

6.7 Experimental Demonstration

6.7.1 Varactor-Based Realization

To realize the space-time modulated permittivity in (6.3), we employ an array of sub-wavelengthly spaced anti-parallel varactors, which is distributed in parallel with the intrinsic capacitance of a microstrip transmission line. Figure 6.19 illustrates the structure of the realized space-time modulated isolator. A sinusoidal RF bias, i.e. the modulation

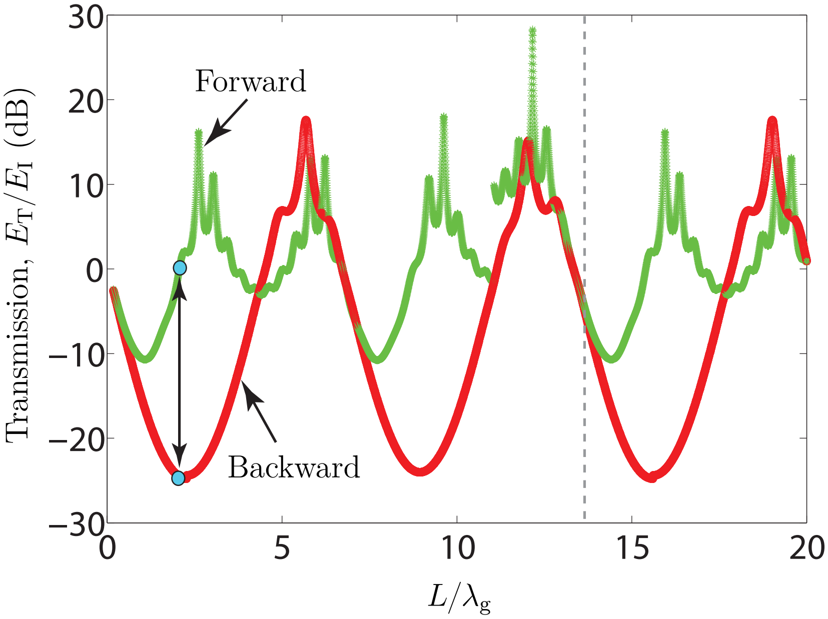

Figure 6.17 Effect of the length L of the space-time modulated isolator in Fig. 6.12 on forward and backward transmissions, computed using (6.9b), for the same parameters as in Fig. 6.15(c), except for varying L and $\epsilon_\mathrm{m} = 0.3\epsilon_\mathrm{e}$.

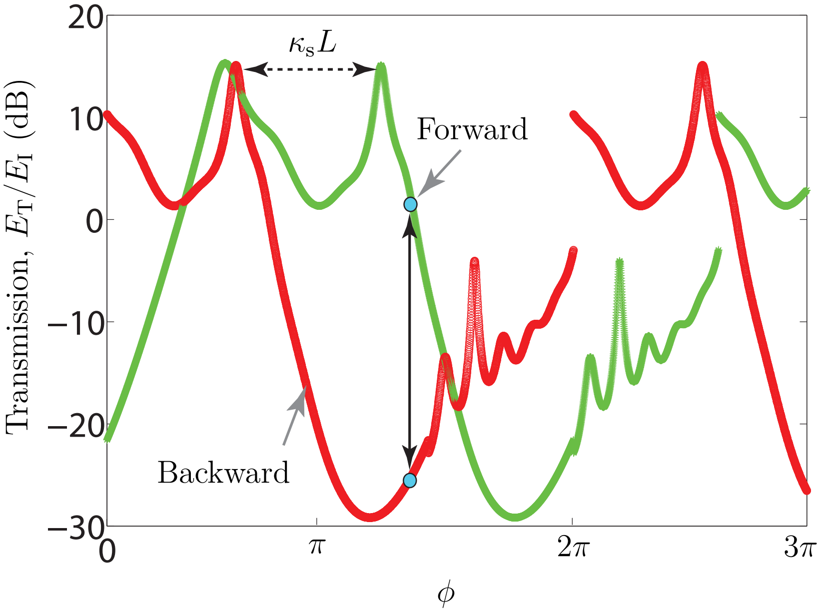

Figure 6.18 Effect of the modulation phase, ϕ, of the space-time modulated isolator in Fig. 6.12 on forward and backward transmissions, computed using (6.9b), for the same parameters as in Fig. 6.15(c), except for varying ϕ and $\epsilon_\mathrm{m} = 0.3\epsilon_\mathrm{e}$.

signal, with frequency ω_s and wave vector β_s, propagating along $+z$ direction, modulates the varactors in space and time such as to provide the space-time dependent capacitance $C(z,t) = C_\mathrm{av} + C_\mathrm{var}\cos(\kappa_s z - \omega_\mathrm{s} t + \phi)$. Note that, C_av and C_var of a microstrip line loaded with array of varactors, with the periodicity of p, can be calculated using the transmission line theory [149]. We first calculate the C_av per meter and then C_av per p can easily be achieved. Next, for a known RF bias voltage modulating the varactors in space and time, C_var will be achieved using the C-V curve of the varactor. As a result, the corresponding effective permittivity of the medium reads $\epsilon(z,t) = \epsilon_\mathrm{av} + \epsilon_\mathrm{m}\ \cos(\kappa_\mathrm{s} z - \omega_\mathrm{s} t + \phi)$, where the modulation depth, ϵ_m, depends on the range of variation of the varactors at a given modulation amplitude. Note that a DC bias line is used to set the varactors in the reverse bias (capacitive) region and also to provide the optimum average permittivity, ϵ_av.

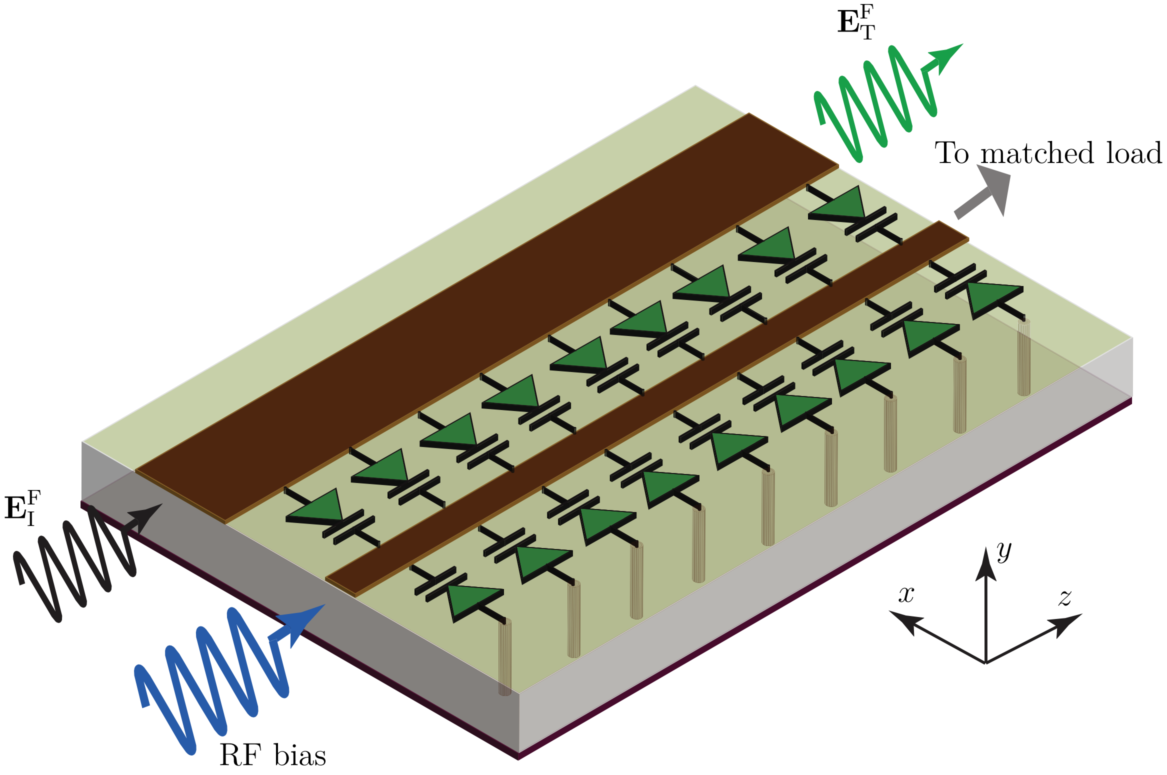

Figure 6.19 Realization of the space-time modulated isolator in Fig. 6.12 using microstrip technology.

6.7.2 Externally Biased Isolator

This subsection presents the implementation of the space-time modulated isolator in 6.19. The isolator uses an external RF bias as the modulation signal, propagating unidirectionally along $+z$ direction, modulates the varactors and ends up to a matched load. Figure 6.20 shows the photo of the fabricated isolator. The modulation specifications are $f_\mathrm{s} = \omega_\mathrm{s}/2\pi = 2$ GHz, $\kappa_\mathrm{s} = 111.24$, $L = 4.65 = 2\lambda_\mathrm{g}$ in and $\epsilon_\mathrm{m} = 0.3\epsilon_\mathrm{av}$, $\gamma = 6.66$, $\phi = 1.318\pi$, where the modulation signal with the amplitude of 10 dBm propagates along $+z$ direction and modulates the varactors in space and time. The modulation circuit is composed of 39 unit cells of antiparallel varactors, as shown in Fig. 6.19, with uniform spacing of $p = 5$ mm, which corresponds to $p/\lambda_\mathrm{s} = p\kappa_\mathrm{s}/(2\pi) \approx 1/11.3$, and therefore safely satisfies medium homogeneity in accordance with (6.3). We employed SMV1247 varactors manufactured by Skyworks Solutions with the capacitance ratio $C_\mathrm{max}/C_\mathrm{min} = 10$. The specifications of the structure are RT6010 substrate with permittivity $\epsilon_\mathrm{e} = 10.2$, thickness $h = 100$ mil and $\tan\delta = 0.0023$.

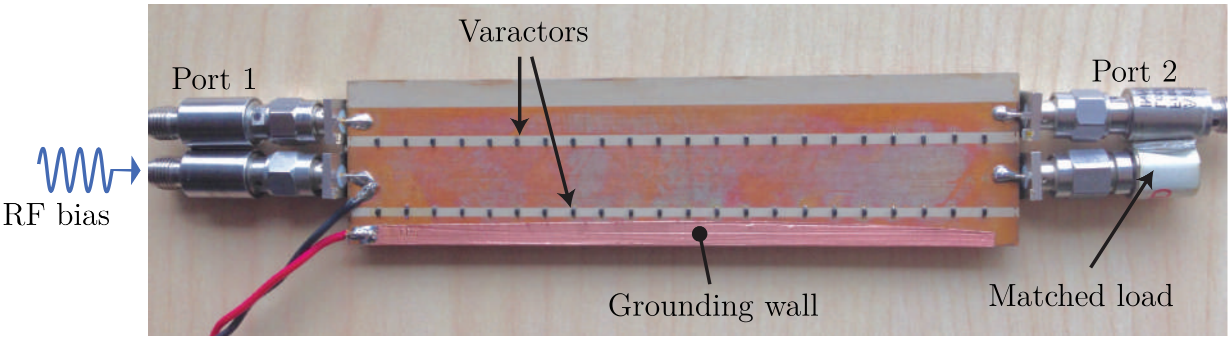

Figure 6.20 Photograph of the fabricated isolator.

Figure 6.21 plots the experimental input matching of the signal and modulation ports of the space-time modulated isolator in Figs. 6.19 and 6.20. An optimal varactor DC bias of 3.8 V ensures the varactors safely operate in the *linear* reverse-biased regime, so that related nonlinear effects are negligible.

Figure 6.22 shows the photograph of the experimental set-up. A directional coupler is used to provide the reflection of the isolator.

Figure 6.23 compares the analytical, simulation with Advanced Design System (ADS), and experimental results forward and backward transmissions. It may be seen that forward transmission of $E_\mathrm{T}^\mathrm{F}/E_\mathrm{I}^\mathrm{F} = -0.56$ dB and backward transmission of $E_\mathrm{T}^\mathrm{B}/E_\mathrm{I}^\mathrm{B} = -26.3$ dB, corresponding to the 25.74 is achieved. Figure 6.24 provides the corresponding reflections for forward and backward problems. Forward problem reflection of $E_\mathrm{R}^\mathrm{F}/E_\mathrm{I}^\mathrm{F} = -16.7$ dB and backward

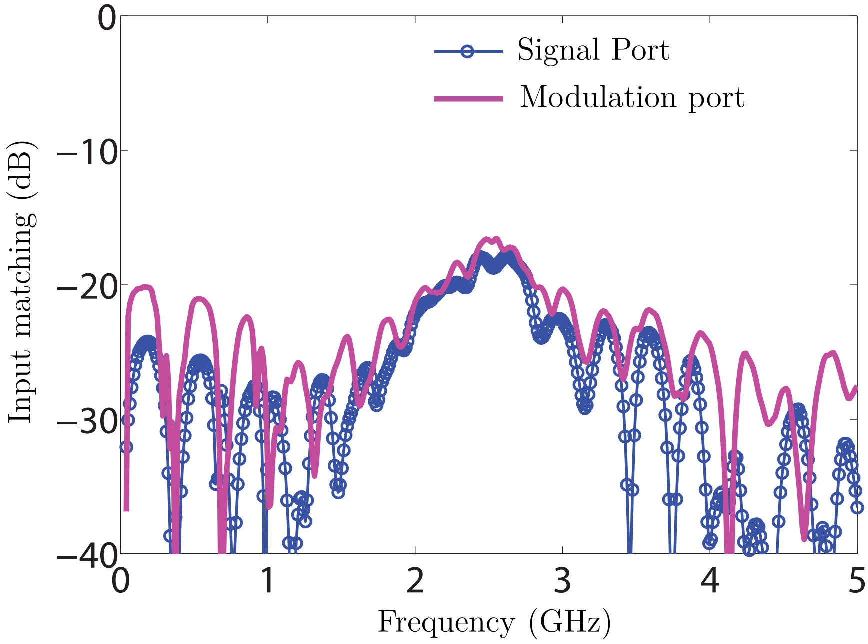

Figure 6.21 Experimental matching of the signal and modulation ports of the isolator in Fig 6.20.

problem reflection of $E_{\mathrm{R}}^{\mathrm{B}}/E_{\mathrm{I}}^{\mathrm{B}} = -2.35$ dB, corresponding to the 25.74 is achieved. This reveals that the isolator passes the input wave in the forward problem, while reflects the input wave in the backward problem.

6.7.3 Self-Biased Isolator

The isolator in Figs. 6.19 and 6.20 requires an external RF bias, with the same frequency as the input wave, to modulate the array of varactors. Therefore, it would be intriguing to take advantage of the input signal and employ it as the source of the RF bias and realize a self-biased space-time modulated isolator. Such structure represents a self-biased isolator, where the modulation signal is provided by the input signal. This results in about 3 dB insertion loss of the transmitted wave due to the insertion loss of the power dividers.

Figure 6.25 plots the simulation experimental results for the frequency bandwidth of the space-time modulated isolator in Figs. 6.19 and 6.20 with the same parameters as in Fig. 6.23. We see that the isolator introduces isolation of more than 15 dB in the frequency band from 1.2 GHz to 3.4 GHz (96% FBW) isolation of more than 8.1 dB in the frequency band from 0.4 GHz to 4 GHz (164% FBW).

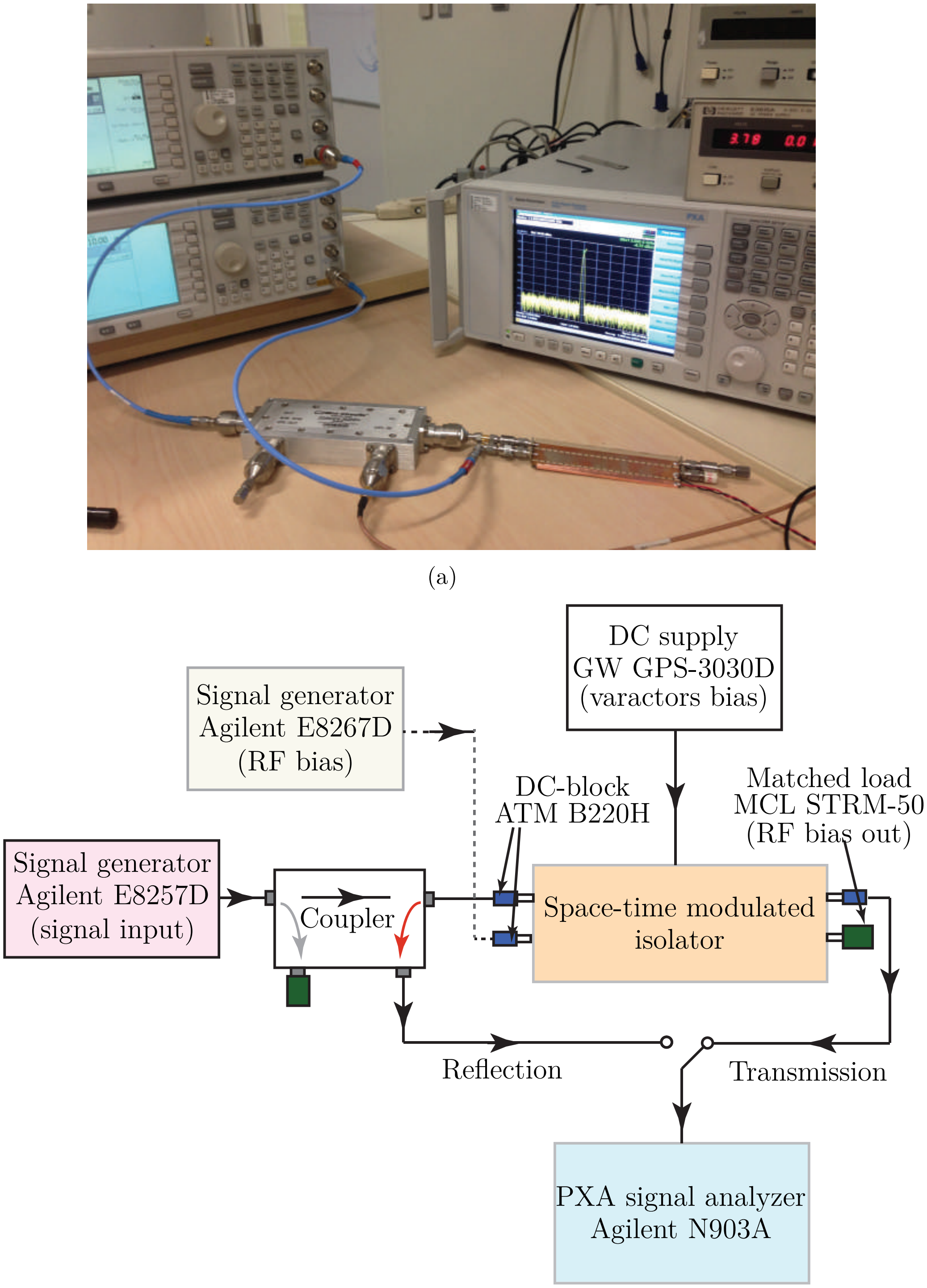

(a)

(b)

Figure 6.22 Measurement set-up. (a) Photograph. (b) Schematic.

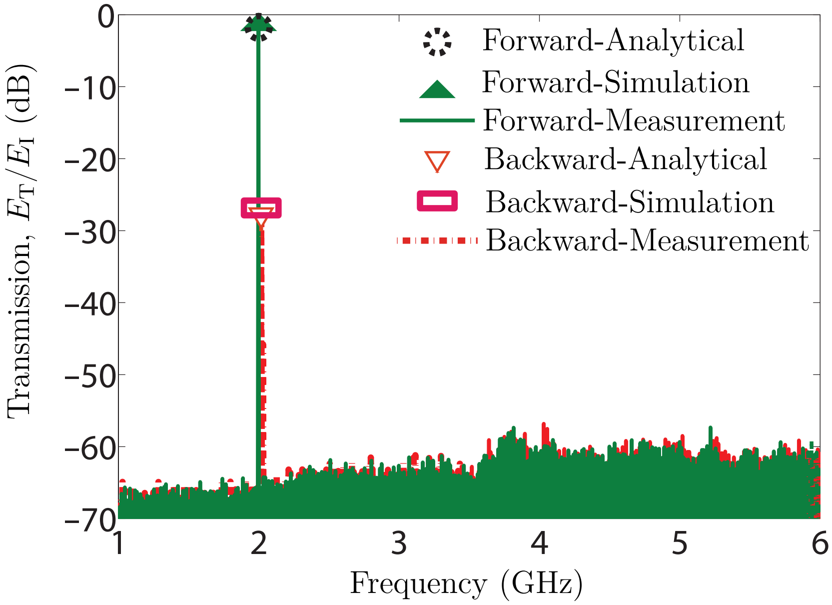

Figure 6.23 Analytical, simulation (using ADS) and experimental results for nonreciproal transmission from the space-time isolator in Figs. 6.19 and 6.20 with $\epsilon_\mathrm{m}/\epsilon_\mathrm{e} = 0.3$, $\phi = 1.318\pi$, $\gamma = 6.66$ and $L = 2\lambda_\mathrm{g}$.

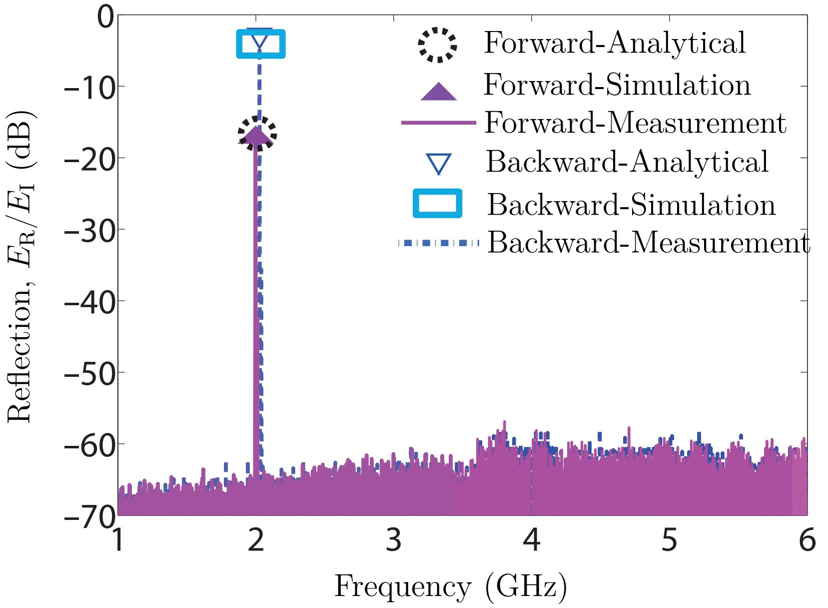

Figure 6.24 Analytical, simulation (using ADS) and experimental results for nonreciproal reflection from the space-time isolator in Figs. 6.19 and 6.20 with the same parameters as in Fig. 6.23.

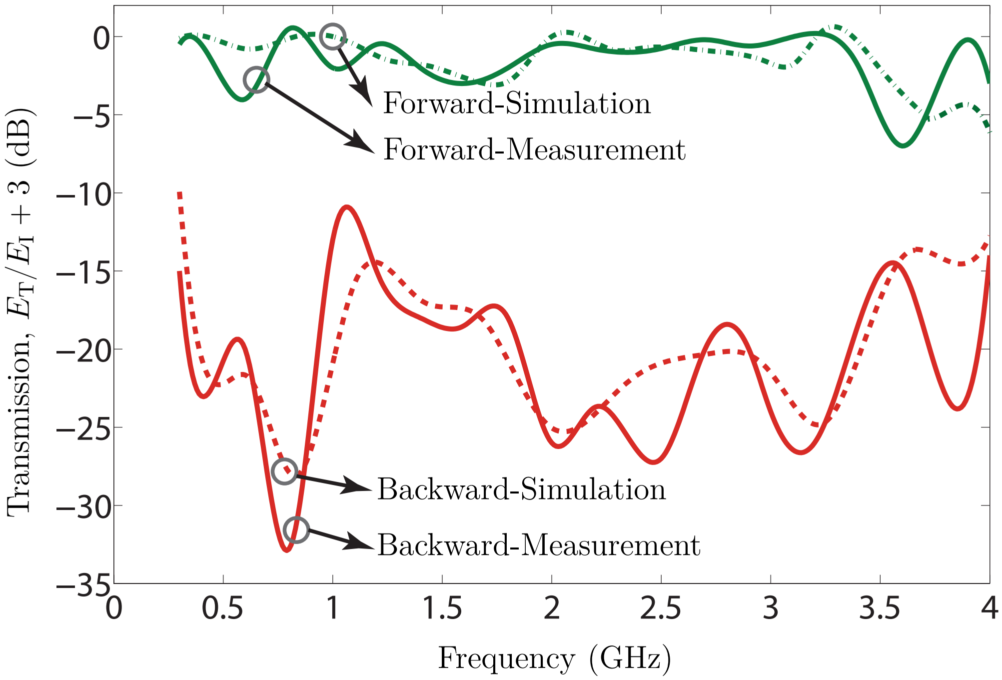

Figure 6.25 Simulation (ADS) and experimental results for the broadband operation of the space-time modulated isolator with $\epsilon_\mathrm{m}/\epsilon_\mathrm{e}=0.3$, $\phi=1.318\pi$, $\gamma=6.25$ and $L=2\lambda_\mathrm{g}$.

6.7.4 Modulated Input Signal

The efficiency of the self biased isolator in **??** may be further investigated by considering an amplitude modulated (AM) input signal. Figure 6.26(a) plots the input AM signal with carrier frequency of 50 KHz, while Fig. 6.26(b) plots the transmitted signals for forward and backward problems. Figure 6.27 shows the time domain response for nonreciprocal transmission from the isolator. It may be seen that forward transmission of $E_\mathrm{T}^\mathrm{F}/E_\mathrm{I}^\mathrm{F}>4$ (dB) and backward transmission of $E_\mathrm{T}^\mathrm{B}/E_\mathrm{I}^\mathrm{B}<-28$ dB, corresponding to more than 25 dB is achieved.

Figure 6.28 shows the corresponding experimental reflection for the forward and backward problems. Forward problem reflection of $E_\mathrm{R}^\mathrm{F}/E_\mathrm{I}^\mathrm{F}>-15$ (dB) and backward problem reflection of $E_\mathrm{R}^\mathrm{B}/E_\mathrm{I}^\mathrm{B}=-4$ (dB) is achieved. This reveals that the isolator passes the input wave in the forward problem, while reflects the input wave in the backward problem.

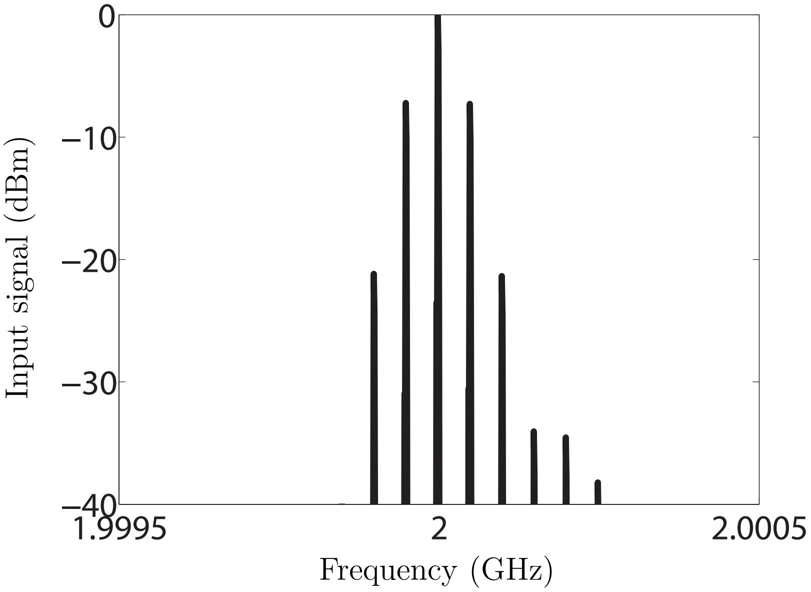

(a)

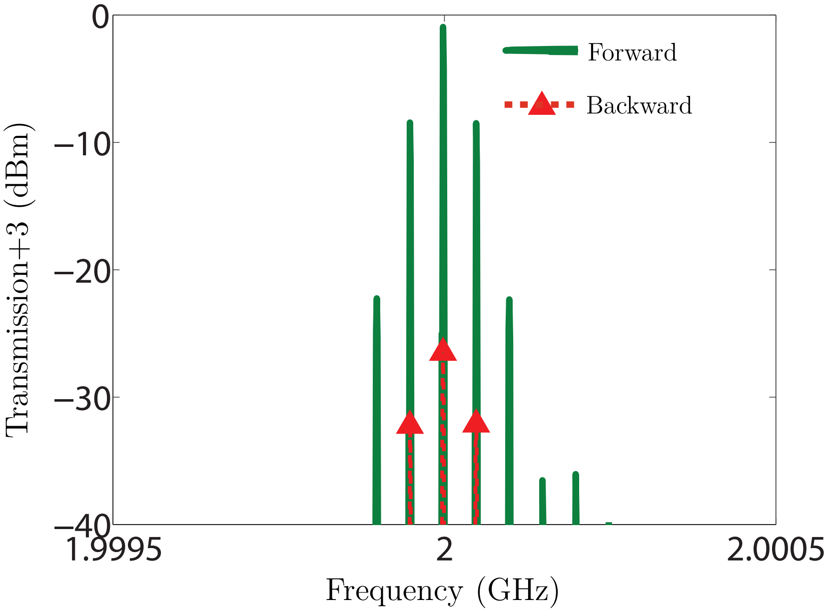

(b)

Figure 6.26 Experimental results for nonreciprocal transmission of AM signal from the space-time isolator with the same parameters as in Fig. 6.25. (a) Spectral domain input AM signal. (b) Spectral domain forward and backward transmissions.

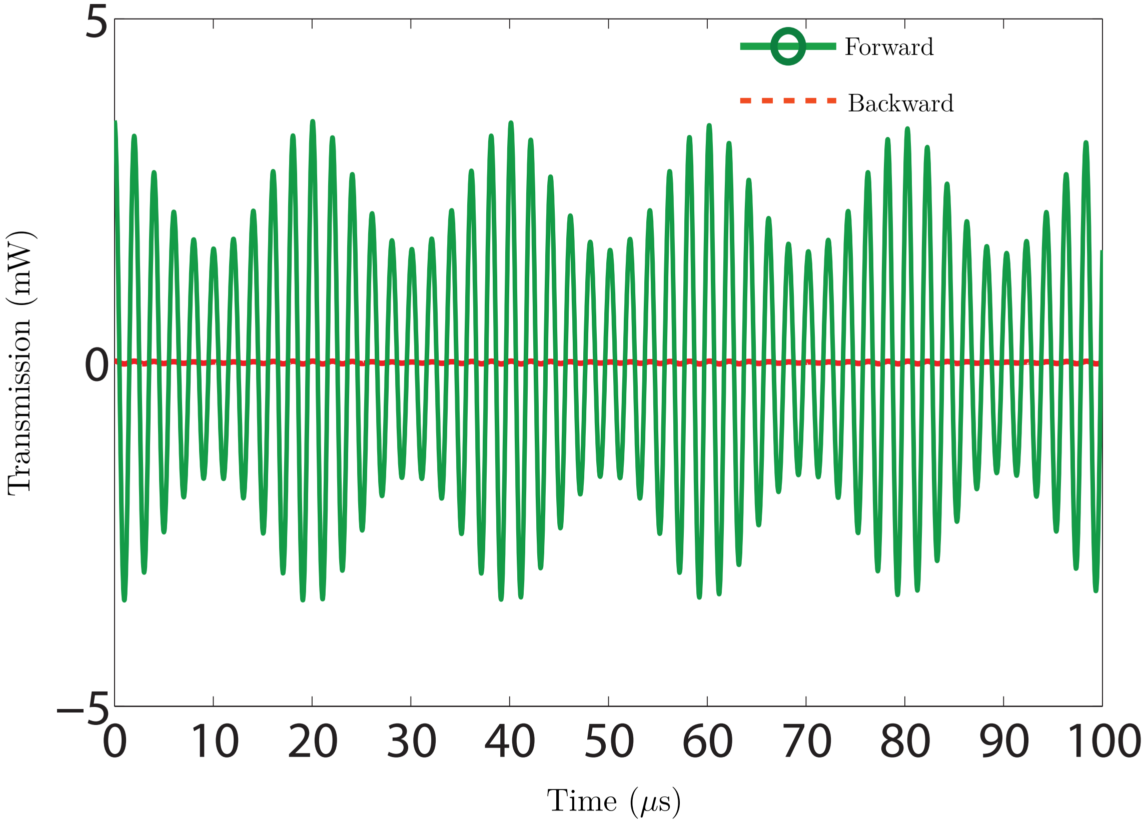

Figure 6.27 Experimental results for nonreciprocal transmission of AM signal from the space-time isolator with the same parameters as in Fig. 6.25. Time domain forward and backward transmissions.

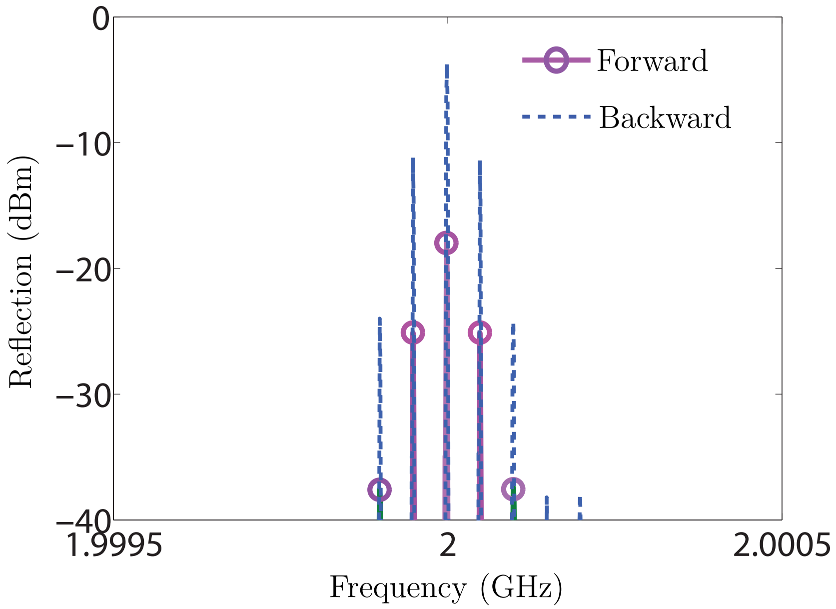

Figure 6.28 Experimental results for nonreciprocal reflection of AM signal from the space-time isolator with the same parameters as in Fig. 6.25

CHAPTER 7 MIXER-DUPLEXER-ANTENNA LEAKY-WAVE SYSTEM USING PERIODIC SPACE-TIME MODULATED SPATIALLY DISPERSIVE MEDIUM

This chapter has been taken from author's published article [9].

A two-port nonreciprocal space-time modulated leaky-wave system is presented which simultaneously performs the tasks of mixing, duplexing and radiation, hence operating as a complete transceiver system. Most of previously reported nonreciprocal leaky-wave systems were based on magnetically biased ferrites [58, 60, 141–144, 144–146], and hence suffer from the drawbacks inherent to ferrite technology, namely bulkiness, heaviness, incompatibility with integrated circuits and high cost, in addition to requiring excessive bias field beyond the X-band for resonance-based components [124]. The first nonreciprocal leaky-wave system based on space-time modulation, and hence requiring no biasing magnet, was independently proposed at the same time in [90] and [96], and the latter proposal was extended to an experimental demonstration in [93].

This chapter, as an extension of [90], presents a nonreciprocal space-time modulated leaky-wave system. However, this work and [90] feature fundamental differences. The system in [90] and [93] is a single-port leaky-wave structure where the input frequency is up-converted to radiate whereas an incoming wave at the radiation frequency is absorbed in the structure and does not reach the input port. In contrast, this chapter presents a two-port structure that performs the operation of a full transceiver system, with uplink and downlink space-time transitions, representing upconversion and downconversion mixing, and separation of the uplink and downlink paths, representing duplexing. Moreover, this chapter demonstrates space-time frequency beam scanning at fixed input frequency by variation of a modulation parameter. Finally, a detailed electromagnetic resolution of the problem for the dispersion relation and field structure is presented.

The chapter is organized as follows. Section 7.1 presents the operation principle and analytical solution of the nonreciprocal space-time modulated leaky-wave structure. Section 7.2 proposes a practical realization of the corresponding mixer-duplexer-antenna system, based on a half-wavelength microstrip leaky-wave antenna incorporating subwavelengthly-spaced modulating varactors. Finally, Sec. 7.3 describes the implementation of the system and characterizes it in terms of its dispersion relation and field distributions. Full-wave and experimental results are provided in Sec. 7.4.

7.1 Space-time Modulated Leaky-Wave Structure

7.1.1 Operation Principle

Figure 7.1 shows the generic representation of a periodically space-time modulated leaky-wave structure. The structure consists of a medium with permittivity

$$\epsilon(z,t)=\epsilon_{\mathrm{e}}(1+\delta_{\mathrm{m}}\cos(\omega_{\mathrm{m}}t-\beta_{\mathrm{m}}z)) \tag{7.1}$$

interfaced with air. In Eq. (7.1), ϵ_{e} is the effective permittivity of the unmodulated medium, $\delta_{\mathrm{m}}=\epsilon_{\mathrm{m}}/\epsilon_{\mathrm{e}}$ is the modulation depth, and ω_{m} and β_{m} are the modulation temporal and spatial frequencies, respectively. Due to the directionally of the space-time modulation, which propagates in the $+z$ direction with velocity $v_{\mathrm{m}}=\omega_{\mathrm{m}}/\beta_{\mathrm{m}}$, the structure is inherently nonreciprocal. The system has two ports, which support a transmitted wave and a received wave in an uplink/downlink transceiver scenario.

Figure 7.2 qualitatively explains the operation principle of the space-time modulated leaky-wave structure in Fig. 7.1. The space-time modulated permittivity is provided by injection of a harmonic wave in a guided-mode of the structure, as will be practically shown in Sec. 7.2, while the wave of interest is supported by a leaky-mode of the structure, where mixing with the space-time modulation induces nonreciprocal uplink and downlink oblique transitions, represented by the green arrow and the magenta arrow, respectively, in Fig. 7.2. The exact operation is as follows.

In the uplink, a signal wave with frequency ω_0 is injected into the transmitter port and propagates in the $+z$ direction, corresponding to the right-hand side of the dispersion diagram in Fig. 7.2, as $E_{\mathrm{t}}=E_0e^{j(\omega_0t-\beta_0z)}$. As a result of mixing with the periodic modulation, this wave experiences progressive temporal frequency transition (up-conversion) from ω_0 to $\omega_1=\omega_0+\omega_{\mathrm{m}}$ along with spatial frequency transition from β_0 to $\beta_1=\beta_0+\beta_{\mathrm{m}}$. The physical explanation for the generation of new frequencies due to medium temporal variations – specifically vertical transitions in the dispersion diagram – has been given in several texts, such as for instance [80]. In the particular case of periodic temporal variations, one may draw an analogy with periodic spatial variations in a one-dimensional spatial periodic structure (or electromagnetic bandgap material). As a result of complex scattering from the spatial periodic modulation, the field solution to Maxwell equations in the structure is spatially non-sinusoidal (e.g. having more or less energy concentrated in the high or low refractive index regions for the lower and higher bands, respectively [197]), except in the long-wavelength regime where homogeneization applies and leads to a well defined refractive index. Being non-sinusoidal, this waveform is actually a superposition of an infinite number of Floquet space harmonics,

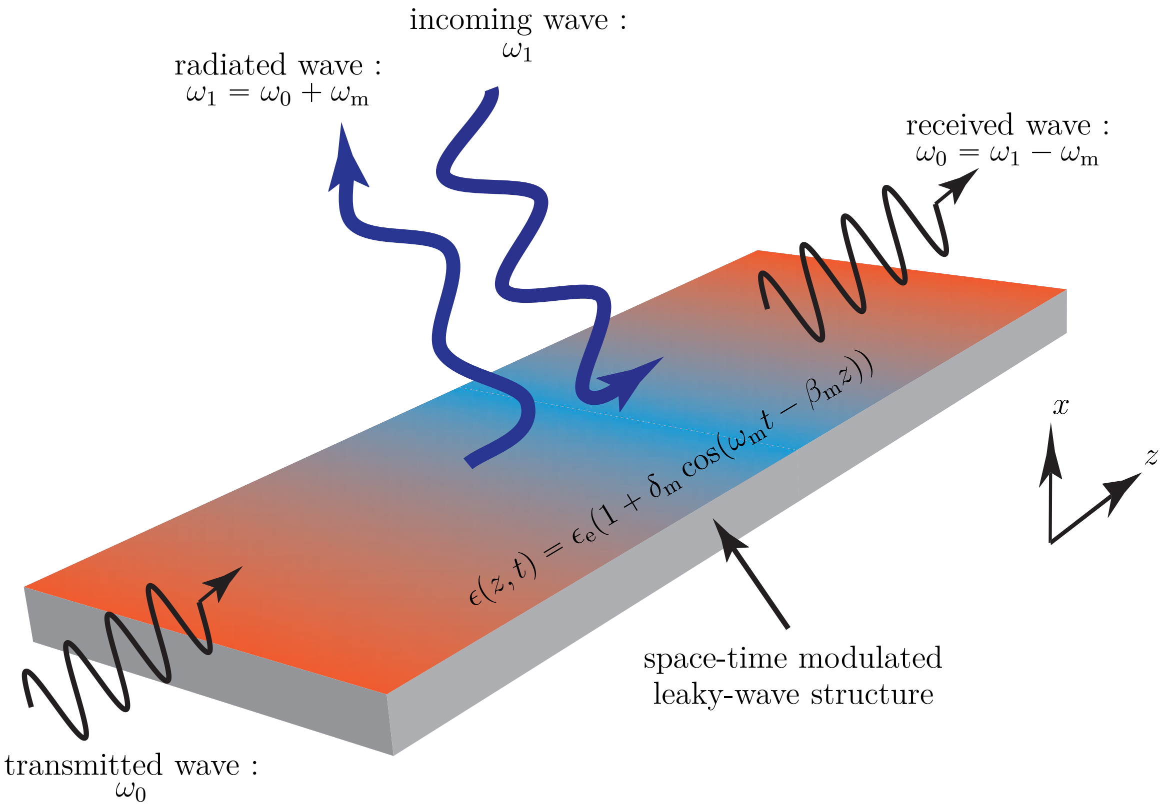

Figure 7.1 Generic representation of a periodically space-time modulated leaky-wave structure, consisting of a medium with permittivity $\epsilon(z,t) = \epsilon_\mathrm{e}(1 + \delta_\mathrm{m} \cos(\omega_\mathrm{m} t - \beta_\mathrm{m} z))$ interfaced with air. The wave transmitted at the left port is frequency up-converted and radiated under a specified angle (uplink), while a wave incoming under the same angle and at the same frequency is down-converted back to the original frequency and received at the right port (downlink). The system is inherently nonreciprocal due to the directionality of the space-time modulation [9].

$\beta_0 + n\beta_\mathrm{m}$, corresponding to horizontal transitions in the dispersion diagram. Similarly, in the case of a temporal periodic modulation, waves get scattered forward and backward [80] to form a temporally non-sinusoidal waveform, corresponding to an infinite number of Floquet *time* harmonics, i.e. new frequencies, $\omega_0 + n\omega_\mathrm{m}$, as will be seen in (7.3b). When the periodic modulation is both spatial and temporal [74], or spatiotemporal, as in (7.1), we have thus the generation of an infinite number of spacetime harmonics, $(\beta_0 + n\beta_\mathrm{m}, \omega_0 + n\omega_\mathrm{m})$, corresponding to oblique transitions in the dispersion diagram [19], as illustrated in Fig. 7.2. In the meanwhile, the up-converted wave, $E_\mathrm{r} = E_1 e^{j(\omega_1 t - (\beta_1 - j\alpha_1)z)}$, operating in the fast wave region of the dispersion diagram, radiates as a leaky-wave under a specified angle θ_1.

In the downlink, a wave with frequency ω_1 is impinging on the structure under the same angle θ_1 and picked up by the structure. It should be noted that directivity of the leaky-wave structure is proportional to its length, i.e. longer structure leads to a more directive

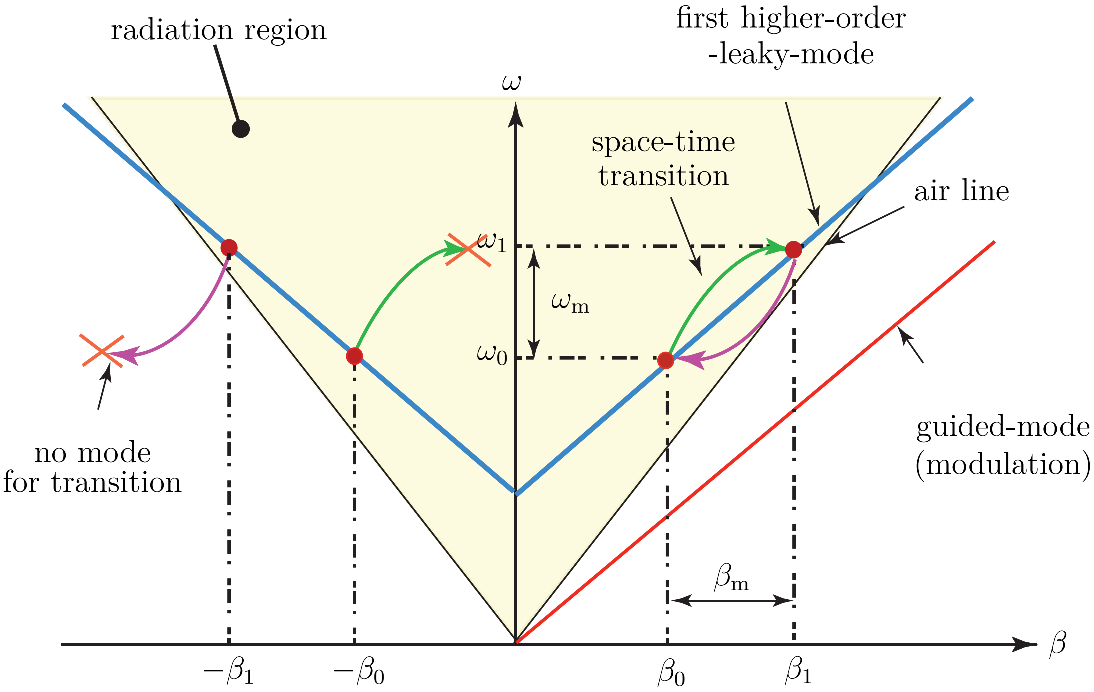

Figure 7.2 Schematic dispersion diagram explaining the nonreciprocal uplink and downlink space-time transitions in the leaky-wave structure of Fig. 7.1 [9].

radiation beam. According to phase matching, the wave can only propagate in the direction of the modulation, i.e. in the $+z$ direction, corresponding to the right-hand side of the dispersion diagram in Fig. 7.2, and experiences progressive temporal frequency transition (down-conversion) from ω_1 to $\omega_0 = \omega_1 - \omega_{\mathrm{m}}$ along with spatial frequency transition from β_1 to $\beta_0 = \beta_1 - \beta_{\mathrm{m}}$, while propagating toward the receiver port.

Given the unidirectional nature of the modulation, the structure is fundamentally nonreciprocal. No space-time transition is allowed for wave propagation in the backward $(-z)$ direction (left-hand side of the dispersion diagram in Fig. 7.2) due to the unavailability of modes at the points $(-\beta_0 + \beta_{\mathrm{m}}, \omega_0 + \omega_{\mathrm{m}})$ from $(-\beta_0, \omega_0)$ for up-conversion and $(-\beta_1 - \beta_{\mathrm{m}}, \omega_0)$ from $(-\beta_1, \omega_0 + \omega_m)$ for down-conversion.

The direction of radiation of the main beam [198] depends on the modulation temporal and spatial frequencies as

$$\theta_1 = \sin^{-1}\left(\frac{\beta_1(\omega)}{k_{01}}\right) = \sin^{-1}\left(\frac{c(\beta_0 + \beta_{\mathrm{m}})}{\omega_0 + \omega_{\mathrm{m}}}\right), \tag{7.2}$$

where c is the velocity of light in vacuum and $k_{01} = \omega_1/c$ is the effective wavenumber at the frequency ω_1. According to (7.2), frequency beam scanning can be achieved at a fixed input frequency, ω_0, by varying the modulation frequency, ω_{m}.

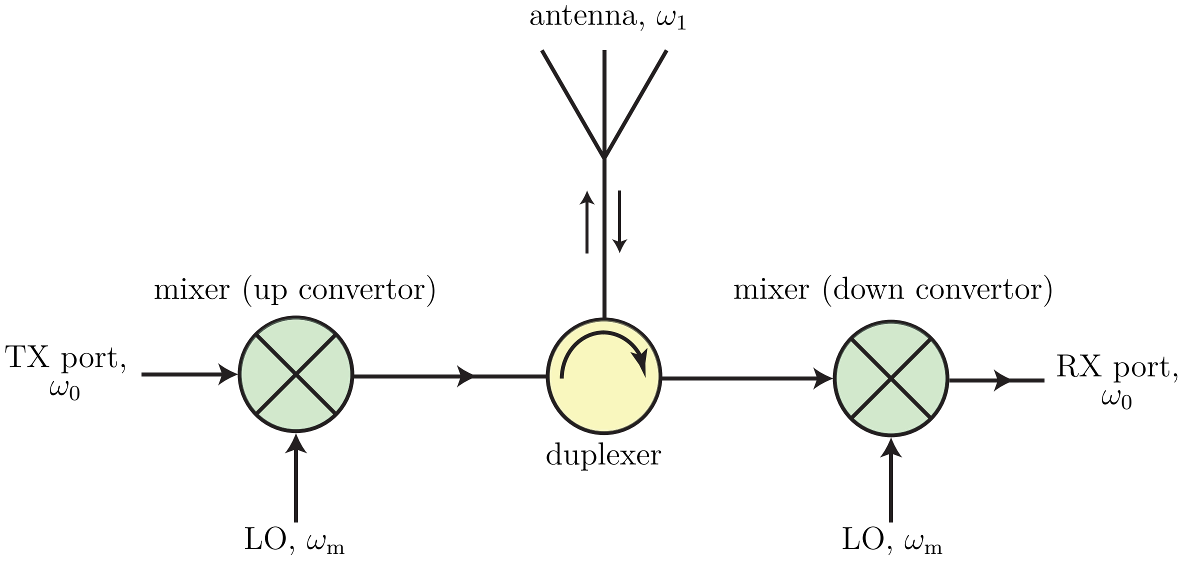

Figure 7.3 Circuital representation of the combined mixer-duplexer-antenna operation of the space-time modulated leaky-wave structure in Fig. 7.1 [9].

Figure 7.3 shows a circuital representation of the space-time modulated leaky-wave structure of Fig. 7.1. The operation of the structure operates as a combined mixer-duplexer-antenna system may be essentially read out from the dispersion diagram of Fig. 7.2. Up-conversion and down-conversion mixing operations are provided by the oblique upwards and downwards oblique transitions, respectively. The duplexing operation (separation of uplink and downlink paths at the same frequency) is provided by nonreciprocity. Finally, the antenna operation is provided by the fast-wave nature of the wave.

7.1.2 General Analytical Solution

Since the structure is periodic in space and time, its electromagnetic field solution can be expressed as the double Floquet expansion

$$E(z,t)=\sum_{n=-\infty}^{\infty}E_n e^{j\omega_n t}e^{-(\alpha_n+j\beta_n)z}, \tag{7.3a}$$

where E_n is the amplitude of the n^{th} space-time harmonic, characterized by the temporal and spatial frequencies

$$\omega_n=\omega_0+n\omega_{\mathrm{m}} \tag{7.3b}$$

and

$$\beta_n(\omega)=\beta_0(\omega)+n\beta_{\mathrm{m}}, \tag{7.3c}$$

respectively, and where $\alpha_n(\omega)$ is the leakage factor of the n^{th} harmonic. For a given input amplitude E_0 and frequency ω_0, E_n in (7.3a), leading to the general field solution, and $\beta_0(\omega)$ in (7.3c), corresponding to the dispersion relation, are unknowns to be determined. The detailed resolution of this problem is presented in Appendix 8.2.

In the case of weak modulation, $\delta_{\text{m}} \ll 1$, the E_n's in (7.3a) for $|n| > 1$ are negligible. Moreover, assuming that the leaky-wave structure is designed to support uplink and downlink radiation mainly at $\omega_1 = \omega_0 + \omega_{\text{m}}$, in the uplink, the amplitude of the lower harmonic E_{-1}, corresponding to the frequency $\omega_0 - \omega_{\text{m}}$, and in the downlink, the amplitude of the higher harmonic E_2 (already negligible from the weak modulation assumption), corresponding to the frequency $\omega_1 + \omega_{\text{m}} = \omega_0 + 2\omega_{\text{m}}$, are negligible. Then we find, as derived in Appendix 8.2, assuming $\alpha_n \ll \beta_n$, that

$$\beta_0(\omega) = \pm\beta_{\text{um}}(\omega_0) \pm \frac{\delta_{\text{m}}}{4}\sqrt{\beta_{\text{um}}(\omega_0)\beta'_{\text{um}}(\omega_0)}, \tag{7.4}$$

where the upper and lower signs correspond to forward and backward propagation, respectively, and where $\beta'_{\text{um}}(\omega_0) = \beta_{\text{um}}(\omega_0) + \beta_{\text{m}}$ with β_{um} being the wavenumber of the unmodulated structure, which, according to (7.2) with $\beta_{\text{m}} = \omega_{\text{m}} = 0$, may be obtained from the main beam radiation angle as

$$\beta_{\text{um}}(\omega_0) = \frac{\omega_0}{c}\sin(\theta(\omega_0)). \tag{7.5}$$

Equation (C-24) shows that, as expected, the change in the wave vector due to the modulation is proportional to the modulation depth, δ_{m}, and to the modulation wavenumber, β_{m}.

As shown in Appendix 8.2, the amplitude of the uplink up-converted electric field is

$$E_1 = \frac{\delta_{\text{m}} E_0 \beta'_{\text{um}}}{\delta_{\text{m}}\sqrt{\beta_{\text{um}}\beta'_{\text{um}}} - 2\alpha_1^2/\beta'_{\text{um}} - j\alpha_1\left(\delta_{\text{m}}\sqrt{\beta_{\text{um}}/\beta'_{\text{um}}} + 4\right)}, \tag{7.6}$$

which is proportional to the input electric field, E_0, and depends on both the modulation depth, δ_{m}, and the leakage factor, α_1. As shown in (C-27), uplink conversion is associated with power conversion gain.

Similarly, as shown in Appendix 8.2, the amplitude of the downlink down-converted electric field, corresponding to $n = 0$, is

$$E_0 = \frac{\delta_{\text{m}} E_1 \beta_{\text{um}}}{\delta_{\text{m}}\sqrt{\beta_{\text{um}}\beta'_{\text{um}}} - 2\alpha_0^2/\beta_{\text{um}} - j\alpha_0\left(\delta_{\text{m}}\sqrt{\beta'_{\text{um}}/\beta_{\text{um}}} + 4\right)}, \tag{7.7}$$

which is proportional to the received electric field, E_1, and depends on both the modulation depth, δ_{m}, and the leakage factor, α_0, and which is associated with power conversion loss.

7.2 Mixer-Duplexer-Antenna System Realization

The space-time modulated permittivity in (7.1) is realized as follows. An array of subwavelengthly spaced varactors is distributed in parallel with the intrinsic capacitance of a microstrip transmission line, while a sinusoidal modulation signal, with frequency ω_m and wave vector β_m, propagating in the guided-mode regime along $+z$ direction, modulates the varactors in space and time such as to provide the space-time dependent capacitance $C(z,t) = C_\mathrm{e} + C_\mathrm{var}\cos(\omega_\mathrm{m}t - \beta_\mathrm{m}z)$. As a result, the corresponding effective permittivity of the medium becomes $\epsilon(z,t) = \epsilon_\mathrm{e}(1 + \delta_\mathrm{m}\cos(\omega_\mathrm{m}t - \beta_\mathrm{m}z))$, where the modulation depth, δ_m, depends on the range of variation of the varactors at a given modulation amplitude. Note that a DC bias line is used to set the varactors in the reverse bias (capacitive) regime.

Figure 7.4(a) shows the structure and operation of the realized space-time modulated mixer-duplexer-antenna system. The structure supports two modes, a dominant even mode, providing a guided-mode channel for the wave modulating the varactors (narrow strip in Fig. 7.4(a)) and a higher order odd (EH_1) mode, providing the leaky-mode channel for radiation (wide strip in Fig. 7.4(a)). The transmit and receive ports are designed in such a way as to excite the leaky mode of the microstrip line. Moreover, an array of grounding vias is placed at the center of the wide microstrip line to suppress the even mode and hence enforce optimal leaky-wave radiation at ω_1, which corresponds to a strip width of $W = \lambda_1/2$. Figure 7.5(a) shows the electric field distribution of the leaky-mode (EH_1) along the microstrip leaky-wave antenna [10, 198, 199]. In contrast, Fig. 7.5(b) shows the electric field distribution of the dominant guided-mode (EH_0) of a microstrip transmission line, where transversally symmetric distribution of the electric field yields a complete propagation of the wave. The narrow line in the realized system of Fig. 7.4(a) supporting the propagation of modulation signal is designed in such a way to support the propagation of the dominant guided-mode of the microstrip line.

7.3 System Implementation and Characterization

This section presents the implementation and characterization of the mixer-duplexer-antenna system. The modulation specifications are $f_\mathrm{m} = \omega_\mathrm{m}/2\pi = 0.18$ GHz, $\beta_\mathrm{m} = \omega_\mathrm{m}\sqrt{\epsilon_\mathrm{e}}/c = 5.16$ rad/m, $\delta_\mathrm{m} = 0.15$ corresponding to a modulation signal with the amplitude of 10 dBm. The modulation circuit is composed of 39 unit cells of antiparallel varactors [Fig. 7.4(a)], with uniform spacing, or period, of $p = 5$ mm, which corresponds to $p/\lambda_\mathrm{m} = p\beta_\mathrm{m}/(2\pi) \approx 1/250$, and hence safely satisfies medium homogeneity in accordance with (7.1). We employed BB833 varactors manufactured by Infineon Technologies where the capacitance ratio (highest over

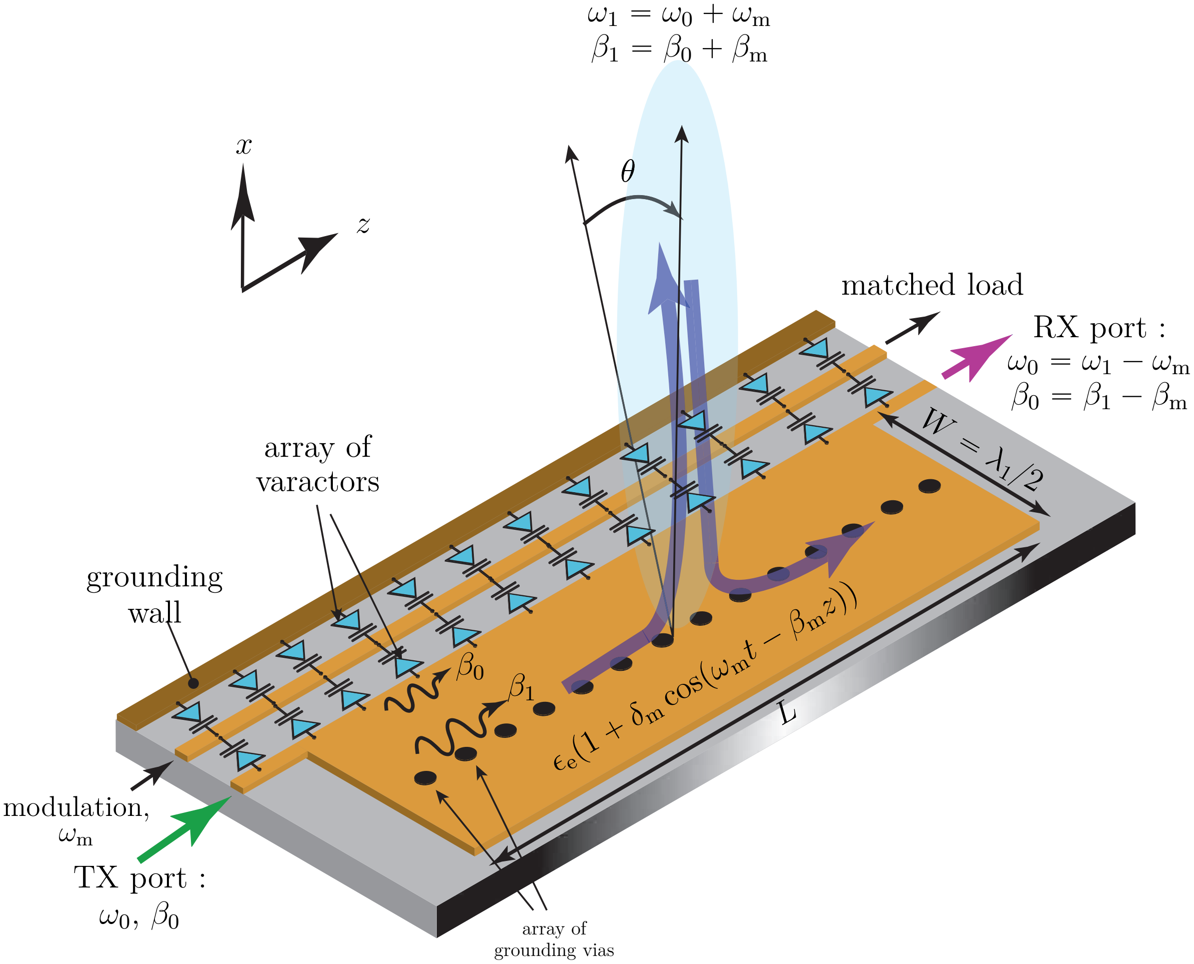

(a)

Figure 7.4 Realization of the space-time modulated mixer-duplexer-antenna system in Fig. 7.3. The structure is based on the half-wavelength microstrip leaky-wave antenna [10] [9]. Note that a sufficiently long structure ($L > 3\lambda_{\mathrm{r}}$) is required To ensure total radiation of the transmitted traveling wave and neglect the reflection of the wave from the receive port [10].

lowest capacitance) is about 12.4. The specifications of the structure are $f_0 = 1.7$ GHz, $f_1 = 1.88$ GHz, $\theta_1 = 4^\circ$ (radiation angle corresponding to the frequency f_1), $\alpha_0 = 1.2$ Np/m, $\alpha_1 = 3.4$ Np/m, $L = 8$ in and $W = 1.8$ in, RT5880 substrate with permittivity $\epsilon_{\mathrm{r}} = 2.2$, thickness $h = 125$ mil and $\tan\delta = 0.0009$. The leakage factors, α_0 and α_1, are experimentally obtained from the scattering parameter S_{21} as $\alpha_k \approx -\ln|S_{21}(\omega_k)|/L$, $k = 0, 1$, since most of the attenuation is due to leakage.

Figure 7.6 shows the dispersion diagram of the realized prototype computed using (C-21) and (7.5) with varying ω_0. This diagram is, as expected, qualitatively similar to that in Fig. 7.2, with a leaky-mode cutoff frequency of about 1.65 GHz. It may be observed that the dispersion of the modulated mode corresponds, also as expected, to an increased momentum

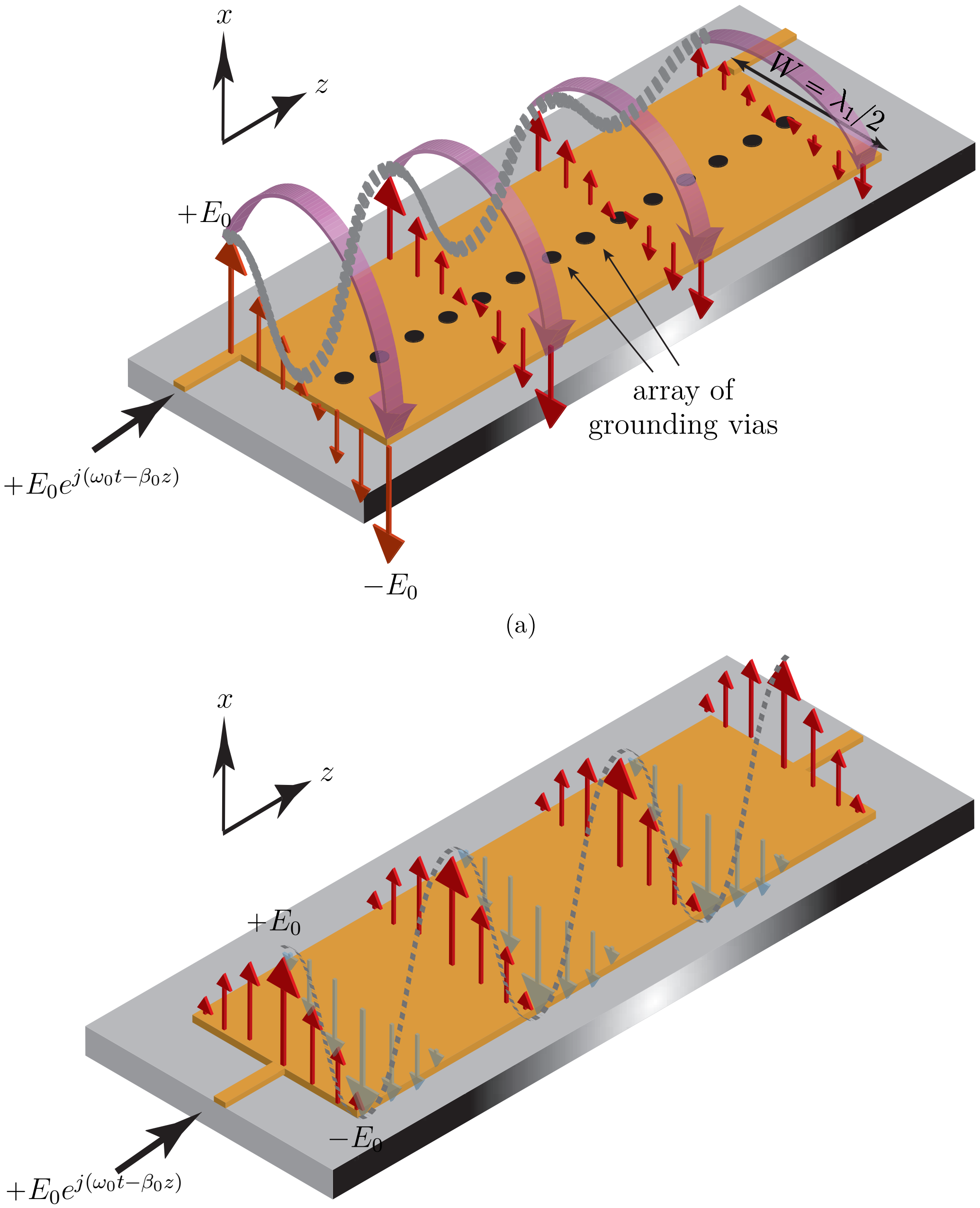

(a)

(b)

Figure 7.5 Field distribution along the LWA. (a) Leaky-mode (EH_1) odd electric, unaffected by the vias given their position in the nodal plane of the mode (xz plane, middle of the strip). (b) Dominant guided-mode (quasi-TEM) even electric field distribution with antinode in the plane mentioned in (b) and hence shorting (suppression) of this mode in the presence of the vias [9].

(β), although the difference with the unmodulated dispersion is negligible in the transition range, consistently with the weak modulation assumption. In uplink (green arrow), the wave is up-converted from $f_0 = 1.7$ GHz to $f_1 = 1.88$ GHz while in the downlink (magenta arrow), it is down-converted from $f_1 = 1.88$ GHz to $f_0 = 1.7$ GHz. The ratio between the frequency pair (f_1, f_0) is practically limited in terms the maximal acceptable size of the antenna. Indeed, as seen in Fig. 7.8, the antenna must be sufficiently long for the input power at f_0 to sufficiently convert, for a specified conversion efficiency, to the output power at f_1, and the antenna must have a length that is at least a couple of wavelengths of the *lowest* frequency. This means that, if $f_1/f_0 = \kappa$, then the antenna must be κ times longer than an antenna that would be conventionally operated at f_1. Figure 7.7 shows the relative error of the approximate dispersion relation, given by (7.4), with respect to the exact dispersion relation, obtained by (C-21), for the modulation indices $\delta_{\mathrm{m}} = 0.05$ and 0.15. As expected, the error is proportional to the modulation depth. Moreover, we see that the approximate solution of the dispersion diagram for $\delta_{\mathrm{m}} = 0.15$, corresponding to the design of Fig. 7.6 would be of less than 4%.

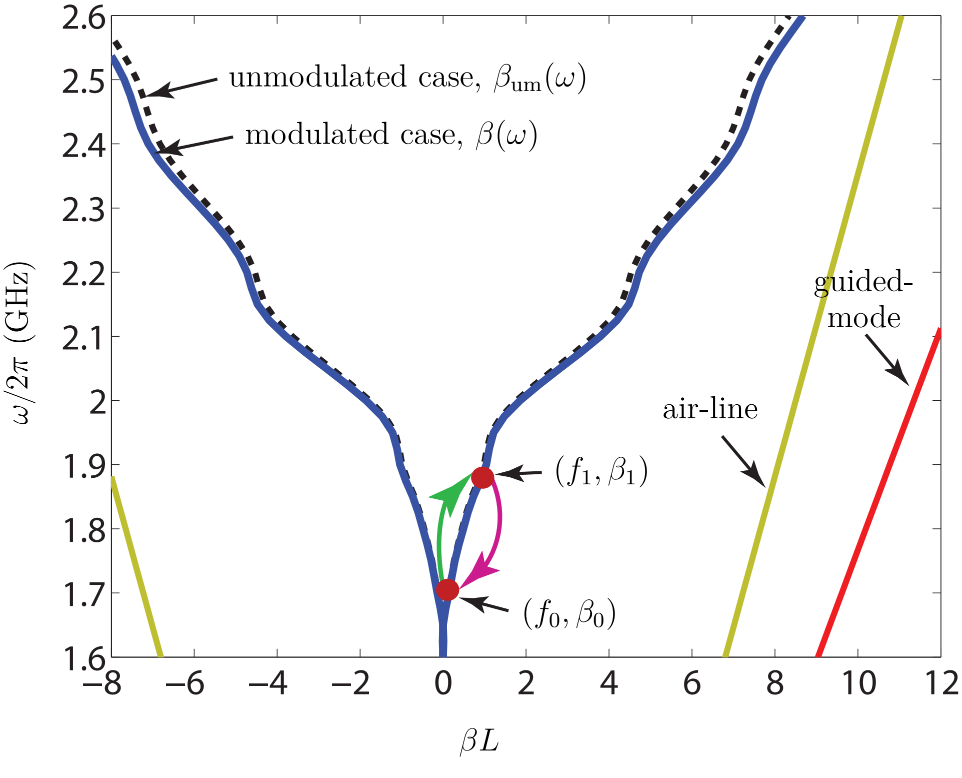

Figure 7.6 Dispersion diagram for the prototype depicted in Fig. 7.4(a) computed using (C-21) and (7.5) [9].

Figure 7.8(a) shows the exact and approximate squared real part of the field propagating along the structure for the uplink, computed using (7.3a) with (C-15) and (C-18) for the exact solutions and using (7.6) and (7.7) for the approximate solutions. The power of the in-

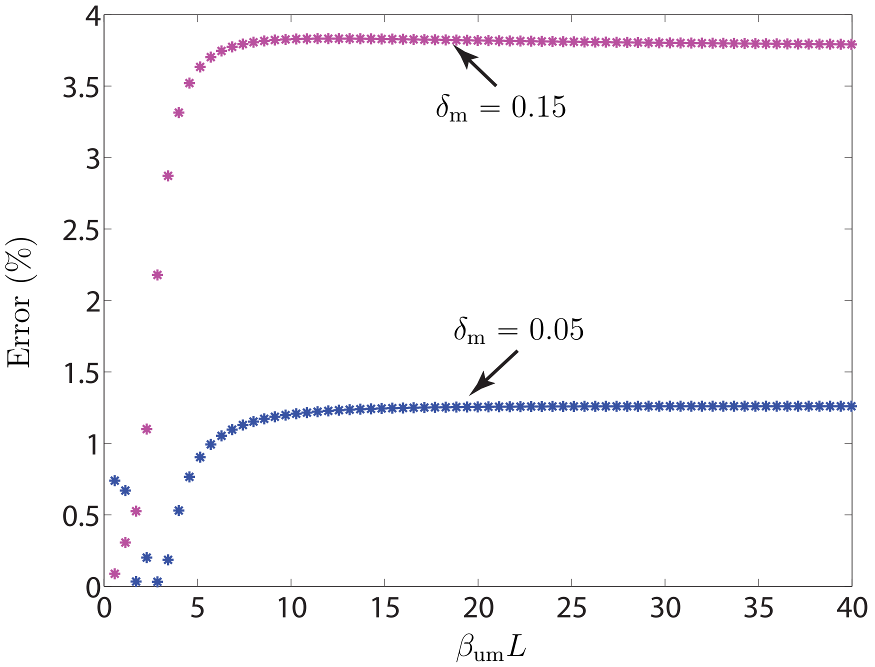

Figure 7.7 Relative error, ($\mid 1-\beta(\omega)/\beta^{\mathrm{exact}}(\omega) \mid \times 100$), of the approximate dispersion, $\beta(\omega)$, computed by (7.4), with respect to the exact dispersion, $\beta^{\mathrm{exact}}(\omega)$, numerically extracted from (C-21) for two specific modulation depths [9].

put wave (E_0^{m}, $f_0 = 1.7$ GHz) progressively transfers to the leaky wave (E_1^{m}, $f_0 = 1.88$ GHz) along the $+z$ direction, with conversion gain, as predicted in Sec. 7.1.2. At the same time, the power of the leaky mode exponentially decreases due to radiation. Similarly, Fig. 7.8(b) shows the squared real part of the field propagating along the structure for the downlink, computed using (7.7). Here, the power of the incoming wave (E_1^{m}, $f_0 = 1.88$ GHz) progressively transfers, still along the $+z$ direction, to the output wave (E_0^{m}, $f_0 = 1.7$ GHz). We see in Figs. 7.8(a) and 7.8(b) that the power level and, more importantly, the power decay, which corresponds to leaky-wave radiation, is much less for higher order space-time harmonics, i.e. E_{-1}^{m} and E_2^{m}, than it is for the input and radiating harmonics, E_0^{m} and E_1^{m}.

Figure 7.9 shows a photograph of the realized prototype. Band-stop filters centered at f_0 are used at the transmit and receive ports to ensure the suppression of unwanted harmonics, such as for instance f_{m} and f_{-1}.

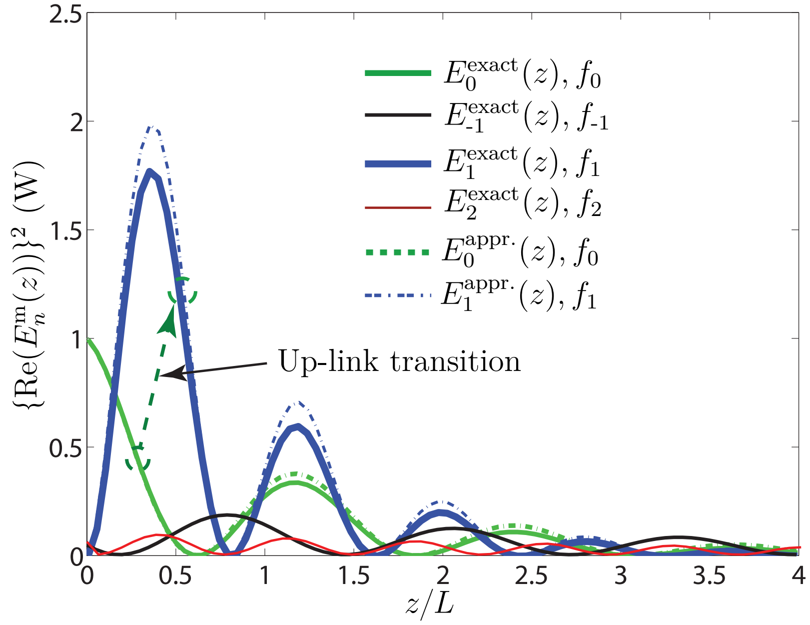

(a)

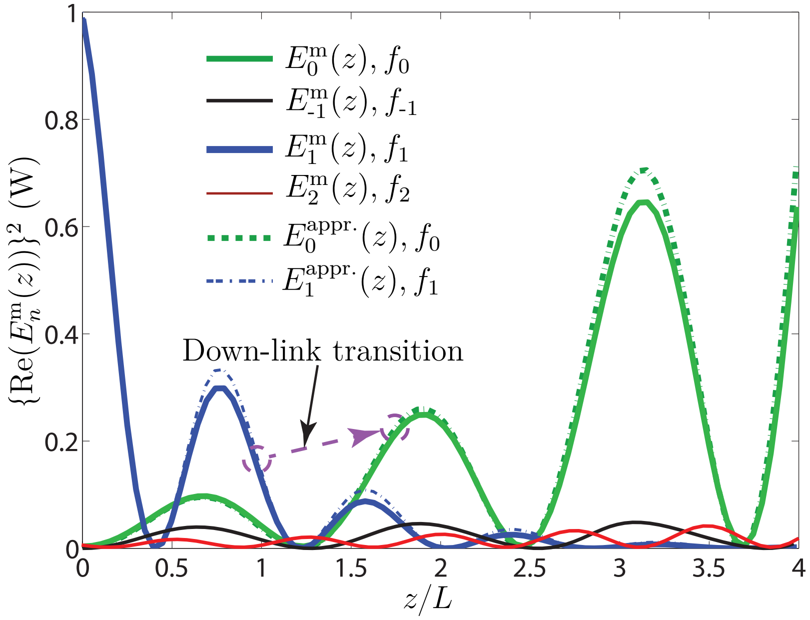

(b)

Figure 7.8 Squared real part of the electric field space-time harmonics, propagating in the $+z$ direction along the antenna for the (a) uplink and (b) downlink, where the approximate wave solutions for the up- and down-links, $E_0^{\mathrm{appr.}}(z)$ and $E_1^{\mathrm{appr.}}(z)$, obtained using (7.6) and (7.7) are compared with the exact wave solutions obtained using (7.3a) with (C-15) and (C-18) [9].

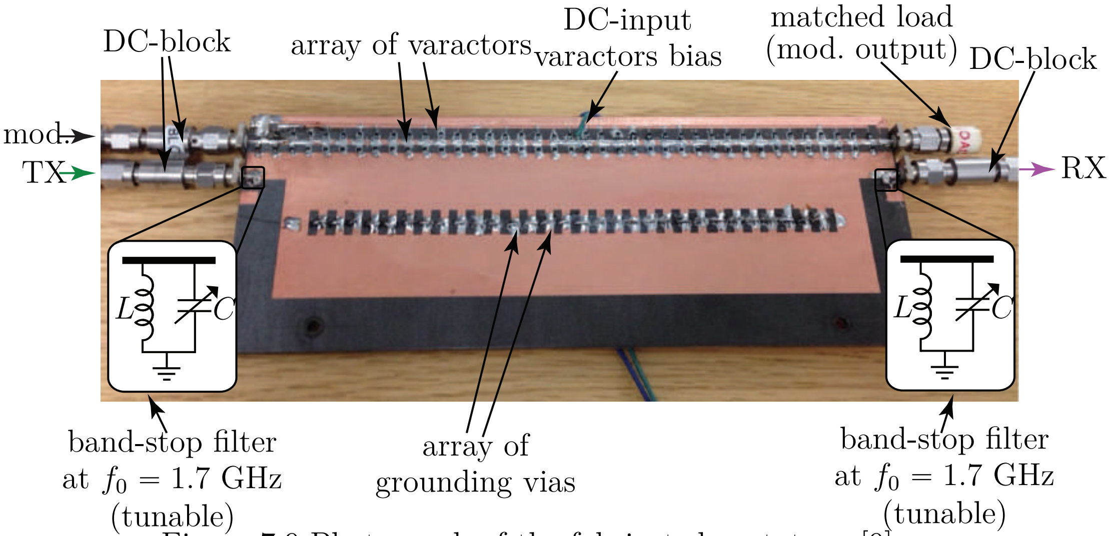

Figure 7.9 Photograph of the fabricated prototype [9].

7.4 Full-wave and Experimental Results

7.4.1 Matching and Measurement Setup

Figure 7.10 shows the full-wave and experimental matching of the transmit and receive ports of the antenna system in Fig 7.9 for an optimal varactor DC bias of 12 V [1] and the band-stop filters at both ports tuned at $f_0 = 1.7$ GHz.

Figure 7.11 shows the experimental setup, which uses a rotating reference antenna as a third port to model far-field radiation in both the transmit and receive regimes. Figure 7.12(a) and (b) show the photograph and schematic of the complete measurement setup, respectively. An Agilent E8267D signal generator, set at frequency $f_{\text{m}} = 0.18$ GHz and amplitude $P_{\text{m}} =$ 15 dBm, provides the modulation signal for the varactors. The distance between the reference and test antennas is about 1 m ($6.3\lambda_0$ at the radiation frequency $f_1 = 1.88$ GHz), which is beyond the far-field distance, $r_{\text{far-field}} \approx 0.5$ m. For the uplink, an Agilent E825D signal generator provides the input signal at the transmit port, with frequency $f_0 = 1.7$ GHz and amplitude $P_0 = 0$ dBm, while two spectrum analyzers (R&S FSIQ-40 and Agilent E4440A) measure the received power at the receive port and at the port of the rotating reference antenna. In the downlink, the Agilent E825D signal generator provides an input signal at the rotating reference antenna port, with frequency $f_1 = 1.88$ GHz and amplitude $P_0 = 0$ dBm, while the two spectrum analyzers measure the received power at the receive and transmit ports.

---

[1] At this voltage level, the component safely operates in the *linear* reverse-biased regime, so that related nonlinear effects are negligible.

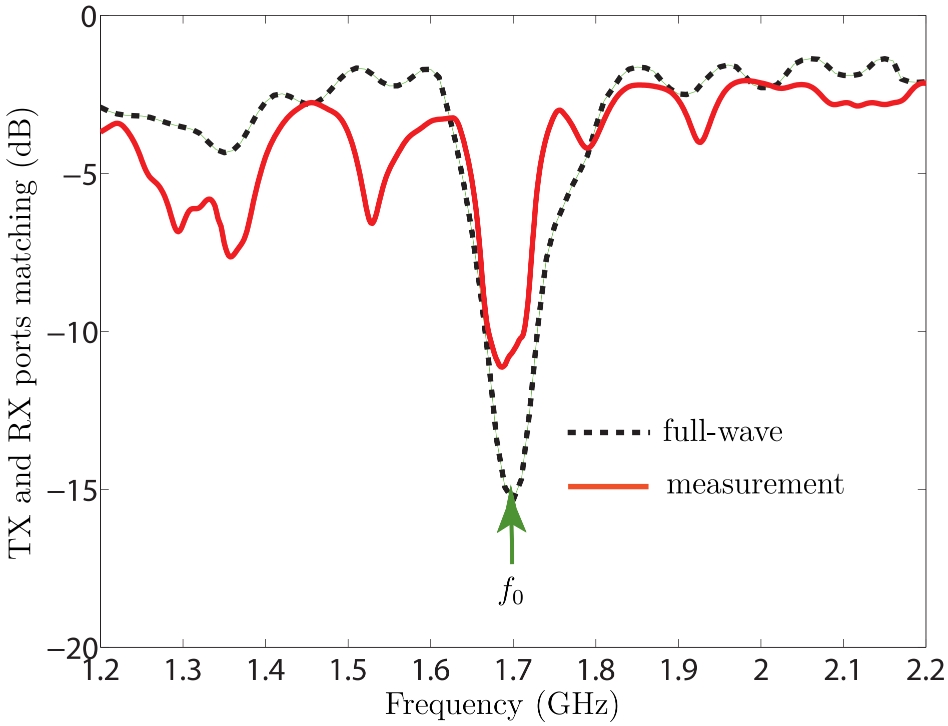

Figure 7.10 Matching of the transmit and receive ports of the antenna system in Fig 7.9 [9].

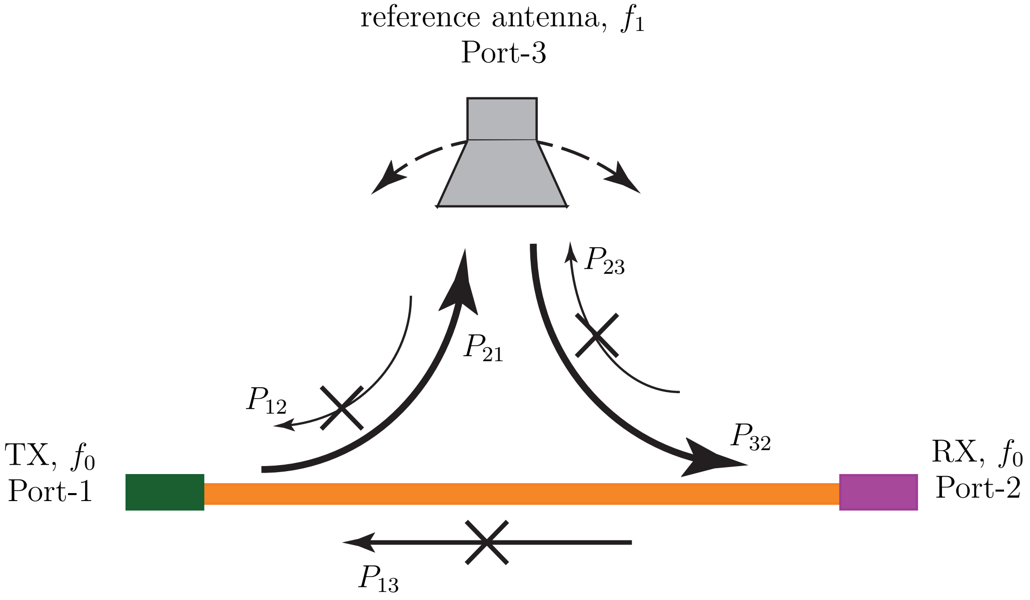

Figure 7.11 Experimental setup for the measurement of the mixer-duplexer-antenna system [9].

7.4.2 Fixed Radiation Beam

Figure 7.13 shows the full-wave and experimental normalized radiated powers at f_1 =1.88 GHz for the uplink, when the transmit port is excited at $f_0 = 1.7$ GHz. The maximum of the radiated power is at $\theta_1 = 4^\circ$. Figure 7.14(a) shows the full-wave and experimental normalized received powers at the receive and transmit ports for the downlink at $f_0 = 1.7$ GHz, when the reference antenna port is excited at $f_1 = 1.88$ GHz. The radiation efficiency is 74 %; it is mainly limited by the shortness of the antenna (due to fabrication limitation), as understood from Fig. 7.8. Figure 7.14(b) plots the isolation between the powers received at the receive and transmit ports. The isolation achieved at specified radiation angle ($\theta_1 = 4^\circ$) is about 31.5 dB. The discrepancy between the simulation and measurement results are mainly attributed to the imperfect modeling of the varactors in the simulation.

7.4.3 Frequency Beam Scanning

Frequency beam scanning is one of the interesting properties of leaky-wave antennas, where the radiation beam angle can be controlled by the operation frequency of the antenna [198]. However, it is more practical to control the radiation beam angle at fixed input frequency. For this reason, we perform here frequency beam scanning at fixed input frequency (f_0) by varying the modulation frequency (f_m) since this also results in varying the radiation frequency ($f_1 = f_0 + f_\mathrm{m}$).

Figures 7.15(a), 7.15(b) and 7.15(c) show the full-wave and experimental normalized radiated powers for uplink frequency beam scanning. The input frequency is $f_0 = 1.7$ GHz, and varying the modulation frequency as $f_\mathrm{m} = \{0.18, 0.22, 0.27, 0.3\}$ GHz yields the radiation frequencies $f_1 = \{1.88, 1.92, 1.97, 2\}$ GHz, corresponding to the radiation beam angles of $\theta_1 = \{4, 11.5, 18, 24.5\}^\circ$.

Figures 7.16(a) and 7.16(b) show the experimental normalized received power at the receive and transmit ports for downlink frequency beam scanning. The input frequency at the reference antenna port varies as $f_1 = \{1.88, 1.92, 1.97, 2\}$ GHz, corresponding to $f_\mathrm{m} = \{0.18, 0.22, 0.27, 0.3\}$ GHz, for a fixed received signal $f_0 = f_1 - f_\mathrm{m} = 1.7$ GHz. Finally, Fig. 7.17 plots the isolation between received powers at the receive and transmit ports.

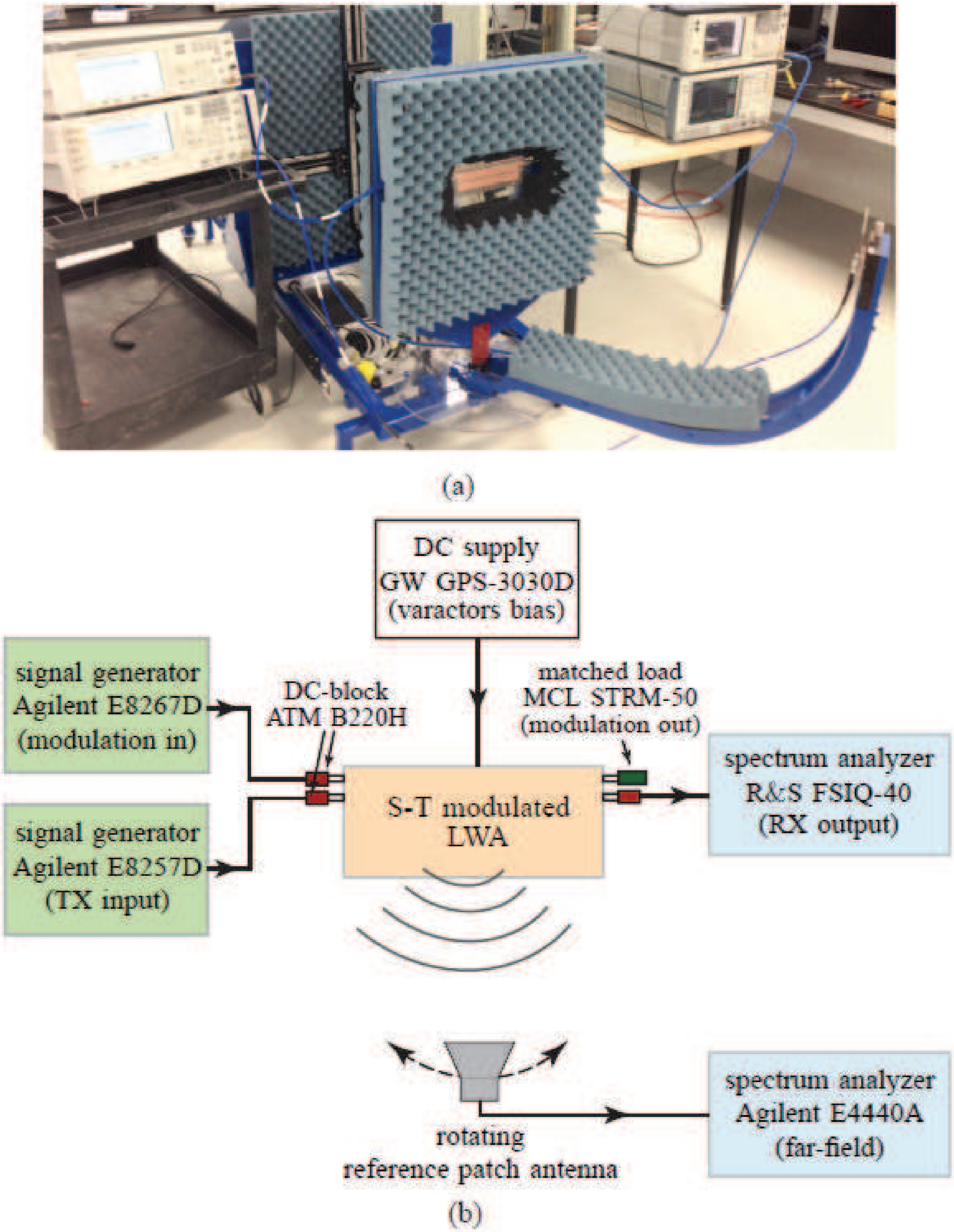

Figure 7.12 Measurement set-up. (a) Photograph. (b) Schematic [9].

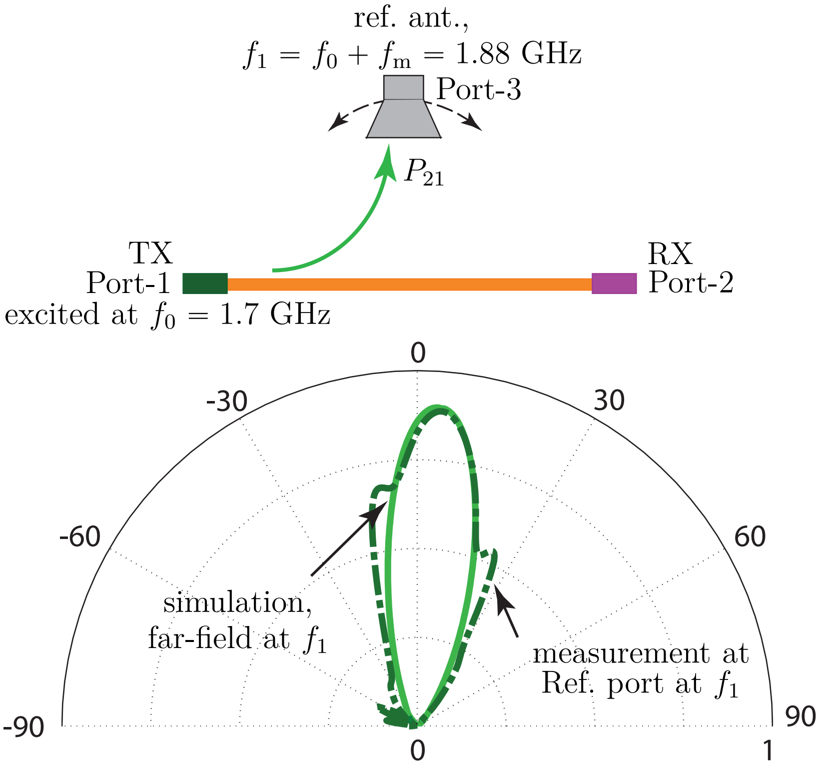

Figure 7.13 Uplink normalized power full-wave and measurement results [9].

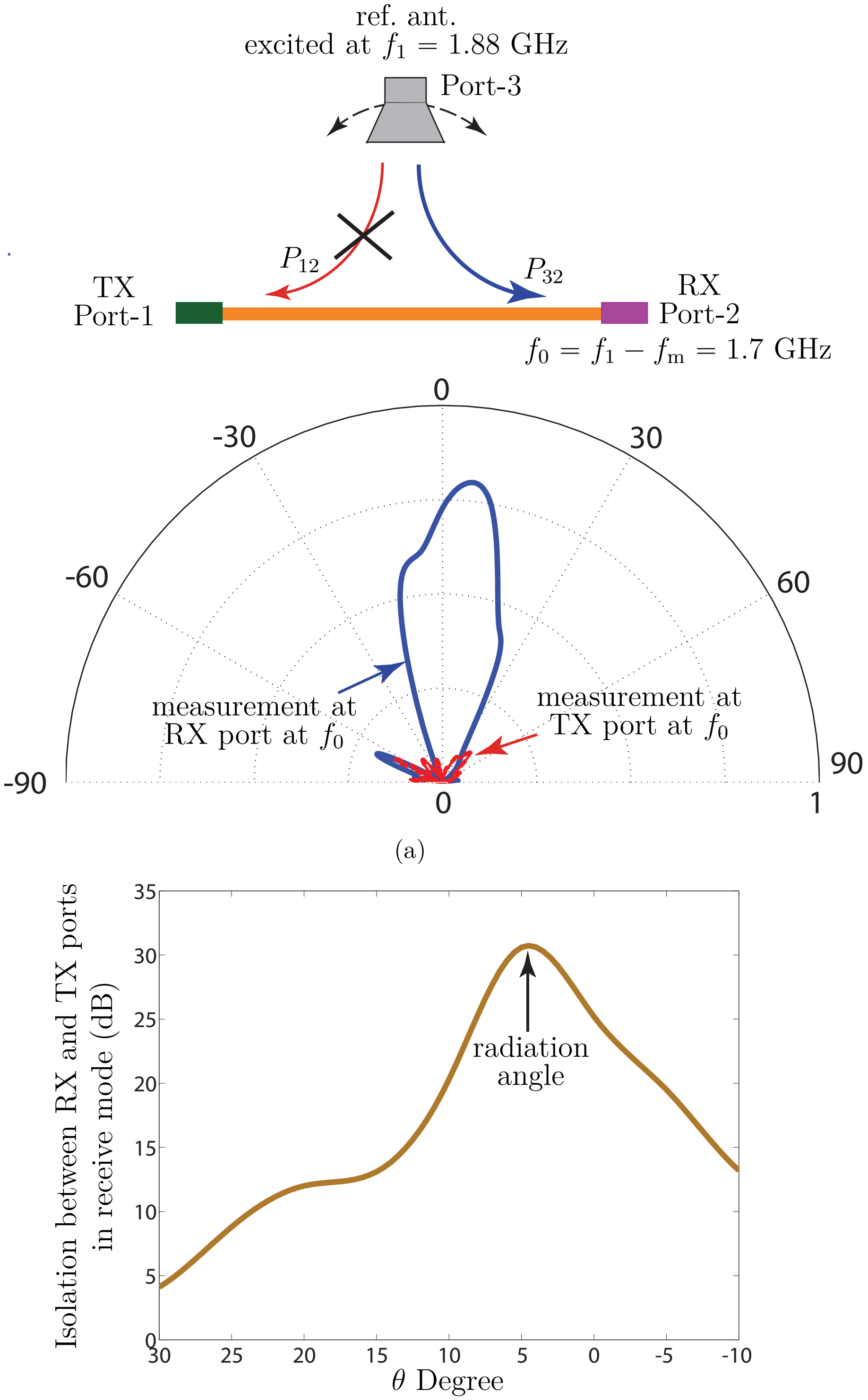

(a)

(b)

Figure 7.14 Downlink measurement results. (a) Normalized received power at the receive and transmit ports at $f_0 = 1.7$ GHz for the incoming wave with frequency $f_1 = 1.88$ GHz. (b) Isolation between received power at the receive and transmit ports [9].

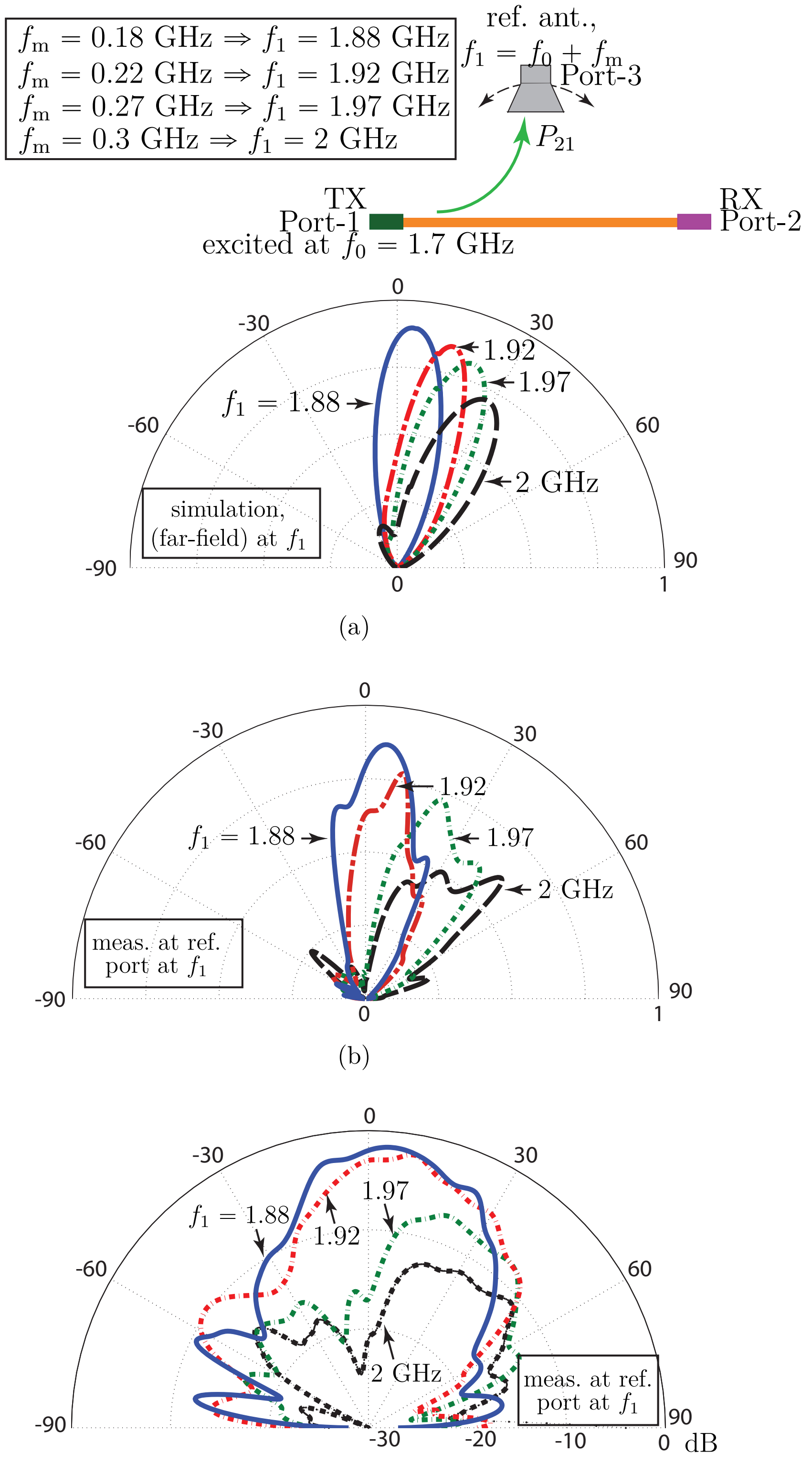

(a)

(b)

(c)

Figure 7.15 Uplink normalized scanning radiated power at $\theta_1 = \{4, 11.5, 18, 24.5\}^\circ$ for $f_1 = 1.88, 1.92, 1.97, 2$ GHz corresponding to $f_\mathrm{m} = 0.18, 0.22, 0.27, 0.3$ GHz for the input frequency $f_0 = 1.7$ GHz. (a) Simulation results. (b) Measurement. (c) Measurement in logarithmic scale [9].

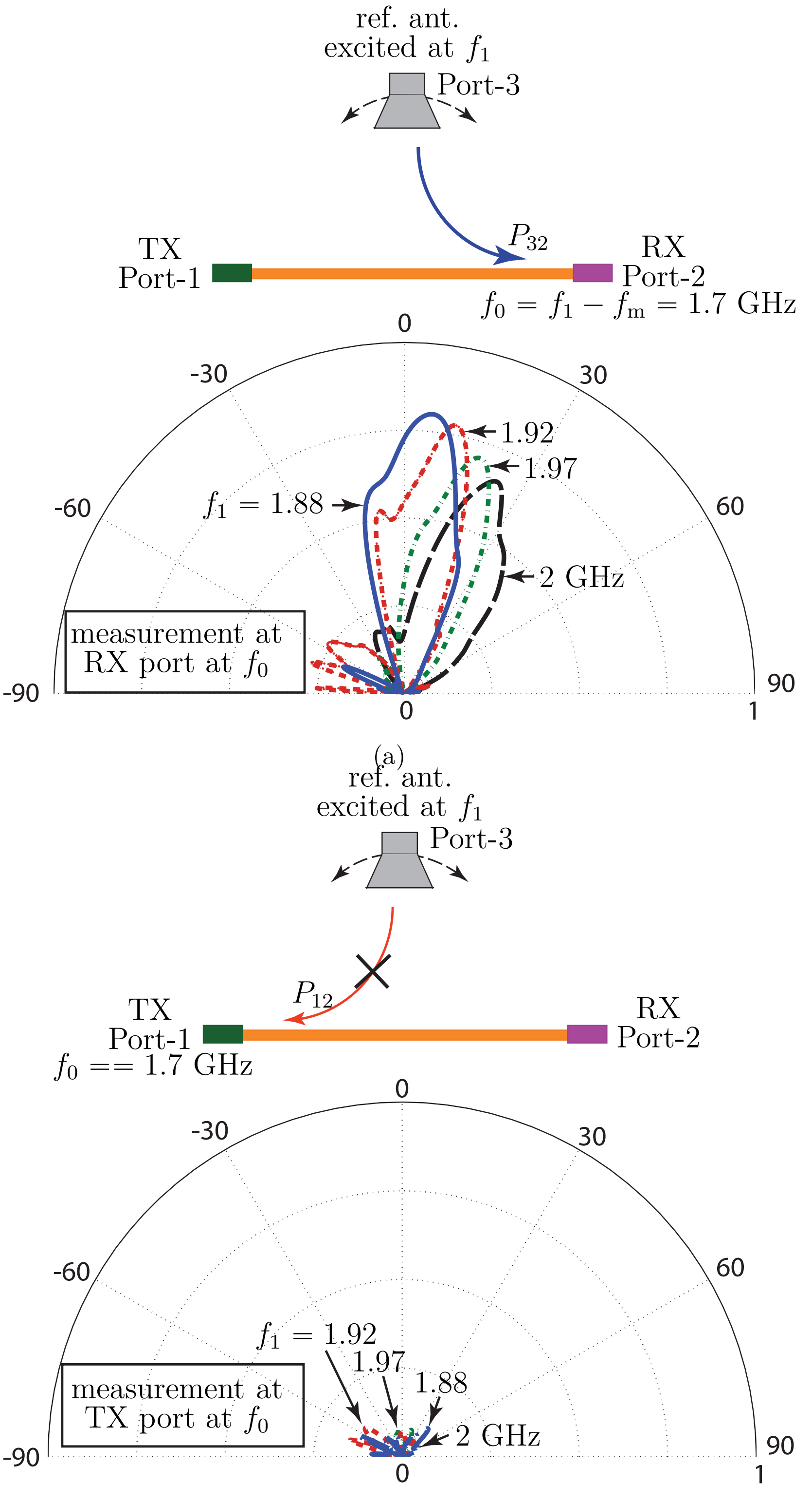

(a)

(b)

Figure 7.16 Downlink frequency beam scanning; Normalized received power at the RX and TX ports of the antenna $f_0 = 1.7$ GHz for different incoming wave frequency $f_1 = \{1.88, 1.92, 1.97, 2\}$ GHz corresponding to $f_m = \{0.18, 0.22, 0.27, 0.3\}$ GHz [9].

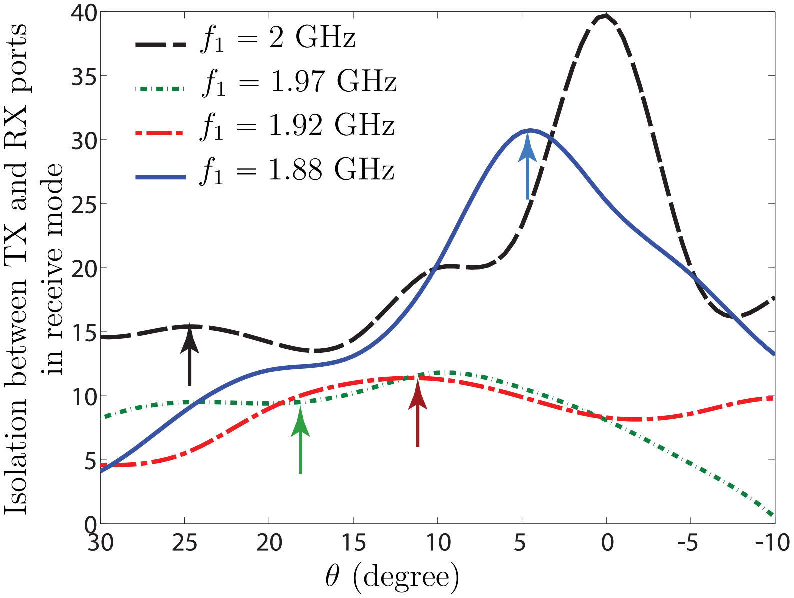

Figure 7.17 Downlink frequency beam scanning; Isolation between the RX and TX ports of the antenna f_0 = 1.7 GHz for different incoming wave frequency f_1 = 1.88, 1.92, 1.97, 2 GHz corresponding to f_m =0.18, 0.22, 0.27, 0.3 GHz [9].

CHAPTER 8 CONCLUSION AND FUTURE WORK

This thesis presented a collection of recent advances in space- and time-modulated dispersion engineered metamaterials.

8.1 Summary

Chapter 2 introduced the spatial and temporal dispersion engineering as well as the concept of continuously space, time and space-time modulation, and presented the general wave solution inside such electromagnetic systems. First, a general perspective on spatial and temporal dispersion engineered structures is given. Then, the realization scenario and general synthesis method of continuously space-modulated media is presented. Next, generic representation, functionality and electromagnetic wave propagation in a time-modulated medium is provided. Moreover, the realization of such a medium using array of distributed varactors is shown. Then, an overview on the operation, functionality and wave transmission through a space-time modulated medium is presented. Finally, realization of such a space-time modulated medium using an array of distributed varactors is demonstrated.

In Chapter 3, static contiguously space modulation has been presented as a mechanism for realization of broadband, flexible and versatile phasers. Two phasers have been introduced as follows.

– A continuously space-modulated coupled-line C-section phaser is introduced for enhanced bandwidth and profile diversity compared to step-discontinuity coupled-line C-section phasers. Such a phaser, that may be further cascaded for oscillation suppression and delay swing enhancement, represents a promising device for real-time analog signal processing (R-ASP).

  This space-varying C-section phaser, thanks to its extra topological degrees of freedom, provides group delay functions that are impossible to achieve by uniform C-section phasers. Moreover, it exhibits enhanced bandwidth, due to group delay periodicity breaking, smaller size, due to greater group delay shape flexibility, and also lower loss, due to shorter overall length. Moreover, phasers exhibiting Chebyshev group delay functions of different orders have been demonstrated.

  Nonuniform C-section phasers provide an efficient solution in radio analog signal processing (R-ASP). For instance, Dispersion Code Multiple Access (DCMA) has been recently proposed as a new technology for multiplexing [175, 176]. In this scheme, the two access points of each wireless channel share mutually conjugate dispersion codes, with corresponding conjugate response phasers, while the other channels use other conjugate dispersion codes and phasers. In this application, the number of channels is equal to the number of phaser responses, and the cross-channel interferences is minimized with optimal dispersion responses, provided by Chebyshev phasers.

- Nonuniform stub-line coupling-free phaser may represent an alternative solution to conventional coupled-line sections based phasers, as they reduce the complexity and lower the cost. Realization of transmission- and reflection-type continuously space-modulated stub-line phasers are experimentally presented, where the reflection-type version of the phaser leverages the high group delay swing of the open/short-terminated stubs and round-trip propagation of the wave inside the structure to enhance the resolution. Moreover, correlation between the group delay shapes and the electromagnetic energy distribution along the structure has been shown.

A nonreciprocal nongyrotropic magnetless metasurface is presented in Chapter 4 as a space-modulated spatiotemporally dispersion engineered medium. This metasurface operates as an active spatial isolator, providing transmission gain, with possible beam scanning, in one direction and transmission loss in the opposite direction, across a frequency bandwidth and a broad angular sector. The nonreciprocity of the metasurface is based on transistors rather than ferromagnetic materials, and therefore the metasurface features small form factor, light weight, and low cost. Moreover, it is nongyrotropic and thus immune of Faraday rotation, so that it is expected to find a specific range of applications, such as radar absorbers, novel one-way screens, illusion cloaks and isolating radomes.

Chapter 5 provided a general perspective of space-time modulation technique. This chapter studies scattering of obliquely incident electromagnetic waves from periodically space-time modulated slabs. It is shown that such a structure operates as a nonreciprocal harmonic generator. It is shown that the structure operates as a high pass filter in oblique incidence, where low frequency harmonics are filtered out in the form of surface waves, while high frequency harmonics are scattered as space waves. In the quasi-sonic regime, where the velocity of the space-time modulation is close to the velocity of the electromagnetic waves in the background medium, the incident wave strongly couples to the space-time harmonics in the forward direction while in the backward direction it exhibits low coupling to other harmonics. It is shown that a space-time modulated slab presents new degrees of freedom in electromagnetic wave transformation, including the transformation from a propagating-wave to surface-wave, electromagnetic wave isolation, mixing and amplification. Normal incidence dispersion diagram, isofrequency diagram and the physical representation of the wave propagation inside such a medium are also provided.

Chapter 6 exhibits how the space-time modulation may be leveraged to realize microwave and optical isolators. Three different isolators have been introduced based on different properties of the spatiotemporally modulated media which may find distinct applications. Following is a brief description of the three proposed isolators.

- The nonreciprocity in the sonic regime has been used for realization of an electromagnetic isolator. The space-time varying medium was realized at microwave frequencies and its operation as a quasi-sonic isolator was experimentally demonstrated.
- Space-time modulated slabs may be excited at the frequency corresponding to a electromagnetic bandgap, exciting the evanescent bandgap mode in the forward direction while exciting a propagating mode in the opposite direction. It has been shown that in the forward direction all the energy is reflected, while in the opposite direction, the incident wave is fully transferred to the other end of the space-time modulated slab by strongly coupling to one of its propagating modes, hence realizing an optical isolator and a reflection-type mixer. Since the attenuation in the block direction of the isolator is based on the progressive reflection of an evanescent wave, such an isolator requires a long structure to provide strong isolation. As a result, it may be more useful for optical isolation.
- Electromagnetic isolation maybe also achieved based on nonreciprocal coherency between the input wave and space-time modulated structure. In this scheme, the modulation and the incident wave have the same frequency and the operation of the structure is dictated by the phase difference between them. At certain phase shifts and modulation depths, corresponding to the coherency condition, the structure operates as an isolator. The proposed structure does not produce undesirable harmonics and has superior efficiency compared to previously reported space-time isolators. Moreover, the input signal modulates the structure itself, and hence it operates as a self biased isolator.

Finally, a mixer-duplexer-antenna leaky-wave nonreciprocal integrated system is presented in Chapter 7 based on periodic space-time modulation. The uplink and downlink conversions and duplexing are based on oblique directional space-time transitions from a microstrip leaky mode to itself. One of the interesting features of the system is its capability to perform beam scanning at a fixed signal frequency by varying modulation parameters, in particular the modulation frequency. The theoretical predictions have been verified by experimental demonstration. The proposed system may find applications in various radar, communication and instruments.

8.2 Future Direction

For future developments, it would be useful to extend the work presented in this thesis to discover unknown properties of space and space-time modulated spatiotemporal dispersion engineered media. This leads to realization of other enhanced efficiency and integrated electromagnetic systems. Below are a few directions to be studied.

- Space-time modulation may be used to realize a frequency multiplier.
- Analysis and experimental demonstration of space-time modulated metasurfaces.
- Further research on the oblique incidence on a space-time modulated slab is required to reveal all interesting features of such a medium.
- This thesis has focused on the spatial modulation in one-dimension, i.e. along z direction. Further researches on the two and three dimensional spatially or spatiotemporally modulated systems may reveal various intriguing phenomenon and their potential applications.
- Another interesting direction is the realization of space-time modulated isolator in optics. The optical version of the proposed isolators may be realized using other modulation techniques, e.g. based on electroptic effect.

REFERENCES

[1] S. Taravati, , S. Gupta, Q. Zhang, and C. Caloz, “Enhanced bandwidth and diversity in real-time analog signal processing (R-ASP) using nonuniform c-section phasers,” *IEEE Microw. Wireless Compon. Lett.*, vol. 26, no. 9, pp. 663–665, Sept. 2016.

[2] W. Rotman, “Plasma simulation by artificial dielectrics and parallel-plate media,” *IRE Trans. Antennas Propag.*, vol. 10, no. 1, pp. 82 – 95, Jan. 1962.

[3] C. Caloz, S. Gupta, Q. Zhang, and B. Nikfal, “Analog signal processing,” *Microw. Mag.*, vol. 14, no. 6, pp. 87–103, Sept. 2013, invited.

[4] S. Gupta, A. Parsa, E. Perret, R. V. Snyder, R. J. Wenzel, and C. Caloz, “Group delay engineered non-commensurate transmission line all-passnetwork for analog signal processing,” *IEEE Trans. Microw. Theory Techn.*, vol. 58, no. 9, pp. 2392–2407, Sept. 2010.

[5] S. Taravati and C. Caloz, “Versatile phasers constituted of coupling-free nonuniform stub-loaded transmission lines,” in *IEEE European Microw. Conf. (EuMC)*, Paris, France, Sept. 2015.

[6] S. Taravati, B. A. Khan, S. Gupta, K. Achouri, and C. Caloz, “Nonreciprocal nongyrotropic magnetless metasurface,” *IEEE Trans. Antennas Propagat.*, vol. 65, no. 7, pp. 3589–3597, Jul. 2017.

[7] S. Taravati, N. Chamanara, and C. Caloz, “Nonreciprocal electromagnetic scattering from a periodically space-time modulated slab and application to a quasi-sonic isolator,” *Accepted in Physical Review B, arXiv preprint arXiv :1705.06311*, 2017.

[8] N. Chamanara, S. Taravati, Z.-L. Deck-Léger, and C. Caloz, “Optical isolation based on space-time engineered asymmetric photonic bandgaps,” *arXiv preprint arXiv :1612.08398*, Dec. 2016.

[9] S. Taravati and C. Caloz, “Mixer-duplexer-antenna leaky-wave system based on periodic space-time modulation,” *IEEE Trans. Antennas Propagat.*, vol. 65, no. 2, pp. 1–11, Feb. 2017.

[10] W. Menzel, “A new travelling wave antenna in microstrip,” in *IEEE European Microw. Conf. (EuMC)*, Paris, France, Sept. 1978, pp. 302–306.

[11] D. R. Smith, W. J. Padilla, D. C. Vier, S. C. Nemat-Nasser, and S. Schultz, “Composite medium with simultaneously negative permeability and permittivity,” *Phys. Rev. Lett.*, vol. 84, no. 18, pp. 4184–4187, May 2000.

[12] J. B. Pendry, “Negative refraction makes a perfect lens,” *Phys. Rev. Lett.*, vol. 85, no. 18, pp. 3966– 3969, Oct. 2000.

[13] R. A. Shelby, D. R. Smith, S. C. Nemat-Nasser, and S. Schultz, “Microwave transmission through a two-dimensional, isotropic, left-handed metamaterial,” *Appl. Phys. Lett.*, vol. 78, no. 4, pp. 489– 491, Jan. 2001.

[14] C. Caloz, C.-C. Chang, and T. Itoh, “Full-wave verification of the fundamental properties of left-handed materials in waveguide configurations,” *J. Appl. Phys.*, vol. 90, no. 11, pp. 5483–5486, Dec. 2001.

[15] C. Caloz and T. Itoh, “Application of the transmission line theory of left-handed (LH) materials to the realization of a miemstrip "LH line",” in *IEEE AP-S Int. Antennas Propagat. (APS)*, DOI : 10.1109/APS.2002.1016111, Jun. 2002.

[16] J. B. Pendry, “Negative refraction,” *Contemporary Physics*, vol. 45, no. 3, pp. 191– 202, Jan. 2004.

[17] N. Engheta and R. W. Ziolkowski, *Metamaterials : Physics and Engineering Explorations.* John Wiley & Sons, 2006.

[18] D. Schurig, J. J. Mock, B. J. Justice, S. A. Cummer, J. B. Pendry, A. F. Starr, and D. R. Smith, “Metamaterial electromagnetic cloak at microwave frequencies,” *Science*, vol. 314, no. 5801, pp. 977–980, Nov. 2006.

[19] Z. Yu and S. Fan, “Complete optical isolation created by indirect interband photonic transitions,” *Nat. Photon.*, vol. 3, pp. 91 – 94, Jan. 2009.

[20] C. L. Holloway, E. F. Kuester, J. Gordon, J. O. Hara, J. Booth, D. R. Smith *et al.*, “An overview of the theory and applications of metasurfaces : The two-dimensional equivalents of metamaterials,” *IEEE Antennas Propag Mag*, vol. 54, no. 2, pp. 10–35, 2012.

[21] N. Yu, P. Genevet, M. A. Kats, F. Aieta, J.-P. Tetienne, F. Capasso, and Z. Gaburro, “Light propagation with phase discontinuities : Generalized laws of reflection and refraction,” *Sciences*, vol. 334, pp. 333–337, 2011.

[22] N. Yu and F. Capasso, “Flat optics with designer metasurfaces,” *Nature Materials*, vol. 13, pp. 139–150, 2014.

[23] V. M. Shalaev, “Optical negative-index metamaterials,” *Nature Photonics*, vol. 1, pp. 41–48, 2007.

[24] F. Capolino, *Theory and phenomena of metamaterials.* CRC Press, 2009.

[25] A. V. Zayats and S. Maier, *Active Plasmonics and Tuneable Plasmonic Metamaterials.* Wiley, 2013.

[26] N. Yu, P. Genevet, F. Aieta, M. A. Kats, R. Blanchard, G. Aoust, J.-P. Tetienne, Z. Gaburro, and F. Capasso, “Flat optics : Controlling wavefronts with optical antenna metasurfaces,” *IEEE J Sel Topics Quantum Electron*, vol. 9, no. 13, p. 4700423, 2013.

[27] M. Khalaj-Amirhosseini, “Wideband or multiband complex impedance matching using microstrip nonuniform transmission lines,” *Prog. Electromag. Res.*, vol. 66, p. 15–25, 2006.

[28] P. H. J. R. Zurita-Sánchez and J. C. Cervantes-González, “Reflection and transmission of a wave incident on a slab with a time-periodic dielectric function $\epsilon(t)$,” *Phys. Rev. A*, vol. 79, p. 053821, May 2009.

[29] H. Lira, Z. Yu, S. Fan, and M. Lipson, “Electrically driven nonreciprocity induced by interband photonic transition on a silicon chip,” *Phys. Rev. Lett.*, vol. 109, p. 033901, Jul. 2012.

[30] K. Lu, “An efficient method for analysis of arbitrary nonuniform transmission lines,” *IEEE Trans. Microw. Theory Techn.*, vol. 45, no. 1, pp. 9–14, Jan. 1997.

[31] A. T. Starr, “The nonuniform transmission line,” *Proc. IRE*, vol. 20, no. 6, pp. 1052–1063, Jun. 1932.

[32] J. Jeong and R. Nevels, “Time-domain analysis of a lossy nonuniform transmission line,” *IEEE Trans. Circ. Systems*, vol. 56, no. 2, pp. 157–161, Feb. 2009.

[33] M. H. Eghlidi, K. Mehrany, and B. Rashidian, “Analytical approach for analysis of nonuniform lossy/lossless transmission lines and tapered microstrips,” *IEEE Trans. Microw. Theory Techn.*, vol. 54, no. 12, pp. 4122–4129, Dec. 2006.

[34] P. Manfredi, D. D. Zutter, and D. V. Ginste, “Analysis of nonuniform transmission lines with an iterative and adaptive perturbation technique,” *IEEE Trans. Electromagnetic Compatibility*, vol. 58, no. 3, pp. 1022–1031, Jun. 2016.

[35] M. Khalaj-Amirhosseini, “Analysis of coupled nonuniform transmission lines using taylor’s series expansion,” *IEEE Trans. Electromagnetic Compatibility*, vol. 48, no. 3, pp. 594–600, Aug. 2006.

[36] E. Gad and M. Nakhla, “An efficient algorithm for sensitivity analysis of nonuniform transmission lines,” *IEEE Trans. Adv. Packaging*, vol. 28, no. 2, pp. 197–208, May 2005.

[37] T. Dhaene, L. Martens, and D. D. Zutter, “Transient simulation of arbitary nonuniform inetrconnection structures characterized by scattering parameters,” *IEEE Trans. Circ. Systems*, vol. 39, p. 928–937, Nov. 1992.

[38] J. E. Schutt-Aine, “Transient analysis of nonuniform transmission lines,” *IEEE Trans. Circ. Systems*, vol. 39, p. 378–385, May 1992.

[39] A. V. Beljaev, A. P. Krenitskiy, V. P. Meschanov, and L. V. Shikova, “Directional filters on coupled nonuniform tem transmission lines,” *IEEE Trans. Microw. Theory Techn.*, vol. 52, no. 1, pp. 133–138, Jan. 2004.

[40] G. Xiao and K. Yashiro, “Impedance matching for complex loads through nonuniform transmission lines,” *IEEE Trans. Microw. Theory Techn.*, vol. 50, no. 6, pp. 1520–1524, Jun. 2002.

[41] M. Khalaj-Amirhosseini and S. A. Akbarzadeh-Jahromi, “To optimally design microstrip nonuniform transmission lines as lowpass filters,” *Journal of Telecommunications*, vol. 2, no. 2, pp. 139–142, May 2010.

[42] S. Taravati and M. Khalaj-Amirhosseini, “Generalised single-section broad-band asymmetrical wilkinson power divider,” *IET Microw. Antennas Propagat.*, vol. 6, no. 10, pp. 1164 –1171, Jul. 2012.

[43] S. Taravati, “Realization of compact broadband rat-race coupler,” *Journal of Electromagnetic Waves and Applications*, vol. 26, no. 13, p. 1708–1715, Sept. 2012.

[44] S. Taravati and M. Khalaj-Amirhosseini, “Compact dual-band stubless branch-line coupler,” *Journal of Electromagnetic Waves and Applications*, vol. 26, no. 10, pp. 1323–1331, Jul. 2012.

[45] S. Taravati, “Miniaturized wide band rat race coupler,” *Int. J. RF Microw. Comput. Aided Eng.*, vol. 23, no. 6, pp. 675–681, Oct. 2013.

[46] S. Taravati and M. Khalaj-Amirhosseini, “An efficient method of designing dual- and wide-band power dividers with arbitrary power division,” *Int. J. RF Microw. Comput. Aided Eng.*, vol. 24, no. 1, p. 118–126, Jan. 2013.

[47] S. Taravati and M. Khalaj-Amirhosseini, “Design method for matching circuits of general multiplexers,” *IET Microw. Antennas Propagat.*, vol. 7, no. 4, pp. 237–244, Mar. 2013.

[48] L. Landau and E. Lifshits, *Electrodynamics of Continuous Media*, seond ed. Oxford, England : Pergamon Press, 1984.

[49] V. D. Shafranov, “Propagation of an electromagnetic field in a medium with spatial dispersion,” *Soviet Physics Jetp*, vol. 34(7), no. 6, pp. 1019–1029, Dec. 1958.

[50] J. Jackson, *Classical Electrodynamics*, 3rd ed. New York : John Wiley and Sons, 1999.

[51] P. A. Belov, R. Marqués, S. I. Maslovski, I. S. Nefedov, M. Silveirinha, C. R. Simovski, , and S. A. Tretyakov, “Strong spatial dispersion in wire media in the very large wavelength limit,” *Phys. Rev. B*, vol. 67, p. 113103, Mar. 2003.

[52] V. D. Shafranov, “Propagation of an electromagnetic field in a medium with spatial dispersion,” *Soviet Physics Jetp*, vol. 34(7), no. 6, pp. 1019–1029, Dec. 1958.

[53] C. Zhang and T. J. Cui, “Spatial dispersion and energy in strong chiral medium,” *Opt. Expr.*, vol. 15, no. 8, pp. 5114–5119, 2007.

[54] V. S. Asadchy, M. Albooyeh, S. N. Tcvetkova, A. Dı́ıaz-Rubio, Y. Ra’di, and S. A. Tretyakov, “Perfect control of reflection and refraction using spatially dispersive metasurfaces,” *Phys. Rev. B*, vol. 94, p. 075142, Aug. 2016.

[55] D. R. Jackson, C. Caloz, and T. Itoh, “Leaky-wave antennas,” *Proc. IEEE*, vol. 100, no. 7, pp. 2194–2206, Jul. 2012, invited.

[56] C. Caloz, T. Itoh, and A. Rennings, “CRLH metamaterial leaky-wave and resonant antennas,” *IEEE Antennas Propagat. Mag.*, vol. 50, no. 5, pp. 25–39, Oct. 2008, invited.

[57] J. L. G.-T. A. J. M.-Ros and G. Goussetis, “‘conformal tapered substrate integrated waveguide leaky-wave antenna,” *IEEE Trans. Antennas Propagat.*, vol. 62, no. 12, pp. 5983–5991, 2014.

[58] T. Kodera and C. Caloz, “Uniform ferrite-loaded open waveguide structure with CRLH response and its application to a novel backfire-to-endfire leaky-wave antenna,” *IEEE Trans. Microw. Theory Techn.*, vol. 57, no. 4, pp. 784–795, Apr. 2009.

[59] T. Kodera and C. Caloz, “Integrated leaky-wave antenna duplexer/diplexer using CRLH uniform ferrite-loaded open waveguide,” *IEEE Trans. Antennas Propagat.*, vol. 58, no. 8, pp. 2508–2514, Aug. 2010.

[60] T. Kodera and C. Caloz, “Low-profile leaky-wave electric monopole loop antenna using the $\beta = 0$ regime of a ferrite-loaded open waveguide,” *IEEE Trans. Antennas Propagat.*, vol. 58, no. 10, pp. 3165–3174, Oct. 2010.

[61] B. M. Schiffman, “A new class of broad-band microwave 90-degree phase shifters,” vol. 3, no. 2, pp. 232 – 237, Oct. 1955.

[62] A. Lujambio, I. Arnedo, M. Chudzik, I. Arregui, T. Lopetegi, and M. A. G. Laso, “Dispersive delay line with effective transmission-type operation in coupled-line technology,” *IEEE Trans. Microw. Theory Techn.*, vol. 21, no. 9, pp. 459–461, Sept. 2011.

[63] M. Chudzik, I. Arnedo, A. Lujambio, I. Arregui, I. Gardeta, F. Teberio, J. A. na, D. Benito, M. A. G. Laso, and T. Lopetegi, “Design of transmission-type nth-order differentiators in planar microwave technology,” vol. 60, no. 11, pp. 3384–3394, Nov. 2012.

[64] Q. Zhang, J. W. Bandler, and C. Caloz, “Design of dispersive delay structures (DDSs) formed by coupled C-sections using predistortion with space mapping,” *IEEE Trans. Microw. Theory Techn.*, vol. 61, no. 12, pp. 4040–4051, Dec. 2013.

[65] P. B. R. K. Mongia, I. J. Bahl and J. Hong, *RF and Microwave Coupled-Line Circuits*, 2nd ed. Artech House, 2007.

[66] W. Steenaart, "The synthesis of coupled transmission line all-pass networks in cascades of 1 to n," *IEEE Trans. Microw. Theory Techn.*, vol. 11, no. 1, p. 23–29, Jan. 1963.

[67] E. G. Cristal, "Analysis and exact synthesis of cascaded commensurate transmission line c-section all pass networks," *IEEE Trans. Microw. Theory Techn.*, vol. 14, no. 6, pp. 285–291, Jun. 1966.

[68] S. Abielmona, H. V. Nguyen, and C. Caloz, "Analog direction of arrival estimation using an electronically-scanned CRLH leaky-wave antenna," *IEEE Trans. Antennas Propagat.*, vol. 59, no. 4, pp. 1408–1412, Apr. 2011.

[69] B. Nikfal, D. Badiere, M. Repeta, B. Deforge, S. Gupta, and C. Caloz, "Distortion-less real-time spectrum sniffing based on a stepped group-delay phaser," *IEEE Microw. Wireless Compon. Lett.*, vol. 22, no. 11, pp. 601–603, Oct. 2012.

[70] B. Nikfal, Q. Zhang, and C. Caloz, "Enhanced-SNR impulse radio transceiver based on phasers," *IEEE Microw. Wireless Compon. Lett.*, vol. 24, no. 11, pp. 778–790, Nov. 2014.

[71] A. L. Cullen, "A travelling-wave parametric amplifier," *Nature*, vol. 181, p. 332, Feb. 1958.

[72] P. K. Tien, "Parametric amplification and frequency mixing in propagating circuits," *J. Appl. Phys.*, vol. 29, no. 9, pp. 1347–1357, Sept. 1958.

[73] A. Oliner and A. Hessel, "Guided waves on sinusoidally-modulated reactance surfaces," *IEEE Trans. Antennas Propagat.*, vol. 7, no. 5, pp. 201–208, Dec. 1959.

[74] E. S. Cassedy and A. A. Oliner, "Dispersion relations in time-space periodic media : part I-stable interactions," *Proc. IEEE*, vol. 51, no. 10, pp. 1342 – 1359, Jun. 1963.

[75] E. S. Cassedy, "Waves guided by a boundary with time-space periodic modulation," *Proc. IEE*, vol. 112, no. 2, pp. 269 – 279, Feb. 1965.

[76] E. S. Cassedy, "Dispersion relations in time-space periodic media : part II-unstable interactions," *Proc. IEEE*, vol. 55, no. 7, pp. 1154 – 1168, Jul. 1967.

[77] S. T. Peng, E. S. Cassedy, and B. R. Rao, "The sonic region for propagation in a parametric medium with harmonic pump modulation," *Proc. IEEE*, vol. 57, no. 2, pp. 224–225, Feb. 1969.

[78] R. Chu and T. Tamir, "Guided-wave theory of light diffraction by acoustic microwaves," *IEEE Trans. Microw. Theory Techn.*, vol. 17, no. 11, pp. 1002–1020, Nov. 1969.

[79] R. Chu and T. Tamir, “Wave propagation and dispersion in space-time periodic media,” *Proc. IEE*, vol. 119, no. 7, pp. 797–806, Jul. 1972.

[80] D. K. Kalluri, *Electromagnetics of Time Varying Complex Media : Frequency and Polarization Transformer*, 2nd ed. CRC, 2010.

[81] K. Fang, Z. Yu, and S. Fan, “Photonic Aharonov-Bohm effect based on dynamic modulation,” *Phys. Rev. Lett.*, vol. 108, p. 153901, Apr. 2012.

[82] M. B. Zanjani, A. R. Davoyan, A. M. Mahmoud, N. Engheta, and J. R. Lukes, “One-way phonon isolation in acoustic waveguides,” *Appl. Phys. Lett.*, vol. 104, p. 081905, Sept. 2014.

[83] S. Qin, Q. Xu, and Y. E. Wang, “Nonreciprocal components with distributedly modulated capacitors,” *IEEE Trans. Microw. Theory Techn.*, vol. 62, no. 10, pp. 2260–2272, Oct. 2014.

[84] J. N. Winn, S. Fan, J. D. Joannopoulos, and E. P. Ippen, “Interband transitions in photonic crystals,” *Phys. Rev. B*, vol. 59, pp. 1551–1554, Jan. 1999.

[85] E. J. Reed, M. Soljačić, and J. D. Joannopoulos, “Reversed Doppler effect in photonic crystals,” *Phys. Rev. Lett.*, vol. 91, no. 13, p. 133901, 2003.

[86] Z.-L. Deck-Léger and C. Caloz, “Wave scattering by superluminal space-time modulated slabs and symmetries with the subluminal case,” *arXiv :1611.01366v2 [physics.class-ph]*, Feb. 2017.

[87] Y. Hadad, D. L. Sounas, and A. Alù, “Space-time gradient metasurfaces,” *Phys. Rev. B*, vol. 92, no. 10, p. 100304, Sept. 2015.

[88] A. Shaltout, A. Kildishev, and V. Shalaev, “Time-varying metasurfaces and Lorentz nonreciprocity,” *Opt. Mat. Exp.*, vol. 5, no. 11, pp. 2459–2467, Oct. 2015.

[89] Y. Shi and S. Fan, “Dynamic non-reciprocal meta-surfaces with arbitrary phase reconfigurability based on photonic transition in meta-atoms,” *Appl. Phys. Lett.*, vol. 108, p. 021110, Jan. 2016.

[90] S. Taravati and C. Caloz, “Space-time modulated nonreciprocal mixing, amplifying and scanning leaky-wave antenna system,” in *IEEE AP-S Int. Antennas Propagat. (APS)*, Vancouver, Canada, 2015.

[91] D. Correas-Serrano, J. S. Gomez-Diaz, D. L. Sounas, Y. Hadad, A. Alvarez-Melcon, and A. Alù, “Non-reciprocal graphene devices and antennas based on spatiotemporal modulation,” *IEEE Antennas Wirel. Propagat. Lett.*, 2015.

[92] D. Ramaccia, D. L. Sounas, A. Alù, F. Bilotti, and A. Toscano, “Nonreciprocal horn antennas using angular momentum-biased metamaterial inclusions,” *IEEE Trans. Antennas Propagat.*, vol. 63, no. 12, pp. 5593–5600, Dec. 2015.

[93] Y. Hadad, J. C. Soric, and A. Alù, "Breaking temporal symmetries for emission and absorption," *Proc. Natl. Acad. Sci. U.S.A.*, vol. 113, no. 13, pp. 3471–3475, Mar. 2016.

[94] D. L. Sounas, C. Caloz, and A. Alù, "Giant nonreciprocity at the subwavelength scale using angular-momentum biased metamaterials," *Nat. Commun*, vol. 4, no. 2407, Sept. 2013.

[95] N. A. Estep, D. L. Sounas, J. Soric, and A. Alù, "Magnetic-free non-reciprocity and isolation based on parametrically modulated coupled-resonator loops," *Nat. Phys.*, vol. 10, pp. 923–927, Nov. 2014.

[96] Y. Hadad, J. Soric, and A. Alù, "Spatiotemporally modulated antennas," in *CNC/USNC URSI National Radio Science Meeting*, Vancouver, Canada, 2015, p. 159.

[97] M. A. G. Laso, T. Lopetegi, M. J. Erro, D. Benito, M. J. Garde, M. A. Muriel, M. Sorolla, and M. Guglielmi, "Real-time spectrum analysis in microstrip technology," *IEEE Trans. Microw. Theory Techn.*, vol. 51, no. 3, pp. 705–717, Mar. 2003.

[98] M. A. G. Laso, T. Lopetegi, M. J. Erro, D. Benito, M. J. Garde, M. A. Muriel, M. Sorolla, and M. Guglielmi, "Chirped delay lines in microstrip technology," *IEEE Trans. Microw. Theory Techn.*, vol. 11, no. 12, pp. 486–488, Dec. 2011.

[99] J. D. Schwartz, M. M. Guttman, J. A. na, and D. V. Plant, "Multichannel filters using chirped bandgap structures in microstrip technology," *IEEE Microw. Wireless Compon. Lett.*, vol. 17, no. 8, pp. 577–579, Aug. 2007.

[100] I. Arnedo, I. Arregui, A. Lujambio, M. Chudzik, M. lA. G. Laso, and T. Lopetegi, "Synthesis of microwave filters by inverse scattering using a closed-form expression valid for rational frequency responses," *IEEE Trans. Microw. Theory Techn.*, vol. 60, no. 5, pp. 1244–1257, May 2012.

[101] J. D. Schwartz, J. A. na, and D. V. Plant, "A fully electronic system for the time magnification of ultra-wideband signals," *IEEE Trans. Microw. Theory Techn.*, vol. 55, no. 2, pp. 327–334, Feb. 2007.

[102] T. Lopetegi, M. A. G. Laso, J. Hernández, M. Bacaicoa, D. Benito, M. J. Garde, M. Sorolla, and M. Guglielmi, "New microstrip "wiggly-line" filters with spurious passband suppression," *IEEE Trans. Microw. Theory Techn.*, vol. 49, no. 9, pp. 1593–1598, Sept. 2001.

[103] W. Hong, T.-L. Chen, C.-Y. Chang, J.-W. Sheen, and Y.-D. Lin, "Broadband tapered microstrip leaky-wave antenna," *IEEE Trans. Antennas Propagat.*, vol. 51, no. 8, p. 1922–1928, 2003.

[104] O. Losito, "A simple design of broadband tapered leaky-wave antenna," *Microw. Opt. Technology Lett.*, vol. 49, no. 11, p. 2933–2838, 2007.

[105] A. J. Martinez-Ros, J. L. Gómez-Tornero, and G. Goussetis, “Conformal tapered substrate integrated waveguide leaky-wave antenna,” *IEEE Trans. Antennas Propagat.*, vol. 62, no. 12, p. 5983–5991, 2014.

[106] A. J. Martinez-Ros, J. L. Gómez-Tornero, V. Losada, F. Mesa, and F. Medina, “Non-uniform sinusoidally modulated half-mode leaky-wave lines for near-field focusing pattern synthesis,” *IEEE Trans. Antennas Propagat.*, vol. 63, no. 3, pp. 1022–1031, Mar. 2015.

[107] S. Taravati, Q. Zhang, and C. Caloz, “Non-uniform c-section phasers for enhanced design flexibility in radio analog signal processing,” in *IEEE European Microw. Conf. (EuMC)*, Rome, Italy, Oct. 2014.

[108] A. G. Gurevich and G. A. Melkov, *Magnetization Oscillations and Waves*, 1st ed. CRC Press, 1996.

[109] Z. Wang and S. Fan, “Optical circulators in two-dimensional magneto-optical photonic crystals,” *Optics Letters*, vol. 30, pp. 1989–1991, 2005.

[110] Z. Yu, G. Veronis, Z. Wang, and S. Fan, “One-way electromagnetic waveguide formed at the interface between a plasmonic metal under a static magnetic field and a photonic crystal,” *Physical Review Letters*, vol. 100, p. 023902, 2008.

[111] L. B. J. Hu, P. Jiang, D. H. Kim, G. F. Dionne, L. C. Kimerling, and C. A. Ross, “On-chip optical isolation in monolithically integrated non-reciprocal optical resonators,” *Nature Photonics*, vol. 5, pp. 758–762, 2011.

[112] A. Parsa, T. Kodera, and C. Caloz, “Ferrite based non-reciprocal radome, generalized scattering matrix analysis and experimental demonstration,” *IEEE Trans. Antennas Propagat.*, vol. 59, no. 3, pp. 810–817, Mar. 2011.

[113] Y. Mazor and B. Z. Steinberg, “Metaweaves : Sector-way nonreciprocal metasurfaces,” *Physical Review Letters*, vol. 112, p. 153901, 2014.

[114] A. M. Mahmoud, A. R. Davoyan, and N. Engheta, “All-passive nonreciprocal metastructure,” *Nature Communications*, vol. 6, pp. 1–7, 2014.

[115] V. K. Valev, J. J. Baumberg, B. D. Clercq, N. Braz, X. Zheng, E. J. Osley, S. Vandendriessche, M. Hojeij, C. Blejean, C. G. Mertens, J.and Biris, V. Volskiy, M. Ameloot, Y. Ekinci, G. A. E. Vandenbosch, P. A. Warburton, V. V. Moshchalkov, N. C. Panoiu, and T. Verbiest, “Nonlinear superchiral meta-surfaces : Tuning chirality and disentangling non-reciprocity at the nanoscale,” *Advanced Materials*, vol. 26, p. 4074–4081, 2014.

[116] Z.-M. Gu, J. Hu, B. Liang, X.-Y. Zou, and J.-C. Cheng, “Broadband non-reciprocal transmission of sound with invariant frequency,” *Sientific Reports*, vol. 6, 2016.

[117] D. L. Sounas, C. Caloz, and A. Alù, "Giant nonreciprocity at the subwavelength scale using angular-momentum biased metamaterials," *Nature Communications*, vol. 4, p. 246293, 2013.

[118] S. Taravati and C. Caloz, "Mixer-duplexer-antenna leaky-wave system based on periodic space-time modulation," *IEEE Trans. Antennas Propagat.*, vol. 65, no. 2, pp. 442 – 452, Feb. 2017.

[119] T. Kodera, D. L. Sounas, and C. Caloz, "Artificial faraday rotation using a ring metamaterial structure without static magnetic field," *Applied Physics Letters*, vol. 99, no. 3, p. 031114, 2011.

[120] Z. Wang, Z. Wang, J. Wang, B. Zhang, J. Huangfu, J. D. Joannopoulos, M. Soljačić, and L. Rana, "Gyrotropic response in the absence of a bias field," *Proc. Natl. Acad. Sci. U.S.A.*, vol. 109, no. 33, p. 13194–13197, Aug. 2012.

[121] T. Kodera, D. L. Sounas, and C. Caloz, "Magnetless non-reciprocal metamaterial (MNM) technology : application to microwave components," *IEEE Trans. Microw. Theory Techn.*, vol. 61, no. 3, pp. 1030–1042, Mar. 2013.

[122] D. L. Sounas, T. Kodera, and C. Caloz, "Electromagnetic modeling of a magnetless nonreciprocal gyrotropic metasurface," *IEEE Trans Antennas Propag*, vol. 61, no. 1, pp. 221–231, 2013.

[123] Y. Shi, Z. Yu, and S. Fan, "Limitations of nonlinear optical isolators due to dynamic reciprocity," *Nature Photonics*, vol. 9, pp. 388–392, 2015.

[124] B. Lax and K. J. Button, *Microwave Ferrites and Ferrimagnetics.* New York : McGraw-Hill, 1962.

[125] S. Tanaka, N. Shimomura, and K. Ohtake, "Active circulators–the realization of circulators using transistors," *Proc. IEEE*, vol. 53, no. 3, pp. 260–267, 1965.

[126] G. Carchon and B. Nanwelaers, "Power and noise limitations of active circulators," *IEEE Trans. Microw. Theory Tech.*, vol. 48, no. 2, pp. 316–319, 2000.

[127] M. Soljačić, C. Luo, J. D. Joannopoulos, and S. Fan, "Nonlinear photonic crystal microdevices for optical integration," *Opt. Lett.*, vol. 28, no. 8, pp. 637–639, 2003.

[128] L. Fan, J. Wang, L. T. Varghese, H. Shen, B. Niu, Y. Xuan, A. M. Weiner, and M. Qi, "An all-silicon passive optical diode," *Sci.*, vol. 335, no. 6067, pp. 447–450, 2012.

[129] A. M. Mahmoud, A. R. Davoyan, and N. Engheta, "All-passive nonreciprocal metastructure," *Nat. Commun.*, vol. 6, 2015.

[130] Y. Shi, Z. Yu, and S. Fan, "Limitations of nonlinear optical isolators due to dynamic reciprocity," *Nat. Photon.*, vol. 9, no. 6, pp. 388–392, 2015.

[131] C. E. Rüter, K. G. Makris, R. El-Ganainy, D. N. Christodoulides, M. Segev, and D. Kip, "Observation of parity–time symmetry in optics," *Nat. Phys.*, vol. 6, no. 3, pp. 192–195, 2010.

[132] Z. Lin, H. Ramezani, T. Eichelkraut, T. Kottos, H. Cao, and D. N. Christodoulides, "Unidirectional invisibility induced by p t-symmetric periodic structures," *Phys. Rev. Lett.*, vol. 106, no. 21, p. 213901, 2011.

[133] U. Al Khawaja, S. Al-Marzoug, H. Bahlouli, and Y. S. Kivshar, "Unidirectional soliton flows in pt-symmetric potentials," *Phys. Rev. A*, vol. 88, no. 2, p. 023830, 2013.

[134] B. Peng, S. K. Ozdemir, F. Lei, F. Monifi, M. Gianfreda, G. L. Long, S. Fan, F. Nori, C. M. Bender, and L. Yang, "Nonreciprocal light transmission in parity-time-symmetric whispering-gallery microcavities," *arXiv Prepr. arXiv :1308.4564*, 2013.

[135] L. Chang, X. Jiang, S. Hua, C. Yang, J. Wen, L. Jiang, G. Li, G. Wang, and M. Xiao, "Parity-time symmetry and variable optical isolation in active-passive-coupled micro-resonators," *Nat. Photon.*, vol. 8, no. 7, pp. 524–529, 2014.

[136] C. He, M.-H. Lu, X. Heng, L. Feng, and Y.-F. Chen, "Parity-time electromagnetic diodes in a two-dimensional nonreciprocal photonic crystal," *Phys. Rev. B*, vol. 83, no. 7, p. 075117, 2011.

[137] L. Feng, Y.-L. Xu, W. S. Fegadolli, M.-H. Lu, J. E. Oliveira, V. R. Almeida, Y.-F. Chen, and A. Scherer, "Experimental demonstration of a unidirectional reflectionless parity-time metamaterial at optical frequencies," *Nat. Mater.*, vol. 12, no. 2, pp. 108–113, 2013.

[138] K. G. Makris, R. El-Ganainy, D. N. Christodoulides, and Z. H. Musslimani, "Pt-symmetric optical lattices," *Phys. Rev. A*, vol. 81, no. 6, p. 063807, 2010.

[139] M. Kulishov, J. Laniel, N. Bélanger, J. Azaña, and D. Plant, "Nonreciprocal waveguide bragg gratings," *Opt. Expr.*, vol. 13, no. 8, pp. 3068–3078, 2005.

[140] L. Poladian, "Resonance mode expansions and exact solutions for nonuniform gratings," *Phys. Rev. E*, vol. 54, no. 3, p. 2963, 1996.

[141] G. Buchta, "Magnetically scanned reciprocal and nonreciprocal leaky-wave antennas," *Proc. IEEE*, vol. 52, no. 5, pp. 625–626, May 1964.

[142] T. Ueda, K. Horikawa, M. Akiyama, and M. Tsutsumi, "Nonreciprocal phase-shift composite right/left handed transmission lines and their application to leaky wave antennas," *IEEE Trans. Antennas Propagat.*, vol. 57, no. 7, pp. 1995–2005, Jul. 2009.

[143] T. Kodera and C. Caloz, "Dual-band full-space scanning leaky-wave antenna based on ferrite-loaded open waveguide," *IEEE Antennas Wirel. Propagat. Lett.*, vol. 8, pp. 1202–1205, Nov. 2009.

[144] T. Kodera, D. L. Sounas, and C. Caloz, “Non-reciprocal magnet-less CRLH leaky-wave antenna based on a ring metamaterial structure,” *IEEE Antennas Wirel. Propagat. Lett.*, vol. 10, pp. 1551–1554, Jan. 2012.

[145] N. Apaydin, K. Sertel, and J. L. Volakis, “Nonreciprocal leaky-wave antenna based on coupled microstrip lines on a non-uniformly biased ferrite substrate,” *IEEE Trans. Antennas Propagat.*, vol. 61, no. 7, pp. 3458–3465, Jul. 2013.

[146] N. Apaydin, K. Sertel, and J. L. Volakis, “Nonreciprocal and magnetically scanned leaky-wave antenna using coupled CRLH lines,” *IEEE Trans. Antennas Propagat.*, vol. 62, no. 6, pp. 2954–2961, Jun. 2014.

[147] M. Khalaj-Amirhosseini, “Analytic solution of non-uniform transmission lines at low frequencies,” *IET Microw. Antennas Propagat.*, vol. 3, no. 8, pp. 1218–1223, Dec. 2009.

[148] C. R. Paul, *Analysis of Multiconductor Transmission Lines.* John Wiley and Sons, 1994.

[149] D. M. Pozar, *Microwave Engineering*, 4th ed. John Wiley & Sons, Inc., 2012.

[150] J. S. Martínez-Romero, O. M. Becerra-Fuentes, and P. Halevi, “Temporal photonic crystals with modulations of both permittivity and permeability,” *Phys. Rev. A*, vol. 93, p. 063813, 2016.

[151] J. R. Reyes-Ayona and P. Halevi, “Electromagnetic wave propagation in an externally modulated low-pass transmission line,” *IEEE Trans. Microw. Theory Techn.*, vol. 64, no. 11, pp. 3449–3459, Nov. 2016.

[152] L. Landau and E. Lifshits, *Electrodynamics of Continuous Media*, seond ed. Oxford, England : Pergamon Press, 1984.

[153] O. Luukkonen, P. Alitalo, F. Costa, C. Simovski, A. Monorchio, and S. Tretyakov, “Experimental verification of the suppression of spatial dispersion in artificial plasma,” vol. 96, no. 8, p. 081501, Feb. 2010.

[154] A. Serdyukov, I. Semchenko, S. Tretyakov, and A. Sihvola, *Electromagnetics of BI-Ansotropic Materials : Theory and Applications.* Gordon and Branch Science Publishers, 2001.

[155] C. R. Simovski and P. A. Belov, “Low-frequency spatial dispersion in wire media,” vol. 70, p. 046616, 2004.

[156] F. Perez-Rodriguez, F. Diaz-Mongel, N. M. Makarov, R. Marquez-1slas, and B. Flores-Desirena, “Spatial-dispersion effects in one-dimensional photonic crystals with metallic inclusions,” in *Sixth International Kharkov Symposium on Physics and Engineering of Microwaves, Millimeter and Submillimeter Waves and Workshop on Terahertz Technologies*, Kharkov, Ukraine, Jun. 2007.

[157] P. Burghignoli, G. Lovat, F. Capolino, D. R. Jackson, and D. R. Wilton, "Directive leaky-wave radiation from a dipole source in a wire-medium slab," *IEEE Trans. Antennas Propagat.*, vol. 56, no. 5, pp. 1329–1339, May 2008.

[158] O. Luukkonen, M. G. Silveirinha, A. B. Yakovlev, C. R. Simovski, I. S. Nefedov, and S. A. Tretyakov, "Effects of spatial dispersion on reflection from mushroom-type artificial impedance surfaces," *IEEE Trans. Microw. Theory Techn.*, vol. 57, no. 11, pp. 2692–2699, Nov. 2009.

[159] P. A. Belov, Y. Hao, and S. Sudhakaran, "Subwavelength microwave imaging using an array of parallel conducting wires as a lens," *Phys. Rev. B*, vol. 73, p. 033108, Jan. 2006.

[160] M. G. Silveirinha, C. A. Fernandes, and J. R. Costa, "Electromagnetic characterization of textured surfaces formed by metallic pins," *IEEE Trans. Antennas Propagat.*, vol. 56, no. 2, pp. 405–415, Feb. 2008.

[161] T. Niemi, A. O. Karilainen, and S. A. Tretyakov, "Synthesis of polarization transformers," *IEEE Trans. Antennas Propagat.*, vol. 61, no. 6, pp. 3102–3111, Jun. 2013.

[162] Y. Zhao and A. Alù, "Manipulating light polarization with ultrathin plasmonic metasurfaces," *Phys. Rev. B*, vol. 84, p. 205428, 2011.

[163] L. Q. Cong, W. Cao, Z. Tian, J. Q. Gu, J. G. Han, and W. L. Zhang, "Manipulating polarization states of terahertz radiation using metamaterials," *New Journal of Physics*, vol. 14, p. 115013, 2012.

[164] L. Zhu, F. Y. Meng, L. Dong, J. H. Fu, F. Zhang, and Q. Wu, "Polarization manipulation based on electromagnetically induced transparency-like (EIT like) effect," *Opt. Expr.*, vol. 21, pp. 32 099–32 110, 2013.

[165] Y. M. Yang, W. Y. Wang, P. Moitra, I. I. Kravchenko, D. P. Briggs, and J. Valentine, "Dielectric meta-reflectarray for broadband linear polarization conversion and optical vortex generation," *Nano Letters*, vol. 14, pp. 1394–1399, 2014.

[166] B. Fong, J. Colburn, J. Ottusch, J. Visher, and D. Sievenpiper, "Scalar and tensor holographic artificial impedance surfaces," *IEEE Trans. Antennas Propagat.*, vol. 58, pp. 3212–3221, 2010.

[167] A. Vakil and N. Engheta, "Transformation optics using graphene," *Science*, vol. 332, pp. 1291–1294, 2010.

[168] L. Chen, K. Achouri, E. Kallos, and C. Caloz, "Simultaneous enhancement of light extraction and spontaneous emission using a partially reflecting metasurface cavity," *Phys. Rev. A*, vol. 95, p. 053808 :1–7, May 2017.

[169] K. Achouri, G. Lavigne, M. A. Salem, and C. Caloz, “Metasurface spatial processor for electromagnetic remote control,” *IEEE Trans. Antennas Propagat.*, vol. 64, no. 5, pp. 1759–1767, May 2016.

[170] M. E. Badawe, T. S. Almoneef, and O. M. Ramahi, “A true metasurface antenna,” *Sci. Rep.*, vol. 6, pp. 19 268 :1–8, May 2016.

[171] G. T. O. Tékam, V. Ginis, J. Danckaert, and P. Tassin, “Designing an efficient rectifying cut-wire metasurface for electromagnetic energy harvesting,” *Appl. Phys. Lett.*, vol. 110, pp. 083 901 :1–5, 2011.

[172] M. Moccia, G. Castaldi, V. Galdi, A. AlÙ, and N. Engheta, “Dispersion engineering via nonlocal transformation optics,” *Optica*, vol. 3, no. 2, p. 179, Feb. 2016.

[173] Y. Pang, J. Wang, H. Ma, M. Feng, Y. Li, Z. Xu, S. Xia, and S. Qu, “Spatial k-dispersion engineering of spoof surface plasmon polaritons for customized absorption,” *Sci. Rep.*, vol. 6, p. 29429, Jul. 2016.

[174] B. E. A. Saleh and M. C. Teich, *Fundamentals of Photonics*, 2nd ed. Wiley-Interscience, 2007.

[175] B. Nikfal, M. Salem, and C. Caloz, “A method and apparatus for encoding data using instantaneous frequency dispersion,” Patent US 62/002,978, Nov., 2013.

[176] S. Gupta, L. Zou, and C. Caloz, “Bit-error-rate (BER) performance in dispersion code multiple access (DCMA),” in *IEEE AP-S Int. Antennas Propagat. (APS)*, Vancouver, Canada, Jul. 2015.

[177] P. T. Boggs and J. W. Tolle, “Sequential quadratic programming.”

[178] M. del Castillo Velázquez-Ahumada, J. Martel, and F. Medina, “Parallel coupled microstrip filters with ground-plane aperture for spurious band suppression and enhanced coupling,” *IEEE Trans. Microw. Theory Techn.*, vol. 52, no. 3, pp. 1082–1086, 2004.

[179] M. Khalaj-Amirhosseini, “Wideband differential phase shifter using microstrip nonuniform transmission lines,” *PIER Letters*, vol. 3, pp. 151–160, 2008.

[180] D. R. Smith, J. B. Pendry, and M. C. K. Wiltshire, “Metamaterials and negative refractive index,” *Science*, vol. 305, pp. 788–792, 2004.

[181] C. Caloz and T. Itoh, *Electromagnetic metamaterials : transmission line theory and microwave applications.* John Wiley & Sons, 2005.

[182] H.-T. Chen, W. J. Padilla, J. M. O. Zide, A. C. Gossard, A. J. Taylor, and R. D. Averitt, “Active terahertz metamaterial devices,” *Nature*, vol. 444, pp. 597–600, 2006.

[183] N. Engheta and R. W. Ziolkowski, *Metamaterials : physics and engineering explorations.* John Wiley & Sons, 2006.

[184] R. Garg, P. Bhartia, I. Bahl, and A. Ittipiboon, *Microstrip Antenna Design Handbook*. Artech House, 2001.

[185] W. C. Chew, *Waves and fields in inhomogeneous media.* IEEE Press, 1995, vol. 522.

[186] A. Oliner and A. Hessel, "Guided waves on sinusoidally-modulated reactance surfaces," *IEEE Trans. Antennas Propagat.*, vol. 7, no. 5, pp. 201–208, Dec. 1959.

[187] G. Carchon and B. Nauwelaers, "Power and noise limitations of active circulators," *IEEE Trans. Microw. Theory Techn.*, vol. 48, no. 2, pp. 316–319, Feb. 2000.

[188] G. M. Roe and M. R. Boyd, "Parametric energy conversion in distributed systems," *Proceeding of the IRE*, vol. 47, no. 7, pp. 1213 – 1218, 1959.

[189] See Supplemental Material for detailed derivations.

[190] F. Biancalana, A. Amann, A. V. Uskov, and E. P. O'Reilly, "Dynamics of light propagation in spatiotemporal dielectric structures," vol. 45, p. 046607, Apr. 2007.

[191] R. F. Soohoo, "Microwave ferrite materials and devices," *IEEE Trans. Magn.*, vol. 4, no. 2, pp. 118–133, Jun. 1968.

[192] J. D. Adam, L. E. Davis, G. F. Dionne, E. F. Schloemann, and S. N. Stitzer, "Ferrite devices and materials," *IEEE Trans. Microw. Theory Techn.*, vol. 50, no. 3, pp. 721–737, 2002.

[193] K. Suzuki and R. Hirota, "Nonreciprocal millimeter-wave devices using a solid-state plasma at room temperature," *IEEE Trans. Electron Devices*, vol. 18, no. 7, pp. 408–411, 1971.

[194] G. N. Jawad, C. I. Duff, and R. Sloan, "A millimeter-wave gyroelectric waveguide isolator," *IEEE Trans. Microw. Theory Techn.*, vol. 65, no. 4, pp. 1249–1256, 2017.

[195] J.-F. Chang, J.-C. Kao, Y.-H. Lin, and H. Wang, "Design and analysis of 24-GHz active isolator and quasi-circulator," *IEEE Trans. Microw. Theory Techn.*, vol. 63, no. 8, pp. 2638–2649, 2015.

[196] S. Taravati, B. A. Khan, S. Gupta, K. Achouri, and C. Caloz, "Nonreciprocal nongyrotropic magnetless metasurface," *IEEE Trans. Antennas Propagat.*, vol. 65, no. 7, pp. 3589 – 3597, Jul. 2017.

[197] J. D. Joannopoulos, S. G. Johnson, J. N. Winn, and R. D. Meade, *Photonic Crystals : Molding the Flow of Light*.

[198] C. Caloz, D. R. Jackson, and T. Itoh, "Leaky-wave antennas (chap. 9)," in *Frontiers in Antennas : Next Generation Design and Engineering*, F. B. Gross, Ed. McGraw Hill, 2011.

[199] A. A. Oliner and D. R. Jackson, "Leaky-wave antennas (chap. 11)," in *Antenna Engineering Handbook*, J. L. Volakis, Ed. McGraw Hill, 2007.

[200] J. Manley and H. E. Rowe, "Some general properties of nonlinear elements-part I : General energy relations," *Proc. IRE*, vol. 44, no. 7, pp. 904 – 913, Jul. 1956.

[201] J. Manley, "Some properties of time varying networks," *IRE Trans. Circ. Theory*, vol. 7, no. 5, pp. 69 – 78, Aug. 1960.

APPENDIX A
Supplemental Material for Chapter 5

Sonic-Regime Interval

The sonic-regime interval was shown to correspond to a singularity and mathematically determined for the particular case of a one-dimensional sinusoidally modulated medium in [3]. Following the same approach, we derive here the sonic-regime interval for the case of a two-dimensional general periodic modulated medium.

We first expand the wave equation in (5.11) inside the modulated slab, as

$$c^2\frac{\partial^2\mathbf{E}_\mathrm{M}}{\partial x^2}+c^2\frac{\partial^2\mathbf{E}_\mathrm{M}}{\partial z^2}=\frac{\partial^2\left[\epsilon(z,t)\mathbf{E}_\mathrm{M}\right]}{\partial t^2}=\mathbf{E}_\mathrm{M}\frac{\partial^2\epsilon(z,t)}{\partial t^2}+\epsilon(z,t)\frac{\partial^2\mathbf{E}_\mathrm{M}}{\partial t^2}+2\frac{\partial\epsilon(z,t)}{\partial t}\frac{\partial\mathbf{E}_\mathrm{M}}{\partial t},\tag{A-1}$$

where $\mathbf{E}_\mathrm{M}=\mathbf{E}_\mathrm{M}(x,z,t)$. Then, we apply the moving medium coordinate transformation

$$x'=x,\qquad u=-\beta_\mathrm{m}z+\omega_\mathrm{m}t,\qquad t'=t.\tag{A-2}$$

Next we express the partial derivatives in (C-3) in terms of the new variable in (A-2), i.e.

$$\frac{\partial}{\partial x}=\frac{\partial x'}{\partial x}\frac{\partial}{\partial x'}+\frac{\partial u}{\partial x}\frac{\partial}{\partial u}+\frac{\partial t'}{\partial x}\frac{\partial}{\partial t'}=\frac{\partial}{\partial x'},\tag{A-3a}$$

$$\frac{\partial}{\partial z}=\frac{\partial x'}{\partial z}\frac{\partial}{\partial x'}+\frac{\partial u}{\partial z}\frac{\partial}{\partial u}+\frac{\partial t'}{\partial z}\frac{\partial}{\partial t'}=-\beta_\mathrm{m}\frac{\partial}{\partial u},\tag{A-3b}$$

$$\frac{\partial^2}{\partial z^2}=\frac{\partial}{\partial z}\left(\frac{\partial}{\partial z}\right)=\beta_\mathrm{m}^2\frac{\partial^2}{\partial u^2},\tag{A-3c}$$

$$\frac{\partial}{\partial t}=\frac{\partial x'}{\partial t}\frac{\partial}{\partial x'}+\frac{\partial u}{\partial t}\frac{\partial}{\partial u}+\frac{\partial t'}{\partial t}\frac{\partial}{\partial t'}=\frac{\partial}{\partial t'}+\omega_\mathrm{m}\frac{\partial}{\partial u},\tag{A-3d}$$

$$\frac{\partial^2}{\partial t^2}=\left(\frac{\partial t'}{\partial t}\right)^2\frac{\partial^2}{\partial t'^2}+\left(\frac{\partial u}{\partial t}\right)^2\frac{\partial^2}{\partial u^2}+2\left(\frac{\partial t'}{\partial t}\right)\frac{\partial u}{\partial t}\frac{\partial^2}{\partial u\partial t'}=\frac{\partial^2}{\partial t'^2}+\omega_\mathrm{m}^2\frac{\partial^2}{\partial u^2}+2\omega_\mathrm{m}\frac{\partial^2}{\partial u\partial t'}.\tag{A-3e}$$

Using (A-3) wherever appropriate, the different terms of (C-3) become

$$c^2\frac{\partial^2\mathbf{E}_\mathrm{M}(x,z,t)}{\partial x^2}=c^2\frac{\partial^2\mathbf{E}_\mathrm{M}c}{\partial x'^2},\tag{A-4a}$$

$$c^2\frac{\partial^2\mathbf{E}_\mathrm{M}(x,z,t)}{\partial z^2}=c^2\beta_\mathrm{m}^2\frac{\partial^2\mathbf{E}_\mathrm{M}(x',u,t')}{\partial u^2},\tag{A-4b}$$

$$\mathbf{E}_\mathrm{M}(x,z,t)\frac{\partial^2\epsilon(z,t)}{\partial t^2} = \mathbf{E}_\mathrm{M}(x',u,t')\frac{\partial^2}{\partial t'^2}\left(\sum_{k=-\infty}^{\infty}\tilde{\epsilon}_k e^{jku}\right) = -\omega_\mathrm{m}^2\mathbf{E}_\mathrm{M}(x',u,t')\sum_{\substack{k=-\infty\\k\neq0}}^{\infty}k^2\tilde{\epsilon}_k e^{jku}, \tag{A-4c}$$

$$\begin{aligned}&\epsilon(z,t)\frac{\partial^2\mathbf{E}_\mathrm{M}(x,z,t)}{\partial t^2}\\ &\quad=\sum_{k=-\infty}^{\infty}\tilde{\epsilon}_k e^{jku}\left(\frac{\partial^2\mathbf{E}_\mathrm{M}(x',u,t')}{\partial t'^2}+\omega_\mathrm{m}^2\frac{\partial^2\mathbf{E}_\mathrm{M}(x',u,t')}{\partial u^2}+2\omega_\mathrm{m}\frac{\partial^2\mathbf{E}_\mathrm{M}(x',u,t')}{\partial u\partial t'}\right),\end{aligned} \tag{A-4d}$$

$$\begin{aligned}2\frac{\partial\epsilon(z,t)}{\partial t}\frac{\partial\mathbf{E}_\mathrm{M}(x,z,t)}{\partial t} &= 2\omega_\mathrm{m}\frac{\partial}{\partial u}\left(\sum_{k=-\infty}^{\infty}\tilde{\epsilon}_k e^{jku}\right)\left(\frac{\partial\mathbf{E}_\mathrm{M}(x',u,t')}{\partial t'}+\omega_\mathrm{m}\frac{\partial\mathbf{E}_\mathrm{M}(x',u,t')}{\partial u}\right)\\ &= 2j\omega_\mathrm{m}\sum_{\substack{k=-\infty\\k\neq0}}^{\infty}k\tilde{\epsilon}_k e^{jku}\left(\frac{\partial\mathbf{E}_\mathrm{M}(x',u,t')}{\partial t'}+\omega_\mathrm{m}\frac{\partial\mathbf{E}_\mathrm{M}(x',u,t')}{\partial u}\right),\end{aligned} \tag{A-4e}$$

Grouping (A-4) according to (C-3) yields then the wave equation in terms of x', u, t' and $\tilde{\epsilon}_k$:

$$\begin{aligned}&\left(c^2\beta_\mathrm{m}^2-\omega_\mathrm{m}^2\sum_{k=-\infty}^{\infty}\tilde{\epsilon}_k e^{jku}\right)\frac{\partial^2\mathbf{E}_\mathrm{M}(x',u,t')}{\partial u^2}+c^2\frac{\partial^2\mathbf{E}_\mathrm{M}(x',u,t')}{\partial x'^2}-\sum_{k=-\infty}^{\infty}\tilde{\epsilon}_k e^{jku}\frac{\partial^2\mathbf{E}_\mathrm{M}(x',u,t')}{\partial t'^2}\\ &-2\omega_\mathrm{m}\sum_{k=-\infty}^{\infty}\tilde{\epsilon}_k e^{jku}\frac{\partial^2\mathbf{E}_\mathrm{M}(x',u,t')}{\partial u\partial t'}-2j\omega_\mathrm{m}\sum_{\substack{k=-\infty\\k\neq0}}^{\infty}k\tilde{\epsilon}_k e^{jku}\left(\frac{\partial\mathbf{E}_\mathrm{M}(x',u,t')}{\partial t'}+\omega_\mathrm{m}\frac{\partial\mathbf{E}_\mathrm{M}(x,z,t)}{\partial u}\right)\\ &\qquad\qquad\qquad\qquad+\omega_\mathrm{m}^2\sum_{\substack{k=-\infty\\k\neq0}}^{\infty}k^2\tilde{\epsilon}_k e^{jku}\mathbf{E}_\mathrm{M}(x',u,t')=0.\end{aligned} \tag{A-5}$$

For this equation to really represent the wave equation, it must maintain all of its order derivatives. This is generally the case, except when the coefficient of the first term vanishes, i.e.

$$c^2\beta_\mathrm{m}^2-\omega_\mathrm{m}^2\tilde{\epsilon}_0-\omega_\mathrm{m}^2\sum_{\substack{k=-\infty\\k\neq0}}^{\infty}\tilde{\epsilon}_k e^{jku}=0, \tag{A-6}$$

or, assuming a real permittivity and hence $\Im\left\{\sum_{k=-\infty}^{\infty}\tilde{\epsilon}_k e^{jku}\right\}=0$,

$$\sum_{\substack{k=-\infty\\k\neq0}}^{\infty}\tilde{\epsilon}_k e^{jku}=\frac{\epsilon_\mathrm{r}}{\gamma^2}-\tilde{\epsilon}_0, \tag{A-7}$$

where (2), (3) and (4) have been used. Assuming that the permittivity variation is bounded to ϵ_m, i.e. $\left|\sum\limits_{\substack{k=-\infty\\k\neq 0}}^{\infty} \tilde{\epsilon}_k e^{jku}\right| \leqslant \epsilon_\mathrm{m}$, and considering that u is real, the condition (A-7) reduces to

$$\left|\frac{\epsilon_\mathrm{r}}{\gamma^2} - \tilde{\epsilon}_0\right| \leqslant \epsilon_\mathrm{m}, \tag{A-8}$$

which may be rearranged as

$$\sqrt{\frac{\epsilon_\mathrm{r}}{\tilde{\epsilon}_0 + \epsilon_\mathrm{m}}} \leqslant \gamma \leqslant \sqrt{\frac{\epsilon_\mathrm{r}}{\tilde{\epsilon}_0 - \epsilon_\mathrm{m}}}. \tag{A-9}$$

This corresponds to the sonic interval, where the solution for $\mathbf{E}_\mathrm{m}$ cannot be computed using the Bloch-Floquet expansion (6).

General Wave Solution To solve the wave equation in (9), we write the product of (5) and (6) as

$$\begin{aligned}\epsilon(z,t)\mathbf{E}_\mathrm{M}(x,z,t) &= \hat{\mathbf{y}} \sum_{n=-\infty}^{\infty} \sum_{k=-\infty}^{\infty} \tilde{\epsilon}_k A_n^{\pm} e^{-j(\pm\beta_0 z + k_x x - \omega_0 t)} e^{-j(n+k)(\beta_\mathrm{m} z - \omega_\mathrm{m} t)} \\ &= \sum_{n=-\infty}^{\infty} \sum_{k=-\infty}^{\infty} \tilde{\epsilon}_k A_{n-k}^{\pm} e^{-j(\pm\beta_0 z + k_x x - \omega_0 t)} e^{-jn(\beta_\mathrm{m} z - \omega_\mathrm{m} t)}.\end{aligned} \tag{A-10}$$

Inserting (6) and (A-10) into (9) yields

$$\begin{aligned}&\left(\frac{\partial^2}{\partial x^2} + \frac{\partial^2}{\partial z^2}\right) \sum_{n=-\infty}^{\infty} A_n^{\pm} e^{-j(\pm\beta_0 z + n\beta_\mathrm{m} z + k_x x)} e^{j(\omega_0 + n\omega_\mathrm{m})t} \\ &\qquad - \frac{1}{c^2}\frac{\partial^2}{\partial t^2} \sum_{n=-\infty}^{\infty} \sum_{k=-\infty}^{\infty} \tilde{\epsilon}_k A_{n-k}^{\pm} e^{-j(\pm\beta_0 z + k_x x - \omega_0 t)} e^{-jn(\beta_\mathrm{m} z - \omega_\mathrm{m} t)} = 0.\end{aligned} \tag{A-11}$$

Applying the second derivatives transforms this equation to

$$\begin{aligned}\sum_{n=-\infty}^{\infty} \Bigg[&\left(-k_x^2 - (\beta_0 \pm n\beta_\mathrm{m})^2\right) A_n^{\pm} e^{-j(\pm\beta_0 z + n\beta_\mathrm{m} z + k_x x)} e^{j(\omega_0 + n\omega_\mathrm{m})t} \\ &+ \frac{(\omega_0 + n\omega_\mathrm{m})^2}{c^2} \sum_{k=-\infty}^{\infty} \tilde{\epsilon}_k A_{n-k}^{\pm} e^{-j(\pm\beta_0 + n\beta_\mathrm{m} z + k_x x)} e^{j(\omega_0 + n\omega_\mathrm{m} t)} \Bigg] = 0.\end{aligned} \tag{A-12}$$

Finally, using the orthogonality property of the complex exponential function to cancel the common terms $e^{-j(\pm\beta_0 z + n\beta_\mathrm{m} z + k_x x)} e^{j(\omega_0 + n\omega_\mathrm{m} t)}$ leads to the recursive set of equations (10).

Application of Boundary Conditions

Forward Problem

The TM_{xz} or E_y incident fields read

$$\mathbf{E}_{\mathrm{I}}^{\mathrm{F}}(x,z,t)=\hat{\mathbf{y}}E_0e^{-j[k_0\sin(\theta_{\mathrm{i}})x+k_0\cos(\theta_{\mathrm{i}})z-\omega_0t]}, \tag{A-13a}$$

where E_0 is the amplitude of the incident field and $k_0=\omega_0/v_{\mathrm{b}}$, and

$$\begin{aligned}\mathbf{H}_{\mathrm{I}}^{\mathrm{F}}(x,z,t)&=\frac{1}{\eta_1}\left[\hat{\mathbf{k}}_{\mathrm{I}}^{\mathrm{F}}\times\mathbf{E}_{\mathrm{I}}^{\mathrm{F}}(x,z,t)\right]\\&=\left[-\hat{\mathbf{x}}\cos(\theta_{\mathrm{i}})+\hat{\mathbf{z}}\sin(\theta_{\mathrm{i}})\right]\sqrt{\frac{\epsilon_0\epsilon_{\mathrm{r}}}{\mu_0}}E_0e^{-j[k_0\sin(\theta_{\mathrm{i}})x+k_0\cos(\theta_{\mathrm{i}})z-\omega_0t]},\end{aligned} \tag{A-13b}$$

where $\eta_1=\sqrt{\mu_0/(\epsilon_0\epsilon_r)}$. The electric and magnetic fields in the slab may be explicitly written using (6) as

$$\mathbf{E}_{\mathrm{M}}^{\mathrm{F}}(x,z,t)=\hat{\mathbf{y}}\sum_{n,p=-\infty}^{\infty}\left(A_{np}^{\mathrm{F}+}e^{-j\left[k_xx+(\beta_{0p}^{+}+n\beta_{\mathrm{m}})z\right]}+A_{np}^{\mathrm{F}-}e^{-j\left[(k_xx-(\beta_{0p}^{-}-n\beta_{\mathrm{m}})z\right]}\right)e^{j(\omega_0+n\omega_{\mathrm{m}})t}, \tag{A-14a}$$

and

$$\begin{aligned}\mathbf{H}_{\mathrm{M}}^{\mathrm{F}}(x,z,t)=&\frac{1}{\eta_2}\left[\hat{\mathbf{k}}_{\mathrm{M}}^{\mathrm{F}}\times\mathbf{E}_{\mathrm{M}}^{\mathrm{F}}(x,z,t)\right]\\=&\sum_{n,p=-\infty}^{\infty}\left(\left[-\hat{\mathbf{x}}\frac{\beta_{0p}^{+}+n\beta_{\mathrm{m}}}{\mu_0(\omega_0+n\omega_{\mathrm{m}})}+\hat{\mathbf{z}}\sin(\theta_{\mathrm{i}})\sqrt{\frac{\epsilon_0\epsilon_{\mathrm{r}}}{\mu_0}}\right]A_{np}^{\mathrm{F}+}e^{-j\left[k_xx+(\beta_{0p}^{+}+n\beta_{\mathrm{m}})z\right]}\right.\\&\left.+\left[\hat{\mathbf{x}}\frac{\beta_{0p}^{-}-n\beta_{\mathrm{m}}}{\mu_0(\omega_0+n\omega_{\mathrm{m}})}+\hat{\mathbf{z}}\sin(\theta_{\mathrm{i}})\sqrt{\frac{\epsilon_0\epsilon_{\mathrm{r}}}{\mu_0}}\right]A_{np}^{\mathrm{F}-}e^{-j\left[k_xx-(\beta_{0p}^{-}-n\beta_{\mathrm{m}})z\right]}\right)e^{j(\omega_0+n\omega_{\mathrm{m}})t}.\end{aligned} \tag{A-14b}$$

where $\eta_2=\sqrt{\mu_0/(\epsilon_0\epsilon_r)}=\eta_1$. The reflected and transmitted electric fields outside of the slab may be defined as

$$\mathbf{E}_{\mathrm{R}}^{\mathrm{F}}(x,z,t)=\hat{\mathbf{y}}\sum_{n=-\infty}^{\infty}E_{\mathrm{r}n}^{\mathrm{F}}e^{-j[k_0\sin(\theta_{\mathrm{i}})x-k_{0n}\cos(\theta_{\mathrm{r}n})z-(\omega_0+n\omega_{\mathrm{m}})t]}, \tag{A-15a}$$

$$\begin{aligned}\mathbf{H}_{\mathrm{R}}^{\mathrm{F}}(x,z,t)&=\frac{1}{\eta_1}[\hat{\mathbf{k}}_{\mathrm{R}}^{\mathrm{F}}\times\mathbf{E}_{\mathrm{R}}^{\mathrm{F}}(x,z,t)]\\&=[\hat{\mathbf{x}}\cos(\theta_{\mathrm{r}n})+\hat{\mathbf{z}}\sin(\theta_{\mathrm{i}})]\sqrt{\frac{\epsilon_0\epsilon_{\mathrm{r}}}{\mu_0}}E_{\mathrm{r}n}^{\mathrm{F}}e^{-j[k_0\sin(\theta_{\mathrm{i}})x-k_{0n}\cos(\theta_{\mathrm{r}n})z-(\omega_0+n\omega_{\mathrm{m}})t]},\end{aligned} \tag{A-15b}$$

$$\mathbf{E}_{\mathrm{T}}^{\mathrm{F}}(x,z,t)=\hat{\mathbf{y}}\sum_{n=-\infty}^{\infty}E_{\mathrm{t}n}^{\mathrm{F}}e^{-j[k_0\sin(\theta_{\mathrm{i}})x+k_{0n}\cos(\theta_{\mathrm{t}n})z-(\omega_0+n\omega_{\mathrm{m}})t]}, \tag{A-15c}$$

$$\begin{aligned}\mathbf{H}_{\mathrm{T}}^{\mathrm{F}}(x,z,t)&=\frac{1}{\eta_3}[\hat{\mathbf{k}}_{\mathrm{T}}^{\mathrm{F}}\times\mathbf{E}_{\mathrm{T}}^{\mathrm{F}}(x,z,t)]\\&=[-\hat{\mathbf{x}}\cos(\theta_{\mathrm{t}n})+\hat{\mathbf{z}}\sin(\theta_{\mathrm{i}})]\sqrt{\frac{\epsilon_0\epsilon_{\mathrm{r}}}{\mu_0}}E_{\mathrm{t}n}^{\mathrm{F}}e^{-j[k_0\sin(\theta_{\mathrm{i}})x+k_{0n}\cos(\theta_{\mathrm{t}n})z-(\omega_0+n\omega_{\mathrm{m}})t]},\end{aligned} \tag{A-15d}$$

where $\eta_3=\sqrt{\mu_0/(\epsilon_0\epsilon_r)}=\eta_1=\eta_2$. We then enforce the continuity of the tangential components of the electromagnetic fields at $z=0$ and $z=L$ to find the unknown field amplitudes $A_{0p}^{\pm}$, $E_{\mathrm{r}n}^{\mathrm{F}}$ and $E_{\mathrm{t}n}^{\mathrm{F}}$. The electric field continuity condition between regions 1 and 2 at $z=0$, $E_{1y}(x,0,t)=E_{2y}(x,0,t)$, reduces to

$$\delta_{n0}E_0+E_{\mathrm{r}n}^{\mathrm{F}}=\sum_{p=-\infty}^{\infty}\left(A_{np}^{\mathrm{F}+}+A_{np}^{\mathrm{F}-}\right), \tag{A-16}$$

while the corresponding magnetic field continuity condition, $H_{1x}(x,0,t)=H_{2x}(x,0,t)$, reads

$$\sqrt{\frac{\epsilon_0\epsilon_{\mathrm{r}}}{\mu_0}}\cos(\theta_{\mathrm{i}})\delta_{n0}E_0-\sqrt{\frac{\epsilon_0\epsilon_{\mathrm{r}}}{\mu_0}}\cos(\theta_{\mathrm{r}n})E_{\mathrm{r}n}^{\mathrm{F}}=\sum_{p=-\infty}^{\infty}\left(\frac{\beta_{0p}^{+}+n\beta_{\mathrm{m}}}{\mu_0(\omega_0+n\omega_{\mathrm{m}})}A_{np}^{\mathrm{F}+}-\frac{\beta_{0p}^{-}-n\beta_{\mathrm{m}}}{\mu_0(\omega_0+n\omega_{\mathrm{m}})}A_{np}^{\mathrm{F}-}\right), \tag{A-17}$$

where $k_n=(\omega_0+n\omega_{\mathrm{m}})/v_{\mathrm{b}}$.

Similarly, the electric field continuity condition between regions 2 and 3 at $z=L$, $E_{2y}(x,L,t)=E_{3y}(x,L,t)$, reduces to

$$\sum_{p=-\infty}^{\infty}\left(A_{np}^{\mathrm{F}+}e^{-j(\beta_{0p}^{+}+n\beta_{\mathrm{m}})L}+A_{np}^{\mathrm{F}-}e^{j(\beta_{0p}^{-}-n\beta_{\mathrm{m}})L}\right)=E_{\mathrm{t}n}^{\mathrm{F}}e^{-jk_{0n}\cos(\theta_{\mathrm{t}n})L}, \tag{A-18}$$

while the corresponding magnetic field continuity condition between regions 2 and 3 at $z=L$, $H_{2x}(x,L,t)=H_{3x}(x,L,t)$, reads

$$\begin{aligned}\sum_{p=-\infty}^{\infty}&\left[\frac{\beta_{0p}^{+}+n\beta_{\mathrm{m}}}{\mu_0(\omega_0+n\omega_{\mathrm{m}})}A_{np}^{\mathrm{F}+}e^{-j(\beta_{0p}^{+}+n\beta_{\mathrm{m}})L}-\frac{\beta_{0p}^{-}-n\beta_{\mathrm{m}}}{\mu_0(\omega_0+n\omega_{\mathrm{m}})}A_{np}^{\mathrm{F}-}e^{j(\beta_{0p}^{-}-n\beta_{\mathrm{m}})L}\right]\\&=\sqrt{\frac{\epsilon_0\epsilon_{\mathrm{r}}}{\mu_0}}\cos(\theta_{\mathrm{t}n})E_{\mathrm{t}n}^{\mathrm{F}}e^{-jk_{0n}\cos(\theta_{\mathrm{t}n})L}\end{aligned} \tag{A-19}$$

Solving (A-18) and (A-19) for $A_{0p}^{\mathrm{F}-}$ yields (14b). Next solving (A-16), (A-17) and (14b) for $A_{0p}^{\mathrm{F}+}$ yields (14a). Finally, the total scattered fields outside the slab are obtained by substituting (14) into (A-15), which yields (16).

Backward Problem

The TM$_{xz}$ or E_y incident fields read

$$\mathbf{E}_{\mathrm{I}}^{\mathrm{B}}(x,z,t)=\hat{\mathbf{y}}E_0e^{-j[k_0\sin(\theta_{\mathrm{i}})x-k_0\cos(\theta_{\mathrm{i}})z-\omega_0t]}, \tag{A-20a}$$

$$\mathbf{H}_{\mathrm{I}}^{\mathrm{B}}(x,z,t)=\frac{1}{\eta_1}[\hat{\mathbf{k}}_{\mathrm{I}}^{\mathrm{B}}\times\mathbf{E}_{\mathrm{I}}^{\mathrm{B}}(x,z,t)]=[\hat{\mathbf{x}}\cos(\theta_{\mathrm{i}})+\hat{\mathbf{z}}\sin(\theta_{\mathrm{i}})]\sqrt{\frac{\epsilon_0\epsilon_{\mathrm{r}}}{\mu_0}}E_0e^{-j[k_0\sin(\theta_{\mathrm{i}})x+k_0\cos(\theta_{\mathrm{i}})z-\omega_0t]}, \tag{A-20b}$$

The electric and magnetic fields in the slab may be explicitly written using (6) as

$$\mathbf{E}_{\mathrm{M}}^{\mathrm{B}}(x,z,t)=\hat{\mathbf{y}}\sum_{n,p=-\infty}^{\infty}\left(A_{np}^{\mathrm{B}+}e^{-j\left[k_xx+(\beta_{0p}^{+}+n\beta_{\mathrm{m}})z\right]}+A_{np}^{\mathrm{B}-}e^{-j\left[k_xx-(\beta_{0p}^{-}-n\beta_{\mathrm{m}})z\right]}\right)e^{j(\omega_0+n\omega_{\mathrm{m}})t}, \tag{A-21a}$$

$$\begin{aligned}\mathbf{H}_{\mathrm{M}}^{\mathrm{B}}(x,z,t)=&\frac{1}{\eta_2}\left[\hat{\mathbf{k}}_{\mathrm{M}}^{\mathrm{B}}\times\mathbf{E}_{\mathrm{M}}^{\mathrm{B}}(x,z,t)\right]\\=&\sum_{n,p=-\infty}^{\infty}\left(\left[-\hat{\mathbf{x}}\frac{\beta_{0p}^{+}+n\beta_{\mathrm{m}}}{\mu_0(\omega_0+n\omega_{\mathrm{m}})}+\hat{\mathbf{z}}\sin(\theta_{\mathrm{i}})\sqrt{\frac{\epsilon_0\epsilon_{\mathrm{r}}}{\mu_0}}\right]A_{np}^{\mathrm{B}+}e^{-j\left[k_xx+(\beta_{0p}^{+}+n\beta_{\mathrm{m}})z\right]}\right.\\&\left.+\left[\hat{\mathbf{x}}\frac{\beta_{0p}^{-}-n\beta_{\mathrm{m}}}{\mu_0(\omega_0+n\omega_{\mathrm{m}})}+\hat{\mathbf{z}}\sin(\theta_{\mathrm{i}})\sqrt{\frac{\epsilon_0\epsilon_{\mathrm{r}}}{\mu_0}}\right]A_{np}^{\mathrm{B}-}e^{-j\left[k_xx-(\beta_{0p}^{-}-n\beta_{\mathrm{m}})z\right]}\right)e^{j(\omega_0+n\omega_{\mathrm{m}})t}.\end{aligned} \tag{A-21b}$$

The reflected and transmitted electric fields outside of the slab may be defined as

$$\mathbf{E}_{\mathrm{R}}^{\mathrm{B}}(x,z,t)=\hat{\mathbf{y}}\sum_{n=-\infty}^{\infty}E_{\mathrm{r}n}^{\mathrm{B}}e^{j[(\omega_0+n\omega_{\mathrm{m}})t-k_{0n}\cos(\theta_{\mathrm{r}n})z-k_0\sin(\theta_{\mathrm{i}})x]}, \tag{A-22a}$$

$$\begin{aligned}\mathbf{H}_{\mathrm{R}}^{\mathrm{B}}(x,z,t)&=\frac{1}{\eta_3}[\hat{\mathbf{k}}_{\mathrm{R}}^{\mathrm{B}}\times\mathbf{E}_{\mathrm{R}}^{\mathrm{B}}(x,z,t)]\\&=[-\hat{\mathbf{x}}\cos(\theta_{\mathrm{r}n})+\hat{\mathbf{z}}\sin(\theta_{\mathrm{i}})]\sqrt{\frac{\epsilon_0\epsilon_{\mathrm{r}}}{\mu_0}}E_{\mathrm{r}n}^{\mathrm{B}}e^{j[(\omega_0+n\omega_{\mathrm{m}})t-k_{0n}\cos(\theta_{\mathrm{r}n})z-k_0\sin(\theta_{\mathrm{i}})x]},\end{aligned} \tag{A-22b}$$

$$\mathbf{E}_{\mathrm{T}}^{\mathrm{B}}(x,z,t)=\hat{\mathbf{y}}\sum_{n=-\infty}^{\infty}E_{\mathrm{t}n}^{\mathrm{B}}e^{-j[k_0\sin(\theta_{\mathrm{i}})x-k_{0n}\cos(\theta_{\mathrm{t}n})z-(\omega_0+n\omega_{\mathrm{m}})t]}, \tag{A-22c}$$

$$\begin{aligned}\mathbf{H}_{\mathrm{T}}^{\mathrm{B}}(x,z,t)&=\frac{1}{\eta_1}[\hat{\mathbf{k}}_{\mathrm{T}}^{\mathrm{B}}\times\mathbf{E}_{\mathrm{T}}^{\mathrm{B}}(x,z,t)]\\&=[\hat{\mathbf{x}}\cos(\theta_{\mathrm{t}n})+\hat{\mathbf{z}}\sin(\theta_{\mathrm{i}})]\sqrt{\frac{\epsilon_0\epsilon_{\mathrm{r}}}{\mu_0}}E_{\mathrm{t}n}^{\mathrm{B}}e^{-j[k_0\sin(\theta_{\mathrm{i}})x-k_{0n}\cos(\theta_{\mathrm{t}n})z-(\omega_0+n\omega_{\mathrm{m}})t]}.\end{aligned} \tag{A-22d}$$

We then enforce the continuity of the tangential components of the electromagnetic fields at $z=0$ and $z=L$ to find the unknown field amplitudes $A_{0p}^{\pm}$, $E_{\mathrm{r}n}^{\mathrm{B}}$ and $E_{\mathrm{t}n}^{\mathrm{B}}$. The electric field continuity condition between regions 2 and 3 at $z = L$, $E_{2y}(x, L, t) = E_{3y}(x, L, t)$, reduces to

$$E_0\delta_{n0}e^{jk_0\cos(\theta_\mathrm{i})L} + E_{\mathrm{r}n}^\mathrm{B}e^{-jk_{0n}\cos(\theta_{\mathrm{r}n})L} = \sum_{p=-\infty}^{\infty}\left(A_{np}^{\mathrm{B}+}e^{-j(\beta_{0p}^{+}+n\beta_\mathrm{m})L} + A_{np}^{\mathrm{B}-}e^{j(\beta_{0p}^{-}-n\beta_\mathrm{m})L}\right), \quad \text{(A-23)}$$

while the corresponding magnetic field continuity condition, $H_{2x}(x, 0, t) = H_{3x}(x, 0, t)$, reads

$$\sqrt{\frac{\epsilon_0\epsilon_\mathrm{r}}{\mu_0}}\cos(\theta_\mathrm{i})\delta_{n0}E_0e^{jk_0\cos(\theta_\mathrm{i})L} - \sqrt{\frac{\epsilon_0\epsilon_\mathrm{r}}{\mu_0}}\cos(\theta_{\mathrm{r}n})E_{\mathrm{r}n}^\mathrm{B}e^{-jk_{0n}\cos(\theta_{\mathrm{r}n})L}$$
$$= \sum_{p=-\infty}^{\infty}\left(-\frac{\beta_{0p}^{+}+n\beta_\mathrm{m}}{\mu_0(\omega_0+n\omega_\mathrm{m})}A_{np}^{\mathrm{B}+}e^{-j(\beta_{0p}^{+}+n\beta_\mathrm{m})L} + \frac{\beta_{0p}^{-}-n\beta_\mathrm{m}}{\mu_0(\omega_0+n\omega_\mathrm{m})}A_{np}^{\mathrm{B}-}e^{j(\beta_{0p}^{-}-n\beta_\mathrm{m})L}\right). \quad \text{(A-24)}$$

Similarly, the electric field continuity condition between regions 1 and 2 at $z = 0$, $E_{1y}(x, 0, t) = E_{2y}(x, 0, t)$, reduces to

$$\sum_{p=-\infty}^{\infty}\left(A_{np}^{\mathrm{B}+} + A_{np}^{\mathrm{B}-}\right) = E_{\mathrm{t}n}^\mathrm{B} \quad \text{(A-25)}$$

while the corresponding magnetic field continuity condition between regions 1 and 2 at $z = 0$, $H_{1x}(x, 0, t) = H_{2x}(x, 0, t)$, reads

$$\sum_{p=-\infty}^{\infty}\left[-\frac{\beta_{0p}^{+}+n\beta_\mathrm{m}}{\mu_0(\omega_0+n\omega_\mathrm{m})}A_{np}^{\mathrm{B}+} + \frac{\beta_{0p}^{-}-n\beta_\mathrm{m}}{\mu_0(\omega_0+n\omega_\mathrm{m})}A_{np}^{\mathrm{B}-}\right] = \sqrt{\frac{\epsilon_0\epsilon_\mathrm{r}}{\mu_0}}\cos(\theta_{\mathrm{t}n})E_{\mathrm{t}n}^\mathrm{B} \quad \text{(A-26)}$$

Solving (A-25) and (A-26) for $A_{0p}^{\mathrm{B}+}$ yields (15b). Next solving (A-23), (A-24) and (15b) for $A_{0p}^{\mathrm{B}-}$ yields (15a). Finally, the total scattered fields outside the slab are obtained by substituting (15) into (A-22), which yields (17).

APPENDIX B
Supplemental Material for Chapter 6

General Closed-Form Solution

This section derives the general electromagnetic field solution inside the space-time modulated isolator in Fig. 6.12.

We start with the Maxwell equations,

$$\nabla \times \mathbf{E}_{\mathrm{M}}(z,t) = -\mu_0 \frac{\partial \mathbf{H}_{\mathrm{M}}(z,t)}{\partial t}, \tag{B-1a}$$

$$\nabla \times \mathbf{H}_{\mathrm{M}}(z,t) = \epsilon_0 \frac{\partial [\epsilon_{\mathrm{eq}}(t,z)\mathbf{E}_{\mathrm{M}}(z,t)]}{\partial t}. \tag{B-1b}$$

Taking the curl of (12), using (13), yields

$$\frac{\partial^2 \mathbf{E}_{\mathrm{M}}(z,t)}{\partial z^2} - \mu_0 \epsilon_0 \frac{\partial}{\partial t}\left(\frac{\partial\left[\epsilon_{\mathrm{eq}}(t,z)\mathbf{E}_{\mathrm{M}}(z,t)\right]}{\partial t}\right) = 0, \tag{B-2}$$

which may be expanded in the form of

$$\begin{aligned}\frac{\partial^2 \mathbf{E}_{\mathrm{M}}(z,t)}{\partial z^2} - \frac{1}{c^2}\frac{\partial^2}{\partial t^2}\Bigg(&\epsilon_{\mathrm{av}}\mathbf{E}_{\mathrm{M}}(z,t) + \frac{\epsilon_{\mathrm{m}}}{2}\mathbf{E}_{\mathrm{M}}(z,t)e^{-j(\kappa_{\mathrm{s}}z-\omega_{\mathrm{s}}t+\phi)} \\ &+\frac{\epsilon_{\mathrm{m}}}{2}\mathbf{E}_{\mathrm{M}}(z,t)e^{j(\kappa_{\mathrm{s}}z-\omega_{\mathrm{s}}t+\phi)}\Bigg) = 0,\end{aligned} \tag{B-3}$$

Considering $\partial \mathbf{E}_{\mathrm{M}}(z,t)/\partial t = (j\omega_{\mathrm{s}})\mathbf{E}_{\mathrm{M}}(z,t)$. Then, (B-3) reduces to

$$\frac{\partial^2 \mathbf{E}_{\mathrm{M}}(z,t)}{\partial z^2} + \frac{\omega_{\mathrm{s}}^2}{c^2}\left(\epsilon_{\mathrm{av}} + 2\epsilon_{\mathrm{m}}e^{j(\kappa_{\mathrm{s}}z-\omega_{\mathrm{s}}t+\phi)}\right)\mathbf{E}_{\mathrm{M}}(z,t) = 0. \tag{B-4}$$

Next, to find a closed form solution, we consider the below change of variable

$$W = \frac{2\sqrt{2\epsilon_{\mathrm{m}}}\omega_{\mathrm{s}}}{c\kappa_{\mathrm{s}}}e^{j(\kappa_{\mathrm{s}}z-\omega_{\mathrm{s}}t+\phi)/2}, \qquad t' = t \tag{B-5}$$

and redefine the spatial derivations as

$$\frac{\partial E_{\mathrm{M}}}{\partial z} = \frac{\partial W}{\partial z}\frac{\partial E_{\mathrm{M}}}{\partial W} + \frac{\partial t'}{\partial z}\frac{\partial E_{\mathrm{M}}}{\partial t'} = j\frac{\kappa_{\mathrm{s}}}{2}W\frac{\partial E_{\mathrm{M}}}{\partial W}, \tag{B-6a}$$

$$\frac{\partial^2 E_{\mathrm{M}}}{\partial z^2} = \frac{\partial}{\partial z}\left(\frac{\partial E_{\mathrm{M}}}{\partial z}\right) = \frac{\partial^2 W}{\partial z^2}\frac{\partial E_{\mathrm{M}}}{\partial W} + \left(\frac{\partial W}{\partial z}\right)^2\frac{\partial^2 E_{\mathrm{M}}}{\partial W^2} \tag{B-6b}$$

$$= -\frac{\kappa_{\mathrm{s}}^2}{4}\left(W\frac{\partial E_{\mathrm{M}}}{\partial W} + W^2\frac{\partial^2 E_{\mathrm{M}}}{\partial W^2}\right). \tag{B-6c}$$

Therefore, (B-6) simplifies to

$$\frac{\partial^2 E_{\mathrm{M}}}{\partial W^2} + \frac{1}{W}\frac{\partial E_{\mathrm{M}}}{\partial W} - \left(1 + \frac{\alpha^2}{W^2}\right)E_{\mathrm{M}} = 0 \tag{B-7}$$

which is the modified Bessel differential equation, with

$$\alpha = \frac{2\omega_{\mathrm{s}}\sqrt{\epsilon_{\mathrm{av}}}}{c\kappa_{\mathrm{s}}}. \tag{B-8}$$

The solution to (B-7) is represented by the first and second modified Bessel function as

$$\mathbf{E}_{\mathrm{M}}(W,t') = \hat{\mathbf{y}}\left[A(t')I_\alpha(W) + B(t')K_\alpha(W)\right] \tag{B-9}$$

Electromagnetic Scattering For Forward and Backward Problems

The two unknown coefficients in (B-9), A and B, shall be found separately for forward and backward problems, by applying the spatial boundary conditions at $z = 0$ and $z = L$. We may define the scattered electric fields outside the isolator slab as

$$\mathbf{E}_{\mathrm{I}}(z,t') = \hat{\mathbf{y}}E_0 e^{-j(\beta_{\mathrm{s}}z-\omega_{\mathrm{s}}t')}, \tag{B-10a}$$

$$\mathbf{E}_{\mathrm{R}}^{\mathrm{F}}(z,t') = \hat{\mathbf{y}}E_{\mathrm{r}}^{\mathrm{F}} e^{j(\beta_{\mathrm{s}}z+\omega_{\mathrm{s}}t')}, \tag{B-10b}$$

$$\mathbf{E}_{\mathrm{T}}^{\mathrm{F}}(z,t') = \hat{\mathbf{y}}E_{\mathrm{t}}^{\mathrm{F}} e^{-j(\beta_{\mathrm{s}}z-\omega_{\mathrm{s}}t')}. \tag{B-10c}$$

The electric field continuity between regions 1 and 2 at $W_0 = W(z = 0)$, i.e. $E_{1y}(W_0,t') = E_{2y}(W_0,t')$, reads

$$(E_0 + E_{\mathrm{r}})e^{j\omega_{\mathrm{s}}t'} = A(t')I_\alpha(W_0) + B(t')K_\alpha(W_0) \tag{B-11a}$$

and the corresponding magnetic field continuity at $W_0 = W(z = 0)$, i.e. $H_{1x}(W_0,t') =$

$H_{2x}(W_0, t')$ reduces to

$$-j\beta_{\mathrm{s}}\left(E_0 - E_{\mathrm{r}}\right)e^{j\omega_{\mathrm{s}}t'} = j\frac{\kappa_{\mathrm{s}}}{2}W_0\left[A(t')I'_{\alpha}(W_0) + (t')K'_{\alpha}(W_0)\right] \tag{B-11b}$$

The electric field continuity condition between regions 2 and 3 $W_L = W(z = L)$, i.e. $E_{2y}(W_L, t') = E_{3y}(W_L, t')$, reads

$$A(t').I_{\alpha}(W_L) + B(t').K_{\alpha}(W_L) = E_{\mathrm{t}}e^{-j(\beta_{\mathrm{s}}L - \omega_{\mathrm{s}}t')} \tag{B-12a}$$

where $W_L = W(z = L)$. Next, the corresponding magnetic field continuity $H_{2x}(W_L, t') = H_{3x}(W_L, t')$ reduces to

$$j\frac{\kappa_{\mathrm{s}}}{2}W_L\left(A(t').I'_{\alpha}(W_L) + B(t').K'_{\alpha}(W_L)\right) = -j\beta_{\mathrm{s}}E_{\mathrm{t}}e^{-j(\beta_{\mathrm{s}}L - \omega_{\mathrm{s}}t')} \tag{B-12b}$$

Solving (B-11) and (B-12) together, using two well-known equalities of bessel functions,

$$x\frac{d}{dx}I_{\alpha}(x) \mp \alpha I_{\alpha}(x) = xI_{\alpha\pm 1}(x) \tag{B-13a}$$

$$x\frac{d}{dx}K_{\alpha}(x) \mp \alpha K_{\alpha}(x) = -xK_{\alpha\pm 1}(x) \tag{B-13b}$$

yields unknown coefficients of (B-9), A and B, as given in (6.10) and (6.11).

Then, we may achieve the reflected and transmitted wave coefficients as

$$E_{\mathrm{r}} = AI_{\alpha}(W_0) - BK_{\alpha}(W_0)e^{-j\omega_{\mathrm{s}}t'} - E_0 \tag{B-14}$$

$$E_{\mathrm{t}} = \left(A.I_{\alpha}(W_L) + B.K_{\alpha}(W_L)\right)e^{j(\beta_{\mathrm{s}}L - \omega_{\mathrm{s}}t')} \tag{B-15}$$

APPENDIX C
Supplemental Material for Chapter 7

Field and Dispersion Relation Derivation

This section derives the electromagnetic field and dispersion relation following a procedure similar to that used (but not detailed) in [74].

Due to space-time periodicity, the permittivity can be expanded in the space-time Fourier series,

$$\epsilon(z,t) = \sum_{p=-\infty}^{+\infty} \epsilon_p e^{jp(\omega_\mathrm{m} t - \beta_\mathrm{m} z)}, \tag{C-1}$$

while the electric field can be expanded in the space-time Floquet series

$$E(z,t) = \sum_{n=-\infty}^{+\infty} E_n e^{j\omega_n t} e^{-(\alpha_n + j\beta_n)z}, \tag{C-2}$$

where $\omega_n = \omega_0 + n\omega_\mathrm{m}$ and $\beta_n(\omega) = \beta_0(\omega) + n\beta_\mathrm{m}$, with $\beta_0(\omega)$ and the E_n's being the unknowns to be found. We will first find the coefficients E_n, to determine the field in (C-2), and then, based on this result, determine $\beta_0(\omega)$, which provides the dispersion relation.

We start with the wave equation,

$$\frac{\partial^2 E(z,t)}{\partial z^2} - \frac{1}{c^2}\frac{\partial}{\partial t}\left(\frac{\partial\left[\epsilon(z,t)E(z,t)\right]}{\partial t}\right) = 0, \tag{C-3}$$

where, using (C-1) and (C-2), the product under the double time derivative operator reads

$$\begin{aligned} &\epsilon(z,t)E(z,t) \\ &\qquad = \sum_{n,p=-\infty}^{+\infty} \epsilon_p E_n e^{j(\omega_0 + (n+p)\omega_\mathrm{m})t} e^{-(\alpha_n + j(\beta_0 + (n+p)\beta_\mathrm{m}))z}. \end{aligned} \tag{C-4}$$

For a sinusoidally space-time modulated permittivity, $\epsilon(z,t) = \epsilon_\mathrm{e}(1 + \delta_\mathrm{m}\cos(\omega_\mathrm{m} t - \beta_\mathrm{m} z))$ [Eq. (7.1)], Eq. (C-1) reduces to

$$\epsilon(z,t) = \epsilon_\mathrm{e}\left(\frac{\delta_\mathrm{m}}{2} e^{-j(\omega_\mathrm{m} t - \beta_\mathrm{m} z)} + 1 + \frac{\delta_\mathrm{m}}{2} e^{+j(\omega_\mathrm{m} t - \beta_\mathrm{m} z)}\right). \tag{C-5}$$

Inserting (C-5) into (C-4), and substituting the result and (C-2) into (C-3) yields

$$\sum_{n=-\infty}^{+\infty}\Bigg(E_n e^{j\omega_n t}e^{-(\alpha_n+j\beta_n)z}((\alpha_n+j\beta_n)^2c^2+\epsilon_{\mathrm{e}}\omega_n^2) + \frac{\delta_{\mathrm{m}}}{2}\omega_{n-1}^2E_ne^{j\omega_{n-1}t}e^{-(\alpha_n+j\beta_{n-1})z} + \frac{\delta_{\mathrm{m}}}{2}\omega_{n+1}^2E_ne^{j\omega_{n+1}t}e^{-(\alpha_n+j\beta_{n+1})z}\Bigg)=0. \quad \text{(C-6)}$$

Considering that the summation runs from $-\infty$ to $+\infty$, this expression may be simplified to

$$\sum_{n=-\infty}^{\infty}e^{j(\omega_n t-(\beta_n-j\alpha_n)z)}\Bigg(((\alpha_n+j\beta_n)^2c^2+\epsilon_{\mathrm{e}}\omega_n^2)E_n + \frac{\delta_{\mathrm{m}}}{2}\omega_n^2(E_{n+1}+E_{n-1})\Bigg)=0. \quad \text{(C-7)}$$

Since this relation must hold for all the values of z and t, it may finally be expressed as

$$E_{n-1}+b_nE_n+E_{n+1}=0, \quad -\infty<n<\infty, \quad \text{(C-8)}$$

where

$$b_n=\frac{2}{\delta_{\mathrm{m}}}\left(1-\frac{(\beta_n-j\alpha_n)^2}{k_{\mathrm{e}n}^2}\right). \quad \text{(C-9)}$$

where $k_{\mathrm{e}n}=\omega_n\sqrt{\epsilon_{\mathrm{e}}}/c$. To find the E_n's for $n<0$, we employ the following set of recursive equations from (C-8) :

$$E_{n-1}+b_nE_n+E_{n+1}=0, \quad \text{(C-10a)}$$

$$E_{n-2}+b_{n-1}E_{n-1}+E_n=0. \quad \text{(C-10b)}$$

Inserting (C-10b) into (C-10a) gives

$$E_{n-1}+b_n\left(-E_{n-2}-b_{n-1}E_{n-1}\right)=-E_{n+1}, \quad \text{(C-11)}$$

and multiplying both sides by E_n yields

$$E_n\left(E_{n-1}+b_n\left(-E_{n-2}-b_{n-1}E_{n-1}\right)\right) = -E_{n+1}\left(-E_{n-2}-b_{n-1}E_{n-1}\right), \quad \text{(C-12)}$$

which can be solved for E_n as

$$E_n = E_{n+1} \frac{E_{n-2} + b_{n-1} E_{n-1}}{-b_n \left(E_{n-2} + b_{n-1} E_{n-1}\right) + E_{n-1}}, \tag{C-13}$$

and may be rewritten as

$$E_n = E_{n+1} \frac{1}{-b_n + \frac{1}{b_{n-1} + \frac{E_{n-2}}{E_{n-1}}}}. \tag{C-14}$$

This relation recursively generalizes to the infinite long division expression

$$E_n = E_{n+1} \frac{1}{-b_n + \frac{1}{b_{n-1} + \frac{1}{-b_{n-2} + \frac{1}{b_{n-3} + \cdots}}}}. \tag{C-15}$$

Similarly, to find E_n for $n > 0$, we form from (C-8) the following set of recursive equations :

$$E_{n-1} + b_n E_n + E_{n+1} = 0, \tag{C-16a}$$

$$E_n + b_{n+1} E_{n+1} + E_{n+2} = 0. \tag{C-16b}$$

Following the same procedure as from in (C-10) to (C-14) for $n < 0$, yields

$$E_n = E_{n-1} \frac{1}{-b_n + \frac{1}{b_{n+1} + \frac{E_{n+2}}{E_{n+1}}}}, \tag{C-17}$$

which generalizes to

$$E_n = E_{n-1} \frac{1}{-b_n + \frac{1}{b_{n+1} + \frac{1}{-b_{n+2} + \frac{1}{b_{n+3} + \cdots}}}}. \tag{C-18}$$

Equations (C-15) and (C-18) recursively provide the amplitude coefficients of the space-time harmonics of the electric field in (C-2) in terms of the excitation electric field E_0 and in terms of the b_n coefficients, which themselves depend on δ_m, ω_m and ω_0.

Let us now derive the dispersion relation, which essentially corresponds to the unknown parameter β_0 depending on ω in (C-2). First, we write (C-8) for $n = 0$, i.e.

$$E_{-1} + b_0 E_0 + E_{+1} = 0. \tag{C-19}$$

where E_{-1} and E_{+1} can also be expressed in terms of E_0 using (C-15) for $n = -1$ and (C-18) for $n = +1$, respectively, transforming (C-19) into

$$\frac{E_0}{-b_{-1}+\frac{1}{b_{-2}+\frac{1}{-b_{-3}+\frac{1}{b_{-4}+\dots}}}}+b_0E_0+\frac{E_0}{-b_1+\frac{1}{b_2+\frac{1}{-b_3+\frac{1}{b_4+\dots}}}}=0. \tag{C-20}$$

Dividing this relation by E_0 finally yields

$$\frac{1}{-b_{-1}+\frac{1}{b_{-2}+\frac{1}{-b_{-3}+\frac{1}{b_{-4}+\dots}}}}+b_0+\frac{1}{-b_1+\frac{1}{b_2+\frac{1}{-b_3+\frac{1}{b_4+\dots}}}}=0, \tag{C-21}$$

which is a relation based on the b_n's in (C-9). For a given set of modulation parameters $(\delta_\mathrm{m}, \epsilon_\mathrm{e}, \omega_\mathrm{m}, \beta_\mathrm{m}, \alpha_n)$ and variables ω_0 and β_0, Eq. (C-21) provides the dispersion diagram of the system, $\beta(\omega) = \beta_0(\omega) + n\beta_\mathrm{m}$. The resolution is performed numerically, setting ω_0 and finding the corresponding β_0 (or vice-versa), and repeating the operation across the frequency range of interest.

Uplink and Downlink Conversions

For weak modulation, $\delta_\mathrm{m} \ll 1$, the wave amplitudes E_n in (C-15) and (C-18) for $\mid n \mid > 1$ are negligible. Moreover, since the leaky-wave antenna is designed to support radiation mostly at $\omega_\mathrm{r} = \omega_\mathrm{s} + \omega_\mathrm{m}$, corresponding to the higher harmonic E_{+1}, the amplitude of the lower harmonic E_{-1}, corresponding to $\omega_\mathrm{s} - \omega_\mathrm{m}$, can be neglected. Then, the system of equations (C-8) reduces to

$$b_0E_0 + E_{+1} = 0, \tag{C-22a}$$

$$E_0 + b_1E_{+1} = 0, \tag{C-22b}$$

which has non-trivial solution only if

$$b_0b_1 = 1. \tag{C-23}$$

Solving (C-23) with (C-9) for $\alpha_n \ll \beta_n$ and $\delta_\mathrm{m}^2 \to 0$ (weak modulation) yields

$$\beta_0 = \pm\beta_\mathrm{um} \pm \frac{\delta_\mathrm{m}}{4}\sqrt{\beta_\mathrm{um}\beta'_\mathrm{um}}, \tag{C-24}$$

where the upper (positive) signs are for forward ($+z$) propagation and the lower (negative) signs are for backward ($-z$) propagation, $\beta'_\mathrm{um} = \beta_\mathrm{um} + \beta_\mathrm{m}$, and β_um is given by (7.5). Then, using (C-22b),

$$E_1 = \frac{\delta_\mathrm{m}E_0\beta'_\mathrm{um}}{\delta_\mathrm{m}\sqrt{\beta_\mathrm{um}\beta'_\mathrm{um}} - 2\alpha_1^2/\beta'_\mathrm{um} - j\alpha_1\left(\delta_\mathrm{m}\sqrt{\beta_\mathrm{um}/\beta'_\mathrm{um}} + 4\right)}, \tag{C-25}$$

and the uplink power conversion gain reads then

$$\begin{aligned}\frac{P_{+1}}{P_0} &= \left|\frac{E_{+1}}{E_0}\right|^2 \\ &= \left|\frac{\delta_\mathrm{m}^2\beta_\mathrm{um}'^2}{(\delta_\mathrm{m}\sqrt{\beta_\mathrm{um}\beta_\mathrm{um}'} - 2\alpha_1^2/\beta_\mathrm{um}')^2 + \alpha_1^2\left(\delta_\mathrm{m}\sqrt{\beta_\mathrm{um}/\beta_\mathrm{um}'} + 4\right)^2}\right|.\end{aligned} \tag{C-26}$$

Note that in the absence of radiation ($\alpha_1 = 0$), this expression would reduce to

$$\frac{P_{+1}}{P_0} = \left|\frac{\beta_\mathrm{um} + \beta_\mathrm{m}}{\beta_\mathrm{um}}\right|, \tag{C-27}$$

which is the Manley-Rowe relation [200, 201], verifying the conservation of energy in the space-time modulated system, and indicating power gain since $\beta_\mathrm{m} > 0$.

A similar procedure provides the corresponding results for the downlink using (C-22a). The results are

$$E_0 = \frac{\delta_\mathrm{m}E_1\beta_\mathrm{um}}{\delta_\mathrm{m}\sqrt{\beta_\mathrm{um}\beta_\mathrm{um}'} - 2\alpha_0^2/\beta_\mathrm{um} - j\alpha_0\left(\delta_\mathrm{m}\sqrt{\beta_\mathrm{um}'/\beta_\mathrm{um}} + 4\right)}, \tag{C-28}$$

and

$$\begin{aligned}\frac{P_0}{P_{+1}} &= \left|\frac{E_0}{E_{+1}}\right|^2 \\ &= \left|\frac{\delta_\mathrm{m}^2\beta_\mathrm{um}^2}{(\delta_\mathrm{m}\sqrt{\beta_\mathrm{um}\beta_\mathrm{um}'} - 2\alpha_0^2/\beta_\mathrm{um})^2 + \alpha_0^2\left(\delta_\mathrm{m}\sqrt{\beta_\mathrm{um}'/\beta_\mathrm{um}} + 4\right)^2}\right|,\end{aligned} \tag{C-29}$$

reducing to the Manley-Rowe relation

$$\frac{P_0}{P_{+1}} = \left|\frac{\beta_\mathrm{um}}{\beta_\mathrm{um} + \beta_\mathrm{m}}\right| \tag{C-30}$$

since $\alpha_0 = 0$, indicating power loss ($\beta_\mathrm{m} > 0$).

APPENDIX D
List of Publications

Peer-Reviewed Journal Publications

1. S. Taravati, N. Chamanara, and C. Caloz, “Nonreciprocal electromagnetic scattering from a periodically space-time modulated slab and application to a quasi-sonic isolator,” *Accepted in Phys. Rev. B, arXiv preprint arXiv :1705.06311*, 2017.
2. S. Taravati, B. A. Khan, S. Gupta, K. Achouri, and C. Caloz, “Nonreciprocal nongyrotropic magnetless metasurface,” *IEEE Trans. Antennas Propagat.*, vol. 65, no. 7, Jul. 2017.
3. N. Chamanara, S. Taravati, Z.-L. Deck-Léger, and C. Caloz, “Optical isolation based on space-time engineered asymmetric photonic bandgaps,” *Phys. Rev. B*, vol. 96, no. 15, Oct. 2017.
4. S. Taravati and C. Caloz, “Mixer-duplexer-antenna leaky-wave system based on periodic space-time modulation,” *IEEE Trans. Antennas Propagat.*, vol. 65, no. 2, pp. 1–11, Feb. 2017.
5. S. Taravati, , S. Gupta, Q. Zhang, and C. Caloz, “Enhanced bandwidth and diversity in real-time analog signal processing (R-ASP) using nonuniform c-section phasers,” *IEEE Microw. Wireless Compon. Lett.*, vol. 26, no. 9, pp. 663–665, Sept. 2016.

Conference Publications

1. N. Chamanara, S. Taravati, Z.-L. Deck-Léger and C. Caloz, “Electromagnetic nonreciprocity and perfect mixing in space-time engineered asymmetric bandgaps,” in *IEEE AP-S Int. Antennas Propagat. (APS)*, San Diego California, USA, July 2017.
2. C. Caloz, K. Achouri, G. Lavigne, Y. Vahabzadeh, L. Chen, S. Taravati and N. Chamanara, “A guided tour in metasurface land : Discontinuity conditions, design and applications,” in 2017 *IEEE International Conference on Computational Electromagnetics (ICCEM)*, pp. 310-311, 2017.
3. S. Taravati and C. Caloz, “Space-time modulated nonreciprocal mixing, amplifying and scanning leaky-wave antenna system,” in *IEEE AP-S Int. Antennas Propagat. (APS)*, Vancouver, Canada, 2015.
4. S. Taravati and C. Caloz, “Versatile phasers constituted of coupling-free nonuniform stub-loaded transmission lines,” in *IEEE European Microw. Conf. (EuMC)*, Paris,

France, Sept. 2015.

5. S. Taravati, Q. Zhang, and C. Caloz, “Non-uniform c-section phasers for enhanced design flexibility in radio analog signal processing,” in *IEEE European Microw. Conf. (EuMC)*, Rome, Italy, Oct. 2014.